



Filipe Daniel Fernandes

# **SURFACE MODIFICATION OF MOLDS AND ACESSORIES FOR THE GLASS INDUSTRY**

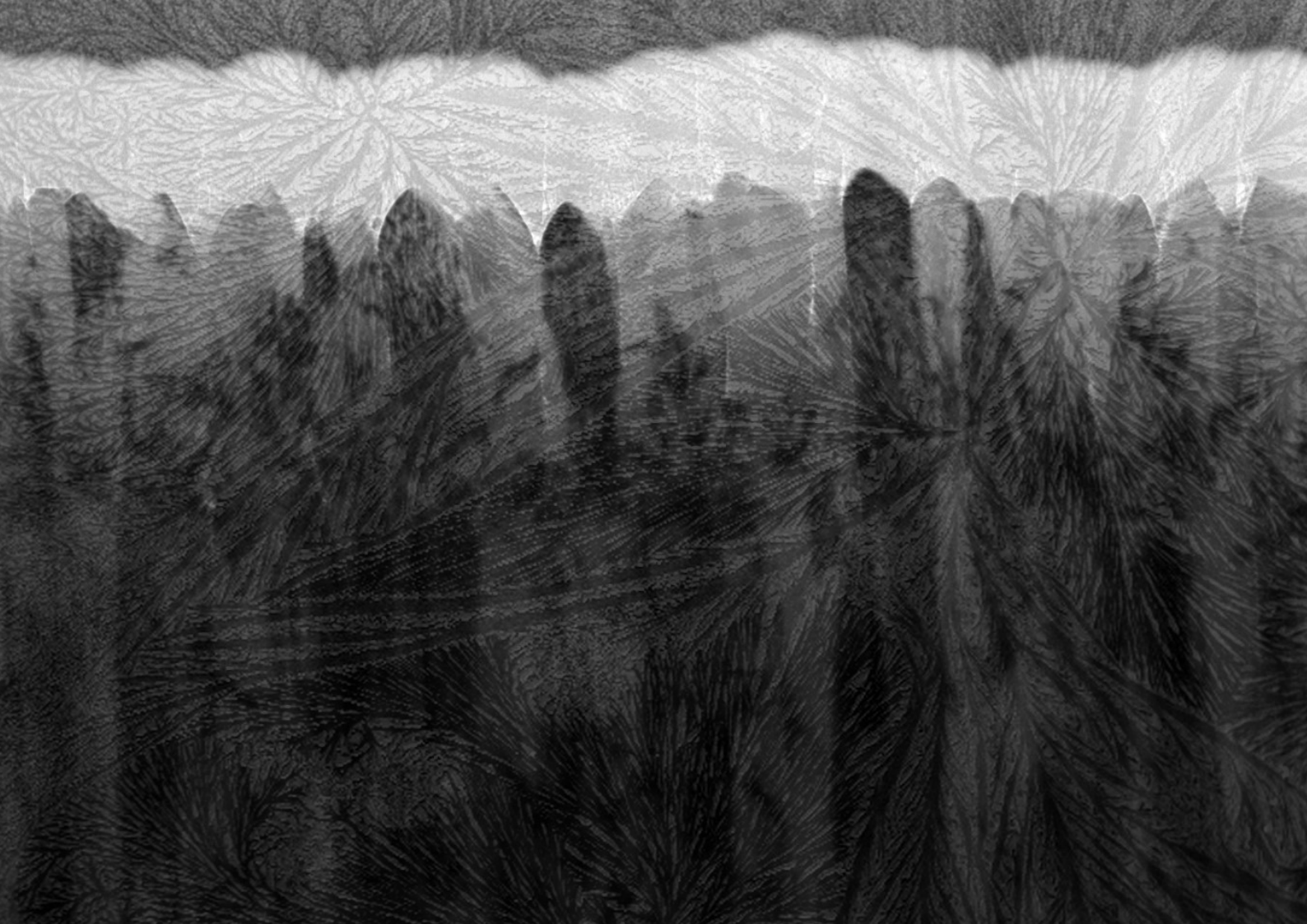
Doctor of Philosophy Thesis in Mechanical Engineering, Production Technology branch, supervised by Professor Altino de Jesus Roque Loureiro and Professor Albano Augusto Cavaleiro Rodrigues de Carvalho and submitted to the Mechanical Engineering Department of the Faculty of Sciences and Technology of the University of Coimbra.

2014



UNIVERSIDADE DE COIMBRA





Filipe Daniel Fernandes

# **SURFACE MODIFICATION OF MOLDS AND ACESSORIES FOR THE GLASS INDUSTRY**

Doctor of Philosophy Thesis in Mechanical Engineering, Production Technology branch, supervised by Professor Altino de Jesus Roque Loureiro and Professor Albano Augusto Cavaleiro Rodrigues de Carvalho and submitted to the Mechanical Engineering Department of the Faculty of Sciences and Technology of the University of Coimbra.

2014



UNIVERSIDADE DE COIMBRA



**Bolsa de Doutoramento (SFRH/BD/68740/2010)**



Governo da República Portuguesa



UNIÃO EUROPEIA  
Fundo Social Europeu



## Acknowledgments

Many people have contributed and encouraged me along all the years of this research, I thank all of them, and I hope I have gathered a bit of their best.

Above all, I want to express my sincere gratitude to my supervisors: *Albano Cavaleiro* and *Altino Loureiro*, for their scientific guidance, commitment and availability during the execution of this thesis. Their bright mind and wisdom brought to me many insights and knowledge that was the key success for this thesis. I'm also extremely indebted to them for all the opportunities I had of involvement with various enterprises and scientific research centers as well as of visiting several wonderful places in the world in the framework of conferences and collaborations.

I have had the pleasure of working with and learning from a huge number of other professors and researchers in different countries. I would like to specially thank professors *Amilcar Ramalho*, *Tomas Polcar*, *Josep Guilemany* and *Jerzy Morgiel* for all the collaboration, scientific discussion and open access to their laboratories.

CEMUC in the person of its chairman, Professor Valdemar Fernandes, is greatly acknowledged by the possibility of carrying out most of this work within this research center.

Thanks are also due to INTERMOLDE company for the support and collaboration in the initial stage of the thesis. Thanks are also extended to TEandM Enterprise.

It is essential to emphasize the crucial role of IPN (Instituto Pedro Nunes) on my work and results, by making available laboratorial equipment for the development and characterization of the samples I produced.

Special thanks to my friends and research colleagues from ECAT, Surface Engineering and Nanomaterials and Micromanufacturing groups of CEMUC. I have spent marvelous moments in their companionship. These thanks are extended to all the young and senior members from

the different international groups (Barcelona, Prague, Southampton and Guangxi (China)) I visited, who welcomed me and helped me during my training periods there.

To my close friends thank you for all the great moments.

I would like to acknowledge the funding provided by the FCT (Fundação para a Ciência e Tecnologia), through SFRH/BD/68740/2010 fellowship and the projects AUTOMATIN “5380”, PLUNGETEC “13545” and PTDC/EME-TME/122116/2010.

Finally, I would like to thank my parents, grandparents and sister who permanently gave me their support during this hard but reward time. Without their patience and good advices, I would not have been able to take advantage of the opportunity I was given to improve my education. This thesis is dedicated to them. Last but not the least, I thank you Cláudia for your daily personal support and encouragement in all good and bad times.



## Abstract

Coatings are frequently applied on molds and accessories for the glass industry in order to restrict surface degradation such as oxidation, corrosion, abrasion and wear of the structural material, thereby decreasing the maintenance costs and increasing the lifetime and performance of the components. However, in order to obtain accurate lifetime expectancies and performance of the coatings it is necessary to have a complete reliable understanding of their properties.

This thesis is on the improvement of the surface properties and integrity of molds, in order to increase their durability, through the application of different types of coatings. Two methodologies were followed to reach such demands: (i) optimization of coatings currently used in molds surface protection (Ni-based alloys deposited by Plasma Transferred Arc - PTA); (ii) synthesis and characterization of new coatings with improved functionalities, deposited by emergent deposition processes such as APS - Atmospheric Plasma Spraying (effect of nanostructured ZrO<sub>2</sub> additions on Ni-based alloy coatings) and DCRMS - Direct Current Reactive Magnetron Sputtering (influence of V additions on the properties of TiSi(V)N thin films).

The dilution of the substrate in PTA process was shown to strongly influence the structure and, consequently, the hardness, the oxidation resistance and the tribological behavior of the coatings; with increasing dilution, a detrimental effect on these properties was observed due to the incorporation of base material. However, in relation to the tribological behavior, a beneficial effect at high temperature was demonstrated due to the fast formation of oxide layers which protect the coating surface against wear. The post-weld heat treatment performed at coatings reduced the hardness of the partially melted and heat affected zones without affecting the coatings hardness; whereas the coatings hardness and wear resistance was improved with annealing treatment. Thus, the best performing coating could only be achieved by a proper selection of the deposition conditions, in order to get the best compromise between mechanical properties, high temperature oxidation behavior and wear resistance of the coatings.

The impact promoted by nanostructured ZrO<sub>2</sub> additions on the microstructure of a Ni-based alloy depended on the way how the coatings were deposited by APS process, using: (i) nanostructured ZrO<sub>2</sub> and Ni-alloy powders previously mixed by mechanical alloying or (ii)

the same powders supplied separately. A homogeneous and compact microstructure with small zirconia particles evenly distributed in the matrix was achieved in the first case, while a porous microstructure, full of semi-melted Ni powders with large particles of  $ZrO_2$  entrapped in their boundaries, suggesting a brittle behavior, was deposited in the second. In both cases the hardness and wear behavior of  $ZrO_2$  rich coatings were improved in relation to the Ni-based alloy. The coatings deposited from mechanically alloyed powders revealed to be much more tribologically performing due to their compact structure and even distribution of zirconia particles. All the APS coatings showed higher hardness values than the Ni-based coatings deposited by PTA; however, their micro-abrasion resistance was worse, due to the lack of cohesion between the powders.

The analysis by XRD of the structure of V rich  $TiSi(V)N$  coatings, deposited by DCRMS, revealed that V incorporation in the  $TiSiN$  system shifted the peaks to higher angles, indicating the formation of a substitutional solid solution based on  $TiN$  phase, where Ti atoms are replaced by the smaller V ones. On the other hand, by similar reason, XRD of  $TiSiN$  films revealed that a nanocomposite structure consisting of  $TiN$  grains enrobed by a Si-N matrix was not formed. In fact, with Si addition a shift of the diffraction peaks of  $TiN$  phase to higher angles was observed which, in combination with similar compressive residual stresses, also supported the formation of a substitutional solid solution. V additions showed to successfully improve the hardness and tribological behavior of  $TiSi(V)N$  films, as a result of the substitutional solid solution formation. On the other hand, the formation of the  $V_2O_5$  phase during the sliding contact acts as a lubricious tribo-film, protecting the coating against wear. The addition of Si or V strongly influenced in opposite directions the oxidation resistance of the coatings. Si incorporations in  $TiN$  increased significantly the oxidation resistance of the films, whereas the opposite occurred in V containing coatings. In this latter case, the rapid V ions out-diffusion through the oxide scale inhibited the formation of a continuous protective silicon oxide layer, which is responsible for the excellent oxidation behavior of  $TiSiN$  films. V rich coatings showed lower oxidation resistance than PTA-deposited Ni-based coatings, but superior hardness values and better tribological behavior was found in relation to both PTA and APS deposited coatings.

**Keywords:** Glass Industry, Molds surface protection, Ni-based thick coatings,  $TiSi(V)N$  thin films, self-lubricant coatings.

## Resumo

Frequentemente são aplicados diferentes tipos de revestimentos em moldes e acessórios para a indústria do vidro, de forma a atenuar a degradação das suas superfícies, devida às condições extremas de oxidação, corrosão, abrasão e desgaste a que estão sujeitas. Deste modo, é possível, diminuir os custos de manutenção e aumentar o tempo de vida e a eficácia destes componentes. No entanto, de forma a maximizar o desempenho dos revestimentos, é necessário compreender a inter-relação entre as suas características e propriedades funcionais.

Esta tese é dedicada à melhoria das propriedades da superfície dos moldes, de forma a aumentar a sua durabilidade e desempenho, através da aplicação de diferentes tipos de revestimentos. No sentido de enfrentar este desafio, foram seguidas duas metodologias alternativas: (i) otimização de revestimentos já utilizados na proteção da superfície de moldes (ligas à base de Ni depositadas por PTA\* (plasma de arco transferido); (ii) síntese e caracterização de novos revestimentos mais resistente e com melhores propriedades, depositados por processos de deposição emergentes no mercado, tal como são os casos do APS\*\* - projeção em plasma atmosférico (efeito da adição de ZrO<sub>2</sub> nanoestruturada numa liga à base de níquel) e do PVD\*\*\* - deposição física em fase de vapor (influência da adição de V nas propriedades de revestimentos cerâmicos do sistema TiSi(V)N).

A diluição do substrato, promovida pelo processo PTA, mostrou influenciar a estrutura e, conseqüentemente, diminuir a dureza, a resistência à oxidação e a resistência ao desgaste à temperatura ambiente dos revestimentos à base de Ni. No entanto, teve um efeito benéfico no comportamento tribológico a temperaturas elevadas, permitindo a rápida formação de uma camada de óxido, que protege a superfície contra o desgaste. O tratamento térmico efectuado aos revestimentos após deposição reduziu a dureza das zonas termicamente afetada pelo calor e parcialmente fundida. Além disso, o tratamento de envelhecimento realizado aos revestimentos permitiu aumentar a sua dureza e a sua resistência ao desgaste. Assim, o revestimento com melhor desempenho só pode ser obtido seleccionando criteriosamente as condições de deposição que originam o melhor compromisso entre propriedades mecânicas, comportamento à oxidação a alta temperatura e resistência ao desgaste.

---

\* PTA – Do inglês – Plasma Transferred Arc

\*\* APS – Do inglês – Atmospheric Plasma Spraying

\*\*\* PVD – Do inglês – Physical Vapor Deposition

A adição de zircônia nano-estruturada à liga de níquel depositada por APS tem um impacto diferente na microestrutura dos revestimentos, consoante são usados pós de Ni e ZrO<sub>2</sub> previamente misturados por síntese mecânica ou os mesmos pós alimentados separadamente. Quando depositados com os pós preparados por síntese mecânica, os revestimentos exibiram uma estrutura homogênea e compacta com pequenas partículas de zircônia uniformemente distribuídas na matriz de Ni. Por outro lado, quando depositados separadamente foi obtida uma estrutura muito porosa com pós de Ni semi-fundidos e com partículas de ZrO<sub>2</sub> inseridas na sua interface, sugerindo um comportamento frágil. Independente do procedimento de deposição, em ambos os casos a dureza e a resistência ao desgaste dos revestimentos foi melhorada com a adição de ZrO<sub>2</sub>. Contudo, os revestimentos depositados usando pós produzidos por síntese mecânica revelaram possuir melhor *performance*, devido à sua estrutura compacta e distribuição uniforme da ZrO<sub>2</sub>. Todos os revestimentos depositados por APS revelaram possuir valores de dureza superiores aos revestimentos depositados por PTA; no entanto, a sua resistência à abrasão mostrou ser bastante inferior devido à falta de coesão entre os pós.

As análises de difracção de raios-X realizadas aos filmes TiSi(V)N ricos em V revelaram que os picos de difracção se deslocam para ângulos superiores com o aumento do teor em V, sugerindo a formação de uma solução sólida substitucional, com o V de menor raio atômico a substituir átomos de Ti na estrutura de base do TiN. Por outro lado, a análise realizada aos revestimentos de TiSiN revelou que a estrutura nanocompósita (grãos de TiN envolvidos numa matriz de Si-N) não foi alcançada. Com efeito, a adição de Si ao sistema TiN também deslocou os picos de difracção para ângulos superiores o que, considerando o mesmo nível de tensões residuais medidos em todos os revestimentos, indicou a formação de uma solução sólida substitucional onde os átomos mais pequenos de Si substituíram os átomos de Ti na rede do TiN. A adição de V ao sistema TiSiN permitiu melhorar as propriedades mecânicas e tribológicas devido à formação da solução sólida substitucional. A melhoria das propriedades tribológicas está relacionada com a formação da fase V<sub>2</sub>O<sub>5</sub>, no topo da superfície do filme, que age como lubrificante sólido e, portanto, protege o revestimento do desgaste. A resistência à oxidação de revestimentos ricos em Si e V mostrou ser influenciada em sentidos contrários por estes elementos. Assim, a adição de Si ao sistema TiN aumentou significativamente a resistência à oxidação dos filmes enquanto a adição de V ao sistema TiSiN promoveu uma diminuição abrupta na resistência à oxidação. Esta diminuição da resistência à oxidação foi atribuída à rápida difusão dos iões de V através da

camada de óxido formada, que inibiu a formação de uma camada contínua e protectora de óxido de silício, contrariamente ao que acontece nos revestimentos TiSiN. Os filmes ricos em V apresentaram menor resistência à oxidação do que os revestimentos espessos depositados por PTA; no entanto, a sua dureza e resistência ao desgaste foram bastante superiores à dos revestimentos espessos depositados por PTA ou APS.

Palavras-chave: Indústria vidreira, Protecção da superfície de moldes, Revestimentos espessos de Níquel, Revestimentos finos de TiSi(V)N, Revestimentos auto-lubrificantes.

\* PTA – Do inglês – Plasma Transferred Arc

\*\* APS – Do inglês – Atmospheric Plasma Spraying

\*\*\* PVD – Do inglês – Physical Vapor Deposition



# Index

Acknowledgments .....	i
Abstract.....	iii
Resumo .....	v
Index .....	ix
List of Figures.....	xi
List of Tables .....	xiii
Nomenclature.....	xv
1. Introduction .....	1
List of papers that are the basis of this thesis .....	7
2. Historical perspective.....	9
3. Effect of the arc current variation on the properties of Ni-based coatings deposited by PTA process.....	21
3.1. Introduction.....	21
3.2. Microstructure and hardness of the coatings .....	22
3.3. Oxidation resistance and diffusion mechanisms.....	26
3.4. Tribological behavior.....	28
3.4.1. Micro-scale abrasion tests .....	28
3.4.2. Pin-on-disc tests .....	30
4. Influence of nanostructured ZrO <sub>2</sub> additions on the wear resistance of Ni-based alloy coatings deposited by APS .....	33
4.1. Introduction.....	33
4.2. Microstructure and hardness of the coatings .....	34
4.3. Tribological behavior.....	35
5. Study of the influence of V additions on the properties of TiSi(V)N films deposited by DC reactive magnetron sputtering .....	39

5.1. Introduction .....	39
5.2. Microstructure, residual stresses and mechanical properties .....	40
5.3. Oxidation resistance and diffusion mechanisms .....	44
5.4. Tribological behavior .....	47
6. Conclusions and Future Research.....	51
7. References.....	59
Annex A .....	71
Annex B .....	87
Annex C .....	97
Annex D .....	113
Annex E .....	123
Annex F .....	145
Annex G .....	159
Annex H .....	171
Annex I .....	187



## List of Figures

Figure 2.1 - Components used in glass containers production.....	10
Figure 3.1 - Dilution induced by PTA process using different weldments: specimen 1 - 100 A, specimen 2 and 3 - 128A, specimen 4 – 140 A. ....	23
Figure 3.2 - Optical micrographs of: a) specimen 1, b) specimen 2, c) specimen 4, d) interface of specimen 1.....	24
Figure 3.3 - Hardness profile across the interface of PTA specimens. ....	25
Figure 3.4 - Hardness profile across the interface after PWHT in specimen 4. ....	26
Figure 3.5 - Isothermal oxidation curves at 800 and 900 °C of the: a) coating deposited using 100 A arc current, b) coating deposited using 128 A arc current. ....	27
Figure 3.6 - Specific wear rate of Ni-based coatings in as-deposited and annealed conditions from Annex A and C, evaluated in a micro-scale abrasion equipment. ....	29
Figure 3.7 - Variation of the wear rate of the as deposited PTA coatings and the gray cast iron with testing temperature. ....	31
Figure 4.1 - SEM morphology of the: a) Ni-based alloy coating, b) nanostructured ZrO <sub>2</sub> coating, c) and d) Ni+20% Dual and Ni+40% Dual, respectively, e) and f) Ni+20% MA and Ni+40% MA, respectively.....	35
Figure 4.2 - Specific wear rate of coatings calculated from the reciprocating tribological tests. ....	37
Figure 4.3 - Evolution of the wear behavior as a function of the parameter “normal load × sliding distance”. ....	38
Figure 4.4 - Specific wear rate of coatings, calculated from the slope of a straight line fitted to the points plotted in Figure 4.3.....	38
Figure 5.1 - XRD patterns of TiSiN coatings with Si content ranging from 0 to 12.6 at.% and S1-y coatings with V additions.....	41
Figure 5.2 - a) Effect of Si content on the hardness and Young’s modulus for the TiN system. b) Effect of V content on the hardness and Young’s modulus for coating S1-0.....	42
Figure 5.3 - a) Adhesion critical loads values for the dissimilar coatings. Coatings were scratched as the normal force was increased linearly from 5 to 70N. L <sub>c2</sub> critical load for TiN coating was > 70 N. b), c) First coating cracking and first chipping observed on the scratch track of coating S2-4, respectively. ....	44

Figure 5.4 - a) Thermogravimetric isothermal analysis of coatings exposed at different temperatures. Cross section morphology of coating: a) S2-0 oxidized at 900 °C during 1 h, b) S2-8 oxidized at 600 °C during 30 min.....	45
Figure 5.5 - Wear rate of the coatings tested against Al <sub>2</sub> O <sub>3</sub> and HSS balls.....	48
Figure 5.6 - Evolution of the wear behavior as a function of the parameter “normal load × sliding distance”.....	49
Figure 5.7 - Specific wear rate of coatings, calculated from the slope of a straight line fitted to the points plotted in Figure 5.6. ....	49
Figure 6.1 - Hardness of coatings studied in the aim of this thesis, deposited by different deposition techniques.....	53
Figure 6.2 - Comparison of the oxidation weight gain of Ni-based coatings deposited by PTA and TiSi(V)N ones deposited by DC reactive magnetron sputtering.....	54
Figure 6.3- Specific wear rate of coatings calculated from the micro-scale abrasion tests. ....	56
Figure 6.4 - Specific wear rate of coatings calculated from the pin-on-disc tests. ....	57
Figure 6.5 - Specific wear rate of coatings calculated from the pin-on-disc tests performed at high temperature. ....	57

## List of Tables

Table 2.1 - Comparison of the characteristics of several hardfacing and thermal spraying processes [9, 55-60].	15
Table 2.2 - Typical sequential tasks used in molds production.	17
Table 5.1 - Coatings deposited and their nomenclature.	40



## Nomenclature

*APS - Atmospheric plasma spraying*

*BM - Base material*

*DC - Direct current*

*DCRMS - Direct current reactive magnetron sputtering*

*FS - Flame spraying*

*FZ - Fusion zone*

*GTAW - Gas tungsten arc welding*

*HAZ - Heat affected zone*

*HT - High temperature*

*HVOF - High velocity oxy-fuel*

*MA - Mechanical alloying*

*PMZ - Partial melted zone*

*PTA - Plasma transferred arc*

*PVD - Physical vapor deposition*

*PWHT - Post-weld heat treatment*

*SEM-EDS - Scanning electron microscopy with energy dispersive spectroscopy*

*STEM - Scanning transmission electron microscope*

*TGA - Thermal gravimetric analysis*

*WDS - Wavelength-dispersive spectroscopy*

*XRD - X-ray Diffraction*



# Chapter I

## **1. Introduction**

The necessity for higher performance and increased efficiency of components working in extreme harsh conditions has been met with the use of more advanced materials. Coatings have been developed over the last decades as a potential solution for these applications due to their superior properties when compared to bulk materials, allowing extending the performance and lifetime of components. This was the case of the glass industry, where the components are actually coated with hard and wear resistant materials in order to resist to the direct contact with the melted glass which promotes very severe abrasion, corrosion and fatigue at high temperature. The current European glass container market is approximately 30-40 billions of containers. Due to globalization, there has been a growing demand for glass containers production at reduced costs, with increasing shape complexity, putting an increasing pressure on glass producers who are seeking molds which allow increasing production rates with higher quality. In these very harsh conditions, further degradation of the mold surfaces occurs due to more intense thermal cycles leading to higher mechanical strains and plastic deformation with the consequent fatigue, oxidation and wear problems. Furthermore, other common problems such as worn-out geometries or surface and base material cracks, often lead to the breakdown of the coating after few working cycles. The combined effect of the harsh conditions with a faulty design or a defective material, associated with bad working practices, induces the premature failure of the components.

Besides the direct costs of the molds, there is a direct impact on the production due to the increasing machine down times, higher process instability, poor product quality and higher maintenance costs. Therefore, any optimized solution to achieve the best performance of molds should be focused on the proper selection of the base material, the coating and its deposition process. Unfortunately, the lack of credible solutions have limited the application of coated components in glass industry, hiding the great relevance and impact they could have for the industrial development in this area. Thus, this thesis is devoted to the improvement of surface properties and integrity of molds, in order to improve their durability, through either the optimization of conventional coatings currently applied on mold surfaces or the development of new coating systems deposited by emergent technologies. Both cases show potential to over-support the in service conditions of the molds, allowing improving their durability, lifetime and performance.

Presently, the molds for glass industry are manufactured either in low cost materials, such as cast iron and low carbon steel, offering a good relative performance at high temperature, or in copper-nickel alloys (bronze), due to their excellent thermal conductivity combined with reasonable hardness and wear resistance, which allow an increasing production rate of glass containers. In some cases, specific zones of the molds are coated, mainly with Fe, Co or Ni-based alloys, with the aim of increasing their service life, owing to their excellent oxidation and mechanical performance under high temperature conditions. Several hardfacing and thermal spraying processes have been used to coat the molds: i) Plasma Transferred Arc (PTA), and Gas Tungsten Arc Welding (GTAW) and ii) Flame Spraying (FS) and High Velocity oxy Fuel (HVOF), respectively. Hardfacing processes have been preferentially used in the protection of molds surface, due to the strong metallurgical bond promoted between the coating and substrate, condition required to avoid the catastrophic failure in service. In thermal spraying processes only a mechanical bonding is established.

Among the hardfacing processes referred above, PTA has been the most versatile and used, due to its ability to deposit very thick coatings with low porosity and high production rates. However, the final quality of coatings is largely influenced by the process parameters; their incorrect selection leads frequently to problems such as the formation of porosity or cracks in both the coating and the substrate, lack of adhesion of the coating to the substrate and changes in the chemical composition of the coating metal alloy, compromising the performance in service. Hence, a reliable understanding of the influence of the deposition parameters on the coatings properties is required, in order to optimize the lifetime expectancies and performance of the coatings. Presently, the tendency is to increase the



dilution of the substrate to avoid adhesion problems and, therefore, not to compromise the molds life, even if the mechanical properties, oxidation resistance and wear performance are deteriorated. This will be the first issue in discussion in this thesis: how the increase in dilution of the base material (cast iron), induced by the change in arc current, influences the properties of Ni-based coatings deposited by the PTA process.

An alternative route to improve the quality and performance of molds is the use of new, thick or thin coatings deposited by emerging technologies that can lead to significant improvements on the mechanical properties. Atmospheric Plasma Spraying (APS) and Physical Vapor Deposition (PVD) are good examples of these deposition processes which allow to achieve either metallic, ceramic or composite coatings. Such technologies and materials have shown already to be potential candidates for improving the performance of mechanical components and parts used in other industries where high oxidation, corrosion and wear resistances are required. When compared to traditional deposition processes (PTA, GTAW and FS), their main disadvantage is related to their high cost of investment and production and, in some cases, lower coatings adhesion. Therefore, any development on this field for molds protection should be focused on solutions that withstand the severe conditions to which molds are submitted, extending their service life sufficiently, in order to justify their higher cost. This is the second part of this thesis: new solutions based on thick and thin coatings, deposited by APS and PVD processes, respectively. In the first case, the influence of nanostructured  $ZrO_2$  additions to Ni-based alloy coatings deposited by APS process was studied. The idea of this study was to take advantage of the high hardness and oxidation resistance of  $ZrO_2$  to improve the oxidation resistance and the mechanical and wear properties of Ni-based coatings. In relation to other thermal spraying processes, such as HVOF, APS was selected due to its high potential to deposit materials with high melting temperature (which is the case of  $ZrO_2$ ), although lower particles velocities are achieved; furthermore, in relation to the PTA process, APS normally gives rise to coatings with much higher hardness. Apart from the higher cost, the main disadvantage of APS coatings is the need of their subsequent fusion when applied in parts for the glass industry, in order to obtain compact and more performing coatings; the application of this operation is not covered in this thesis.

On the other hand, PVD technique has been extensively used to develop new coating materials, due to its versatility. This process allows "sweep" the chemical composition of a coating system composed by two or more chemical elements, by changing the deposition parameters, producing small quantities of material that can be characterized in order to optimize the best formulation. Moreover, in comparison to thick coatings, PVD allows the

deposition of films with much better properties, particularly the mechanical properties, for which it is common to have improvements of two to four times. However, despite the excellent properties of the films and the versatility of the process, its application in components for the glass industry has been postponed, since the much smaller thickness, in the micrometer order, has been seen unattractive to the industrial eyes when compared to thick coatings. However, the experience gained in the application of such PVD films in other fields of the metalworking industries (for example in machining, stamping, etc), where the life-time of the coated parts has been easily increased by one to two orders of magnitude, allows predicting the success of these films in the protection of molds surfaces for the glass industry. Over the last decades a large number of films (ceramic and composite) have been developed for high temperature applications, among which the most studied systems were nitrides, carbides and oxides of Ti, Cr or Al, whose properties (mechanical, oxidation, corrosion, wear, etc) have been successfully improved by the addition of other chemical elements. One of the biggest advantages of thin coatings over thick ones is the possibility of using ceramics as protection material. In fact, ceramic materials cannot be used in the surface protection of molds for glass parts, due to their low thermal conductivity, which impede the efficient cooling of the base material, decreasing the productivity of the process. This difficulty can be overcome if these materials are deposited as thin coatings.

In this thesis, the addition of a specific element (vanadium) to ceramic films (TiSiN), deposited by DC reactive magnetron sputtering, was studied. TiSiN is one of the best PVD deposited coatings for high temperature applications and, with V incorporation, it is expected to improve the mechanical properties and, at the same time, make them self-lubricant at high temperatures. Currently, in the glass containers production, the walls of the molds are frequently wet with liquid lubricant to avoid the adhesion of the melted glass to the molds surface facilitating the removal of glass containers. Frequently, these lubricants (graphite based lubricants) contain small amounts of sulfur which combined to oxygen forms sulfuric acid that erodes the mold surfaces creating holes and, therefore, defects that lead to the premature failure of the mold. Although V additions have been reported to improve the mechanical properties and the tribological performance of some binary and ternary coating systems, at high temperature V rapidly diffuses to the surface leading to the loss of its lubricious effect after a critical short time. Hence, TiSiN system was selected due to its very high oxidation resistance, similar to the ternary systems CrAlN and TiAlN, where V incorporation was already studied, but with much better mechanical properties. Moreover, if deposited with a nanocomposite structure (TiN grains embedded in a Si<sub>3</sub>N<sub>4</sub> matrix) by

changing the thickness of the antidiffusion barrier  $\text{Si}_3\text{N}_4$  matrix, the control of V diffusion can be achieved.

Thus, the objectives of this research can be summarized as follows:

i) To analyze the effect of the arc current variation on the substrate dilution and, therefore, on the chemical composition, microstructure, oxidation and tribological performance of Ni-based coatings deposited by PTA process over gray cast iron. The influence of an annealing treatment on the morphology, mechanical properties, and wear performance of coatings will be also discussed.

ii) To study the influence of the addition of nanostructured  $\text{ZrO}_2$  to Ni-based coatings, deposited by APS process, on their microstructure, mechanical properties and tribological performance. The properties of the composite coatings will be compared with those of the unmodified Ni and nanostructured  $\text{ZrO}_2$  coatings.

iii) To study the influence of V additions on the microstructure, mechanical properties, oxidation and tribological behavior of  $\text{TiSi(V)N}$  thin films, containing different Si and V contents, deposited by DC reactive magnetron sputtering. The properties of the V rich coatings will be compared with  $\text{TiSiN}$ ,  $\text{TiN}$  and  $\text{TiVN}$  coatings deposited as reference; special attention will be focused on the oxidation mechanisms occurring during high temperature exposure.

Taking into account these objectives, besides this introductory part, this thesis is organized in six chapters. In chapter II, a historical perspective is presented about the main problems addressed in molds for glass containers production, as well as on the main materials and protection processes currently and possible use on their fabrication. In chapter III, IV and V, the main achievements resulting from the experimental work on the deposition and characterization of the coatings will be analyzed in relation to the three deposition techniques above presented. Finally, in chapter VI the outputs of this thesis, a comparative synthesis and discussion of all the results and future research topics will be presented.

The structure of the thesis is based on a short presentation and synthesis of the research work performed in the scope of each deposition technique, which is further supported by the papers already published and/or under submission by the author. The chapters dedicated to the experimental studies are as follows:

Chapter III is dedicated to establish the correlations between the process parameters of Ni-based coatings deposited by PTA and the chemical composition, morphology, structure, mechanical properties (hardness), oxidation resistance, mechanisms of oxidation, structural and morphology evolution after annealing and tribological behavior (evaluated by micro-scale abrasion and pin-on-disc-tests) of the coatings. This chapter is supported by the papers presented in annexes A to E.

Chapter IV is focused on the study of the influence of nanostructured ZrO<sub>2</sub> additions on the wear resistance of Ni-based alloy coatings deposited by APS. This analysis includes the characterization of structure, morphology, mechanical properties and tribological behavior (evaluated in a reciprocating sliding pin-on-disk equipment and micro-scale abrasion) of the coatings. This chapter is supported by the paper in Annex F.

Chapter V is concentrated on the analysis of TiSiN films deposited by DC reactive magnetron sputtering with different Si and V contents. The influence of V on the chemical composition, structure, mechanical properties, residual stresses, oxidation resistance and mechanisms of oxidation, thermal stability and tribological performance of the coatings is addressed. This chapter is supported by the papers in Annexes G to I.

## List of papers that are the basis of this thesis

Annex A - F. Fernandes, B. Lopes, A. Cavaleiro, A. Ramalho, A. Loureiro, *Effect of arc current on microstructure and wear characteristics of a Ni-based coating deposited by PTA on gray cast iron*, Surface and Coatings Technology, 205 (2011) 4094-4106.

Annex B - F. Fernandes, A. Cavaleiro, A. Loureiro, *Oxidation behavior of Ni-based coatings deposited by PTA on grey cast iron*, Surface and Coatings Technology, 207 (2012) 196-203.

Annex C - F. Fernandes, A. Ramalho, A. Loureiro, A. Cavaleiro, *Wear resistance of a nickel-based coating deposited by PTA on grey cast iron*, International Journal of Surface Science and Engineering, 6 (2012) 201-213.

Annex D - F. Fernandes, A. Ramalho, A. Loureiro, A. Cavaleiro, *Mapping the micro-abrasion resistance of a Ni-based coating deposited by PTA on gray cast iron*, Wear, 292-293 (2012) 151-158.

Annex E - F. Fernandes, T. Polcar, A. Loureiro, A. Cavaleiro, *Room and high temperature tribological behavior of Ni-based coatings deposited by PTA on gray cast iron*, (2014), under review, "Tribology International".

Annex F - F. Fernandes, A. Ramalho, A. Loureiro, J.M. Guilemany, M. Torrell, A. Cavaleiro, *Influence of nanostructured ZrO<sub>2</sub> additions on the wear resistance of Ni-based alloy coatings deposited by APS process*, Wear, 303 (2013) 591-601.

Annex G - F. Fernandes, A. Loureiro, T. Polcar, A. Cavaleiro, *The effect of increasing V content on the structure, mechanical properties and oxidation resistance of Ti-Si-V-N films deposited by DC reactive magnetron sputtering*, Applied Surface Science, vol. 289, (2014) 114-123.

Annex H - F. Fernandes, J. Morgiel, T. Polcar, A. Cavaleiro, *Oxidation and diffusion processes during annealing of TiSi(V)N films*, (2014), under review, "Thin Solid Films".

Annex I - F. Fernandes, T. Polcar, A. Cavaleiro, *Tribological properties of self-lubricating TiSiVN coatings at room temperature*, (2014), accept for publication, “Surface and Coatings Technology”, DOI: 10.1016/j.surfcoat.2014.10.016

*Reprints of the papers were made with the written consent of the Publisher and can be found in annex.*

# Chapter II

In the current chapter, the base and coating materials, processes of deposition currently used in molds protection and the main causes for failure problems are reviewed. Moreover, an overview of possible solutions, regarding processes and materials, for improving the efficiency of molds is presented.

## **2. Historical perspective**

Glass was discovered by the Phoenicians around the year of 3000 BC. The history tells that glass was discovered when these explorers lit fires near the beaches and observed the changes occurring to the sand under the action of the intense heat of the fire. Time passed and Romans began to master the technique of glass production being able to produce some rudimentary bottles, intended for the storage of a large variety of liquids. Over the following centuries, glass containers progressed significantly from the design point of view, having been regarded as a luxury item in the middle age. At that time, only few wealthiest families used glass containers to the storage of perfumes and other liquids. The industrialization of glass containers started in England in the year 1600 when the coal was introduced as a solid fuel. The glass containers were originally produced manually, but due to the increasing market demand associated to technological development, in the XIX century glass production started to be mechanically automated. Glass containers were seen as an ecologic and versatile product, giving rise to their rapid expansion through the market. Since then, to achieve the required higher production rates to satisfy the market needs, the use of more advanced materials was always the preferred solution. During the 20th century, materials science and

technology knowledge was introduced in the industry and, from the second half of the century, researchers and engineers poured a part of the materials development efforts on the modification of materials surface through coatings application. Their superior properties when compared to bulk materials, allowed extending the performance and lifetime of components working in severe conditions. Since then, application of coatings has been one of the preferred ways to modify the surface of materials permitting to extend their use to new potential applications.

In glass industry, molds and accessories are in direct contact with the melted glass (temperature about 1050 °C) being submitted to very severe abrasion, corrosion, wear and fatigue at high temperature. Molds, mouthpieces and plungers used for glass production are shown in Figure 2.1. These mechanical components started to be produced in gray cast iron and low carbon steel due to their relatively good high-temperature performance, allowing keeping a fairly acceptable thermal conductivity, at an extremely low cost [1, 2]. In fact, the functionality of these materials was not only to support the severe environment high-temperature conditions but also to provide an efficient heat transfer which allows to rapidly cool down the melted glass in order to either decrease the time of containers production or obtain products without glass distorting under its own weight [2, 3]. Therefore, later on, copper-alloys (bronze-aluminum) have been introduced as mold material due to their superior thermal conductivity combined with good properties of hardness and wear resistance [4]. These materials allowed increasing production rates, despite of their much higher cost when compared to the previous ferrous alloys. Independently of the mold material, some cooling channels and fins had been performed in some components in order to help the heat extraction.



Figure 2.1 - Components used in glass containers production.



The higher oxidation and wear resistance required at high temperatures (HT) for achieving higher production rates, in order to satisfy market demands, led to the application of new high performing bulk materials, such as Ni cast alloys, that allowed extend service life of components [5, 6]. However, despite of their excellent performance at high temperature, their price of acquisition/production was extremely high which have hindered their widespread application in glass industry. Nevertheless, their attractive properties at high temperatures pushed to overcome the cost barrier by their application under the form of thick coatings on components fabricated in cheaper base materials. Currently, the molds are made in a low performing low cost material (such as the mentioned above, i.e. cast iron, low carbon steel and copper alloys) but coated in specific zones with hard and more resistant HT alloys, allowing to support the harsh service conditions [2, 3, 7, 8]. The base material provides the necessary mechanical strength to resist to the overall applied loads and the thermal fatigue, whereas the coatings allow extending these properties to an upper end of their performance capabilities while protecting them against wear, corrosion, oxidation, abrasion, etc [9, 10]. Even if the material withstands high temperature conditions without coating, the life period of the component can be enhanced. In conclusion, the advantages of coatings application can be summarized as follows [9, 11, 12]:

- Cost of the coating is significantly lower than that of a component integrally fabricated in HT alloys.
- Unique structures and microstructures can be achieved in coatings which are not possible in bulk materials.
- Very high flexibility concerning the chemical composition of the deposited material allowing the best selection and consequent optimization for a specific solicitation/application.
- With coatings, surface properties can be improved keeping the required mechanical properties in the bulk of the structural component.

A wide variety of coating materials, such as cobalt, iron and nickel alloys, has been successfully used to extend the working life of molds [2, 13-15]. The selection of the appropriate coating composition depends on the environment to which the coating is exposed and the substrate on which it is applied. The complexity of interactions between environment, coating and substrate makes the design and selection of coatings very hard and, in general, a

compromise should be achieved between the mechanical strength, the corrosion/oxidation resistance and the adhesion. Among the above referred coatings, nickel-based superalloys have gained an important role for the protection of surfaces of components for the glass industry, due to their excellent performance under conditions of abrasion, corrosion, wear and oxidation at elevated temperature, at a reasonable low cost [16-19]. Ni alloys typically used in molds protection are divided into two groups: chromium-containing and chromium-free, e.g NiCrBSi and NiBSi, respectively. The chromium containing alloys are characterized as low Cr (~8 wt%), medium Cr (~11 wt%) and high Cr (~20 wt%) [20]. The alloys compositions can be varied in order to optimize specific properties, such as the tribological behavior, the oxidation resistance, the wettability, etc. Nickel, as the base element of Ni-based alloys, is responsible for the excellent oxidation and corrosion resistance at high temperature [21, 22]. Other properties can be achieved with alloying elements. B is added to reduce the melting point of these alloys (concentrations up to 2.5 wt%) favoring the manufacturing ability [22, 23]. Silicon increases the self-fluxing properties, the castability and the wetting characteristics [22]. Both B and Si act as deoxidizers, forming borosilicate phases, which prevent the oxidation of the active elements in the alloys [24]. B and C react with chromium to produce hard borides and carbides and, hence, rising the cavitation and wear resistance of the coatings [25, 26]. Cr and Al form chromia and alumina which improve the protection of the coatings against oxidation [27, 28]. The addition of hard and stable carbides and oxides, such as WC, CrC, SiC, Al<sub>2</sub>O<sub>3</sub>, TiO<sub>2</sub>, ZrO<sub>2</sub>, CeO<sub>2</sub>, etc, is used to improve their tribological performance [29-33]. In conclusion, this wide range of compositions makes these alloys very versatile, allowing to achieve the desired properties for a particular application.

Ceramic coatings have been extensively applied in components submitted to extremely high temperature conditions due to their superior properties when compared to metallic coatings [24-36]. However, their use as thick coatings in the protection of parts for the glass industry is limited due to their extremely low thermal conductivity. This is a fundamental parameter for the productivity, which can determine the selection and the applicability of any solution in glass molds. As it will be referred later, the applicability of ceramic materials can only be envisaged if this shortcoming is overcome. In order to take advantage of the excellent high temperature properties of ceramic materials, the only solution is to deposit them in the form of thin films. An emergent deposition process able to satisfy this requirement is the PVD technique.

Independently of the base material and the coatings on it applied, the failures in the molds during service depend on a high number of factors, loading conditions and functional

requirements. Whenever a failure occurs, the most important factor is not the cost of the component but the costs due to machine down time, process instability and poor production. Therefore a proper design and fabrication procedure of the molds, as well as their appropriate use in service, should be carefully analyzed. The factors that lead to the molds failure are the thermal and mechanical strains, the wear plastic deformation, the thermal fatigue and the action of the oxidative, abrasive and corrosive environments occurring in service conditions [37-39]. The synergetic effect of the harsh conditions with a faulty design, a defective material or bad working practices is the perfect combination to induce the premature failure of components, expressed as: worn-out geometries, plastic deformation, surface and bulk material cracks, breakdown of the coatings. For example, the presence of sharp corners, notches and sudden changes in the cross section should be avoided in molds design. They act as hot spots which potentiate the failure by thermal fatigue, wear and cracking due to the high temperature there reached [38, 40, 41]. With the components of molds being constantly heated and cooled down during glass containers production, large thermal gradients are created causing the mold tension during heating and compression during cooling down [37, 42]. Thus, surface cracks are frequently produced resulting in a poor product surface finishing. Moreover, if the thermal expansion coefficients of the base materials and the coatings are very different, cracks can appear on either base material, base material/coating interface or, even, only in the coating, leading also to the mold failure. Thermal shock is also reported as a cause for premature mold failure [37, 38]. In conclusion, the increase of molds lifetime, the improvement in glass containers quality, the decrease in the rejection rate and the reduction of costs production can only be achieved through a convenient selection of new materials (substrate and coatings), the optimization of molds geometries, application of innovative processes of deposition and adoption of new working practices.

As it was referred to in Chapter I, the main processes used to apply coatings to protect the mold surfaces in glass industry, are: (i) hardfacing processes such as Plasma Transferred Arc (PTA) or Gas Tungsten Arc Welding (GTAW), and (ii) thermal spraying processes such as Flame Spraying (FS) and High Velocity Oxy Fuel (HVOF). Ones more than the others, in general, these processes often lead to problems of adhesion of the coating to the substrate, high rate of porosity (5-15%), high residual stresses, excess of dilution with the consequent changes in microstructural and functional properties of the coatings and base materials, in all cases compromising the performance of the molds and the final quality of the produced parts [43-47]. FS is the oldest process used for depositing coatings on molds for the glass industry, since it is simple, easy to be applied and of low cost when compared with other deposition

methods. However, the adhesion of the coating to the substrate is very low and it presents a high level of porosity, which frequently reduces significantly the life time of the molds in service [9]. To avoid adhesion problems, hardfacing processes have been preferentially used (GTAW and PTA), since they promote a strong metallurgical bond between the coating and substrate, condition required to avoid their catastrophic failure in service. This technique gives rise to much better results than thermal spraying processes, for which the adhesion is only due to a mechanical bonding. GTAW process deposits thicker coatings with lower porosity and high production rates than flame spraying [48]. However, it is generally restricted to flat or horizontal surfaces. On the other hand, PTA process produces better results than GTAW in terms of efficiency and quality of the coatings, at a lower cost. It is a very versatile process allowing depositing any kind of material, with lower porosity at a higher production rate than FS and GTAW [49-52]. This process assures a deep penetration of the coating material into the bulk substrate with a narrow heat affected zone and a relatively small weld bead due to its high velocity plasma jet when compared to GTAW. However, it is not portable and cannot be used to coat complex forms, being its main disadvantages. Presently, PTA is being increasingly used in components for glass industry, mainly on the mold edges, zone submitted to a high abrasion by the hot plasticized glass. Furthermore, despite the good adhesion promoted by the hardfacing processes due to the formation of a metallurgical bond, in some cases this can be a disadvantage. In fact, to reach high adhesion values it is frequently necessary to increase the level of dilution of the base material with the coating. Such a procedure leads to changes in the chemical composition of the deposited filler metal, which can compromise the properties of the coatings and their performance in service. Hence, a proper selection of the deposition parameters should be carefully done to accomplish the commitment between the requirements of mechanical strength, corrosion/oxidation resistance and adhesion [44]. Normally, coatings with thickness in the range of 2 - 5 mm are applied in the molds surfaces with these processes.

HVOF process provides coatings with higher hardness than PTA do, since it allows higher cooling rates which promote refined microstructures [9, 53, 54]. Furthermore, owing to the high energy of the particles jet, better mechanical interlocking can be achieved with the consequent increase of the bond strength of the coatings to the substrate in relation to FS process; however, it continues significantly lower than that of the hardfacing processes [55]. As this process is based on the spraying of powders in the melted state over a cooled substrate, the heat affected zone of the base material remains very low, avoiding the formation of brittle phases resulting from the metallurgical melting process occurring frequently in

hardfacing processes, which lead very often to failure problems by cracking. The main disadvantage of this process is the need of fusion of the coating after deposition, since the rapid cooling down of the powders from the melted state does not allow a good intermixing among them and a “poor” cohesion of the particles is normally achieved. HVOF allows to deposit uniform coatings (without dilution) keeping heat extraction conditions uniform in the entire molds surface, which is a required condition to evenly cool down the glass containers and, therefore, to produce glass parts without defects. HVOF is being used to coat critical components in the glass industry, for example the plungers shown on the right in Figure 2.1, where an efficient and uniform heat transfer is required [2, 3, 8]. The typical thickness of the coatings for molds surface protection is in the range of 100 - 500  $\mu\text{m}$ . A summary of the main and typical characteristics of thermal spraying and hardfacing processes is shown in Table 2.1.

Table 2.1 - Comparison of the characteristics of several hardfacing and thermal spraying processes [9, 55-60].

Dep. process	Material feed type	Spray gun temperature ( $^{\circ}\text{C}$ )	Temperature reached in the electric arc ( $^{\circ}\text{C}$ )	Particle velocity (m/s)	Relative bond strength	Porosity level vol. %	Dep. rate (Kg/h)
FS	Powder	3000	-	30-120	Fair	10 - 15	1 - 10
GTAW	Wire	-	6000-11000	-	Excellent	0.01 - 20	6
PTA	Powder	-	12000-18000	-	Excellent	0.1 - 1.5	8
HVOF	Powder	4000	-	2000	Good to Excellent	0.1 - 2	2 - 12

Recently, other deposition techniques, such as Atmospheric Plasma Spraying (APS) and Physical Vapor Deposition (PVD), have emerged, showing a promising potential for application in glass industry. APS process is a thermal spraying process very similar to HVOF since both are based on the projection of melted powders towards the substrate [61, 62]. However, whilst in HVOF process the material in the form of powder is heated based on the generation of a hot flame obtained by combustion of gases, in APS process melting is promoted by the powder injection into a very high temperature plasma generated by a discharge, where it is rapidly heated and accelerated. The main advantage of the APS process is the much higher temperatures that can be reached in the plasma, making it suitable to deposited materials of high melting points, as it is the case of cermets and ceramics [59]. In HVOF the temperature reached is around 4000  $^{\circ}\text{C}$  and the particle velocity 2000 m/s, while in plasma spraying the temperature reaches 20000  $^{\circ}\text{C}$  and the velocity 400 m/s. However, the very high temperatures and lower velocity occurring in the APS process results in coatings with microstructures containing oxides, nitrides and, also, some porosity as well as lower

adhesion to the substrate. Despite these disadvantages, APS deposition of cermet and ceramic coatings was shown in some cases to lead to much better properties than when they are deposited by HVOF [59]. Thus, the use of the APS process to deposit either the previous referred cermet coatings (Ni-based alloys reinforced with stable carbides and oxides), which are normally used to improve the wear behavior, or new cermet coating systems, should be taken into account. In spite of the extremely high number of studies regarding the effect of carbide and oxide additions on the tribological behavior of Ni-based alloys, no reports have been published regarding the effect of nanostructured zirconia additions on their properties. Presently, pure tetragonal zirconia coatings are one of the main materials used on the turbine blades surface protection due to their extremely high performance at high temperature [63-66]. As in glass industry, such material cannot be used as pure coating to protect the mold surfaces due to its very lower thermal conductivity; however, owing to its high level of hardness, wear and oxidation resistance, its use as reinforcement material in Ni-based alloy coatings should be considered.

PVD is a process of deposition of thin films (thickness in the range from few to thousands nanometers) that produces coatings with outstanding mechanical properties. It is common in this process, depending on the coating system, to deposit films with two to four times better mechanical properties than those of the thick coatings described above. The application of this technique to protect molds for the glass industry is still embryonic, since their much smaller thickness seems, at industrial eyes, unpromising and unattractive when compared to that of thick coatings. However, in other industries, where parts are submitted to extreme high temperature and mechanical loading conditions, these coatings have shown to successfully increase the life-time and performance of the coated parts, in some cases in more than one or two orders of magnitude [67-73], allowing predict a potential use of these films to protect glass molds surfaces. From the development point of view, this technique has been shown to be very versatile. It easily allows scan the chemical composition of a coatings system, containing one or more elements, permitting the optimization of the deposition of a specific film, i.e. the coating with the best compromise between e.g. mechanical, tribological, oxidation and corrosion properties. Moreover, it allows overcoming the problems of using ceramic coatings in molds protection. In fact, the lower thermal conductivity of the ceramics materials can be avoided if the thickness of the non-thermal conductive film is very low. The main disadvantages of this process are its high investment and production costs, although in some cases the latter can be decreased. In fact, using PVD process some steps of the molds production can be removed (for example post-deposition machining tasks, see Table 2.2 for

more detail) and, depending on the mold dimensions, several parts can be coated at the same time. Therefore, sometimes the final cost of molds production can reach values similar to those achieved with thick films processes. Finally, it should be taken into account the costs of glass containers production. On the one hand, the much better properties of thin films in comparison to thicker ones, may envisage an extended lifetime of the components and therefore, even if the cost of mold surface protection is higher, the final production costs can decrease. On the other hand, due to the very low thickness, the possibility of an increased heat extraction, during glass forming process, gives rise to either important savings in energy, decrease of the production times or improvement of the final quality of the produced parts.

Table 2.2 - Typical sequential tasks used in molds production.

	Deposition processes					
	FS	GTAW	PTA	HVOF	APS	PVD
Base material machining	x	x	x	x	x	x
Open of U-shaped grooves for coating deposition	x	x	x	-	-	-
Cleaning	x	x	x	x	x	x
Grit blasting	-	-	-	x	x	-
Coating deposition	x	x	x	x	x	x
Machining	x	x	x	x	x	-
Cleaning	x	x	x	x	x	-
Remelting	-	-	-	x	yes if cermets no if ceramics	-
Polishing	-	-	-	x	x	-

In the last decades, the development of thin coatings for mechanical applications was concentrated in solutions that could ensure simultaneously the specifications required for a longer lifetime and an increased productivity, high hardness and high toughness, associated with high thermal resistance, which should accomplish the desired excellent tribological behavior at high temperatures. The first generation of hard coatings was concentrated in single carbides, nitrides and oxides (e.g. TiN, WN, TiC, AlN, WC, Al<sub>2</sub>O<sub>3</sub>) [67, 74-76]. The following generations comprised the mixed compounds, such as TiCN, WCN, (TiAl)N, TiSiN, etc. [77-81] and the multilayer and multiphase structures (TiN/NbN, TiN/AlN, TiN/W, WN/Ti, TiSiN, TiBN) [80, 82-84]. Finally, super hard coatings were developed as for example, c-BN, c-B<sub>4</sub>C, etc [85, 86]. In all these cases, the extension of the lifetime and performance of the coated components was successfully achieved.

The development process of hard coatings based on transition metal nitrides started with single nitrides, such as TiN and CrN, which have been widely used as protective

coatings [87-90]. However, the need for using these coatings in more severe and demanding environments (particularly, at high temperature applications) led to their alloying with chemical elements that could in anyway improve their thermal behavior; here multi-element nitride films appeared [91, 92]. The most known of these is TiAlN, which has higher mechanical strength and oxidation resistance than TiN [93, 94]. The entire range of Ti/Al ratios was scanned and, globally, the use of very high Al/Ti ratio gives rise to a significant improvement of the oxidation resistance at high temperatures [95, 96]. With the same aim, improvement of the oxidation resistance, the addition of Cr to TiN film has also been extensively studied [92, 97, 98]. Cr was better in some situations, Al or Si were in others. Therefore, development of quaternary (e.g. TiAlCrN, TiAlSiN, CrAlSiN) and higher (e.g. TiAlCrSiN) systems, was performed by the incorporation of other elements such as Si, B, Cr, Al [71, 99, 100]. Among the ternary coatings, TiSiN was one of the most extensively studied [101, 102]. Depending on the deposition conditions, these coatings have been reported consisting of: i) nano-sized TiN crystallites surrounded by a Si-N amorphous matrix [103-105], or ii) substitutional solid solution of Si in TiN structure (not predicted by the Ti-Si-N phase diagram) [103, 106, 107]. Their main advantage in relation to previous ternary coatings is the much higher hardness values that can be achieved, between 40 and 50 GPa, for the same level of oxidation resistance, particularly if a nanocomposite structure is deposited [95, 103, 108].

Currently, during glass containers production, liquid lubricants are used to avoid the adhesion between the molds surface and the melted glass. In service, most of the lubricant is volatilized, due to the high temperatures, promoting the glass adhesion to the surface and, thus, accelerating the wear of the component and giving rise to poor quality in the produced parts. Furthermore, these lubricants contain commonly small amounts of sulfur which, combined to oxygen, forms sulfuric acid that erodes the mold surfaces creating holes and leading to the premature failure of the mold. Thus, the use on mold surfaces of solid lubricants, instead of the liquid ones, is of great interest, since their low vapor pressure and, hence, sublimation does not occur so easily. A wide range of solid lubricant coatings have been developed in the last decades and successfully applied in tribological components. Solid lubricant coatings such as WC/C, MoS<sub>2</sub>, diamond-like carbon (DLC), hex-BN, etc, as well as their combination in nanocrystalline or multilayer structures, are some examples [70, 109, 110]. However, considerable degradation of the tribological effectiveness of these coatings at high temperature has been reported due to their low oxidation resistance. To overcome this shortcoming, new concepts of lubrication have been proposed. Solid lubricants for high



temperature applications can be divided into three categories [111-113]: (i) soft metals (e.g. Ag, Cu, Au, Pb, and In); (ii) fluorides (e.g.  $\text{CaF}_2$ ,  $\text{BaF}_2$ , and  $\text{CeF}_3$ ); and, (iii) metal oxides (e.g.  $\text{V}_2\text{O}_5$ ,  $\text{Ag}_2\text{Mo}_2\text{O}_7$ ). These coatings were developed by combining the intrinsic properties of some binary or ternary coatings, that are resistant to oxidation, with specific elements in order to get the lubricious properties.

All the above three types of solid lubricants materials plastically deform and/or form low-shear-strength surfaces at elevated temperatures, characteristics responsible for the lubricious effect. Among them, special attention has been given to the coatings based on the formation of lubricious oxides, being vanadium the preferred element, reason why particular attention has been given to the vanadium-containing coatings with the expectation of formation of Magnéli phases  $\text{V}_n\text{O}_{3n-1}$ . These coatings showed interesting tribological properties in the temperature range 500 – 700 °C [70, 114-119]. Various series of V rich coatings have been developed, such as ternary (V,Ti)N [120], CrVN multilayered AlN/VN [121] and quaternary single layer or multilayered CrAlVN [122, 123] and TiAlVN [116, 124-126]. A detailed description of the effect of V additions on the mechanical, tribological and oxidation, properties of these coatings can be found in a recent paper review published by Franz et. al [127]. In summary, the most important conclusions of these studies are: (i) the relative amounts of  $\text{V}_2\text{O}_5$  detected at the oxidized surface of V rich films successfully decreases the wear rate and friction coefficient of the coatings; (ii) a strong out-diffusion of V significantly degrades the oxidation resistance of the coatings; (iii) the out-diffusion only permits a short time efficiency of solid lubrication with the V-oxides.

The control of the V out-diffusion is now one of the major challenges to reach an adequate oxidation resistance and suitable tribological properties without compromising the original properties of the host binary and ternary films. One of the possible proposals to solve this problem will be to use coatings systems composed by a dual phase, in which one of the phases act as a diffusion barrier to vanadium. This can be the case of TiSiN system. If deposited as a nanocomposite structure (nano-sized TiN crystallites surrounded by an amorphous matrix of  $\text{Si}_3\text{N}_4$ ), the Si-N phase may work as an anti-diffusion barrier [128] and, therefore, if V is incorporated in solid solution in the lattice of the TiN grains, the controlled release of V can be achieved. By tailoring the nanostructure of the Ti-Si-N films, i.e producing coatings with different Si-N layer thickness, the V out-diffusion can be controlled as well as its release as oxide in the coatings surface. An alternative method would be to deposit a multilayer structure with Si-N layers of increasing thicknesses from the top to the bottom of the coating.



# **Chapter III**

## **3. Effect of the arc current variation on the properties of Ni-based coatings deposited by PTA process**

### **3.1. Introduction**

This chapter is dedicated to the analysis of the effect of the arc current variation on the microstructure, hardness, oxidation performance, structural and morphology evolution after annealing and tribological behavior of Ni-based coatings deposited by PTA process, and is supported by the publications presented in the Annexes A to E.

The effect of the PTA current variation on the microstructure and hardness of the coatings is presented in annex A. The microstructural changes in the coatings as well as in the respective heat affected zones were analyzed in this paper. Further, the effect of a post-weld heat treatment (PWHT) on the microstructure and hardness of the coatings and base material was also examined as well as their wear performance evaluated in micro-scale abrasion. This method was selected to reproduce the main wear mechanism (3 body abrasion) identified in the surface of molds which have been in service for long time, although it does not allow consider the high temperature effect. An exhaustive investigation of the test conditions that produce such kind of wear mechanism was carried out and it is detailed in the paper of Annex D. The wear resistance of the coatings, in particular their abrasion resistance was evaluated before and after annealing in order to understand the effect of temperature on the wear

performance of the coatings (publication in Annex C). The influence of the heat treatment on the hardness and microstructure of the coatings was also discussed. The high temperature tribological behavior of the coatings was assessed in a pin-on-disc tribometer (publication in Annex E). Besides the effect of the increasing dilution on the wear behavior of the coatings at room and increasing temperatures, the base material used in the molds production (gray cast iron) was also investigated. The publication in Annex B is dedicated to the study of the effect of substrate dilution on the oxidation behavior of coatings. The oxidation mechanisms occurring during coatings heat treatment were also discussed in this paper.

The experimental procedure and conditions adopted for the coatings deposition and characterization are described in detail for each specific investigation on the papers of the annexes. In the following sections, the main results achieved are summarized.

### **3.2. Microstructure and hardness of the coatings**

Ni-based coatings were deposited by PTA process, using the same process parameters with exception of the arc current, on flat surfaces of gray cast iron blocks in order to study the effect of substrate dilution on their properties. The following arc currents were used: 100 A for specimen 1, 128 A for specimen 2 and 140 A for specimen 4. Further, the edges of a block with a machined U-shaped groove were coated with the same parameters of specimen 2 (specimen 3).

The effect of the arc current variation on the dilution of the coatings is shown on the macrographs displayed in Figure 3.1. With the arc current increase in the range 100 - 140 A, the dilution steadily increased from 28% to 59%. Both flat and U-shaped groove machined specimens revealed to have similar dilution and macrostructures suggesting that the deposition conditions on flat surfaces blocks could be extrapolated to molds. As it would be expected, the increasing dilution had a significant influence on the chemical composition of the coatings, being the main changes related to the decrease of the Ni content and the increase of Fe, Si, C and Mo contents, in good agreement with the chemical composition of the base material.

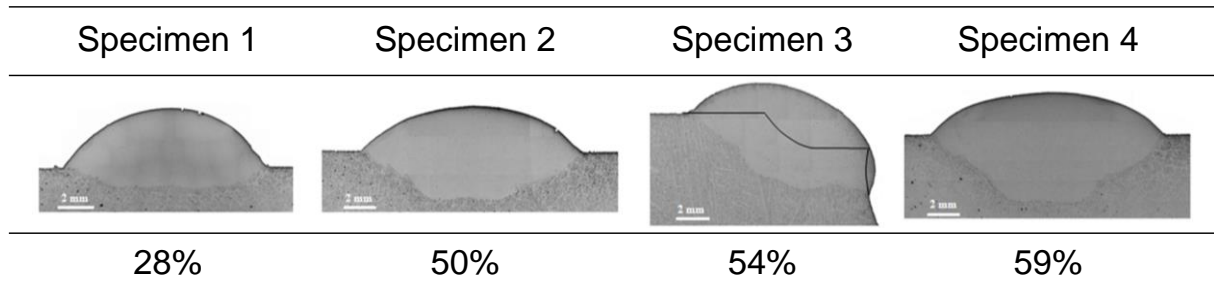


Figure 3.1 - Dilution induced by PTA process using different weldments: specimen 1 - 100 A, specimen 2 and 3 - 128A, specimen 4 – 140 A.

After deposition, four distinct regions could be observed on the cross section of the coatings, as follows: the fusion zone (FZ), which corresponds to the coating material (the nickel alloy), the partially melted zone (PMZ), which is the area close to the FZ where liquation can occur during weld, the heat affected zone (HAZ), which is not melted but undergoes microstructural changes, and the base material (BM) which structure remains unaffected by the deposition process. In all the cases the fusion zone showed a dense microstructure, free of microcracks and few solidification voids. Increasing substrate dilution was shown to reduce the content of porosity in the coatings, correlated with the refinement of the dendritic microstructure (Figure 3.2). The microstructure consisted of dendrites of a Ni-Fe solid solution phase aligned along the direction of the heat flow. Furthermore, torturous grain boundaries were displayed, with C flakes (dark-floret structures) evenly distributed in the matrix. The large number of C flakes on the microstructure was attributed to the dilution of the base material. Moreover, the dendritic structure became finer as the arc current and, therefore, dilution increased.

For higher arc currents the heat input during deposition increased, being expected a coarsened microstructure; however, an opposite behavior was witnessed. According to the WDS maps (wavelength dispersion spectroscopy) of the most abundant elements of the coatings, the refinement of the dendritic structure was attributed to the higher number of precipitates and C-flakes in the grain boundaries, due to substrate dilution. In fact, these phases normally segregate in the grain boundaries, which increased the rate of heterogeneous transformation during solidification, hindering the grain growth. A detailed analysis in the elements distribution with increasing dilution can be confirmed in Annex A.

According to X-ray diffraction patterns of the as-deposited coatings, the major phases of their structure were primarily (Ni, Fe) face centered cubic solid solution, with the occurrence of  $N_3Si$ ,  $Cr_5B_3$  and  $Fe_3Mo_3C$  phases. This phase distribution was in good agreement with the elemental maps distribution drawn for the coatings. Moreover, according

to WDS analysis, other precipitates such as C-B, and Mo-C were also observed in the grain boundaries, contributing to the microstructure refinement, although they were not detected by XRD analysis, probably due to their small size and/or content. Close to the interface coating/base material, a cellular microstructure, finer than the dendritic structure, was observed for all the specimens (see Figure 3.2 d) for specimen 1). This refinement may be attributed to the high solidification rates involved owing to the efficient thermal exchange ensured by the high volume ratio substrate/coating.

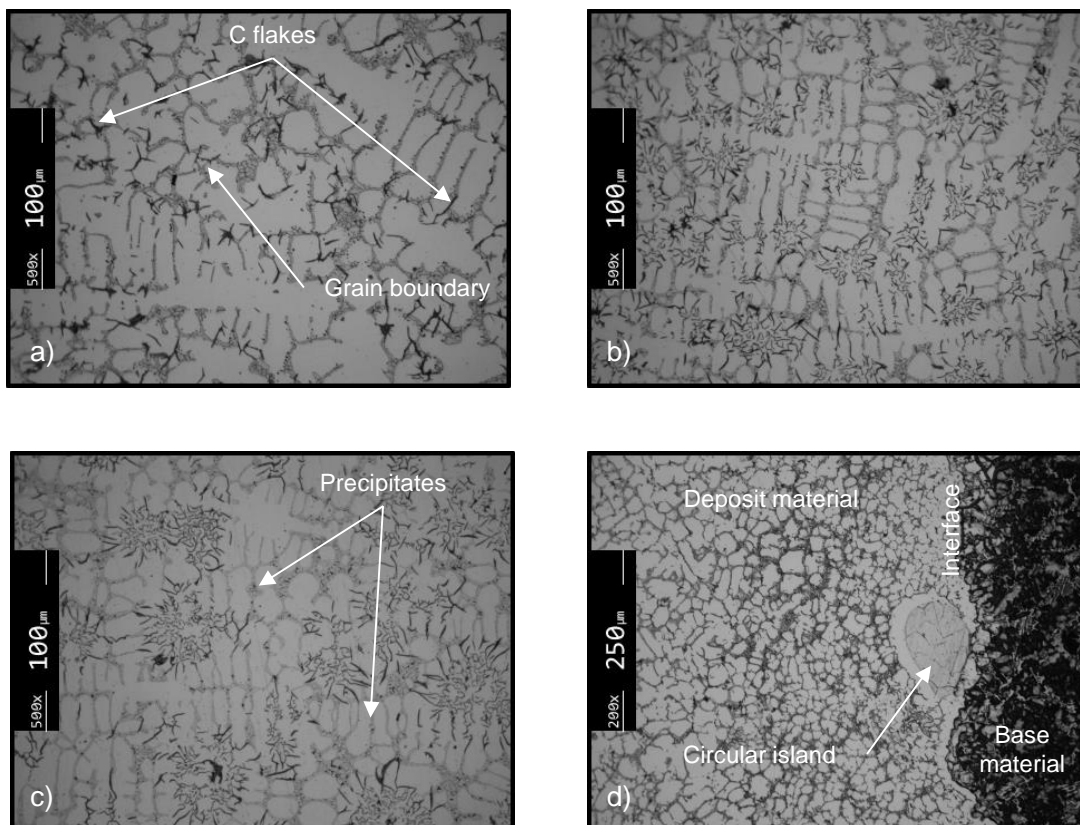


Figure 3.2 - Optical micrographs of: a) specimen 1, b) specimen 2, c) specimen 4, d) interface of specimen 1.

Despite the previous refinement of the coating microstructure with increasing dilution, which would suggest an increase of the hardness, an opposite trend was registered, i.e. the hardness of coatings decreased with increasing arc current, as it is shown in Figure 3.3. This behavior is undesirable in terms of wear resistance and could only be explained by the changes in the chemical composition reported above. In all the cases the hardness throughout the melted material revealed to be approximately constant.

The highest hardness value was observed close to the interface coating/fusion zone, more specifically on the PMZ (538 HV<sub>0.5</sub> for specimen 1), being lower with increasing arc current, which may be favorable in terms of the toughness of that region. This zone has been

found to be formed by hard cementite and martensite phases which are usually responsible for the brittle behavior of Fe-C alloys. The hardness of the HAZ was significantly higher than the base material but lower than the PMZ material, as a consequence of the presence of martensite and the absence of cementite. The proportion of martensite in the microstructure decreased with increasing distance from the fusion line and, thus, the hardness dropped down too.

The microstructure of heat-affected zones and the induced mechanical properties were directly related to the heat input and, therefore, to the current intensity. The high hardness values found in the PMZ and HAZ made these regions potentially responsible for many of the mechanical problems occurring in cast iron welds since they were brittle. Thus, a post-weld heat treatment (PWHT) at 850 °C for 1h was performed to the specimens in order to reduce the presence of brittle phases. As can be observed in Figure 3.4 for specimen 4, the heat treatment successfully reduced the hardness of the PMZ and HAZ zones down to the base material values without significant changes of the coating hardness. In this case, PMZ, HAZ and BM zones were formed basically by a perlitic/ferritic structure, justifying the large scatter of hardness measurements, as shown in Figure 3.4.

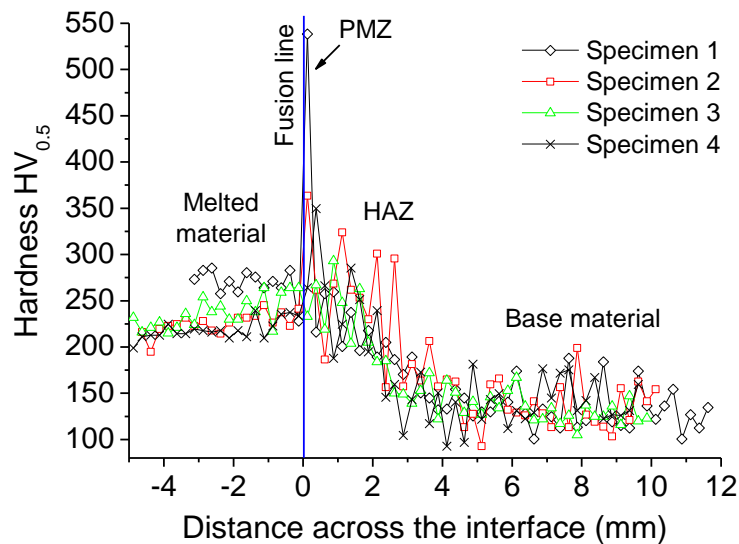


Figure 3.3 - Hardness profile across the interface of PTA specimens.

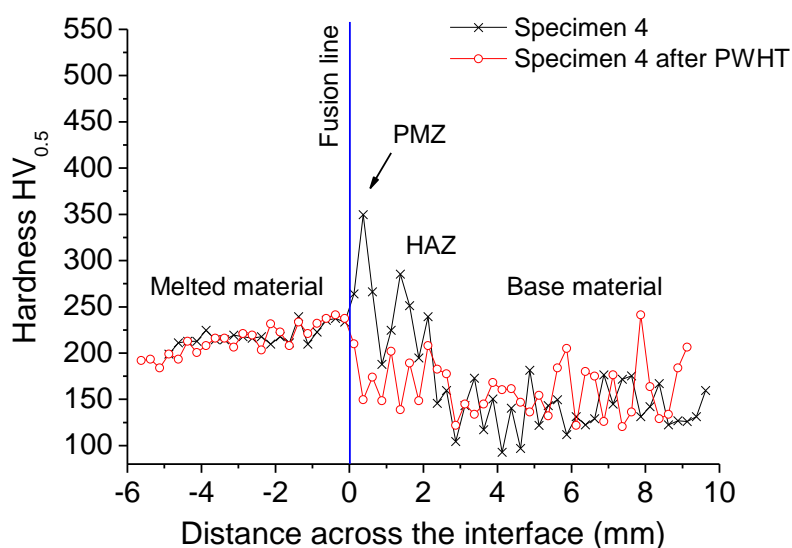


Figure 3.4 - Hardness profile across the interface after PWHT in specimen 4.

### 3.3. Oxidation resistance and diffusion mechanisms

Two of the previous coatings (specimens 1 and 3) were held at 800 °C and 900 °C in air atmosphere during 2 h in a thermogravimetric equipment (TGA), in order to study the influence of the substrate dilution on the oxidation resistance of the coatings. The surface, as well as the cross-section, of the oxidized coatings were observed by scanning electron microscopy (SEM) and analyzed with both energy dispersive X-ray spectroscopy (EDS) and XRD diffraction. The results are fully presented in Annex B; specimens 1 and 3 were termed as coatings C100 and C128, respectively. The thermogravimetric analysis revealed that increasing the substrate dilution the oxidation resistance of coatings decreased, as shown in Figure 3.5. This behavior was correlated to the chemical composition changes occurred due to dilution; in particular due to the high iron content introduced in the coating. As a consequence, different oxide phases were detected in the two coatings, although in each coating the phases indexed after thermal exposure at 800 and 900 °C were similar. According to XRD and SEM-EDS analyses performed at the oxidized surface of the coatings, the oxide phase sets detected at 800 °C and 900 °C were: (i)  $B_2O_3$ ,  $SiO_2$ ,  $Cr_3B_3$  and OAIB for coatings produced with lower dilution and (ii)  $Fe_2O_3$  (hematite),  $Fe_3O_4$  (magnetite), spinels of  $NiFe_2O_4$ , and small amounts of  $NiO$ ,  $B_2O_3$  and  $B_6O$  for higher dilution coatings. In the latter, carbon particles were also detected.



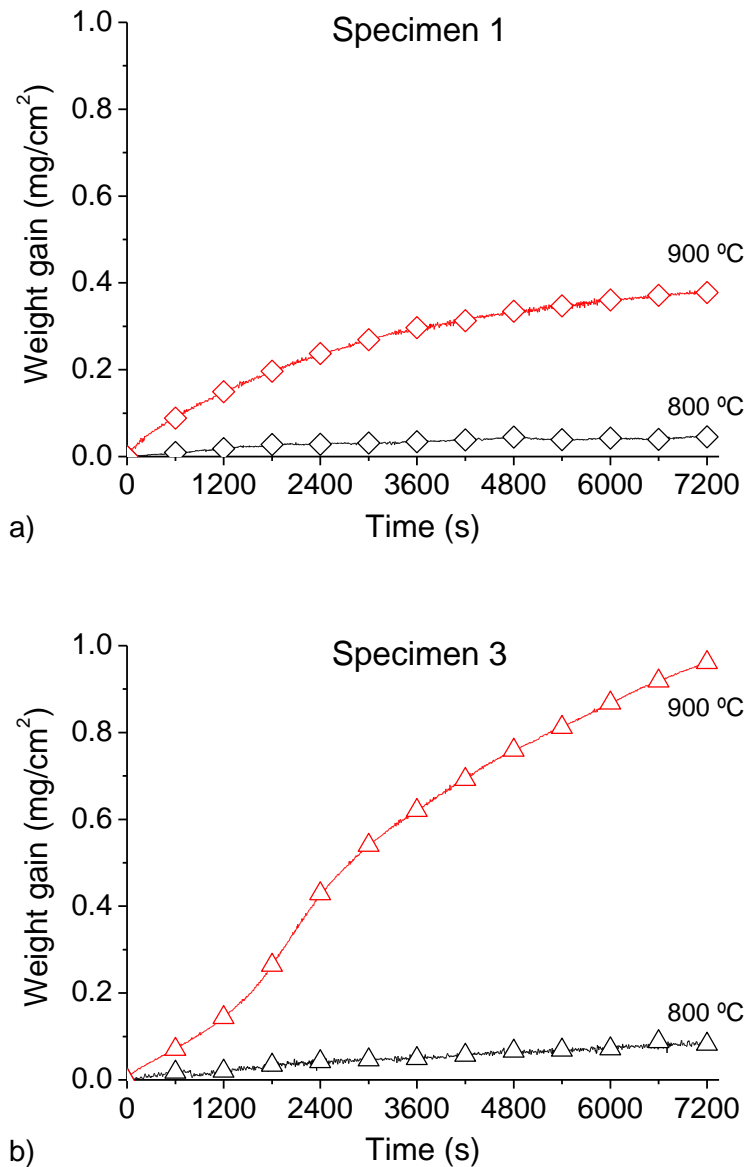


Figure 3.5 - Isothermal oxidation curves at 800 and 900 °C of the: a) coating deposited using 100 A arc current, b) coating deposited using 128 A arc current.

Moreover, the analysis performed on the cross section of coatings showed different types of oxide layers after isothermal oxidation. In the coating with lower dilution the oxide scale showed to be mainly formed by a protective thick layer of Si-O in which small amounts of a phase rich in Ni, Si, Al and B (Si-O, Ni-Si and Al-B-O phases) were uniformly distributed. On the top a B rich oxide was detected too. On the other hand, a dual layer structure was formed in the case of the coating with high dilution: an external layer of Fe<sub>2</sub>O<sub>3</sub>, with small features of Fe<sub>3</sub>O<sub>4</sub> and NiFe<sub>2</sub>O<sub>4</sub> spinel rich phases, and an internal Fe<sub>3</sub>O<sub>4</sub> layer with small amounts of an evenly distributed dark phase rich in silicon, nickel and iron. Similar to specimen 1, small amounts of B-O were also detected on the top. Furthermore, between the

outer and inner layers, a very thin Si-O layer was also identified. Thermogravimetric curves showed that the coating with lower dilution displayed a parabolic oxidation weight gain as a function of the time, typical indicating an oxide growth controlled by a protective Si-O layer. The coating with higher dilution followed the same trend at 800 °C; however, at 900 °C two stages in the oxidation curve were detected, the first with a linear increase in mass gain, has been shown to be a compromise between the outward Fe diffusion through a growing layer of Fe<sub>2</sub>O<sub>3</sub> and the loss of carbon by decarburization and formation of CO<sub>2</sub>. The second step obeyed a parabolic law starting at the moment that the oxide scale, above described, thickened to a critical value impeding the C liberation, leaving the ion diffusion through the scale the only mechanism controlling the mass gain. A detailed description of the oxidation resistance and the diffusion mechanisms occurring with these coatings can be found in Annex B.

### **3.4. Tribological behavior**

The influence of substrate dilution on the tribological performance of coatings was investigated using two different wear equipments: micro-scale abrasion and pin-on-disc apparatuses. The first equipment was used since it is among wear tests one of the simplest to reproduce the wear mechanism closest to what is occurring on the surface of molds in contact with melted glass (3 body abrasion). However this equipment did not allow high temperature testing. Therefore, the high temperature tribological behavior of the coatings was assessed in another tribometer (pin-on-disk), although it did not allow reproducing so well the interaction conditions between melted glass and the surface of molds.

#### **3.4.1. Micro-scale abrasion tests**

In order to use micro-scale abrasion tests to evaluate the effect of substrate dilution on the abrasive wear resistance of the coatings, an exhaustive investigation of the test conditions (different abrasive concentrations, loads and sliding distances) that produces 3 body abrasion wear mechanism was carried out and detailed in Annex D. It was observed that low loads and higher fraction of abrasive slurry enable 3-body abrasion, whilst, 2-body abrasion becomes stable at high loads and low volume fraction of abrasive slurry. Moreover, it was perceived that the specific wear rate essentially depends on the wear rate mechanisms (rolling or grooving) involved and not on the test conditions employed, since these do not produce changes in the wear mechanism; i.e. different test conditions which produce similar wear mechanism can be used to calculate the specific wear rate of coatings. The influence of the

substrate dilution on the micro-abrasion resistance of Ni-based coatings was evaluated in Annex A and Annex C, using a combination of test conditions that would produce 3-body abrasion wear mechanism. In both cases the wear results showed that dilution slightly decreased the wear rate of the coatings (see Figure 3.6), in good agreement with the decrease in their hardness. However, due to the high concentration of abrasive slurry used (103 g per  $1 \times 10^{-4} \text{ m}^3$  in Annex C against 34 g per  $1 \times 10^{-4} \text{ m}^3$  in Annex A), and owing to the different ball surface preparation done in Annex C, the wear rate of the specimens revealed to be one order of magnitude higher. In addition, the wear scars promoted by the tests revealed the presence of two different wear mechanisms (3-body and 2-body abrasion), although 3-body abrasion was predominant. Therefore, although a pure 3-body wear mechanism was not produced, as it would be expected by the results of Annex D, the tests allowed closely reproduced the wear mechanism present on the molds surface although the high temperature effect had not been considered.

The heat treatment performed at specimen 4 (at 500 °C) during 5 and 10 days revealed not promote changes in their specific wear rate of coatings. However, sample exposed during 20 days exhibited a lower specific wear rate (see Figure 3.6). This was attributed to the increasing of coating hardness with thermal exposure, due to the precipitation of a Ni-P phase in the coating matrix. A detailed description on the influence of the annealing treatment on the properties of coatings can be seen in Annex C.

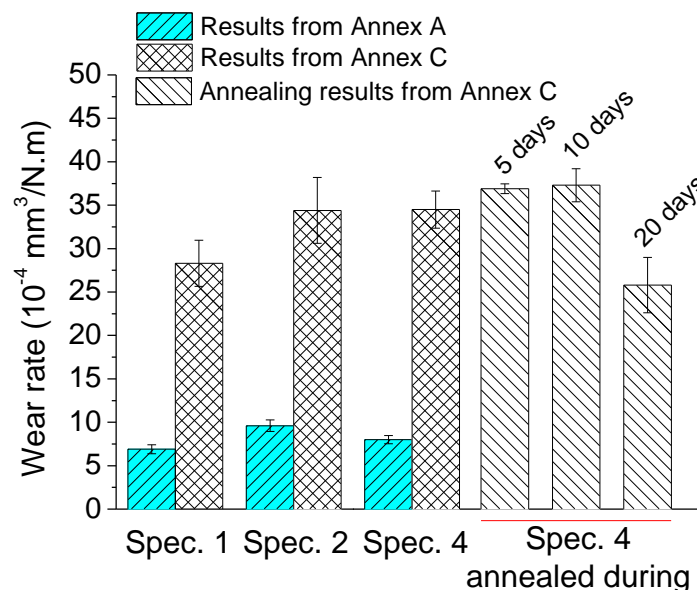


Figure 3.6 - Specific wear rate of Ni-based coatings in as-deposited and annealed conditions from Annex A and C, evaluated in a micro-scale abrasion equipment.

### 3.4.2. Pin-on-disc tests

Several weld beads of specimen 1 and 4 (different dilutions – 28 and 59%, respectively) were deposited in parallel on the flat surface of cast iron blocks, ensuring some overlapping between them in order to produce coatings large enough to allow perform tribological tests. The tribological performance of the coatings was evaluated at three different temperatures: room temperature, 550 and 700 °C, and compared to the uncoated gray cast iron. Although in the real working conditions of molds glass acts as an abrasive material, due to its melted state at high temperature, for the tribological tests we have selected as counterpart a harder and more resistant material: Al<sub>2</sub>O<sub>3</sub> balls. All the wear tests were conducted at a constant linear speed of 0.10 m.s<sup>-1</sup>, a load of 5 N, a relative humidity of 48±5%, and 5000 cycles. The radius of the wear tracks was set to 5.3 mm.

The tribological tests revealed that at room temperature, the wear rate of the coatings was independent of the substrate dilution and similar to the gray cast iron (see Figure 3.7). In all coatings the wear was governed by tribo-oxidation. Similar friction values were measured in all coatings which were understood by the similar wear debris detected on the worn surface of the coatings, despite of their discrepancy in hardness and chemical composition due to the different dilution. Gray cast iron showed a similar level of wear rate as Ni coatings at RT in spite of its lower hardness (2 times lower than the Ni coatings). This was explained by the presence of graphite on the worn surface, which acting as a solid lubricant led to lower friction coefficient and compensated a possible higher wear rate due to the lower hardness.

The wear rate of the coatings abruptly increased when tested at 550 °C; however, it dropped with further increase to 700 °C. Globally, specimen 1 displayed much higher wear rate than specimen 4 at high temperatures, result that could be interpreted on the basis of the oxidation resistance of coatings. At 550 °C, due to the lower oxidation resistance of the specimen 4, a continuous oxide tribo-layer was formed on their worn surface, protecting it against wear. In case of specimen 1, due to its higher resistance to oxidation, the oxidation rate is reduced. Due to the movement of the ball, the destruction of the growing oxide layer is relatively easier, hindering the formation of a stable oxide layer over the surface and, thus, leading to high wear volumes due to the direct contact between the alumina ball and the virgin coating. At 700 °C, the wear rate of both coatings is reduced due to the formation of continuous and thick oxide-layers on the worn surfaces. This was not the trend for gray cast iron for which a monotonous increase of the wear rate with increasing temperature was observed. In this case, the very low oxidation resistance of the material allowed an easy

removal of the tribo-layer and the depletion of graphite from the wear track. This tribological behavior is presented and discussed in detail in Annex E.

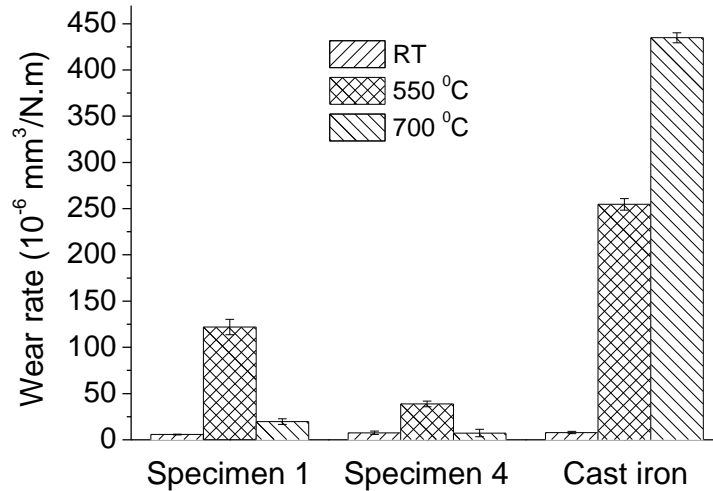


Figure 3.7 - Variation of the wear rate of the as deposited PTA coatings and the gray cast iron with testing temperature.

In conclusion, the increase in the arc current, and therefore in the dilution of the substrate, has detrimental effect on the hardness, oxidation resistance and tribological behavior of the coatings at room temperature. However, beneficial effect on the high temperature tribological behavior was observed due to the fast formation of oxide layers which protect the coating surface against wear. Therefore, the dilution degree should be optimized in order to get the best compromise between the level of oxidation, wear resistance, mechanical properties and adhesion to make possible to achieve coatings with the best performance.



# **Chapter IV**

## **4. Influence of nanostructured ZrO<sub>2</sub> additions on the wear resistance of Ni-based alloy coatings deposited by APS**

### **4.1. Introduction**

This chapter is dedicated to the study of the effect of nanostructured ZrO<sub>2</sub> additions on the microstructure, micro-hardness and wear performance of Ni-based alloy coatings, deposited by atmospheric plasma spraying (APS) on a low carbon steel, and is supported by the paper presented in Annex F.

The coatings with nanostructured ZrO<sub>2</sub> additions were produced by either powders of Ni-based alloy and nanostructured zirconia mixed by mechanical alloying or separate powders using a dual powder injection system available at the APS equipment. In both cases, two contents of nanostructured zirconia were added to the Ni-based alloy: 20% and 40% in volume. All the properties of the coatings were compared, interpreted and discussed in relation to either unalloyed nickel or nanostructured zirconia coatings and based on the deposition parameters. The coatings produced with powders prepared by mechanical alloying using 20% and 40 % of nanostructured ZrO<sub>2</sub> were denominated as “Ni+20% MA” and “Ni+40% MA”, respectively, and the coatings deposited using the dual system of powder injection with 20% and 40 % of nanostructured ZrO<sub>2</sub> were designated as “Ni+20% Dual” and “Ni+40% Dual”, respectively.

## 4.2. Microstructure and hardness of the coatings

All the coatings showed a typical morphology of plasma sprayed materials, with pores, lamellae, and partially/un-melted particles (see Figure 4.1). Ni pure coating displayed a compact and homogeneous microstructure (Figure 4.1 a)), while pure ZrO<sub>2</sub> coating showed an extremely high level of porosity with some cracks, resulting from the tensile residual stresses generated during cooling down to room temperature (Figure 4.1 b)). Ni+ZrO<sub>2</sub> MA coatings displayed a homogeneous and compact microstructure, with small zirconia particles evenly distributed in the matrix, whilst Ni+ZrO<sub>2</sub> Dual coatings exhibited a porous microstructure, full of semi-melted Ni powders with large particles of ZrO<sub>2</sub> entrapped in their boundaries suggesting a brittle behavior. Nanostructured zirconia additions progressively increased the hardness of the coatings. However, coatings deposited using powders prepared by mechanical alloying displayed much higher hardness than Dual coatings (7.0 - 7.6 against 5.4 - 5.9 GPa, respectively). This was in good agreement with their lower porosity, higher level of compactness and finer and more homogeneous distribution of the nanostructured zirconia. In relation to the structure, the main phases detected corresponded to the ones identified in both pure Ni-based and ZrO<sub>2</sub> coatings, i.e: Ni, Ni-Cr-Fe, Cr<sub>23</sub>C<sub>6</sub>, Cr<sub>5</sub>B<sub>3</sub> and ZrO<sub>2</sub>.



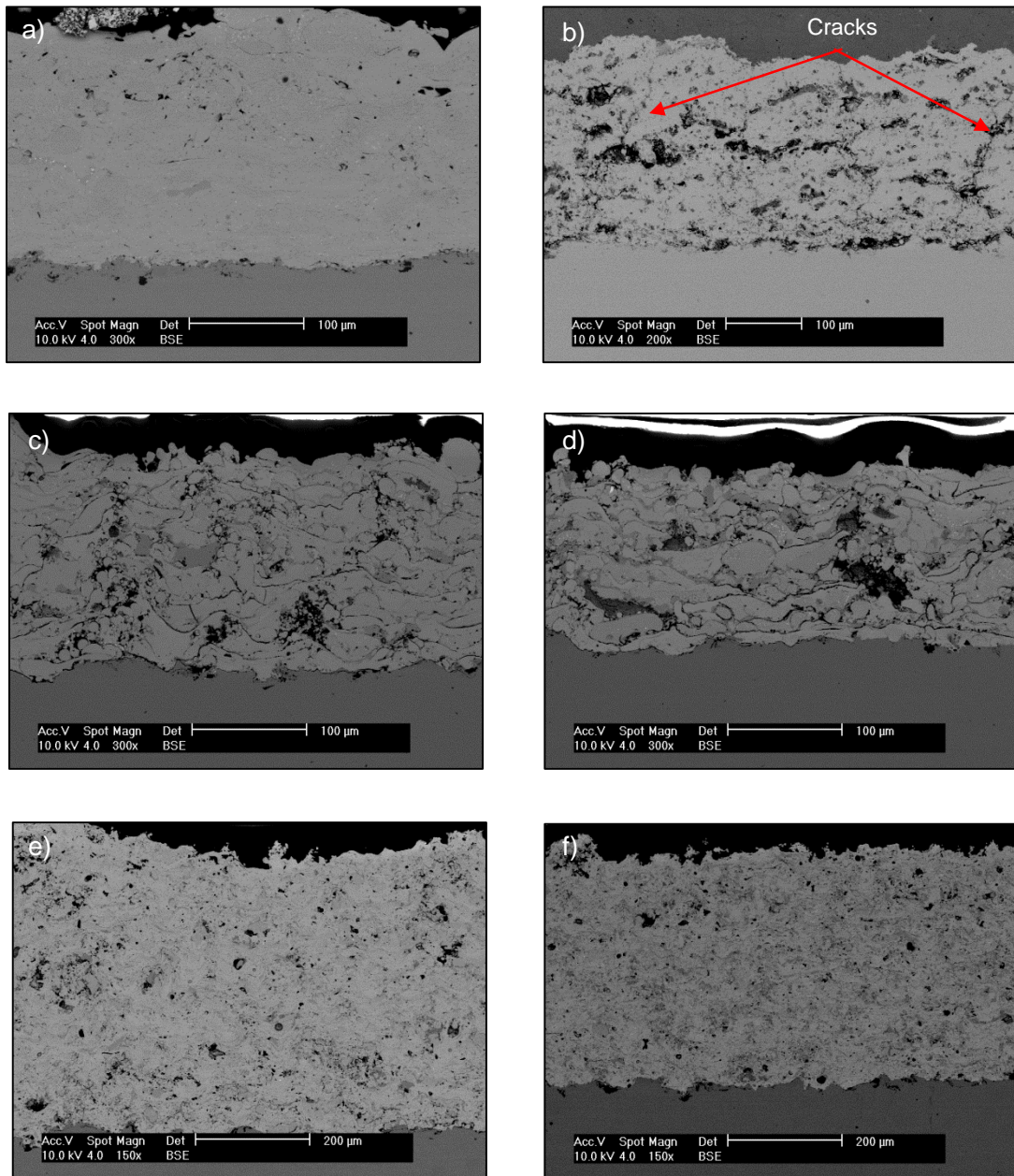


Figure 4.1 - SEM morphology of the: a) Ni-based alloy coating, b) nanostructured ZrO<sub>2</sub> coating, c) and d) Ni+20% Dual and Ni+40% Dual, respectively, e) and f) Ni+20% MA and Ni+40% MA, respectively.

### 4.3. Tribological behavior

The influence of the nanostructured zirconia addition on the wear behavior of a Ni-based coating was studied using reciprocating tribological testing equipment with a ball-on-plate configuration. A harmonic wave generated by an eccentric and rod mechanism imposed a stroke length of 2.05 mm at a frequency of 1 Hz. A soda-lime glass sphere of 10 mm in diameter was used as counterpart, as the most suitable material to study the interaction of glass with the coatings. All the tests were conducted at room temperature during two hours.

Four different values of normal load were applied to the coated samples and the volume loss, specific wear rate and friction coefficient were evaluated.

ZrO<sub>2</sub> incorporation successfully decreased the specific wear rate and the friction coefficient of the Ni-based coating, independently of the deposition procedure adopted (see Figure 4.2). However, this trend is more accentuated in Ni+ZrO<sub>2</sub> MA than in Ni+ZrO<sub>2</sub> Dual coatings. Furthermore, increasing ZrO<sub>2</sub> content in MA coatings has a decreasing monotonous effect on the wear rate whereas an inverse trend was observed in Dual coatings for the highest ZrO<sub>2</sub> content. Several factors, such as the hardness, the microstructure and the wear mechanisms occurring during sliding, were used to interpret those different trends in the specific wear rates of coatings, as follows:

(i) Ni+ZrO<sub>2</sub> MA coatings showed clean wear tracks with longitudinal scratches identifying grooving abrasion. Thus, the uniform distribution of small ZrO<sub>2</sub> particles, combined with the higher hardness and toughness of these coatings, impeded the liberation of large wear debris from the coatings, their plastic deformation and adhesion, leading to low specific wear rate.

(ii) In the case of Dual coatings, the main wear mechanism observed on the worn surfaces was of adhesion type, as for pure Ni coating, due to the large areas of nickel exposed to the counterpart. The semi-melted state of Ni powders, the high level of porosity and the agglomeration of ZrO<sub>2</sub> particles located in-between Ni-based lamellae, made the coatings less tough, inducing an increase of their wear rate.

(iii) The increase of nanostructured zirconia from 20 to 40% in Dual coatings, promoted higher levels of brittleness in the Ni lamellae boundaries, increasing the volume loss of the material.

(iv) Pure ZrO<sub>2</sub> coating displayed the highest specific wear rate among all the coatings, due to its brittle behavior.

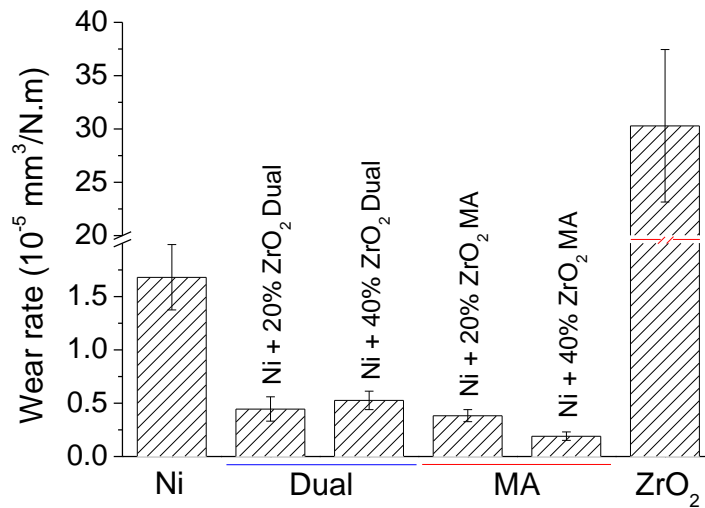


Figure 4.2 - Specific wear rate of coatings calculated from the reciprocating tribological tests.

The influence of nanostructure zirconia additions on the abrasion resistance of a Ni-based coating was also studied. The tests were performed at the most promising coatings (MA coatings) using the same test conditions as for Ni-based coatings in Annex A, with the exception of the sliding distances, which were adapted based on the wear mechanism. In fact for these tests conditions (AISI 52100 steel ball bearing with 25.4 mm in diameter rotating at a speed of 75 rpm under a load of 0.1 N and an proportion of abrasive slurry of 28% (34 g per  $1 \times 10^{-4} \text{ m}^3$  of silica in water)), sliding distances higher than 400 turns showed produce a mixed-mode wear mechanism (3-body plus 2-body abrasion). Thus, in order to ensure 3-body abrasion formation the experiments were performed using lower test durations (50, 80, 150, 200 and 300 rpm). The volume loss plotted as a function of the “load  $\times$  sliding distance” parameter is plotted in Figure 4.3 and the respective specific wear rate, calculated from the slope of a straight line fitted to these points, is shown in Figure 4.4. In all cases the main wear mechanism observed on the wear track was three-body abrasion, in good agreement to the wear mechanism defined on the surface of molds in real applications. The addition of nanostructured ZrO<sub>2</sub> successfully increased the abrasion resistance of coatings, as above demonstrated in the reciprocating tribological tests. However, the specific wear rate values calculated with abrasion tests were two to three orders of magnitude higher than those achieved in reciprocating sliding tests.

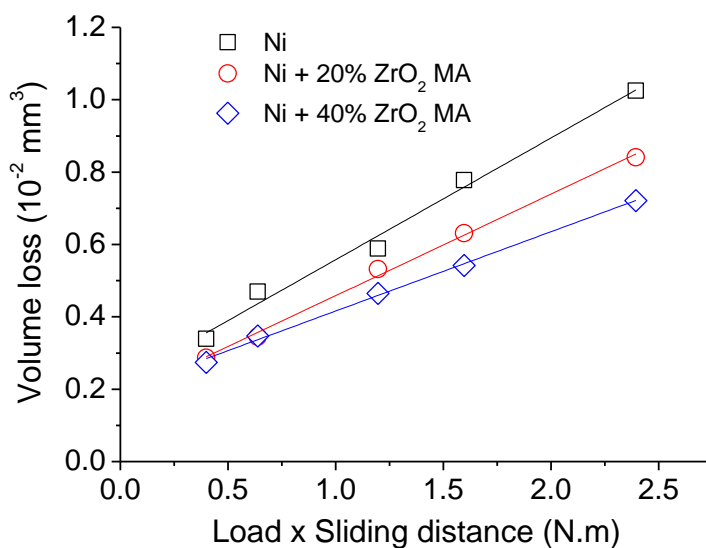


Figure 4.3 - Evolution of the wear behavior as a function of the parameter “normal load × sliding distance”.

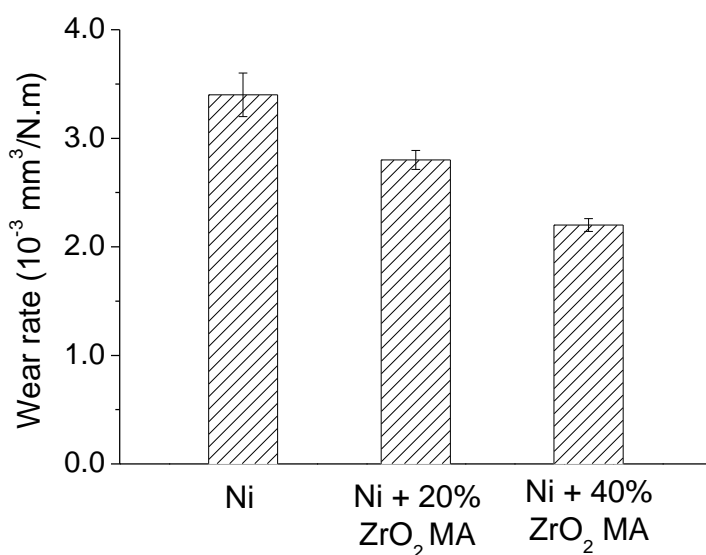


Figure 4.4 - Specific wear rate of coatings, calculated from the slope of a straight line fitted to the points plotted in Figure 4.3.

As a global conclusion, it was demonstrated that nanostructured ZrO<sub>2</sub> additions increased the hardness and improved the tribological behavior of Ni-based coatings. Furthermore, it was observed that the best properties were achieved when coatings were produced with mechanically alloyed powders, which promoted an evenly distribution of ZrO<sub>2</sub> particles and therefore, an improvement on the mechanical and tribological properties.

# **Chapter V**

## **5. Study of the influence of V additions on the properties of TiSi(V)N films deposited by DC reactive magnetron sputtering**

### **5.1. Introduction**



This chapter is on the study of the effect of V incorporation on the chemical composition, microstructure, mechanical properties, residual stresses, oxidation behavior, thermal stability and tribological performance of TiSi(V)N thin films, containing different Si contents, deposited by DC reactive magnetron sputtering. The results presented in this chapter are supported by the papers in Annexes G to I.

Annex G details the influence of V additions on the chemical composition, microstructure, mechanical properties (hardness and Young's Modulus) and oxidation resistance of TiSi(V)N coatings. The effect of Si incorporation on the properties of the TiN system was also assessed in this paper, for comparison purposes. The thermal stability and the diffusion processes occurring during the annealing of TiSiN and TiSi(V)N films are presented and discussed in Annex H. Annex I is dedicated to the study of the effect of V incorporation on the tribological behavior of TiSi(V)N coatings at room temperature and its comparison with that of TiN, TiVN and TiSiN films prepared as references.

## 5.2. Microstructure, residual stresses and mechanical properties

Three series of TiSiN films with different Si contents, each series with increasing V content, were deposited in a d.c. reactive magnetron sputtering machine, set with two rectangular magnetron cathodes working in unbalanced mode. A Ti target, with holes distributed throughout the preferential erosion zone, and a TiSi<sub>2</sub> composite target were used for the depositions. The different silicon contents were achieved by changing the power density applied to each target and the V content was varied by changing the number of high purity rods of Ti and V placed in the holes of the Ti target. Three V contents were added to the films by using 4, 8 and 12 pellets of V. In all cases the total power applied to the targets was 1500 W. To serve as reference, a TiN film was deposited from the Ti target using 2000 W of power. Ti and TiN interlayers were deposited as bonding layers, in order to increase the adhesion of the coatings. The interlayer also contained V when V pellets are placed in the Ti target. In all the depositions the time was adjusted in order to obtain coatings with approximately 2.5 μm of total thickness (including interlayers). The total working gas pressure was kept constant at 0.3 Pa, using approximately 30 and 17 sccm of Ar and N<sub>2</sub>, respectively. A summary of the studied coatings and the nomenclature for them adopted (used in Annex G) is shown in Table 5.1.

Table 5.1 - Coatings deposited and their nomenclature.

		<b>Increasing V content</b> 			
		0P V	4P V	8P V	12P V
		(0 at.%)	(~3 at.%)	(~7 at.%)	(~11 at.%)
<b>Increasing Si content</b> 	Ti 1000 TiSi <sub>2</sub> 500	S3-0 (TiSiN)	S3-4 (TiSiVN)	S3-8 (TiSiVN)	S3-12 (TiSiVN)
	Ti 1200 TiSi <sub>2</sub> 300	S2-0 (TiSiN)	S2-4 (TiSiVN)	S2-8 (TiSiVN)	S3-12 (TiSiVN)
	Ti 1300 TiSi <sub>2</sub> 200	S1-0 (TiSiN)	S1-4 (TiSiVN)	S1-8 (TiSiVN)	S3-12 (TiSiVN)
Ti 2000		TiN			

As it would be expected, the simultaneous decrease in the power density of Ti target and its increase in TiSi<sub>2</sub> target, allowed producing coatings with increasing Si contents. In a similar way, increasing the number of V pellets allowed to deposit coatings with increasing V contents. In all cases, coatings with nitrogen contents close to 50 at.% were achieved. All

films showed a columnar micro-structure. As Si content was increased, the columns size and the surface roughness were firstly reduced and, then, increased for the highest silicon content. V additions did not change the global type of the cross section morphology.

As a general trend, the structure of the films could be assigned to a fcc NaCl-type crystalline phase as e.g. TiN (ICDD card 87-0628). The influence of increasing Si content on the TiN system and the effect of V content on the TiSiN coating with the lowest silicon content (S1-y series) is shown in Figure 5.1. Concerning TiSiN films, a loss of crystallinity was observed for the coating with the highest Si content, suggesting an amorphization of the structure. Furthermore, a shift of the diffraction peaks to higher angles was observed with increasing Si content, suggesting the formation of a substitutional solid solution. In fact, with Si in solid solution, its smaller atomic radius promoted the contraction of the TiN lattice and the consequent shift of XRD peaks for higher angles. Residual stresses could not be the cause for the peaks shift since they were compressive and similar in all the films (approximately 3 GPa). The formation of a substitutional solid solution was explained by the low deposition temperature, together with a low substrate ion bombardment, condition that do not provide the necessary mobility of the arriving species for Si-N phase segregation and consequent formation of a nanocomposite arrangement, i.e. nanocrystalline TiN grains embedded in a Si<sub>3</sub>N<sub>4</sub> matrix. V incorporation in TiSiN films also made moving the peaks to higher angles, behavior once again related to a smaller unit cell due to the replacement of Ti by the smaller V atoms. In these coatings the compressive residual stresses were also in the range of ~3 to ~4 GPa.

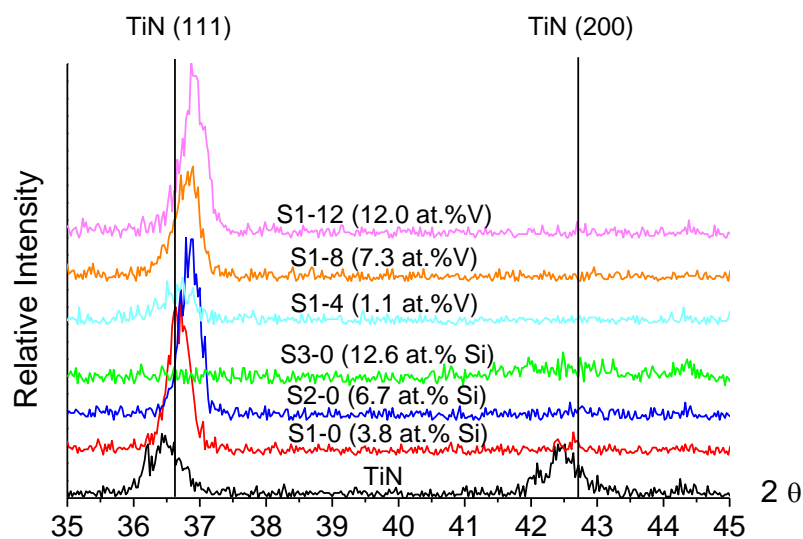


Figure 5.1 - XRD patterns of TiSiN coatings with Si content ranging from 0 to 12.6 at.% and S1-y coatings with V additions.

The dependence of hardness and Young's Modulus on the Si and V contents is shown in Figure 5.2. With Si incorporation, the hardness of the coatings increased up to a maximum value of 27 GPa (6.7 at.% Si), trend attributed exclusively to a solid solution hardening mechanism since, as above referred, the level of compressive residual stresses was similar for all the films. A further increase in the silicon content led to a decrease in the hardness, in good agreement with the loss of crystallinity of this coating. The Young's Modulus monotonously decreased with Si incorporation, which is related to the progressive importance of Si-bonds in the TiN lattice.

Concerning the effect of V additions, similar evolution was observed for all the Si compositions (see Figure 5.2 b) for S1-y series). A slight increase in the hardness and Young's modulus was observed for lower V contents, followed by a drop for the highest one. Similar explanation was suggested, the hardness enhancement was attributed to solid solution hardening since, again, the compressive residual stress values are very similar. The coatings with the highest Si content displayed the lowest hardness and Young's modulus among all the V rich coatings, in good agreement with their low crystallinity.

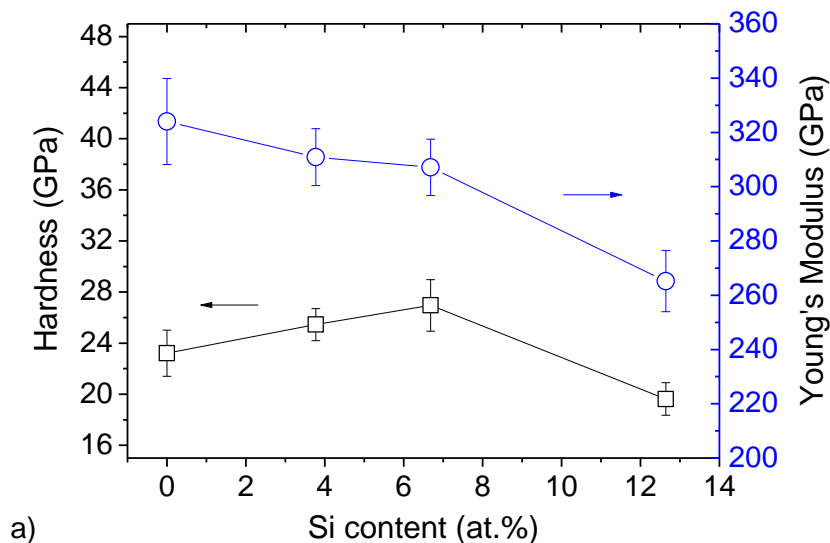


Figure 5.2 - a) Effect of Si content on the hardness and Young's modulus for the TiN system. b) Effect of V content on the hardness and Young's modulus for coating S1-0.



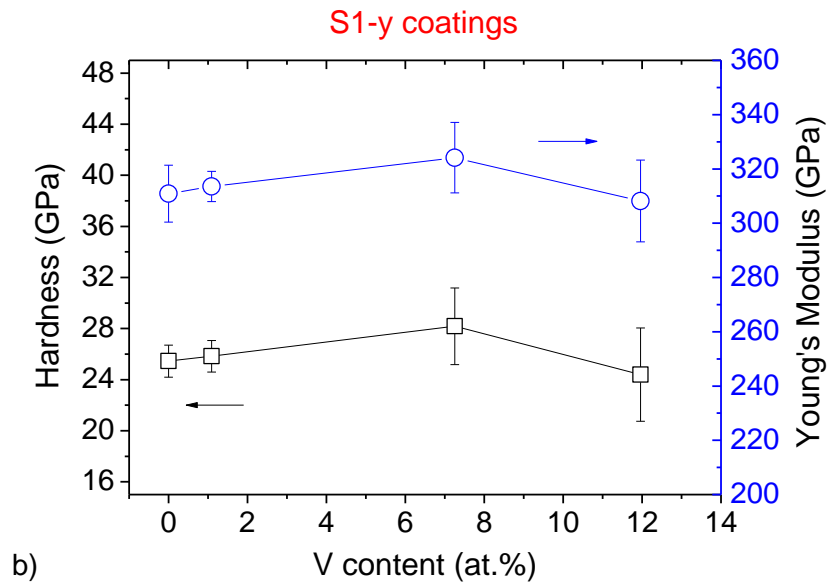


Figure 5.2 (continued).

In relation to the adhesion of coatings, only two failure modes were observed on the scratch track of the coatings; the first cracking and the first chipping. Globally all the coatings showed to be well adherent to the substrate, exhibiting high critical load values. In general V incorporation did not have significant influence in the critical loads whereas, globally, the addition of Si gave rise to a small decrease of their values, particularly for  $Lc_1$  (see Figure 5.3).

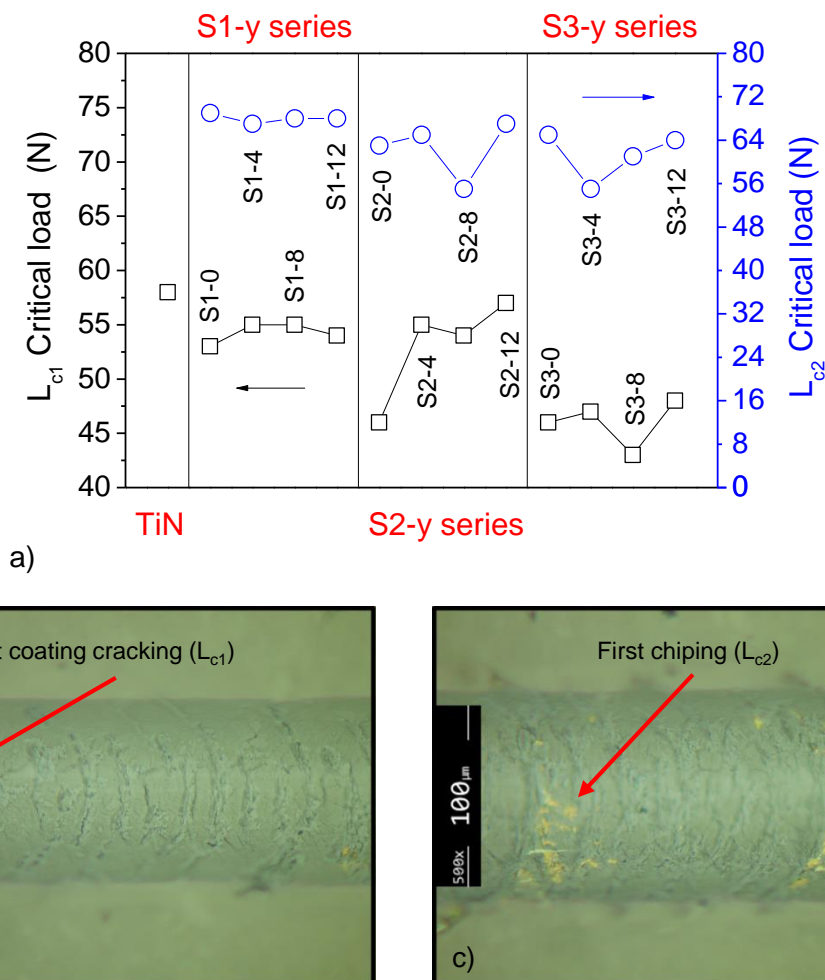


Figure 5.3 - a) Adhesion critical loads values for the dissimilar coatings. Coatings were scratched as the normal force was increased linearly from 5 to 70N.  $L_{c2}$  critical load for TiN coating was > 70 N. b), c) First coating cracking and first chipping observed on the scratch track of coating S2-4, respectively.

### 5.3. Oxidation resistance and diffusion mechanisms

The effect of increasing Si and V content on the onset point of oxidation of TiSi(V)N systems were studied in a TGA equipment. The films were annealed from room temperature up to 1200 °C at a ramp temperature of 20 °C/min. Si incorporation in TiN film strongly increased the onset of oxidation, being S3-0 sample the most oxidation resistant. On the other hand, V addition to TiSiN decreased the onset point of oxidation down to a value close to 500 °C, independently of the Si and V contents, value even lower than for TiN film.

In order to better study the oxidation resistance of the coatings, isothermal annealing at selected temperatures and times were performed. TiN was annealed at 600 °C during 30 min, S2-0 was heat treated at 900 °C during 1h and finally S2-8 was annealed at three different temperatures: 550 °C during 1h, 600 °C during 30 min and 700 °C during 10 min. The results

are plotted in Figure 5.4. When time and temperature are considered, TiSiN is far the best resistant to oxidation. Furthermore, it is also confirmed that V incorporation decreased significantly the oxidation resistance of TiSiN coatings, even to lower values than TiN.

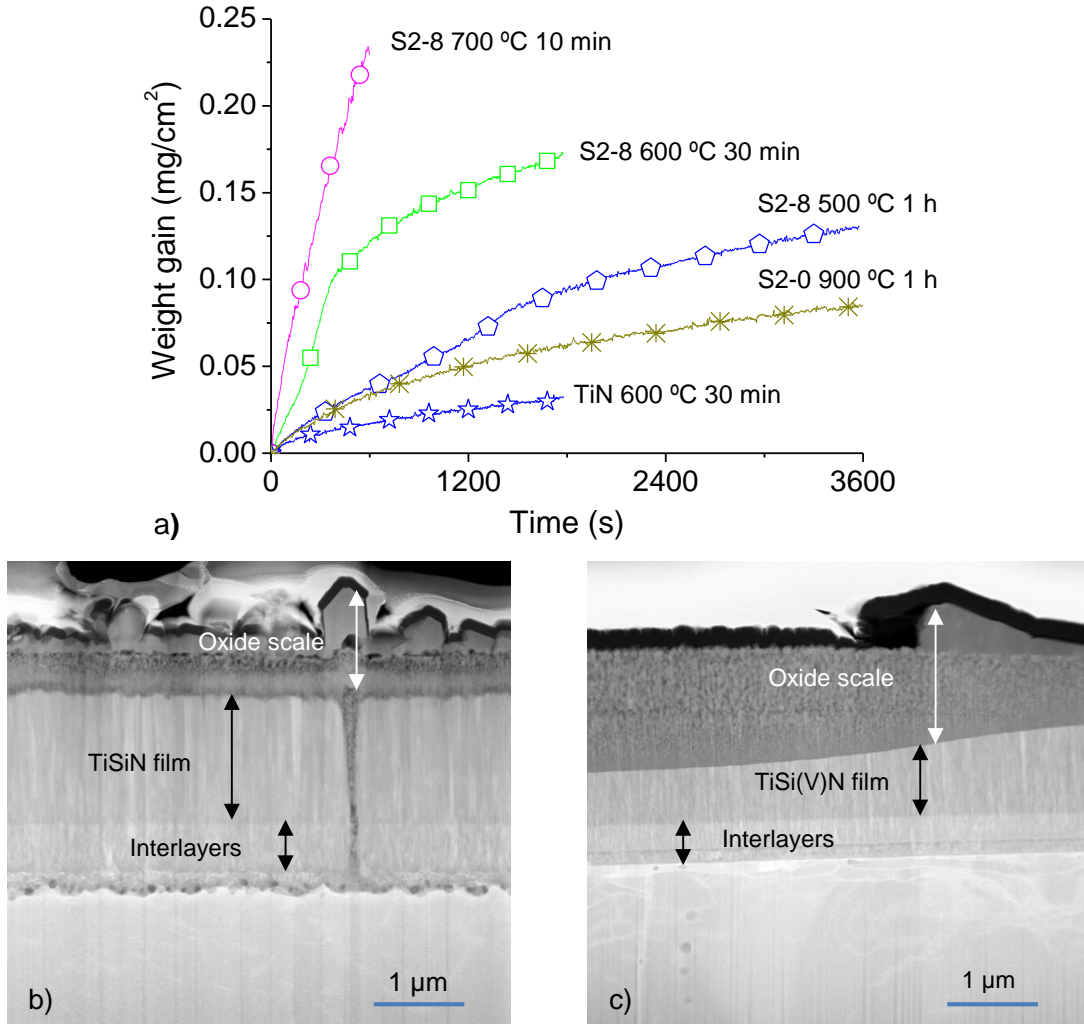


Figure 5.4 - a) Thermogravimetric isothermal analysis of coatings exposed at different temperatures. Cross section morphology of coating: a) S2-0 oxidized at 900 °C during 1 h, b) S2-8 oxidized at 600 °C during 30 min.

The main oxides detected on the surface of the coatings after annealing can be summarized as follows: i) in TiN and TiSiN films,  $\text{TiO}_2$  - rutile and anatase, were the main oxides detected; however, in the last case,  $\text{SiO}_2$  was also present, localized beneath the  $\text{TiO}_2$  layer; ii) in TiSi(V)N at 550 and 600 °C the main oxides were  $\text{Ti(V)O}_2$  and  $\alpha\text{-V}_2\text{O}_5$ , the latter displaying different orientations depending on the isothermal temperature and time; at 700 °C, which is a temperature higher than the melting temperature of  $\alpha\text{-V}_2\text{O}_5$ ,  $\beta\text{-V}_2\text{O}_5$  was formed, resulting from a reduction process of  $\alpha\text{-V}_2\text{O}_5$ . In situ XRD analysis performed in TiSi(V)N coatings in the range from 500 – 750 °C (see Annex H) allowed to demonstrate that the first

oxide being formed was  $\text{Ti(V)O}_2$  phase. TiSiN film exhibited a typical parabolic oxidation weight gain as a function of the time. According to STEM elemental maps analysis a double oxide layer was formed in this case: on top a  $\text{TiO}_2$  layer followed by a  $\text{SiO}_2$  layer. Thus, the excellent oxidation resistance of the TiSiN film was a result of the formation of a continuous protective  $\text{SiO}_2$  layer in the interface film/oxide scale (for more detail see Annex H) that hindered the ions diffusion and, thus, protecting the coating from further oxidation. In the case of the V rich coating, the isothermal curves tested at 550 and 600 °C showed two steps: at an early stage, the weight gain increase over time is linear whilst, in the second stage, a parabolic evolution can be fitted. For higher temperatures (700 °C) only the parabolic evolution was observed but with a strong increase in the mass gain due to the melting of V-O phases.

The structural analysis of the oxide scale when the oxidation temperatures are lower than the melting point of  $\alpha\text{-V}_2\text{O}_5$  showed that a two layer-oxide structure was formed, with a thick porous inner layer ( $\text{SiO}_2$  plus  $\text{Ti(V)O}_2$ ) and an outer discontinuous layer of  $\alpha\text{-V}_2\text{O}_5$ . To the first linear step in the oxidation curves was suggested the growing of  $\text{Ti(V)O}_2$ , as a conjugation of a fast rate of mass transport in the oxide with a slower surface step accompanying the gas dissociation, adsorption and subsequent entry of oxygen into the  $\text{Ti(V)O}_2$  lattice. In fact, at the very beginning of the oxidation process, due to the high Ti content, a  $\text{TiO}_2$  layer started growing. The presence of V ions and its high solubility with Ti promoted the formation of  $\text{Ti(V)O}_2$  solid solution, which comprised vanadium cations with lower oxidation states, as  $\text{V}^{3+}$  ions [119, 129]. The substitution of  $\text{Ti}^{4+}$  by  $\text{V}^{3+}$  ions in the  $\text{TiO}_2$  lattice would increase the concentration of interstitial metallic  $\text{Ti}^{4+}$  ions and, simultaneously, would decrease the number of excess electrons. The oxidation mechanism was inverted in relation to Ti-N, being the outwards diffusion of metallic ions ( $\text{Ti}^{3+}$   $\text{Ti}^{n+}$ ) more favorable than the inwards diffusion of  $\text{O}^{2-}$  ions. There were several consequences of this inversion: (i) the oxidation rate increased substantially, (ii) the kinetics of the oxidation was not controlled any more by a diffusion process but by the rate of dissociation, adsorption and combination at the surface of  $\text{O}^{2-}$  with metallic ions, and (iii) the continuous and compact Si-rich layer cannot be formed.  $\alpha\text{-V}_2\text{O}_5$  and  $\beta\text{-V}_2\text{O}_5$  phase showed to be to be formed exclusively on the top of the inner layer due to the V ions reduction on the surface. The parabolic behaviour after the first linear increase in mass was explained by the oxide scale thickness increase, making harder the ion transport. Then, from a threshold thickness on, the ionic diffusion is the controlling step of oxidation, over the dissociation mechanism, giving rise to the parabolic behavior characteristic of ion diffusion controlled processes.

A detailed description of the oxidation mechanism occurring in TiSiN and TiSi(V)N coatings oxidation can be found in Annex H.

## 5.4. Tribological behavior

The tribological behavior of TiSi(V)N coatings at room temperature was assessed in a pin on disc equipment using two different balls, alumina ( $\text{Al}_2\text{O}_3$ ) and high speed steel (HSS). The tests were performed with the same test conditions used for Ni-based coatings deposited by PTA. Coatings S2-4 and S2-8 were used to study the effect of V additions to the TiSiN (S2-0) and S3-8 film, which had a higher silicon and similar vanadium contents in relation to S2-8 coating, was used to understand the role of the Si on the films. Besides TiSiN (S2-0) film, the properties of the V-containing coatings were compared and discussed in relation to the TiN and TiVN films. The TiVN coating had a hardness of 23.8 GPa, a Young's Modulus of 398 GPa, a similar level of residual stresses and slight higher adhesion critical load than any of the other coatings.

The wear rate of the coatings tested at room temperature is shown in Figure 5.5. TiSiN was the coating showing the highest wear rate. With increasing V content the wear rate progressively dropped. Furthermore, for  $\text{Al}_2\text{O}_3$  balls the wear rate was much lower than when the coatings slid against HSS balls. These results were in good agreement with the lower friction coefficient achieved when  $\text{Al}_2\text{O}_3$  balls were used. The addition of V had the same influence for the TiN reference coating with a clear improvement of the tribological behavior. The worst performance of TiSiN among all the tested coatings was attributed to its low fracture toughness. When TiN and TiSiN coatings were tested against  $\text{Al}_2\text{O}_3$  balls, an abrasion wear mechanism was shown to occur on both wear tracks. However, due to the lower fracture toughness of the TiSiN, deeper scratches and large loosely wear particles were formed in the wear track, leading to a strong abrasion of the surface and, thus, a higher wear rate.

The decreased of the wear rate and the friction coefficient with vanadium incorporation was attributed to the formation of the  $\text{V}_2\text{O}_5$  phase on the wear track of the coatings. This oxide acted as a lubricious tribo-film, protecting the coating from wear, being the protective effect as efficient as higher is the amount of  $\text{V}_2\text{O}_5$  formed. In relation to S2-8 film, TiVN coating (both with similar V content) presented lower wear rate. Such behavior was explained based on the effect of Si on the inhibition of  $\text{V}_2\text{O}_5$  formation, resulting in higher wear rate and friction coefficient.

When tested against HSS ball, the counterparts were covered with both as-deposited and oxidized material; however, in TiSiN coating higher amounts of big wear debris were detected, resulting from the lower fracture toughness of this coating. Therefore, a higher abrasion of the surface was produced with consequent higher wear rate. For V-containing coatings, the much higher wear rates and friction values measured with HSS in comparison to  $\text{Al}_2\text{O}_3$  balls were attributed to a less  $\text{V}_2\text{O}_5$  oxide formation on the worn surfaces.

A detailed characterization of the effect of V additions on the coatings wear and their correlation to the main wear mechanisms is shown in Annex I.

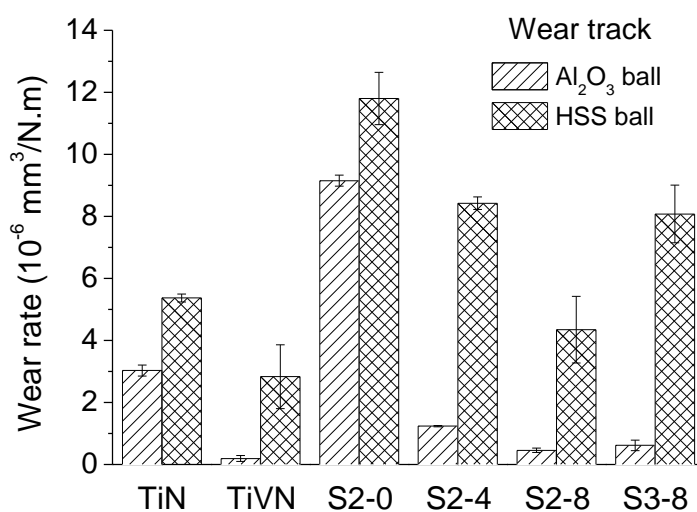


Figure 5.5 - Wear rate of the coatings tested against  $\text{Al}_2\text{O}_3$  and HSS balls.

The effect of V incorporation on the abrasion resistance of TiSiN coatings (series S2-y films) was also assessed using the same test conditions as for the Ni-based coatings evaluated in Annex A. However, in this case, lower sliding distances were selected due to a different wear mechanism and a much lower coating thickness. The volume loss of coatings plotted as a function of the load times sliding distance parameter is presented in Figure 5.6; the respective results for the specific wear rate are plotted in Figure 5.7. As for the other tribological tests, the addition of vanadium gave rise to lower specific wear rates. This trend was more notorious for coatings with low V content. In all cases, the main wear mechanism, suggested by the analysis of the wear scars produced by the ball was 3-body abrasion, which reproduced the wear observed on the surface of real molds after a period of service. In comparison to pin-on-disc tests, the specific wear rate achieved with this abrasion test was higher about two orders of magnitude.

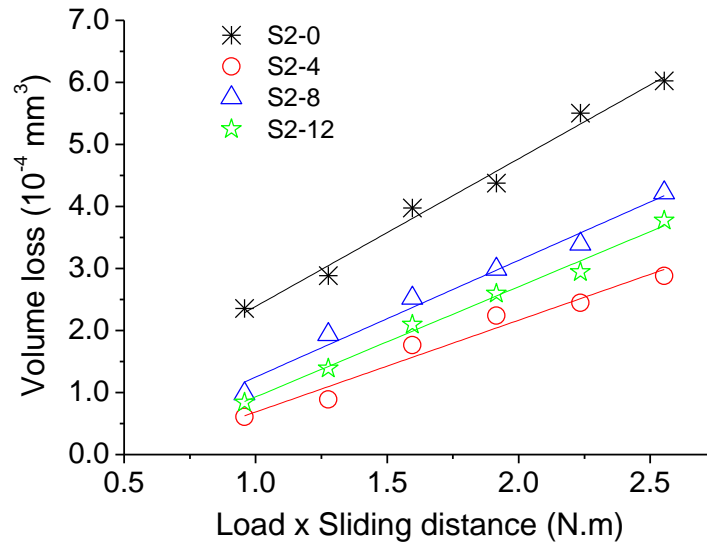


Figure 5.6 - Evolution of the wear behavior as a function of the parameter “normal load × sliding distance”.

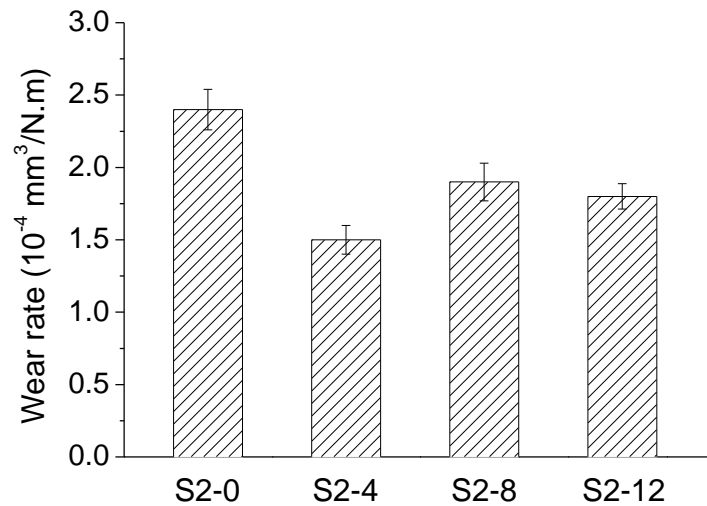


Figure 5.7 - Specific wear rate of coatings, calculated from the slope of a straight line fitted to the points plotted in Figure 5.6.

In summary, although the nanocomposite structure was not formed in TiSi(V)N films, V additions significantly improve their mechanical and tribological properties; however, it has a detrimental effect on their oxidation resistance due to the outwards V ions diffusion to the surface impeding the formation of a continuous Si-O protective layer. The improvement of the tribological properties with V incorporations was related to V<sub>2</sub>O<sub>5</sub> formation on the sliding contact that acted as a lubricious tribo-film, decreasing the friction and protecting the coating from wear.





# Chapter VI

## 6. Conclusions and Future Research

The main aim of the research activity carried out in this thesis was the improvement of the surface properties of molds used in glass containers production, through the application of several types of coatings. Two methodologies were assessed: i) the optimization of conventional Ni-based coatings currently applied on mold surfaces; ii) the development of new coating systems deposited by emergent technologies. In the first part, the effect of base material (cast iron) dilution, induced by the change in arc current, on the properties of Ni-based coatings deposited by the PTA process was investigated, while in the second part two different topics were explored. Firstly, the influence of nanostructured ZrO<sub>2</sub> additions on the properties of Ni-based alloy coatings deposited by APS process were studied while, in the second topic, the influence of V additions on the properties of TiSi(V)N thin films, containing different Si contents, deposited by DC reactive magnetron sputtering, was evaluated. The coatings have markedly different morphological features, physical, mechanical, oxidation and tribology properties depending on the deposition technology and, thus, their direct comparison becomes sometimes without sense. Nevertheless, although individual comparisons were already drawn in each chapter, some common aspects among different coatings deserve comparison, mainly those directly related with the potential industrial applicability, as it will be described below.

The dilution degree of the substrate promoted by changing the arc current affected all the functional properties of the Ni-based alloy coatings. Their hardness, oxidation resistance and tribological behavior were strongly influenced by the micro-structure which consisted typically in Ni-Fe fcc solid solution phase, with interdendritic phases rich in Cr-B, Ni-Si and Fe-Mo-C. Although, the number of precipitates in the grain boundaries increased with the dilution, the hardness of the coatings was reduced due to the growing influence of the softer material of the substrate. As a consequence, also the abrasion wear resistance, calculated from tests performed at room temperature with silica slurry, decreased with increasing substrate dilution. The same trend was observed in another tribological test (pin-on-disc), having been observed specific wear rates varying as much as two up to three orders of magnitude. At high temperature, dilution showed a beneficial effect on the wear resistance of coatings, behavior explained by the decrease of the oxidation resistance due to the incorporation of base material elements. In fact, due to the lower oxidation resistance of the coatings produced with higher dilution, an easy and fast formation of a high amount of oxide debris on the worn surface occurred, which by agglomeration gave rise to a protective tribo-layer improving the wear resistance of the coating. The post-deposition heat treatment of the coatings induced a reduction of the hardness restricted to the partially melted and heat affected zones. In conclusion, the advantages and drawbacks associated with the degree of dilution indicate that to produce the best and most performing coating compromises should be found between the mechanical properties, level of oxidation and wear resistance of coatings.

Nanostructured ZrO<sub>2</sub> additions to Ni-based alloy coatings had different impact when mechanically alloyed mixed powders (MA) or separated powders (Dual) were used. MA powders deposited coatings displayed a homogeneous and compact microstructure with small zirconia particles evenly distributed in the matrix; contrasting with a porous microstructure, full of semi-melted Ni powders with large particles of ZrO<sub>2</sub> entrapped in grain boundaries, responsible for a brittle behavior. In both cases, addition of ZrO<sub>2</sub> improved the hardness and wear behavior. The brittleness of the coatings was determinant on the wear resistance; therefore, the wear rates increased when going from MA powders, through Dual powders up to pure ZrO<sub>2</sub> coatings. All the APS coatings showed higher hardness values than the PTA deposited Ni-based ones; however, their micro-abrasion resistance was worse, differing one order of magnitude, fact explained by the low cohesion between powders. In conclusion, for any possible application of ZrO<sub>2</sub>-containing coatings in the protection of glass molds, an additional melting treatment will be required, in order to improve the cohesion and overcome the brittleness problems.

Si and V additions to TiN and TiSiN systems, respectively, did not change significantly either the global type of columnar morphology or the diffraction peaks indexed to a crystalline fcc TiN-type phase. A shift of the diffraction peaks to higher angles was always observed with either Si or V additions, indicating the placement of those elements in substitutional solid solution in the TiN lattice. Therefore, the required nanocomposite structure needed for the control of vanadium diffusion was not deposited. The presence of Si and V incorporation in solid solution in TiN gave rise to a slight increase in the hardness, although for the high contents an inverse trend was observed. In comparison to previous thick coatings, much higher hardness values could be achieved with the thin films, as shown in Figure 6.1, which is an indication of a possible compensation of their lower thickness for glass molds protection.

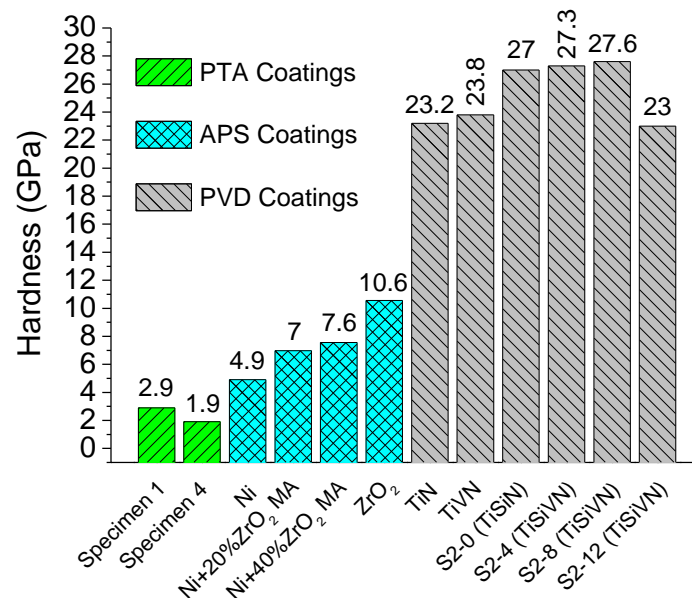


Figure 6.1 - Hardness of coatings studied in the aim of this thesis, deposited by different deposition techniques.

Si and V had an antagonist behavior in relation to oxidation resistance and tribological behavior. Moreover, contrarily to what could be expected, silicon which improved significantly the oxidation resistance of TiN system, had a deleterious influence on the wear resistance. On the other hand, vanadium that promoted an abrupt drop in the oxidation resistance of the TiSiN coatings presented an excellent tribological behavior. The low oxidation resistance of TiSi(V)N films was attributed to the rapid V ions diffusion throughout the oxide scale, which inhibited the formation of a continuous protective silicon oxide layer which, in case of TiSiN is the responsible for the high oxidation resistance. However, the

vanadium at the oxidized surface was promptly oxidized forming a lubricious and protective oxide, the  $V_2O_5$ . Therefore, despite the observed decrease in oxidation resistance of films containing vanadium, this should not be regarded as a disadvantage from the tribological point of view, as the  $V_2O_5$  phase detected can act as a solid lubricant. Among all the studied coatings, V-containing coatings displayed the worst oxidation resistance (see comparison in Figure 6.2). Although TiSiN coating was the most oxidation resistant coating, even in comparison with the Ni-based coatings (specimens 1 and 3) well known for applications at high temperature, the addition of vanadium to TiSiN degraded completely its oxidation behavior. At temperatures higher than the melting point of the  $V_2O_5$  phase ( $\sim 675$  °C), the integrity of the V rich coatings is lost due to rapid oxidation. This can be a drawback for the application of TiSi(V)N coatings in molds surface protection. Thus, further studies to control the V diffusion and, consequently, to improve the oxidation resistance of the coatings, are required. The objective will be the deposition of these films with different structures, i.e. as a nanocomposite (TiVN grains embedded in a  $Si_3N_4$  matrix) or as a multilayer structure (TiVN layers alternating with  $Si_3N_4$  layers).

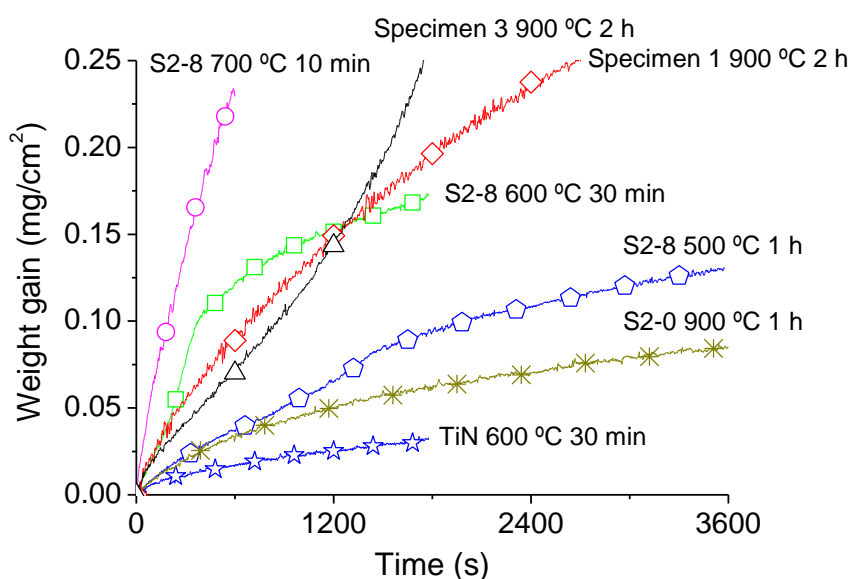


Figure 6.2 - Comparison of the oxidation weight gain of Ni-based coatings deposited by PTA and TiSi(V)N ones deposited by DC reactive magnetron sputtering.

The tribological experiments performed at room temperature, either by micro-scale abrasion or pin-on-disc testing revealed that V additions could improve the wear behavior of TiN and TiSiN films. A comparison of the specific wear rate of all the films calculated from the tests achieved by both techniques using the same test conditions (see Figures 6.3 and 6.4) showed that V-containing thin films performed much better than the thicker coatings.

Preliminary tribological tests performed by pin-on-disc of a TiSi(V)N film at high temperature also revealed a better performance in relation to the thicker ones (Ni-based coatings deposited by PTA). In fact, even for a testing temperature 50 °C higher (see Figure 6.5), TiSi(V)N film showed close to one or two orders of magnitude lower wear rates than Ni-based coatings and uncoated gray cast iron, respectively.

In conclusion, although further studies at high temperature are required to better characterize the tribological behavior of V rich coatings, the preliminary tests showed that TiSi(V)N films had potential for the protection of mold surfaces, despite their low thickness in comparison to thick coatings. Nevertheless, it should be remarked that pin-on-disc and micro-scale abrasion apparatus did not reproduce well the loading conditions to which molds are submitted. Therefore the development of new tribology equipment is recommended for reproducing the real working conditions, i.e. tests should simulate abrasion at high temperature. Only with such equipment it will be possible to have a proper prediction of the coatings wear during service.

Finally, several remarks should be considered in this comparison between thin and thick coatings. In a first glance, it could be thought that a higher coating thickness (typical of PTA and APS coatings) could compensate a lower wear resistance. However, in glass containers production, many times dimensional tolerances in the molds are just a few microns, values incompatible with a possible wear out of the total thickness of a thick coating, increasing that way, the viability of thin films as a solution for molds protection. On the other hand, the use of thin films also allows overcome the poor thermal conductivity attributed to the use of thick ceramic coatings. In fact, their lower thickness permits a much more efficient cooling of the coating and base material in spite of the base thermal conductivity of both types of coatings could be the same. Therefore, lower power consumption for molds cooling down can be expected, thereby reducing production costs. Hence, for future work, thermal conductivity tests are recommended to compare the cooling rate of molds protected by thick and thin coatings. In relation to maintenance problems, the use of these self-lubricant coatings can also remedy the drawbacks that normally liquid lubricant brings (corrosion and disassembling problems), which frequently led to the molds failure and, therefore, to increasing production costs. In fact solid lubricious oxides are not as reactive as liquid lubricants are and the global amount used is much lower. Thus, the probability of corrosion is much lower allowing more uniform, durable and efficient lubrication of the produced parts. Furthermore, the use of these coatings has a huge advantage from the environmental point of view, since they are not as harmful for the environment as the liquid ones are. In relation to

the production of the coatings, despite the high production costs of sputtered films, the reduction of the steps in molds production, such as final machining and polishing (see Table 2.2 in chapter II) and the high number of components that can be coated at the same time, when compared to the technology used for the production of thicker ones, mitigate the costs of protection of the molds. With the expectancy of increasing lifetime, due to their superior mechanical and tribological properties, thin sputtered films should be considered in relation to thick coatings in the protection of molds for glass industry. Specifically, V rich coatings are of great relevance and promising for molds protection. Furthermore, its application could be extended to related areas where high temperature resistance and lubricious properties are required, such as the protection of machining tools for high-speed cutting and dry machining processes.

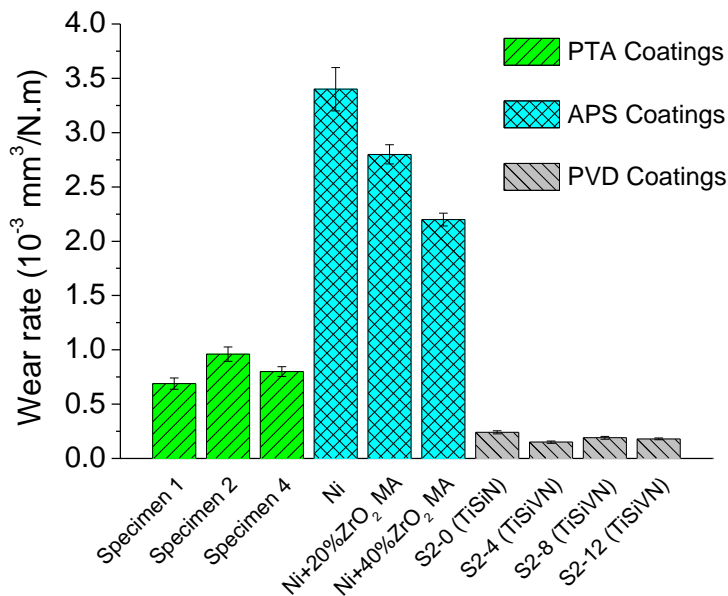


Figure 6.3- Specific wear rate of coatings calculated from the micro-scale abrasion tests.

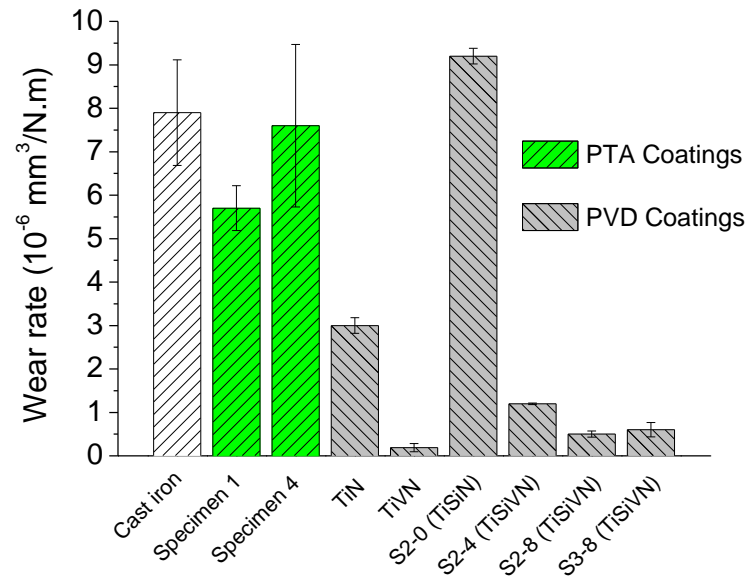


Figure 6.4 - Specific wear rate of coatings calculated from the pin-on-disc tests.

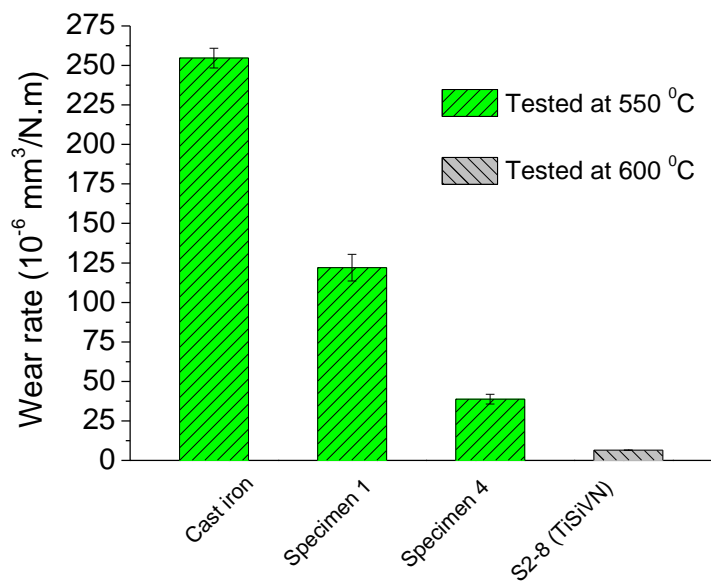


Figure 6.5 - Specific wear rate of coatings calculated from the pin-on-disc tests performed at high temperature.





## 7. References

- [1] M. Cingi, F. Arisoy, G. Başman, K. Şeşen, *The effects of metallurgical structures of different alloyed glass mold cast irons on the mold performance*, Mater. Lett., 55 (2002) 360-363.
- [2] M. Sarwar, A.W. Armitage, *Tooling requirements for glass container production for the narrow neck press and blow process*, J. Mater. Process. Technol., 139 (2003) 160-163.
- [3] R. Penlington, M. Sarwar, D.B. Lewis, *Application of advanced coatings to narrow neck press and blow plungers in the glass container industry*, Surf. Coat. Technol., 76-77 (1995) 81-85.
- [4] J.F. Dakan, D.G. Schmidt, *Bronze alloy for glass container molds*, Patent US4732602 A, 1998.
- [5] *Franklin Bronze and alloy company*, Glass Mold Accessory Castings, web reference: <http://www.franklinbronze.com/investment-casting/glass-mold-accessory-castings.htm>.
- [6] *Zhoushan Putuo HongYu Mold Co. Ltd.*, An analysis of glass mold material and its development, web reference: [http://pthymj.com/en/news\\_view.asp?id=106](http://pthymj.com/en/news_view.asp?id=106).
- [7] E. Romero, R.J. DuMola, *Alloy coating for aluminum bronze parts such as molds*, Patent US5441554 A, 1995.
- [8] P. Ngankeu, E. Miravete, *An analysis of plunger temperature during glass parison pressing*, Excerpt from the Proceedings of the COMSOL Conference, Boston 2008.
- [9] T.S. Sidhu, S. Prakash, R.D. Agrawal, *Studies on the properties of high-velocity oxy-fuel thermal spray coatings for higher temperature applications*, Materials Science, 41 (2005) 805-823.
- [10] M.H. Li, X.F. Sun, J.G. Li, Z.Y. Zhang, T. Jin, H.R. Guan, Z.Q. Hu, *Oxidation behavior of a single-crystal Ni-Base superalloy in Air at 800 and 900 °C*, Oxid. Met., 59 (2003) 591-605.
- [11] C.T. Liu, J. Ma, X.F. Sun, *Oxidation behavior of a single-crystal Ni-base superalloy between 900 and 1000 °C in air*, J. Alloys Compd., 491 (2010) 522-526.
- [12] I. Podchernyaeva, A. Panasyuk, *Protective coatings on heat-resistant Nickel alloys (Review)*, Powder Metallurgy and Metal Ceramics, 39 (2000) 434-444.

- [13] L. Luo, S. Liu, J. Li, W. Yucheng, *Oxidation behavior of arc-sprayed FeMnCrAl/Cr<sub>3</sub>C<sub>2</sub>-Ni<sub>9</sub>Al coatings deposited on low-carbon steel substrates*, Surf. Coat. Technol., 205 (2011) 3411-3415.
- [14] Y. Wu, S. Hong, J. Zhang, Z. He, W. Guo, Q. Wang, G. Li, *Microstructure and cavitation erosion behavior of WC-Co-Cr coating on 1Cr18Ni9Ti stainless steel by HVOF thermal spraying*, International Journal of Refractory Metals and Hard Materials, 32 (2012) 21-26.
- [15] R.A. Mahesh, R. Jayaganthan, S. Prakash, *Oxidation behavior of HVOF sprayed Ni-5Al coatings deposited on Ni- and Fe-based superalloys under cyclic condition*, Materials Science and Engineering: A, 475 (2008) 327-335.
- [16] J.H. Chang, C.P. Chang, J.M. Chou, R.I. Hsieh, J.L. Lee, *Microstructure and bonding behavior on the interface of an induction-melted Ni-based alloy coating and AISI 4140 steel substrate*, Surf. Coat. Technol., 204 (2010) 3173-3181.
- [17] W. Li, Y. Li, C. Sun, Z. Hu, T. Liang, W. Lai, *Microstructural characteristics and degradation mechanism of the NiCrAlY/CrN/DSM11 system during thermal exposure at 1100 °C*, J. Alloys Compd., 506 (2010) 77-84.
- [18] C. Guo, J. Zhou, J. Chen, J. Zhao, Y. Yu, H. Zhou, *High temperature wear resistance of laser cladding NiCrBSi and NiCrBSi/WC-Ni composite coatings*, Wear, 270 (2011) 492-498.
- [19] K. Gurumoorthy, M. Kamaraj, K.P. Rao, A.S. Rao, S. Venugopal, *Microstructural aspects of plasma transferred arc surfaced Ni-based hardfacing alloy*, Materials Science and Engineering: A, 456 (2007) 11-19.
- [20] I. Hemmati, V. Ocelík, J.T.M. De Hosson, *Effects of the alloy composition on phase constitution and properties of laser deposited Ni-Cr-B-Si coatings*, Physics Procedia, 41 (2013) 302-311.
- [21] M.G. Hobby, G.C. Wood, *The role of nickel in the high-temperature oxidation of Fe-Cr-Ni alloys in oxygen*, Oxid. Met., 1 (1969) 23-54.
- [22] M.J. Tobar, C. Álvarez, J.M. Amado, G. Rodríguez, A. Yáñez, *Morphology and characterization of laser clad composite NiCrBSi-WC coatings on stainless steel*, Surf. Coat. Technol., 200 (2006) 6313-6317.
- [23] S. Lebaili, M. Durand-Charre, S. Hamar-Thibault, *The metallurgical structure of as-solidified Ni-Cr-B-Si-C hardfacing alloys*, J. Mater. Sci., 23 (1988) 3603-3611.
- [24] I.C. Grigorescu, C. Di Rauso, R. Drira-Halouani, B. Lavelle, R. Di Giampaolo, J. Lira, *Phase characterization in Ni alloy-hard carbide composites for fused coatings*, Surf. Coat. Technol., 76-77, Part 2 (1995) 494-498.

- [25] T. Liyanage, G. Fisher, A.P. Gerlich, *Influence of alloy chemistry on microstructure and properties in NiCrBSi overlay coatings deposited by plasma transferred arc welding (PTAW)*, Surf. Coat. Technol., 205 (2010) 759-765.
- [26] M.C. Lin, L.S. Chang, H.C. Lin, C.H. Yang, K.M. Lin, *A study of high-speed slurry erosion of NiCrBSi thermal-sprayed coating*, Surf. Coat. Technol., 201 (2006) 3193-3198.
- [27] V.P. Deodeshmukh, S.J. Matthews, D.L. Klarstrom, *High-temperature oxidation performance of a new alumina-forming Ni-Fe-Cr-Al alloy in flowing air*, International Journal of Hydrogen Energy, 36 (2011) 4580-4587.
- [28] D.W. Yun, S.M. Seo, H.W. Jeong, Y.S. Yoo, *The effects of the minor alloying elements Al, Si and Mn on the cyclic oxidation of Ni-Cr-W-Mo alloys*, Corros. Sci., 83 (2014) 176-188.
- [29] S. Buytoz, M. Ulutan, S. Islak, B. Kurt, O. Nuri Çelik, *Microstructural and wear characteristics of high velocity oxygen fuel (HVOF) sprayed NiCrBSi-SiC composite coating on SAE 1030 steel*, Arabian Journal for Science and Engineering, 38 (2013) 1481-1491.
- [30] C. Guo, J. Chen, J. Zhou, J. Zhao, L. Wang, Y. Yu, H. Zhou, *Effects of WC-Ni content on microstructure and wear resistance of laser cladding Ni-based alloys coating*, Surf. Coat. Technol., 206 (2012) 2064-2071.
- [31] S. Harsha, D. Dwivedi, A. Agarwal, *Influence of CrC addition in Ni-Cr-Si-B flame sprayed coatings on microstructure, microhardness and wear behaviour*, Int. J. Adv. Manuf. Technol., 38 (2008) 93-101.
- [32] Q.Y. Hou, Z. Huang, J.T. Wang, *Influence of nano- $Al_2O_3$  particles on the microstructure and wear resistance of the nickel-based alloy coating deposited by plasma transferred arc overlay welding*, Surf. Coat. Technol., 205 (2011) 2806-2812.
- [33] H.-y. Wang, D.-w. Zuo, M.-d. Wang, G.-f. Sun, H. Miao, Y.-l. Sun, *High temperature frictional wear behaviors of nano-particle reinforced NiCoCrAlY cladded coatings*, Trans. Nonferrous Met. Soc. China, 21 (2011) 1322-1328.
- [34] R. Ghasemi, R. Shoja-Razavi, R. Mozafarinia, H. Jamali, M. Hajizadeh-Oghaz, R. Ahmadi-Pidani, *The influence of laser treatment on hot corrosion behavior of plasma-sprayed nanostructured yttria stabilized zirconia thermal barrier coatings*, Journal of the European Ceramic Society, 34 (2014) 2013-2021.
- [35] Ş. Yılmaz, *An evaluation of plasma-sprayed coatings based on  $Al_2O_3$  and  $Al_2O_3$ -13 wt.%  $TiO_2$  with bond coat on pure titanium substrate*, Ceram. Int., 35 (2009) 2017-2022.
- [36] R. Vaßen, M.O. Jarligo, T. Steinke, D.E. Mack, D. Stöver, *Overview on advanced thermal barrier coatings*, Surf. Coat. Technol., 205 (2010) 938-942.

- [37] C. Chen, Y. Wang, H. Ou, Y. He, X. Tang, *A review on remanufacture of dies and moulds*, *Journal of Cleaner Production*, 64 (2014) 13-23.
- [38] S. Jhavar, C.P. Paul, N.K. Jain, *Causes of failure and repairing options for dies and molds: A review*, *Engineering Failure Analysis*, 34 (2013) 519-535.
- [39] S. Barella, A. Gruttadauria, C. Mapelli, D. Mombelli, *Investigation of failure and damages on a continuous casting copper mould*, *Engineering Failure Analysis*, 36 (2014) 432-438.
- [40] G. Pantazopoulos, S. Zormalia, *Analysis of the failure mechanism of a gripping tool steel component operated in an industrial tube draw bench*, *Engineering Failure Analysis*, 18 (2011) 1595-1604.
- [41] G.C.R. Moura, M.T.P. Aguilar, A.E.M. Pertence, P.R. Cetlin, *The materials and the design of the die in a critical manufacturing step of an automotive shock absorber cap*, *Materials & Design*, 28 (2007) 962-968.
- [42] D. Mellouli, N. Haddar, A. Köster, H.F. Ayedi, *Thermal fatigue failure of brass die-casting dies*, *Engineering Failure Analysis*, 20 (2012) 137-146.
- [43] T.C. Hanson, G.S. Settles, *Particle temperature and velocity effects on the porosity and oxidation of an HVOF corrosion-control coating*, *Journal of Thermal Spray Technology*, 12 (2003) 403-415.
- [44] V. Balasubramanian, A.K. Lakshminarayanan, R. Varahamoorthy, S. Babu, *Application of response surface methodology to prediction of dilution in plasma transferred arc hardfacing of stainless steel on carbon steel*, *J. Iron. Steel Res. Int.*, 16 (2009) 44-53.
- [45] M. Pouranvari, *On the weldability of grey cast iron using nickel based filler metal*, *Materials & Design*, 31 (2010) 3253-3258.
- [46] S.W. Banovic, I.N. DuPont, A.R. Marder, *Dilution control in gas-tungsten-arc welds involving superaustenitic stainless steels and nickel-based alloys*, *Metallurgical and Materials Transactions B*, 32 (2001) 1171-1176.
- [47] V. Ramasubbu, G. Chakraborty, S.K. Albert, A.K. Bhaduri, *Effect of dilution on GTAW Colmonoy 6 (AWS NiCr-C) hardface deposit made on 316LN stainless steel*, *Materials Science and Technology*, 27 (2011) 573-580.
- [48] A.K. Lakshminarayanan, V. Balasubramanian, K. Elangovan, *Effect of welding processes on tensile properties of AA6061 aluminium alloy joints*, *Int. J. Adv. Manuf. Technol.*, 40 (2009) 286-296.

- [49] A.J. Ramirez, J.W. Sowards, J.C. Lippold, *Improving the ductility-dip cracking resistance of Ni-base alloys*, J. Mater. Process. Technol., 179 (2006) 212-218.
- [50] K. Siva, N. Murugan, R. Logesh, *Optimization of weld bead geometry in plasma transferred arc hardfaced austenitic stainless steel plates using genetic algorithm*, Int. J. Adv. Manuf. Technol., 41 (2009) 24-30.
- [51] C. Sudha, P. Shankar, R.V.S. Rao, R. Thirumurugesan, M. Vijayalakshmi, B. Raj, *Microchemical and microstructural studies in a PTA weld overlay of Ni-Cr-Si-B alloy on AISI 304L stainless steel*, Surf. Coat. Technol., 202 (2008) 2103-2112.
- [52] A. Gatto, E. Bassoli, M. Fornari, *Plasma Transferred Arc deposition of powdered high performances alloys: process parameters optimisation as a function of alloy and geometrical configuration*, Surf. Coat. Technol., 187 (2004) 265-271.
- [53] H.-J. Kim, S. Grossi, Y.-G. Kweon, *Characterization of Fe-Cr-B based coatings produced by HVOF and PTA processes*, Metals and Materials, 5 (1999) 63-72.
- [54] P. Kulu, A. Zikin, A. Surženkov, R. Tarbe, *Structure and properties of HVOF-sprayed and PTA-welded cermet hard phase reinforced Fe-matrix-based coatings*, International Journal of Microstructure and Materials Properties, 9 (2014) 4-14.
- [55] J.R. Davis, *Handbook of thermal spray technology*, first edition, ASM International and Thermal Spray Society, USA, 2004.
- [56] W.L. Daugherty, G.R. Cannell, *Analysis of porosity associated with Hanford 3013 outer container welds*, Practical Failure Analysis, 3 (2003) 56-62.
- [57] M. Oksa, E. Turunen, T. Suhonen, T. Varis, S.-P. Hannula, *Optimization and characterization of high velocity oxy-fuel sprayed coatings: techniques, materials, and applications*, Coatings, 1 (2011) 17-52.
- [58] D. Thirumalaikumarasamy, K. Shanmugam, V. Balasubramanian, *Influences of atmospheric plasma spraying parameters on the porosity level of alumina coating on AZ31B magnesium alloy using response surface methodology*, Progress in Natural Science: Materials International, 22 (2012) 468-479.
- [59] B.G. Mellor, *Surface coatings for protection against wear*, Woodhead publishing in Materials and CRC Press LLC, North America, 2006.
- [60] K. Weman, *Welding Processes Handbook*, CRC Press, USA, 2003.

- [61] R.S. Lima, B.R. Marple, *From APS to HVOF spraying of conventional and nanostructured titania feedstock powders: a study on the enhancement of the mechanical properties*, Surf. Coat. Technol., 200 (2006) 3428-3437.
- [62] G. Bolelli, L. Lusvarghi, T. Manfredini, F.P. Mantini, R. Polini, E. Turunen, T. Varis, S.P. Hannula, *Comparison between plasma- and HVOF-sprayed ceramic coatings. Part I: microstructure and mechanical properties*, Int. J. Surf. Sci. Eng., 1 (2007) 38-61.
- [63] Y. Bai, Z.H. Han, H.Q. Li, C. Xu, Y.L. Xu, Z. Wang, C.H. Ding, J.F. Yang, *High performance nanostructured ZrO<sub>2</sub> based thermal barrier coatings deposited by high efficiency supersonic plasma spraying*, Applied Surface Science, 257 (2011) 7210-7216.
- [64] T. Kakuda, A. Limarga, A. Vaidya, A. Kulkarni, T.D. Bennett, *Non-destructive thermal property measurements of an APS TBC on an intact turbine blade*, Surf. Coat. Technol., 205 (2010) 446-451.
- [65] S.M. Naga, 21 - *Ceramic matrix composite thermal barrier coatings for turbine parts*, in: I.M. Low (Ed.) Advances in Ceramic Matrix Composites, Woodhead Publishing, 2014, 524-536.
- [66] Y.H. Sohn, E.Y. Lee, B.A. Nagaraj, R.R. Biederman, R.D. Sisson Jr, *Microstructural characterization of thermal barrier coatings on high pressure turbine blades*, Surf. Coat. Technol., 146-147 (2001) 132-139.
- [67] J.L. Mo, M.H. Zhu, *Tribological oxidation behaviour of PVD hard coatings*, Tribology International, 42 (2009) 1758-1764.
- [68] J.L. Mo, M.H. Zhu, B. Lei, Y.X. Leng, N. Huang, *Comparison of tribological behaviours of AlCrN and TiAlN coatings-Deposited by physical vapor deposition*, Wear, 263 (2007) 1423-1429.
- [69] P.E. Hovsepian, A.P. Ehiasarian, A. Deeming, C. Schimpf, *Novel TiAlCN/VCN nanoscale multilayer PVD coatings deposited by the combined high-power impulse magnetron sputtering/unbalanced magnetron sputtering (HIPIMS/UBM) technology*, Vacuum, 82 (2008) 1312-1317.
- [70] N. Fateh, G.A. Fontalvo, G. Gassner, C. Mitterer, *Influence of high-temperature oxide formation on the tribological behaviour of TiN and VN coatings*, Wear, 262 (2007) 1152-1158.
- [71] T. Polcar, A. Cavaleiro, *Structure and tribological properties of AlCrTiN coatings at elevated temperature*, Surf. Coat. Technol., 205, Supplement 2 (2011) S107-S110.
- [72] T. Polcar, N.M.G. Parreira, A. Cavaleiro, *Structural and tribological characterization of tungsten nitride coatings at elevated temperature*, Wear, 265 (2008) 319-326.

- [73] T. Polcar, N.M.G. Parreira, A. Cavaleiro, *Tribological characterization of tungsten nitride coatings deposited by reactive magnetron sputtering*, *Wear*, 262 (2007) 655-665.
- [74] H.C. Barshilia, A. Jain, K.S. Rajam, *Structure, hardness and thermal stability of nanolayered TiN/CrN multilayer coatings*, *Vacuum*, 72 (2003) 241-248.
- [75] D. Lin, B. Yan, W. Yu, *Composition and structure characterization of W<sub>N</sub>x films produced by RF reactive sputtering*, *MRS Online Proceedings Library*, 187 (1990) 161.
- [76] O. Rist, P.T. Murray, *Growth of TiC films by pulsed laser evaporation (PLE) and characterization by XPS and AES*, *Fresenius' Journal of Analytical Chemistry*, 341 (1991) 360-364.
- [77] Z. Qi, P. Sun, Z. Wang, *Microstructure and mechanical properties of TiCN coatings prepared by MTCVD*, in: J. Luo, Y. Meng, T. Shao, Q. Zhao (Eds.) *Advanced Tribology*, Springer Berlin Heidelberg, 2010, 796-800.
- [78] R. Ospina, D. Escobar-Rincón, P.J. Arango, E. Restrepo-Parra, J.F. Jurado, *Structural and chemical composition analysis of WCN produced by pulsed vacuum arc discharge*, *Surf. Coat. Technol.*, 232 (2013) 96-100.
- [79] G. Pezzotti, I. Tanaka, Y. Ikuhara, M. Sakai, T. Nishida, *Evidences for dilute solid solutions in the Si<sub>3</sub>N<sub>4</sub>-TiN system*, *Scripta Metallurgica et Materialia*, 31 (1994) 403-406.
- [80] S. Vepřek, S. Reiprich, L. Shizhi, *Superhard nanocrystalline composite materials: The TiN/Si<sub>3</sub>N<sub>4</sub> system*, *Applied Physics Letters*, 66 (1995) 2640-2642.
- [81] E. Lugscheider, O. Knotek, F. Löffler, C. Barimani, S. Guerreiro, H. Zimmermann, *Deposition of arc TiAlN coatings with pulsed bias*, *Surf. Coat. Technol.*, 76-77, Part 2 (1995) 700-705.
- [82] L. Hultman, C. Engström, M. Odén, *Mechanical and thermal stability of TiN/NbN superlattice thin films*, *Surf. Coat. Technol.*, 133-134 (2000) 227-233.
- [83] S.H. Yao, Y.L. Su, W.H. Kao, T.H. Liu, *Tribology and oxidation behavior of TiN/AlN nano-multilayer films*, *Tribology International*, 39 (2006) 332-341.
- [84] L. García-González, J. Hernández-Torres, P.J. García-Ramírez, J. Martínez-Castillo, Á. Saucedo, A.L. Herrera-May, F.J. Espinoza-Beltrán, *Structure and mechanical properties of TiBN coatings fabricated by dc reactive sputtering technique*, *J. Mater. Process. Technol.*, 186 (2007) 362-366.

- [85] W.L. Wang, K.J. Liao, S.X. Wang, Y.W. Sun, *Microstructure and semiconducting properties of c-BN films using r.f. plasma CVD thermally assisted by a tungsten filament*, Thin Solid Films, 368 (2000) 283-286.
- [86] M.D.A. Rahman, N. Soin, P. Maguire, R.A. D'Sa, S.S. Roy, C.M.O. Mahony, P. Lemoine, R. McCann, S.K. Mitra, J.A.D. McLaughlin, *Structural and surface energy analysis of nitrogenated ta-C films*, Thin Solid Films, 520 (2011) 294-301.
- [87] R. Buhl, H.K. Pulker, E. Moll, *TiN coatings on steel*, Thin Solid Films, 80 (1981) 265-270.
- [88] G. Paller, B. Matthes, W. Herr, E. Broszeit, *Tribological properties of r.f.-sputtered titanium-based hard coatings and their behaviour under plastics-processing conditions*, Materials Science and Engineering: A, 140 (1991) 647-654.
- [89] J. Lin, N. Zhang, W.D. Sproul, J.J. Moore, *A comparison of the oxidation behavior of CrN films deposited using continuous dc, pulsed dc and modulated pulsed power magnetron sputtering*, Surf. Coat. Technol., 206 (2012) 3283-3290.
- [90] P.H. Mayrhofer, H. Willmann, C. Mitterer, *Oxidation kinetics of sputtered Cr-N hard coatings*, Surf. Coat. Technol., 146-147 (2001) 222-228.
- [91] P.H. Mayrhofer, C. Mitterer, L. Hultman, H. Clemens, *Microstructural design of hard coatings*, Progress in Materials Science, 51 (2006) 1032-1114.
- [92] J. Krzanowski, D. Foley, *The effect of Cr content on the oxidation behavior of Ti-Cr-N films*, Coatings, 4 (2014) 308-319.
- [93] Y.C. Chim, X.Z. Ding, X.T. Zeng, S. Zhang, *Oxidation resistance of TiN, CrN, TiAlN and CrAlN coatings deposited by lateral rotating cathode arc*, Thin Solid Films, 517 (2009) 4845-4849.
- [94] L.W. Ma, J.M. Cairney, M.J. Hoffman, P.R. Munroe, *Deformation and fracture of TiN and TiAlN coatings on a steel substrate during nanoindentation*, Surf. Coat. Technol., 200 (2006) 3518-3526.
- [95] J.H. Hsieh, A.L.K. Tan, X.T. Zeng, *Oxidation and wear behaviors of Ti-based thin films*, Surf. Coat. Technol., 201 (2006) 4094-4098.
- [96] D. McIntyre, J.E. Greene, G. Håkansson, J.E. Sundgren, W.D. Münz, *Oxidation of metastable single-phase polycrystalline Ti<sub>0.5</sub>Al<sub>0.5</sub>N films: Kinetics and mechanisms*, Journal of Applied Physics, 67 (1990) 1542-1553.



- [97] D.B. Lee, M.H. Kim, Y.C. Lee, S.C. Kwon, *High temperature oxidation of TiCrN coatings deposited on a steel substrate by ion plating*, Surf. Coat. Technol., 141 (2001) 232-239.
- [98] Y. Otani, S. Hofmann, *High temperature oxidation behaviour of  $(Ti_{1-x}Cr_x)N$  coatings*, Thin Solid Films, 287 (1996) 188-192.
- [99] T.D. Nguyen, S.K. Kim, D.B. Lee, *High-temperature oxidation of nano-multilayered TiAlCrSiN thin films in air*, Surf. Coat. Technol., 204 (2009) 697-704.
- [100] M. Pfeiler, J. Zechner, M. Penoy, C. Michotte, C. Mitterer, M. Kathrein, *Improved oxidation resistance of TiAlN coatings by doping with Si or B*, Surf. Coat. Technol., 203 (2009) 3104-3110.
- [101] S.H. Kim, J.K. Kim, K.H. Kim, *Influence of deposition conditions on the microstructure and mechanical properties of Ti-Si-N films by DC reactive magnetron sputtering*, Thin Solid Films, 420-421 (2002) 360-365.
- [102] M. Nose, Y. Deguchi, T. Mae, E. Honbo, T. Nagae, K. Nogi, *Influence of sputtering conditions on the structure and properties of Ti-Si-N thin films prepared by r.f.-reactive sputtering*, Surf. Coat. Technol., 174-175 (2003) 261-265.
- [103] S. Veprek, H.D. Männling, P. Karvankova, J. Prochazka, *The issue of the reproducibility of deposition of superhard nanocomposites with hardness of  $\geq 50$  GPa*, Surf. Coat. Technol., 200 (2006) 3876-3885.
- [104] J. Musil, *Physical and mechanical properties of hard nanocomposite films prepared by reactive magnetron sputtering*, in: A. Cavaleiro, J.M. De Hosson (Eds.) Nanostructured Coatings, Springer New York, 2006, 407-463.
- [105] S. Vepřek, S. Reiprich, *A concept for the design of novel superhard coatings*, Thin Solid Films, 268 (1995) 64-71.
- [106] F. Vaz, L. Rebouta, P. Goudeau, J. Pacaud, H. Gareme, J.P. Rivière, A. Cavaleiro, E. Alves, *Characterisation of  $Ti_{1-x}Si_xN_y$  nanocomposite films*, Surf. Coat. Technol., 133-134 (2000) 307-313.
- [107] A. Flink, T. Larsson, J. Sjöln, L. Karlsson, L. Hultman, *Influence of Si on the microstructure of arc evaporated (Ti,Si)N thin films; evidence for cubic solid solutions and their thermal stability*, Surf. Coat. Technol., 200 (2005) 1535-1542.
- [108] K.D. Bouzakis, G. Skordaris, S. Gerardis, G. Katirtzoglou, S. Makrimalakis, M. Pappa, E. Lili, R. M'Saoubi, *Ambient and elevated temperature properties of TiN, TiAlN and TiSiN PVD films and their impact on the cutting performance of coated carbide tools*, Surf. Coat. Technol., 204 (2009) 1061-1065.

- [109] E. Badisch, G.A. Fontalvo, M. Stoiber, C. Mitterer, *Tribological behavior of PACVD TiN coatings in the temperature range up to 500 °C*, Surf. Coat. Technol., 163-164 (2003) 585-590.
- [110] M. Stoiber, E. Badisch, C. Lugmair, C. Mitterer, *Low-friction TiN coatings deposited by PACVD*, Surf. Coat. Technol., 163-164 (2003) 451-456.
- [111] J.S. Zabinski, J.H. Sanders, J. Nainaparampil, S.V. Prasad, *Lubrication using a microstructurally engineered oxide: performance and mechanisms*, Tribology Letters, 8 (2000) 103-116.
- [112] M.S. Bogdanski, H.E. Sliney, C. Dellacorte, *The effect of processing and compositional changes on the tribology of PM212 in air*, Lubric. Eng. 48 (1992) 675-683.
- [113] S.M. Aouadi, H. Gao, A. Martini, T.W. Scharf, C. Muratore, *Lubricious oxide coatings for extreme temperature applications: A review*, Surf. Coat. Technol., In Press, DOI: 10.1016/j.surfcoat.2014.05.064
- [114] D.B. Lewis, S. Creasey, Z. Zhou, J.J. Forsyth, A.P. Ehiasarian, P.E. Hovsepian, Q. Luo, W.M. Rainforth, W.D. Münz, *The effect of (Ti+Al)-V ratio on the structure and oxidation behaviour of TiAlN/VN nano-scale multilayer coatings*, Surf. Coat. Technol., 177-178 (2004) 252-259.
- [115] K. Kutschej, P.H. Mayrhofer, M. Kathrein, P. Polcik, C. Mitterer, *A new low-friction concept for  $Ti_{1-x}Al_xN$  based coatings in high-temperature applications*, Surf. Coat. Technol., 188-189 (2004) 358-363.
- [116] K. Kutschej, P.H. Mayrhofer, M. Kathrein, P. Polcik, C. Mitterer, *Influence of oxide phase formation on the tribological behaviour of Ti-Al-V-N coatings*, Surf. Coat. Technol., 200 (2005) 1731-1737.
- [117] G. Gassner, P.H. Mayrhofer, K. Kutschej, C. Mitterer, M. Kathrein, *A New low friction concept for high temperatures: lubricious oxide formation on sputtered VN coatings*, Tribology Letters, 17 (2004) 751-756.
- [118] P.H. Mayrhofer, P.E. Hovsepian, C. Mitterer, W.D. Münz, *Calorimetric evidence for frictional self-adaptation of TiAlN/VN superlattice coatings*, Surf. Coat. Technol., 177-178 (2004) 341-347.
- [119] A. Glaser, S. Surnev, F.P. Netzer, N. Fateh, G.A. Fontalvo, C. Mitterer, *Oxidation of vanadium nitride and titanium nitride coatings*, Surface Science, 601 (2007) 1153-1159.
- [120] J.H. Ouyang, S. Sasaki, *Tribo-oxidation of cathodic arc ion-plated (V,Ti)N coatings sliding against a steel ball under both unlubricated and boundary-lubricated conditions*, Surf. Coat. Technol., 187 (2004) 343-357.

- [121] J.-K. Park, Y.-J. Baik, *Increase of hardness and oxidation resistance of VN coating by nanoscale multilayered structurization with AlN*, Mater. Lett., 62 (2008) 2528-2530.
- [122] R. Franz, J. Neidhardt, R. Kaindl, B. Sartory, R. Tessadri, M. Lechthaler, P. Polcik, C. Mitterer, *Influence of phase transition on the tribological performance of arc-evaporated AlCrVN hard coatings*, Surf. Coat. Technol., 203 (2009) 1101-1105.
- [123] Y. Qiu, S. Zhang, J.-W. Lee, B. Li, Y. Wang, D. Zhao, *Self-lubricating CrAlN/VN multilayer coatings at room temperature*, Applied Surface Science, 279 (2013) 189-196.
- [124] M. Pfeiler, K. Kutschej, M. Penoy, C. Michotte, C. Mitterer, M. Kathrein, *The effect of increasing V content on structure, mechanical and tribological properties of arc evaporated Ti-Al-V-N coatings*, International Journal of Refractory Metals and Hard Materials, 27 (2009) 502-506.
- [125] W. Tillmann, S. Momeni, F. Hoffmann, *A study of mechanical and tribological properties of self-lubricating TiAlVN coatings at elevated temperatures*, Tribology International, 66 (2013) 324-329.
- [126] Q. Luo, *Temperature dependent friction and wear of magnetron sputtered coating TiAlN/VN*, Wear, 271 (2011) 2058-2066.
- [127] R. Franz, C. Mitterer, *Vanadium containing self-adaptive low-friction hard coatings for high-temperature applications: A review*, Surf. Coat. Technol., 228 (2013) 1-13.
- [128] K. Jun, Y. Shimogaki, *Development of TiSiN CVD process using TiCl<sub>4</sub>/SiH<sub>4</sub>/NH<sub>3</sub> chemistry for ULSI anti-oxidation barrier applications*, Science and Technology of Advanced Materials, 5 (2004) 549-554.
- [129] S. Thongtem, T. Thongtem, M. McNallan, *High-temperature nitridation and oxidation of Ti-based alloys*, Surface and Interface Analysis, 32 (2001) 306-309.



---

## Annex A

---

**F. Fernandes, B. Lopes, A. Cavaleiro, A. Ramalho, A. Loureiro, *Effect of arc current on microstructure and wear characteristics of a Ni-based coating deposited by PTA on gray cast iron*, Surface and Coatings Technology, 205 (2011) 4094-4106.**





## Effect of arc current on microstructure and wear characteristics of a Ni-based coating deposited by PTA on gray cast iron

F. Fernandes<sup>a,b,\*</sup>, B. Lopes<sup>b</sup>, A. Cavaleiro<sup>a</sup>, A. Ramalho<sup>a</sup>, A. Loureiro<sup>a</sup>

<sup>a</sup> CEMUC, Department of Mechanical Engineering, University of Coimbra, Rua Luís Reis Santos, 3030–788 Coimbra, Portugal

<sup>b</sup> Intermolde, Rua de Leiria, 95, Apartado 103, 2431–902 Marinha Grande, Portugal

### ARTICLE INFO

#### Article history:

Received 16 December 2010

Accepted in revised form 3 March 2011

#### Keywords:

Plasma transferred arc

Ni based alloy

Microstructure

Wear

### ABSTRACT

The plasma transferred arc (PTA) technique is currently used to coat the edges of moulds for the glass industry with nickel-based hardfacing alloys. However the hardness and wear performance of these coatings are significantly affected by the procedure adopted during the deposition of coatings. The aim of the present investigation is to study the effect of arc current on the microstructure, hardness and wear performance of a nickel-based hardfacing alloy deposited on gray cast iron, currently used in molds for the glass industry. Microstructure, hardness and wear assessments were used to characterize the coatings. Electron probe micro analysis (EPMA) mapping, scanning electron microscopy/energy dispersive X-ray analysis (SEM/EDAX) and X-ray diffraction (XRD) were used to characterize the microstructure of the deposits. The effect of post weld heat treatment (PWHT) on the microstructure and hardness was also studied. The typical microstructure of the coatings consists of dendrites of Ni–Fe, in the FCC solid solution phase, with interdendritic phases rich in Cr–B, Ni–Si and Fe–Mo–C. Increasing the arc current reduces the proportion of porosity and hardness of the coatings and modifies their composition due to the increasing dilution of the cast iron. The partial melted zone (PMZ) had a typical white cast iron plus martensite microstructure, while the heat affected zone (HAZ) had only a martensite structure. The wear tests showed decreasing wear resistance with decreasing hardness of the coatings. PWHT reduces the hardness of the PMZ and HAZ but does not significantly alter the hardness of the bulk coating.

© 2011 Elsevier B.V. All rights reserved.

### 1. Introduction

Traditionally, molds for the glass industry are manufactured from gray cast iron or copper alloys due to their superior thermal behavior, relatively low cost and excellent thermal conductivity. This is associated with high hardness and good wear resistance and leads to a high production rate of glass parts. However, the edges of the molds made of these materials are sensitive to wear in heavy duty cycles; so they need to be coated with materials that are more resistant to high temperature and wear [1].

The coating of these edges is frequently done by plasma transferred arc (PTA), using nickel-based filler metals [2]. Normally the PTA process produces very high quality, thicker deposits, offering optimal protection with minimal thermal distortion of the parts, low environmental impact and high deposition rates in single layer deposits [3]. It allows perfectly controlled deposition of alloys on mechanical parts that are subject to harsh environments, significantly extending their service life [4]. The composition and properties of the coating are greatly influenced by the

type and dilution of the substrate. Balasubramanian et al. [5] suggest that the dilution of coatings should be controlled through the relevant process parameters (transferred arc current, travel speed, powder feed rate, torch oscillation frequency and stand-off distance). Takano et al. [6] studied the influence of arc current variation, arc constriction and plasma gas flow on the characteristics of Co coatings. They concluded that current intensity is the parameter that most significantly affects the characteristics of the deposits as higher currents increase the dilution of the base material and decrease the hardness of the coatings. Díaz et al. [7] mentioned that the dilution also increases with gas plasma flow in stellite 6 coatings.

Nickel-based hardfacing alloys have become increasingly popular in recent years owing to their excellent performance in environments where abrasion, corrosion and elevated temperature are factors. The microstructure of Ni-based hardfacing alloy deposits has been studied using various alloy compositions and different substrates [8–10]. However, most of the studies consider the deposition of nickel alloys on stainless steels; there are no references to characterization of such deposits applied to gray cast iron.

Gurumoorthy et al. [8], who worked with nickel-base superalloys deposited by PTA on stainless steel, reported that the microstructure of the deposit consists of  $\gamma$ -Ni solid solution dendrites, carbides, and interdendritic eutectics composed of  $\gamma$ -Ni and other phases identified as

\* Corresponding author at: CEMUC, Department of Mechanical Engineering, University of Coimbra, Rua Luís Reis Santos, 3030–788 Coimbra, Portugal. Tel.: +351 239 790 700; fax: +351 239 790 701.

E-mail address: [filipe.fernandes@dem.uc.pt](mailto:filipe.fernandes@dem.uc.pt) (F. Fernandes).

being Ni-rich borides. The microstructure and mechanical properties of Ni base alloys are greatly influenced by the alloying elements. For example aluminum, titanium and niobium are added to strengthen the material through the formation of  $\gamma'$  gamma prime ( $\text{Ni}_3(\text{Al,Ti})$ ) and boron and zirconium are added to improve the creep strength and ductility [9,10].

This paper details an investigation of the microstructure, hardness and 3-body abrasion behavior of a nickel-based hardfacing alloy deposited by PTA on gray cast iron with different weld currents. Microstructural changes in the HAZ as well as the effect of the post weld heat treatment on the microstructure and hardness of the coatings are also examined.

## 2. Experimental procedure

The coatings were deposited by PTA technology (using a Commercald Group ROBO 90 machine) on flat surfaces of gray cast iron blocks using a nickel-based hardfacing alloy. This technique obtains thicker coatings with lower porosity and higher production rate than the Flame Spraying and Gas Tungsten Arc Welding processes. The composition of base and deposit materials is given in Table 1. The same process parameters were used for each deposition with the exception of the arc current, which was 100 A for specimen 1, 128 A for specimen 2 and 140 A for specimen 4. The edges of a mold made of the same material but with a machined U-shaped groove were coated with the same alloy using the parameters of specimen 2. This specimen is referred to as specimen 3. The surfacing parameters used in the tests are listed in Table 2. The blocks of base material were induction heated before coating, in order to reduce thermal shock, thus reducing the tendency to crack. After coating, the blocks were left to cool to room temperature in still air. Samples containing coating and base material were removed from each block and the mold for further analysis.

The samples for microstructural analysis were polished and etched following conventional procedures. Etching was performed using equal parts of nitric acid and glacial acetic acid, to reveal the microstructure of the deposits. Marble's solution ( $\text{HCl}$  (50 ml) +  $\text{CuSO}_4$  (10 g) +  $\text{H}_2\text{O}$  (50 ml)) was used to reveal the microstructure of the cast iron. The microstructure of the different regions of the samples was characterized by optical microscopy (OP), scanning electron microscopy (SEM), X-ray diffraction (XRD) and energy dispersive X-ray analysis (EDAX). The chemical composition was evaluated by Electron Probe Microanalysis (EPMA). The hardness profile across the interface of the coatings was determined with Vickers testing using a 5 N load at 15 s.

Some specimens were subjected to a subsequent heat-treatment at 850 °C for 1 h and then cooled in the furnace to room temperature, in order to reduce brittle phases present in the partially melted and heat affected zones. Microstructural and hardness profiles of these specimens were obtained.

Wear tests on the coated surfaces were carried out at room temperature in ball-cratering devices. In these devices, a ball is placed on a flat specimen in the presence of abrasive slurry and rotated while being submitted to a specific load in order to produce a spherical cup-shaped depression. This process was used in order to reproduce the wear mechanism present at the surface of the coatings on glass molds which have been in service for a long time. An AISI 52100 steel ball bearing 25.4 mm in diameter was used at constant rotational speed of 75 rpm. High purity SS40 silica with angular particles averaging

**Table 2**  
Deposition parameters for PTA weld surfacing.

	Specimen 1	Specimens 2 and 3*	Specimen 4
Main arc current (A)	100	128	140
Powder feed rate (rpm)	20	20	20
Travel speed (mm/s)	2	2	2
Powder feed gas flow rate (l/min)	2	2	2
Plasma gas flow rate (l/min)	2.2	2.2	2.2
Shielding gas flow rate (l/min)	20	20	20
Torch work distance (mm)	13	13	13
Oscillation (mm)	4	4	4
Preheat temperature °C	480–500	480–500	480–500

\*See text.

3.10  $\mu\text{m}$  in size was used as an abrasive to replicate the effect of the melted glass. The slurry used was prepared with a proportion of 28 vol.% of silica in water.

The duration of the test, measured by the number of rotations, was selected according to the material and the test conditions employed. The normal load used was 0.1 N.

Photographs of the spherical depressions were taken in order to measure their dimensions. The wear volume was calculated by Eq (1), where R is the ball radius and b is the crater chordal diameter.

$$V = (\pi \times b^4) / (64 \times R) \quad (1)$$

Archard's model, given by Eq (2), is the one most commonly applied to wear results to determine a parameter to quantify the wear behavior of materials. In this equation P is the normal load, l is the sliding distance and k is the specific wear rate. The specific wear rate is the parameter which quantifies the wear behavior.

$$V = k \times P \times l \quad (2)$$

To quantify the specific wear rate a linear version of Archard's model was applied and statistical analysis was used to estimate the error of measurement [11].

## 3. Results and discussion

### 3.1. Microstructure

Four distinct regions were observed in the cross section of each of the coatings deposited with the different welding conditions, as illustrated in Fig. 1 A) for sample 3. Those regions are the fusion zone (FZ), composed of the Ni-alloy and the base material melted during the process, the partially melted zone (PMZ), which is the area immediately outside the FZ where liquation can occur during welding, the heat-affected zone (HAZ), which was not melted but underwent microstructural changes and the base material (BM), whose microstructure remains unaffected during the coating deposition thermal cycle. The same regions were observed by M. Pouranvari [12], who studied the welding of gray cast iron using nickel filler metal deposited by shielded metal arc welding.

**Table 1**  
Nominal chemical composition (wt.%) of substrate and hardfacing alloy.

Base material	C	Mn	Si	P	S	Cr	Ni	Mo	V	Ti	Fe
Grey cast iron	3.60	0.60	2.00	<0.20	<0.04	<0.20	<0.50	0.50	0.10	0.20	Balance
Hardfacing alloy			C	Cr	Si	B	Fe	Al	F	Co	Ni
Ni-alloy			0.14	2.45	2.56	0.86	1.08	1.30	0.01	0.08	Balance



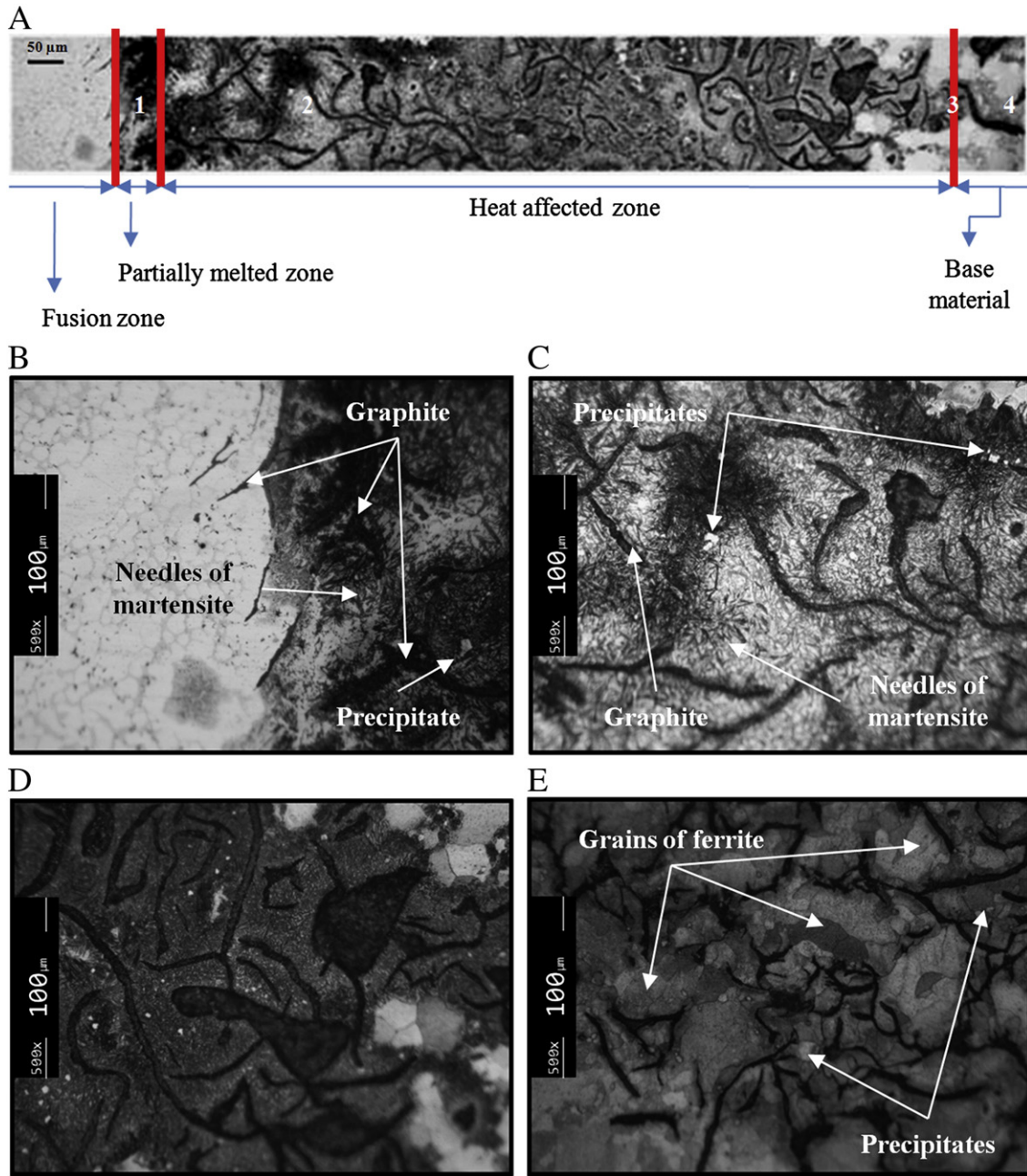


Fig. 1. (A) microstructure of various regions in gray cast iron weld in as-weld condition, (B) partially melted zone, (C) heat affected zone, (D) transition heat affected zone–base material, (E) base material.

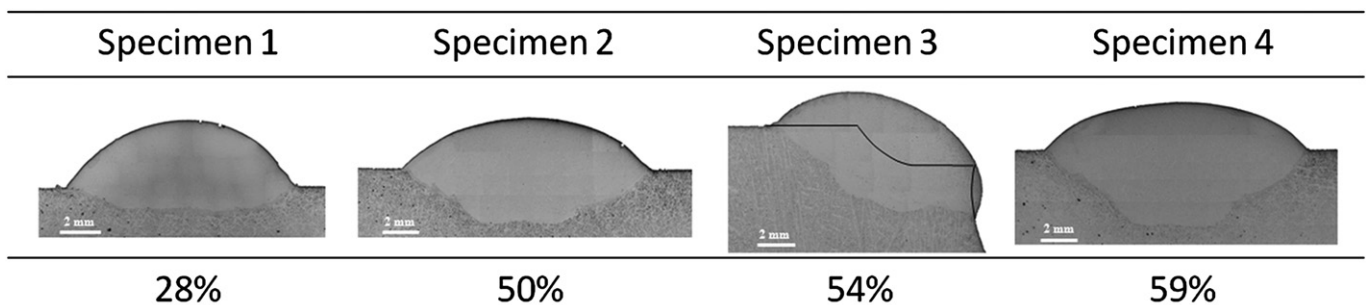


Fig. 2. Dilution induced by PTA process using different weldments: specimen 1 – 100 A, specimens 2 and 3 – 128A, specimen 4 – 140 A.

**Table 3**  
EPMA punctual examination of the deposit and base material of specimen 3.

	Elements (% W)							
	Al	Si	Ti	Cr	Fe	Ni	Mo	
1	1.00	2.52	0.00	2.36	27.37	56.12	0.23	Coating
2	0.96	3.06	0.00	2.50	26.48	56.11	0.17	
3	0.14	0.79	0.06	4.64	16.46	62.24	0.24	
4	0.01	2.17	0.00	0.03	91.73	0.07	0.27	Interface
5	0.02	2.05	0.01	0.03	93.81	0.10	0.32	Base material

Fig. 1 B) to E) illustrates the microstructures of the zones marked with the digits 1 to 4 in Fig. 1 A) in higher magnification.

Fig. 1 B) shows the transition zone between the coating and the partially melted zone. Fig. 1 C) illustrates that the HAZ is basically composed of a martensitic structure (needle shape), which is found mainly in the region closer to the fusion line, however, precipitates and graphite flakes are also present. The microstructure of the base material is principally ferritic with flakes of graphite and precipitates uniformly distributed in the matrix (Fig. 1 E)). Fig. 1 D) illustrates the transition between the HAZ and the base material. The nature and relative size of those zones are determined by the coating procedure, mainly the heat input during the process, and the composition of the cast iron and hardfacing alloy used. The constitution of the main zones will be discussed separately, in order to provide a better understanding of the effect of current on their characteristics.

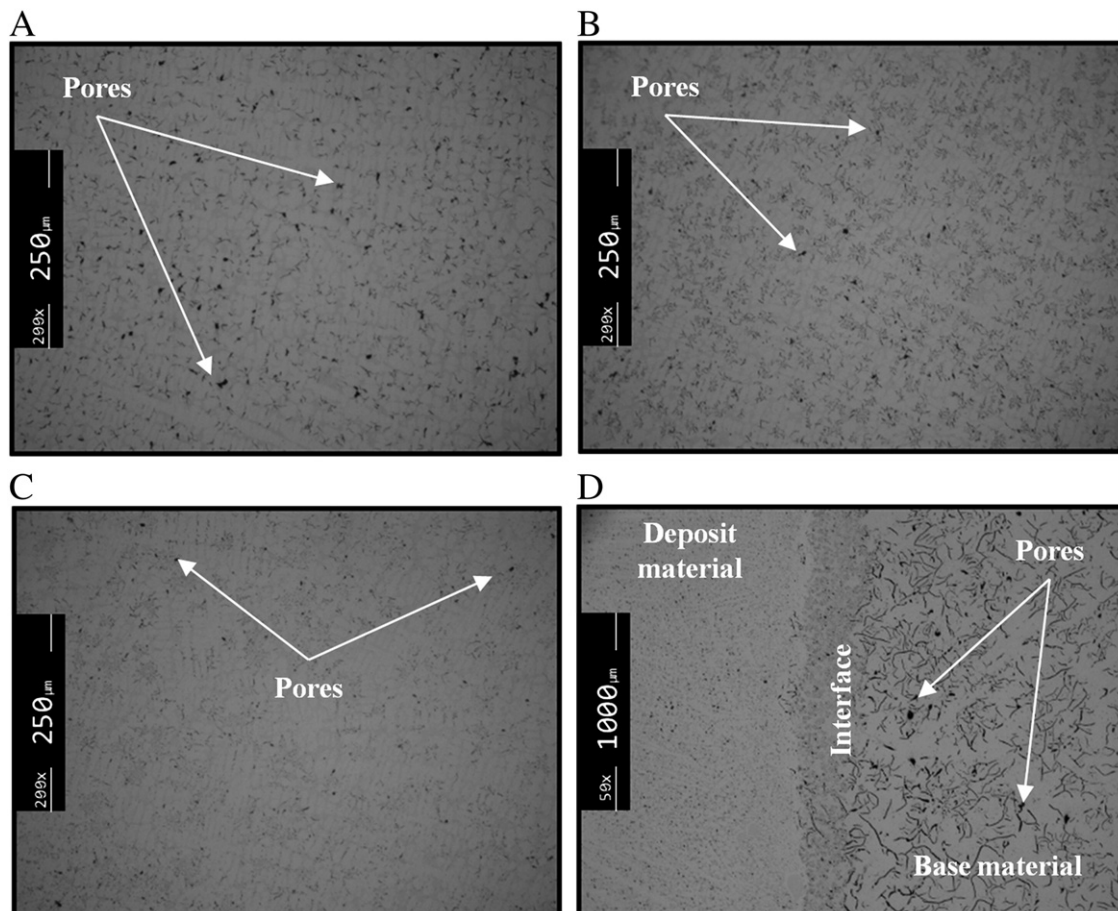
### 3.1.1. Melted zone

Fig. 2 illustrates the effect of the current on the dilution produced in each sample. The dilution is defined as the proportion between the area of melted base material and the total area of the melted zone,

both measured from the cross section of the coating using Photoshop image analysis. These images show that as the current is increased in the range 100–140 A, the dilution steadily increases from 28% to 59%. Specimen 3 in the image illustrates the groove shape usually machined in the mold before coating. Comparing specimens 2 and 3, which were both coated using the same current, it is possible to see that the groove produces only a small change in the dilution and the results obtained from the flat blocks can be extrapolated to molds.

The dilution of cast iron modifies the composition of the coatings, as illustrated in Table 3, which shows the chemical composition measured by EPMA at various points of the coating and the substrate of specimen 3. Point 1 is located close to the coating surface, point 2 at the mid-thickness of the coating, point 3 in the coating close to the interface and the other two points are in the bulk cast iron; point 4 close to the interface and point 5 distant from it. The amount of iron in the coating (>16%) is much higher than that provided by the hardfacing alloy (1.08%), producing a consequent reduction in the nickel content. According to Ezugwu et al. [9] the increase in iron content in the coatings tends to decrease their oxidation resistance because of the formation of a less adherent oxide scale. The increase in Mo content in the coating is also caused by the dilution of the cast iron because it is absent in the hardfacing alloy. Although the true carbon content value could be skewed by contamination, carbon is present in the coating in large quantities, again due to the contribution of the graphite from the cast iron. Thus, increasing the arc current will increase the dilution and the chemical composition of the coating will change accordingly.

All coatings contained small random pores throughout the cross section, as shown in Fig. 3. According to F. A. L. Dullien [13], the “volumetric” and “area” porosity proportions are equivalent for random-structured porous media, which agrees with our results. The area of the



**Fig. 3.** Aspect of the coatings of: A) specimen 1, B) specimen 2, C) specimen 4, and D) fusion interface of specimen 1.

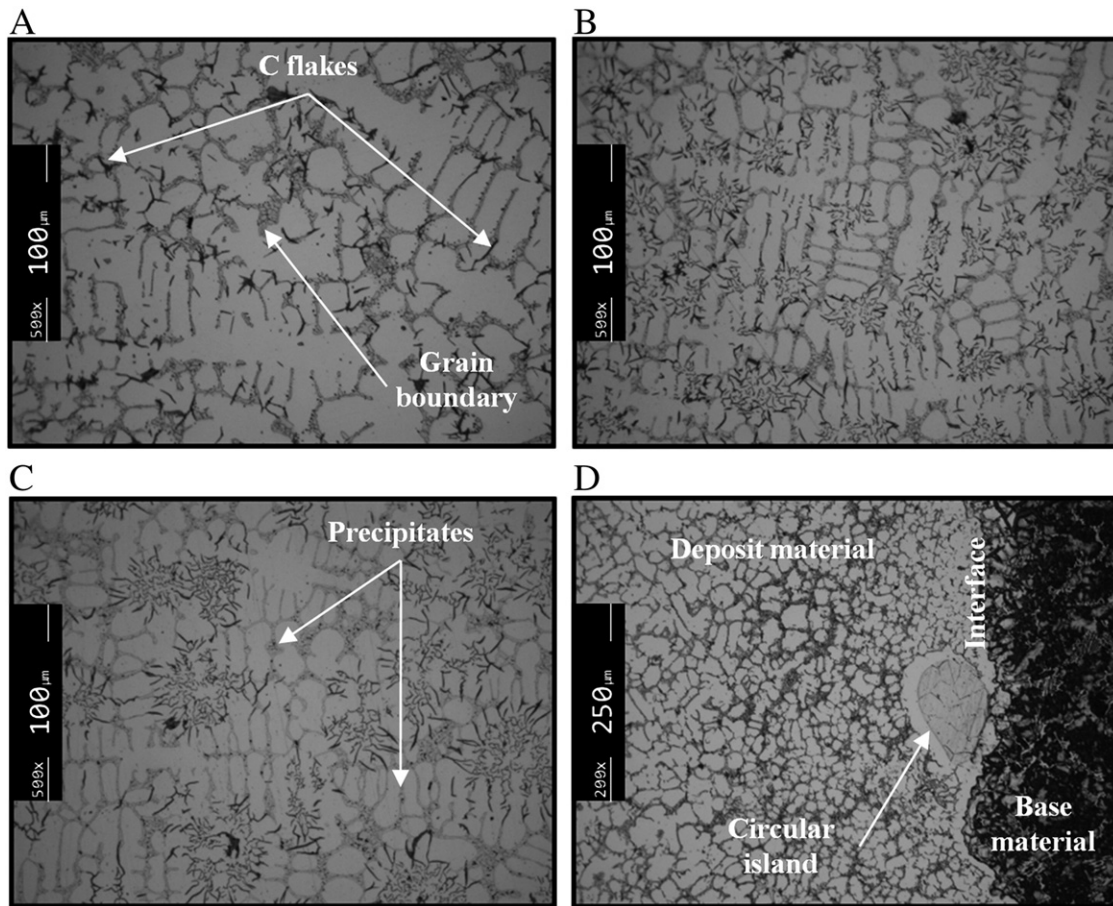


Fig. 4. Optical micrograph of: A) specimen 1, B) specimen 2, C) specimen 4, and D) interface specimen 1.

pores visible under the optical microscope was calculated using the ImageJ program (developed at the National Institutes of Health, United States). The proportion of porosity calculated is very low for all specimens: 0.35% for specimen 1 with an average pore size of  $1.45 \pm 0.58 \mu\text{m}$ , 0.32% for specimen 2 with an average pore size of  $1.61 \pm 0.65 \mu\text{m}$  and 0.28% for specimen 4 with an average pore size of  $1.37 \pm 0.40 \mu\text{m}$ . This decrease in the proportion of micropores in the coatings as current increases can be correlated with the refinement of the dendritic microstructure mentioned below. The decrease in dendrite size reduces the amount of liquid metal trapped by dendrites during solidification, reducing the number of voids in the microstructure. Charmeux et al [14] mentioned this mechanism in the solidification of Al micro castings. On the other hand the cast iron also exhibits significant porosity, with pores reaching  $17 \mu\text{m}$  in diameter, as illustrated in Fig. 3 D).

The typical microstructure of the coatings is shown in Fig. 4. The microstructures consist of dendrites of the Ni–Fe solid solution phase, with columnar morphology oriented along the direction of heat flow and torturous grain boundaries. The microstructure contains C flakes (dark floret-like structures) equally distributed through the microstructure. The chemical composition of the Ni-based powder (low carbon content see Table 1) does not explain the large number of these flakes which can only be attributed to the dilution of cast iron induced by the PTA process. Furthermore, small interdendritic precipitates can also be detected. These are possibly carbides, as explained below. Fig. 4 A–C) shows that an increase in the arc current and, therefore, an increase in dilution, allows carbides and C-flakes in the microstructure to be more easily detected and observed. It was thought that there could be some coarsening of the microstructure as

the current was increased due to greater heat input. However this was not observed. Fig. 4 shows that the dendritic structure becomes finer as the current increases. For example, the average ternary dendrite spacing for the specimens 1 and 4 is  $15.4$  and  $11.2 \mu\text{m}$ , respectively. As explained below, this refinement can be related to the change in the composition of the deposited material due to its increasing dilution as the arc current increases.

The phenomenon of circular “islands”, which frequently occur close to the interface of the coating, is common to all the specimens (see Fig. 4 D) for specimen 1). These islands are characterized by the total absence of graphite. According to the Commercald company [15] they are caused when powder grains not melted by the plasma arc subsequently melt in contact with the pool. Near the interface a cellular microstructure finer than the dendritic structure was observed for all the samples, as illustrated in Fig. 4 D) for specimen 1, where the grain size is approximately  $12 \mu\text{m}$ . This refinement may be due to the higher solidification rates involved in the boundary because of the efficient thermal exchange ensured by the high volume ratio substrate/coating of the base material, as suggested by Gatto et al. [3].

SEM analysis gives a more detailed view of the microstructure of the coatings. Fig. 5 shows a SEM image of the microstructure of the coating of specimen 1. The image shows that in addition to the dendrites of the Ni–Fe solid solution phase and graphite flakes the grain boundary is formed of two phases: a light gray phase (like-grain) and a dark gray one. EDAX spectra showed that the light gray phase and the dark gray phase are rich in silicon and chromium, respectively.

A detailed analysis was carried out to study the main constituents of the coatings using EPMA. WDS (wavelength dispersion spectroscopy)

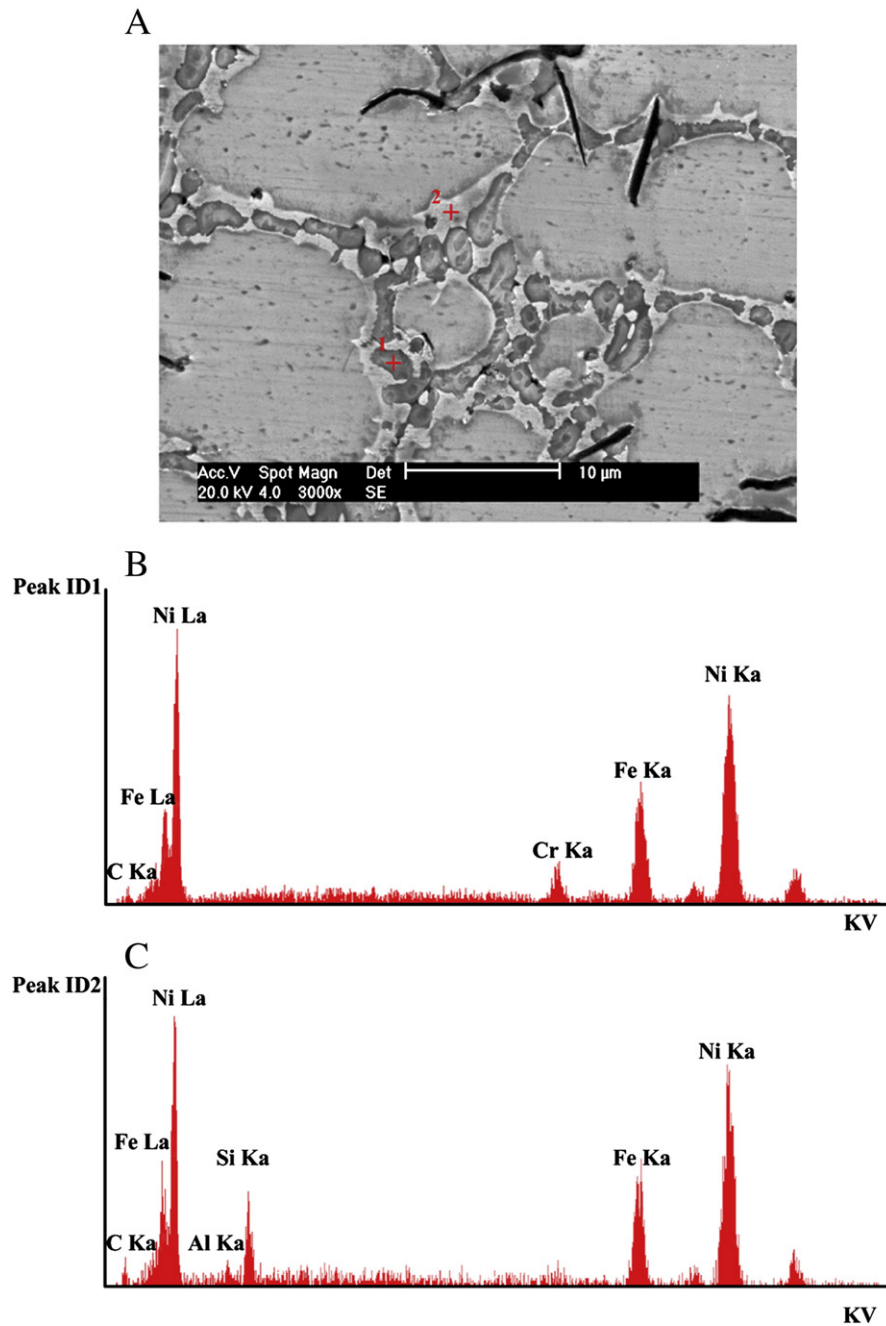
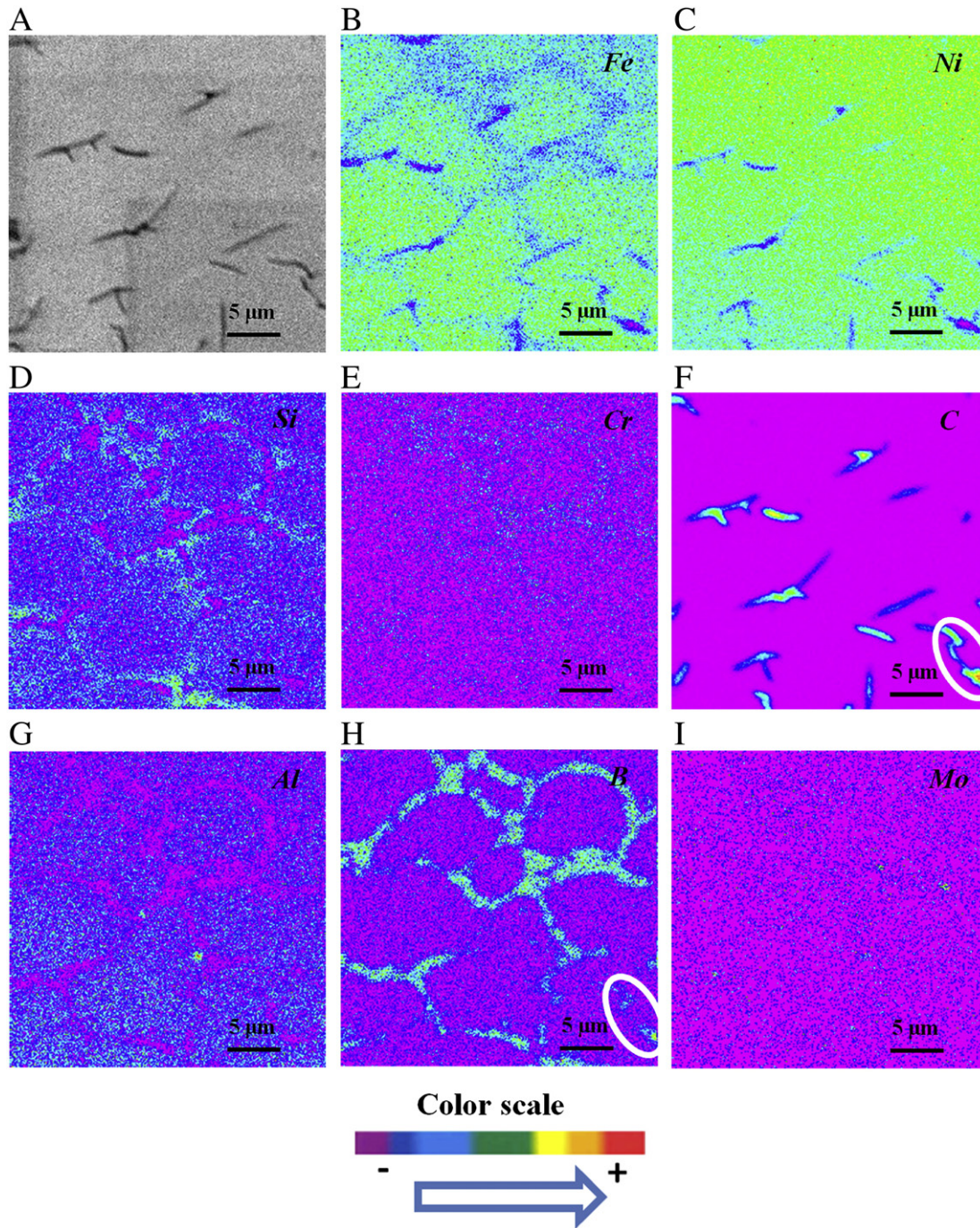


Fig. 5. A) Typical SEM micrograph (etched) revealing the grain boundaries of specimen 1; SEM EDAX spectra of: B) dark gray phase, and C) light gray phase.

maps of the most abundant elements of the coating for all the specimens were obtained. Fig. 6 A) represents a SEM image of the microstructure of the deposit for the specimen 1. The respective elemental maps of Fe, Ni, Si, Cr, Al, B, C and Mo are shown in Fig. 6 B–I), color-coded such that the lowest concentration of the element analyzed is indicated in purple and the highest in red. The results of the WDS maps for specimen 1 reveal that the dendrites are rich in iron, silicon and aluminum, while boundaries are rich in boron, silicon and chromium. Nickel is distributed almost uniformly throughout the structure, except in areas where graphite flakes are present. In the boundary chromium appears, to exclude silicon as these elements do not overlap. However, chromium and boron do overlap in the boundaries, as illustrated in Fig. 6 E) and H). Thus, it can be concluded that the borders of the boundary are rich in Si whereas the middles of the boundaries are mainly composed of B and Cr. Comparing the information from Figs. 5 and 6 it is possible to conclude

that the light gray (like-grain) phase is rich in silicon and the dark gray phase is rich in chromium, which agrees with the EDAX analysis. Carbon concentrates chiefly in the graphite flakes, as shown in Fig. 6 F), though at some particular points the increment in the C signal was also observed in the boundary, mainly coinciding with the B signal (see circled zone in B and C maps) suggesting that carbides may have precipitated. Although not visible in the C-map, very small agglomerates of Mo can be detected in Fig. 6 also suggesting formation of carbides. However, as shown below by XRD analysis, these carbides were not identified, probably due to their small size and/or content.

The increase in the arc current and, consequently, in the dilution of cast iron brought some changes in the distribution of the main elements in the microstructure, as shown by the WDS maps for specimen 4, illustrated in Fig. 7. For this specimen, in comparison to sample 1, the main difference is related to the Ni and Fe signals. It is clear from Fig. 7 that the zones in the



**Fig. 6.** WDS maps of the coating of specimen 1: (A) SEM image of the microstructure of the deposit, (B) iron, (C) nickel, (D) silicon, (E) chromium, (F) carbon, (G) aluminum, (H) boron, and (I) molybdenum.

interdendritic boundaries richer in iron are depleted in nickel and silicon but that in the boundary these zones overlap with Cr and B. The grouping of these maps suggests the presence of a Fe–Cr–B phase in the boundaries, however, as can be seen later from the XRD analysis this is not identified, as only a preferential association with the B–Cr phase is indicated, leading free iron to combine with other elements. The Si rich zones, see Fig. 7 D), are depleted of Fe and rich in Ni. In specimen 4, as well as the strong signal given by the C flakes tiny molybdenum and carbon traces could be detected in the surrounding material (where C is hardly present), which is a clear contrast with the results from specimen 1. These elements are distributed preferentially in the boundaries overlapping the Fe map, suggesting the formation of a mixed carbide containing Fe and Mo. The increase in the content of these elements is caused by the increased

dilution, since they are present only in the cast iron. Collins and Lippold [16] and Ramirez et al. [17] mention that the presence of precipitates in the interdendritic regions results in the formation of very tortuous grain boundaries and the excess of these precipitates stops the migration of the grain boundaries. This can justify the lower grain size of the coating deposited with 140 Å in spite of the higher energy supplied to the coating process. The literature also indicates that an increase in the molybdenum and carbon content improves the rate of heterogeneous transformation during solidification. These elements normally segregate in the grain boundaries, thereby hindering grain growth [18]. Nevertheless, the influence of the much higher number and content of graphite flakes presented in the 140 Å sample, these being segregated from the grain boundaries during material solidification, should therefore also be

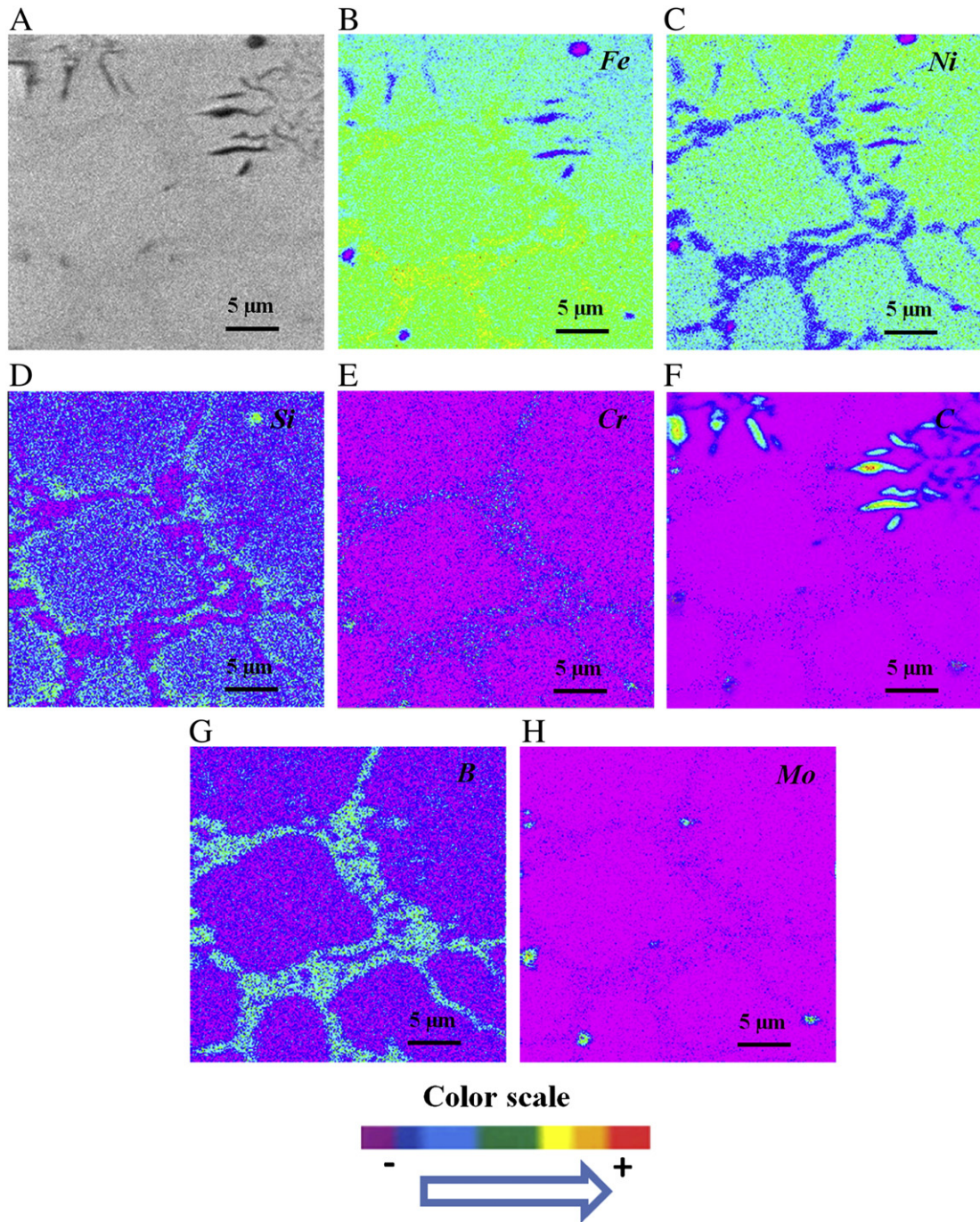


**Fig. 7.** WDS maps of the coating of specimen 4: (A) SEM image of the microstructure of the deposit, (B) iron, (C) nickel, (D) silicon, (E) chromium, (F) carbon, (G) boron, and (H) molybdenum.

considered as an explanation for the lower grain size in this sample. As can be seen in Fig. 4, C flakes are common in the grain boundaries.

The distribution of the chemical elements in the microstructure in specimens 2 and 3 follows the trend mentioned above.

Fig. 8 shows the XRD spectra of specimens 1, 2 and 4. The analysis of this data revealed that the major phase present in the coatings is a (Ni, Fe) solid solution face centered cubic (ICDD card 47–1405-(111), (200), (220), (311), and (222) peaks at  $2\theta \sim 51.1^\circ$ ,  $59.8^\circ$ ,  $89.6^\circ$ ,  $111.42^\circ$  and  $119.3^\circ$ , respectively). WDS maps show that in Cr and B rich zones, Si does not exist as it is connected to Ni. The overlapping of Ni and Si signals in WDS maps suggests the presence of a Ni–Si phase, such as  $\text{Ni}_3\text{Si}$  (ICDD card 32–0699) shown in Fig. 8, corresponding to some of

the lower intensity experimental XRD peaks. The other peaks can be adjusted either to a Cr-boride phase  $\text{Cr}_5\text{B}_3$  (ICDD card 32–0278) or to the Fe, Mo mixed carbide of  $\text{M}_6\text{C}$  ( $\text{Fe}_3\text{Mo}_3\text{C}$  – ICDD 47–1191) type. The increasing content of this latter phase through samples 1 to 4 sits well with the WDS maps presented and interpreted above. Furthermore, the indexation is in agreement with the results from the literature where similar phases were also detected in a nickel alloy deposit on an austenitic stainless steel [8]. In summary, the increase in the arc current increased the dilution of the cast iron, raising the iron, carbon and molybdenum content in the coating, promoting dendrite refinement of the microstructure due to the increase in precipitates (Fe–Mo–C) and C flakes in the grain boundaries.

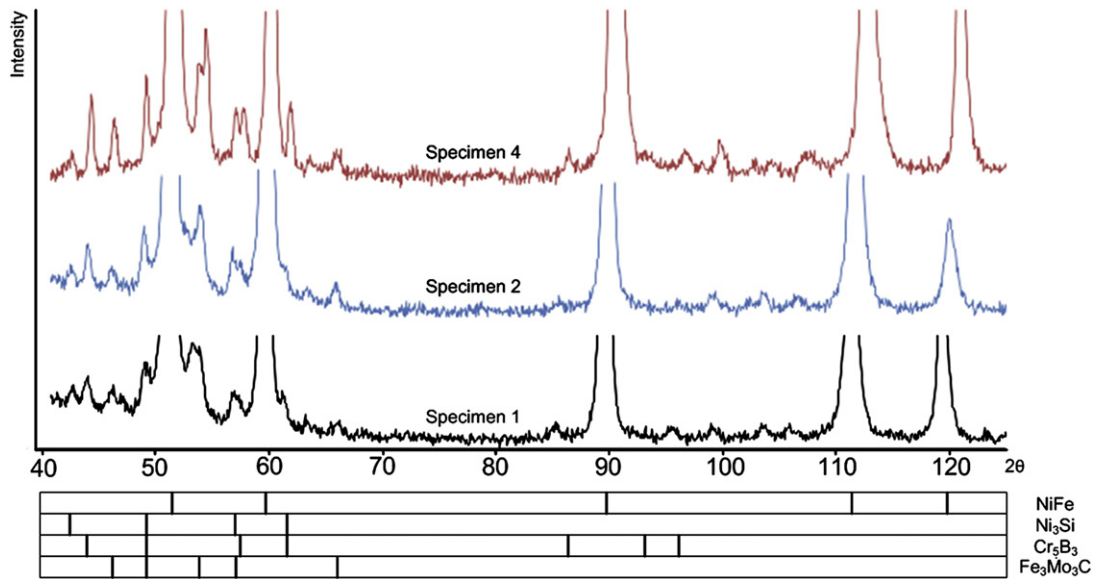


Fig. 8. X-ray diffraction pattern of the deposit material obtained for the specimens 1, 2 and 4.

### 3.1.2. Partially melted zone (PMZ) and heat affected zone (HAZ)

These zones are critical in cast irons since the material can solidify as white iron if cooling is rapid enough. If the amount of graphite dissolved during welding is high enough it is likely that it will also give rise to a continuous carbide network. This is undesirable as a brittle carbide matrix can cause durability problems in the final part. Fig. 9 shows the microstructure of this zone in specimen 3. In this image, cementite ( $\text{Fe}_3\text{C}$  – white phase) can be seen concentrated near the interface. Fig. 9 B) shows the microstructure of the PMZ zone under high magnification. The image displays a large amount of cementite in the grain boundaries with acicular martensite inside the grains. Some precipitates, identified as mixed titanium and molybdenum carbides (marked respectively with the numbers 1 and 2 in Fig. 9 and identified in Fig. 10), were also found. As these phases are hard and brittle this region is sensitive to in-service crack initiation and propagation due to thermal and mechanical fatigue, as discussed below. M. Pouranvari [12] also reported that a continuous brittle network of coarse carbides along the weld fusion line may lead to initiation of cracking.

In the heat affected zone, carbon can diffuse into the austenite during welding and the austenite may subsequently transform into brittle martensite due to the high cooling rate. Martensite is also

susceptible to cracking. The amount of martensite formed depends on the composition of the cast iron and the thermal history of the zone.

### 3.2. Hardness

Fig. 11 shows the hardness profiles across the interface for all the studied specimens. The vertical line in the graph represents the fusion line. The hardness through the melted material is approximately constant and tends to decrease with increasing weld current. This can be related to the higher dilution induced by the process.

For all the samples, the highest hardness values were measured in the area near the fusion line. A maximum hardness of 538 HV was observed in specimen 1 and decreases with increasing arc current for the other specimens. As previously documented, the microstructure in that region consisted of hard martensite and cementite. The proportion of martensite in the microstructure decreases with increasing distance from the fusion line and, thus, the hardness decreases too. The microstructure in the HAZ is directly related to the heat input in the process and therefore to the current intensity used.

The high hardness values found in the PMZ and HAZ make these regions potentially responsible for many of the mechanical problems experienced in welds in cast iron. The most effective way to reduce

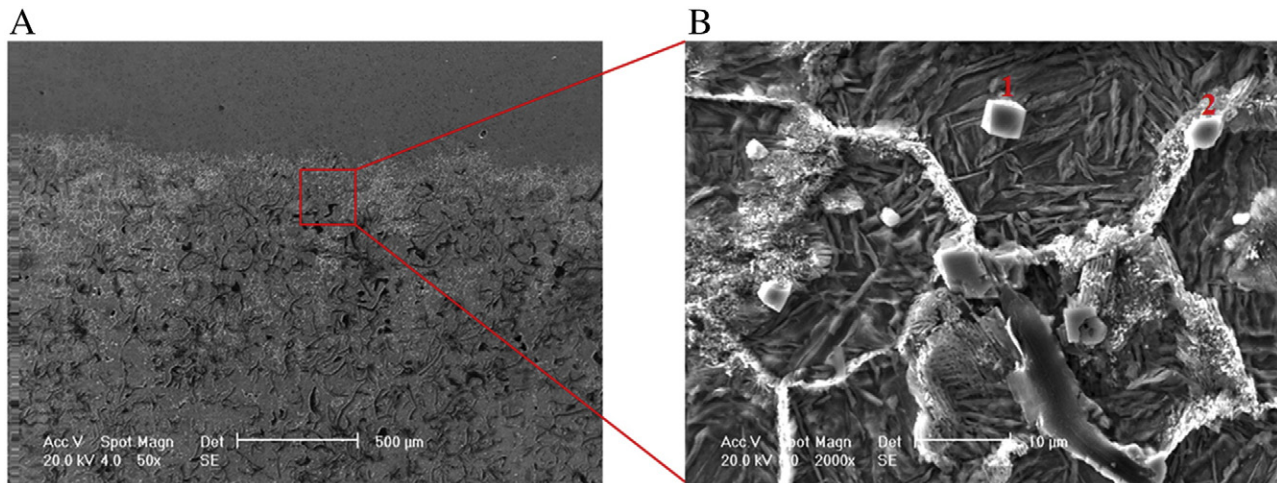


Fig. 9. SEM image of partial melted zone and heat affected zone of specimen 3, (A) transition between coating and the substrate, and (B) magnification of PMZ.

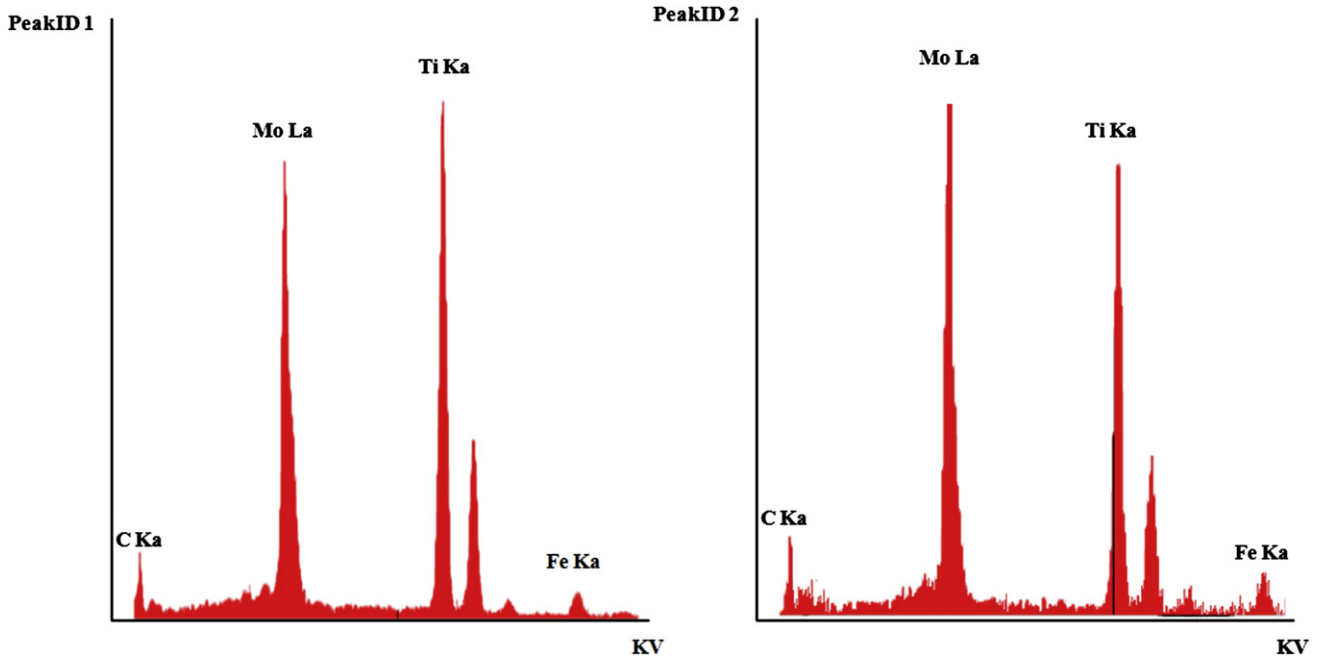


Fig. 10. Energy dispersive X-ray analysis (EDAX) of the particles shown in Fig. 9 b), (1) titanium carbide with square shape, and (2) molybdenum carbide with rounded shape.

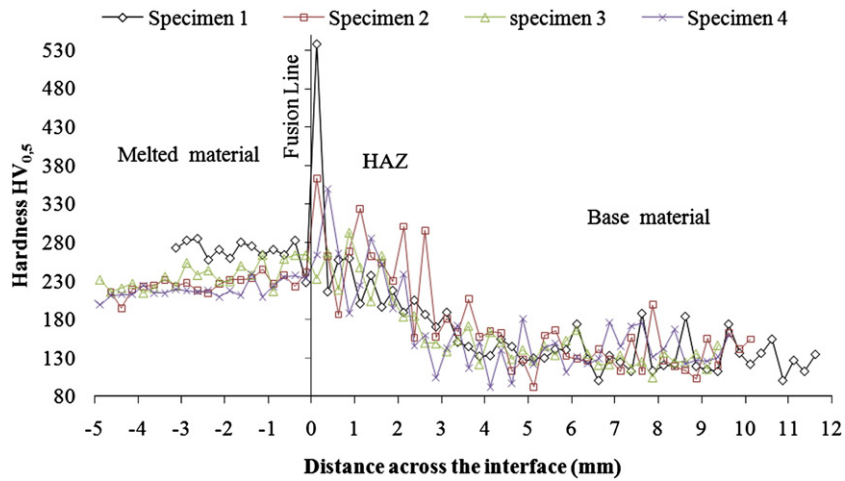


Fig. 11. Hardness profile across the interface.

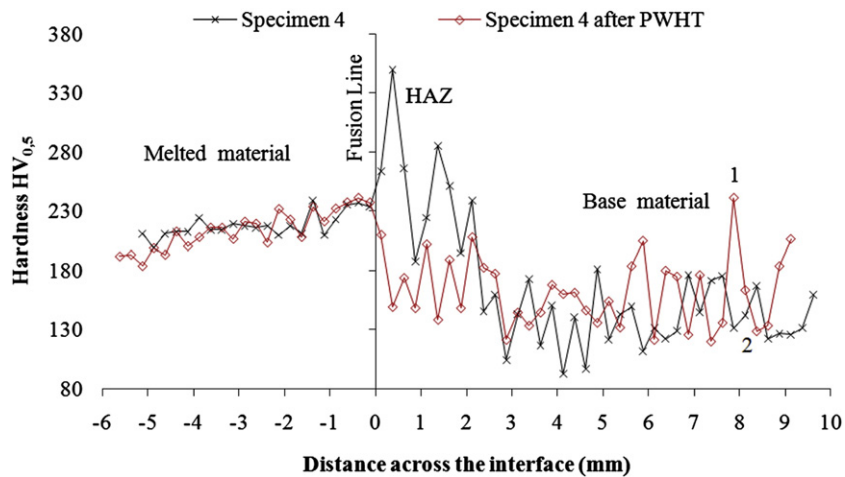


Fig. 12. Hardness profile across the interface after PWHT in specimen 4.



hardness and cracking problems in these regions is to reduce the severity of the thermal cycle produced by the process. This can be done by controlling the heat input and preheating during coating. Another way to reduce the hardness in these zones is to submit the parts to an annealing treatment, although this solution is expensive.

The precipitates, the porosity and the random distribution of graphite flakes in the cast iron matrix can be linked to the variability of hardness in the base material.

### 3.3. Effect of post-weld heat treatment (PWHT) on the microstructure and hardness

Although the heat treatment did not induce significant changes in the microstructure and hardness of the coatings, it induced substantial changes in the PMZ and HAZ, as illustrated by the hardness profiles before and after PWHT shown in Fig. 12 for specimen 4. This specimen was produced with the highest arc current, and had the lowest hardness values in the PMZ, as shown in Fig. 11. Fig. 12 shows that even in this case the heat treatment (holding at 850 °C for 1 h) produced little change in the coating but a substantial decrease in the hardness of the PMZ and HAZ of the specimen. Similar behavior was observed for the other specimens. This reduction in hardness can be attributed to the reduction in the proportion of hard phases, cementite and martensite, in these zones. After PWHT the base material displays basically a perlitic/ferritic structure.

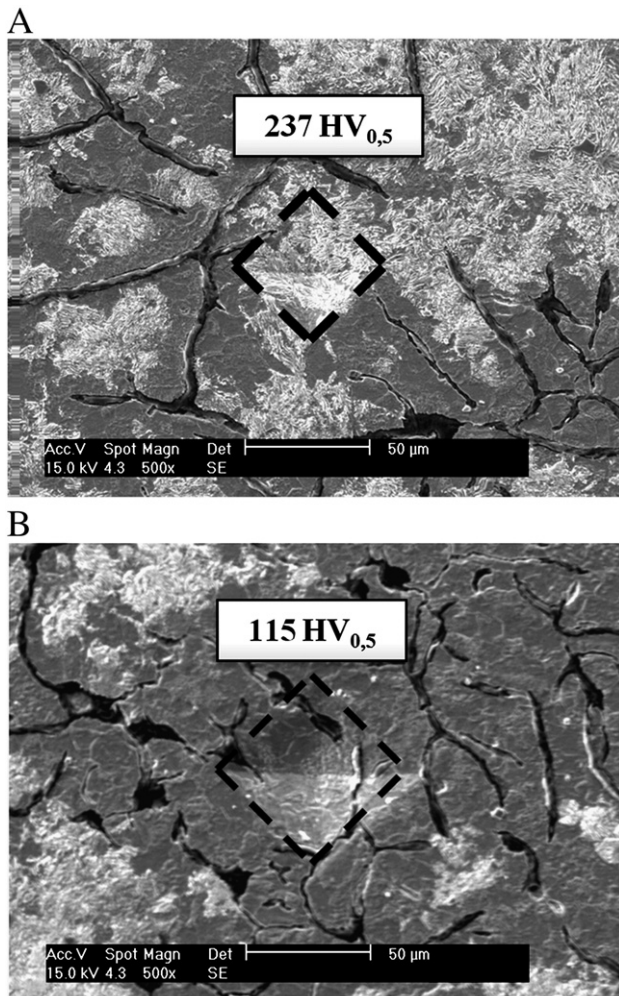


Fig. 13. Indentations in base material (specimen 4) after PWHT. A) indentation made in the perlitic structure, and B) indentation made in the ferritic structure.

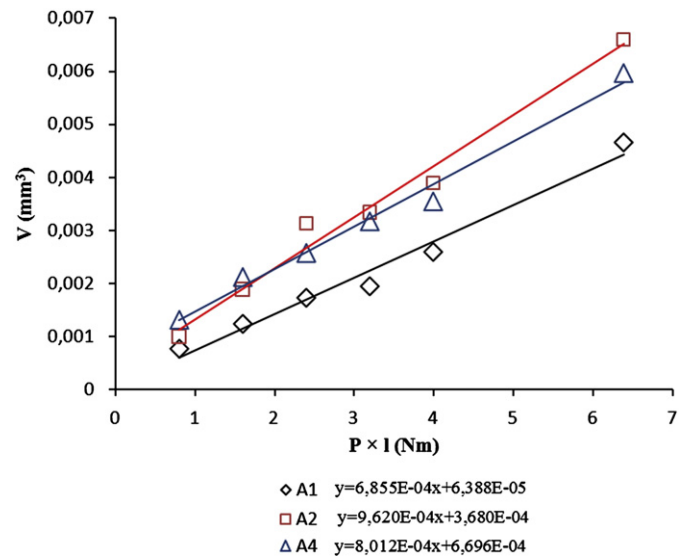


Fig. 14. Evolution of the wear behavior as a function of the parameter “normal load × sliding distance”.

After heat treatment a large scatter of hardness measurements continues to be observed in the cast iron. This scatter can be attributed to local alterations in the microstructure, as shown in Fig. 13, which represents the aspect of the indentations marked with the numbers 1 and 2 in the hardness profile in Fig. 12. The image reveals that if the indentation impacts mainly the perlitic structure, the white zone in Fig. 13 A), the hardness will be greater than if the indentation is performed in the ferritic structure, the gray zone in Fig. 13 B). In conclusion, PWHT is beneficial because it reduces hardness in the PMZ and HAZ, without producing significant alterations in the melted zone.

### 3.4. Wear test

The wear tests were performed to predict the effect of the different process parameters on the in-service wear behavior of the coated components. The ball-cratering test results are shown in Fig. 14, as the volume of material loss plotted against the product of sliding distance (l) and normal load (P). A complete reliability analysis is summarized in Table 4. The wear volume displays linear evolution with  $P \times l$ , and the slope corresponds to the specific wear rate. Specimen 1 exhibits both the lowest wear volumes and the lowest specific wear rate, therefore, it is the most resistant to wear. This is compatible with the greatest hardness displayed by the coating of this specimen, as illustrated in Fig. 11. Samples 2 and 4 display very similar wear volumes, which is confirmed by similar hardness values; even so, sample 2 has a specific wear rate slightly higher than sample 4.

Fig. 15 A) shows a SEM micrograph of a wear scar induced by the ball-cratering device and Fig. 15 B) the surface of a coating of a mold after a long time in service, which allows pitting to be identified as the major failure mechanism. The image also shows some cracks that can be attributed to the localized melting of hard, brittle phases.

Table 4  
Results of the linearization analysis.

	Specific wear rate, $k$ (mm <sup>3</sup> /Nm)			$r^2$
	Average	STD	Confidence interval 90%	
Specimen 1	$6.9 \times 10^{-4}$	$5.2 \times 10^{-5}$	$5.7 \times 10^{-4}$ to $8.0 \times 10^{-4}$	0.977
Specimen 2	$9.6 \times 10^{-4}$	$6.6 \times 10^{-5}$	$8.2 \times 10^{-4}$ to $1.1 \times 10^{-3}$	0.982
Specimen 4	$8.0 \times 10^{-4}$	$4.6 \times 10^{-5}$	$7.0 \times 10^{-4}$ to $9.0 \times 10^{-4}$	0.987

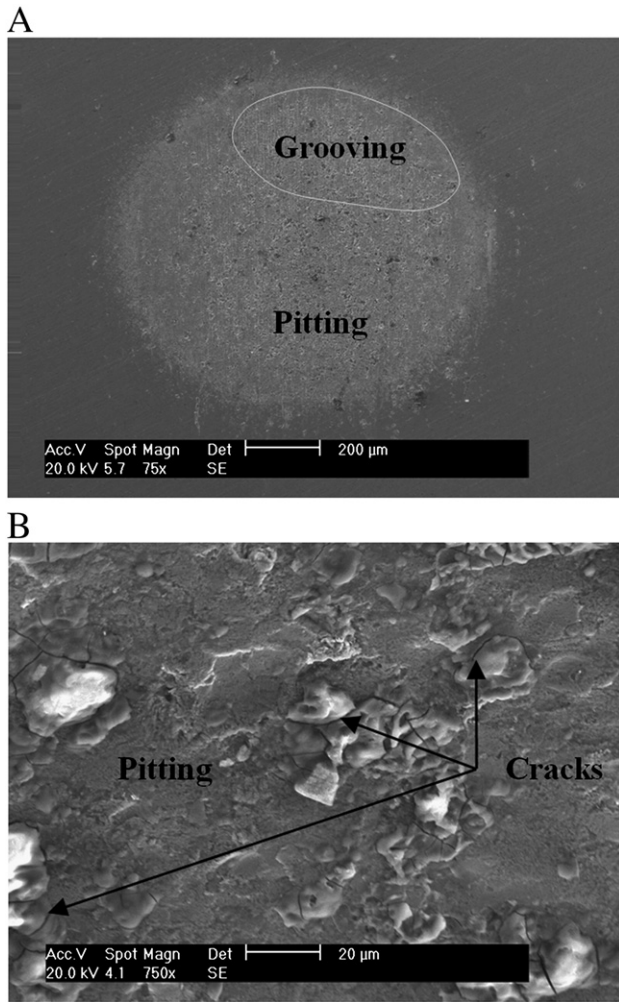


**Fig. 15.** SEM micrograph of: A) wear scars of specimen 1, and B) of the surface of a coating after testing in service.

Ball cratering is a micro-abrasion technique in which test conditions can be tailored to adjust the wear mechanism to grooving, which is plastic deformation controlled, or rolling, which is a fracture controlled process [19]. Prior tests were used to select test parameters compatible with rolling wear, designed to induce pitting failure.

The wear scar displays two modes of wear: pitting and grooving, pitting being the more extensive. Grooving occurs when particles slip onto the surface. Fig. 16 shows the morphology of these two wear modes in higher magnification. The wear mechanism present in the spherical cup depressions (essentially 3-body rolling wear) accurately represents the wear mechanism in the molds. However one should keep in mind that the molds in service are subject to other damage mechanisms such as thermal and mechanical fatigue and corrosion at high temperature.

#### 4. Conclusions

The influence of the arc current used in the plasma transferred arc process (PTA), as well as the effect of post-weld heat treatment, on the microstructure, hardness and wear resistance of deposited layers was analyzed in this study. The increase in the arc current increased the dilution of the cast iron, changing the composition and microstructure of the coatings. Moreover, the increase in current raises the quantity of precipitates and C flakes at the grain boundaries, which leads to the refinement of the microstructure. Increasing the arc current gives rise to a reduction in the hardness in all regions of the coatings. The

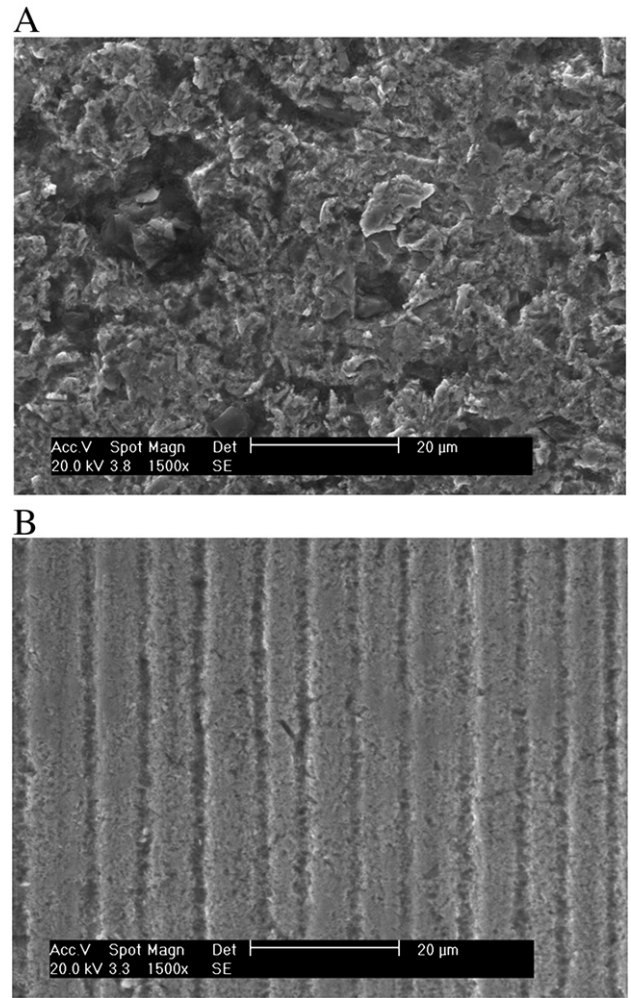


**Fig. 16.** SEM micrograph of: A) 3-body abrasion or rolling wear mechanism, and B) 2-body abrasion or grooving wear mechanism.

reduction in the hardness of the coatings is accompanied by a reduction in their wear resistance in wear tests performed at room temperature with silica slurry. Post-weld heat treatment reduces the hardness in the partially melted zone and heat affected zone as opposed to the coatings themselves, where hardness remains unaffected.

In the future, abrasion and oxidation tests at high temperature will be done, in order to reproduce the conditions of industry application.

#### Acknowledgements

The authors wish to express their sincere thanks to the company Intermolde, to Instituto Pedro Nunes (IPN) and the Portuguese Foundation for the Science and Technology (FCT) through COMPETE program from QREN and to FEDER for financial support.

#### References

- [1] M. Cingi, F. Arisoy, G. Basman, K. Sesen, *Mater. Lett.* 55 (2002) 360.
- [2] E.B. Hinshaw, *ASM HANDBOOK*, 1993, p. 740.
- [3] A. Gatto, E. Bassoli, M. Fornari, *Surf. Coat. Technol.* 187 (2004) 265.
- [4] K. Siva, N. Murugan, R. Logesh, *Int. J. Adv. Manuf. Technol.* 41 (2009) 24.
- [5] V. Balasubramanian, A.K. Lakshminarayanan, R. Varahamoorthy, S. Babu, *J. Iron. Steel Res. Int.* 16 (2009) 44.
- [6] E.H. Takano, D. Queiroz, A.S.C.M. D' Oliveira, *Soldagem Insp. São Paulo* 13 (2008) 210.
- [7] V.V. Díaz, J.C. Dutra, A.S.C. D' Oliveira, *Soldagem Insp. São Paulo* 15 (2010) 41.
- [8] K. Gurumoorthy, M. Kamaraj, K.P. Rao, A.S. Rao, S. Venugopal, *Mater. Sci. Eng., A* 456 (2007) 11.
- [9] E.O. Ezugwu, Z.M. Wang, A.R. Machado, *J. Mater. Process. Technol.* 86 (1998) 1.

- [10] A.J. Ramirez, J.C. Lippold, *Mater. Sci. Eng., A* 380 (2004) 245.
- [11] A. Ramalho, *Wear* 269 (2010) 213.
- [12] M. Pouranvari, *Mater. Des.* 31 (2010) 3253.
- [13] F.A.L. Dullien, *Porous media, Fluid transport and pore structure*, Academic Press, 1992.
- [14] J.-F. Charmeux, R. Minev, S. Dimov, E. Minev, Borovetz, *Proceedings of International Conference, 4M2007*, Whittles Publishing (2007) 217–220.
- [15] Commercald, in: C.P. Technology (Ed.) Commercald PTA Technology, Modena (Italy), <http://www.commercald.com>, (2009).
- [16] M.G. Collins, J.C. Lippold, *Welding J.* 82 (2003) 288S.
- [17] A.J. Ramirez, J.W. Sowards, J.C. Lippold, *J. Mater. Process. Technol.* 179 (2006) 212.
- [18] R.M. Imayev, V.M. Imayev, M. Oehring, F. Appel, *Intermetallics* 15 (2007) 451.
- [19] R.I. Trezona, D.N. Allsopp, I.M. Hutchings, *Wear* 225–229 (1999) 205.



---

## Annex B

---

**F. Fernandes, A. Cavaleiro, A. Loureiro, *Oxidation behavior of Ni-based coatings deposited by PTA on grey cast iron*, Surface and Coatings Technology, 207 (2012) 196-203.**





## Oxidation behavior of Ni-based coatings deposited by PTA on gray cast iron

F. Fernandes<sup>\*</sup>, A. Cavaleiro, A. Loureiro

CEMUC - Department of Mechanical Engineering, University of Coimbra, Rua Luís Reis Santos, 3030-788 Coimbra, Portugal

### ARTICLE INFO

#### Article history:

Received 28 February 2012

Accepted in revised form 20 June 2012

Available online 29 June 2012

#### Keywords:

High temperature oxidation

Oxide scales

Surface morphology

Nickel alloys

Plasma transferred arc

Thermogravimetric measurements

### ABSTRACT

The aim of this investigation was to study the effect of PTA current (100 and 128 A) on the oxidation behavior of nickel-based hardfacing coatings deposited on gray cast iron. The oxidation behavior of coatings held at 800 and 900 °C for 2 h in air was studied by thermogravimetry (TGA). The surface, as well as the cross-section, of the coatings was characterized by scanning electron microscopy combined with energy-dispersive X-ray spectroscopy (SEM/EDS) and X-ray diffraction (XRD). TGA results indicate that the coating produced with lower arc current exhibits more effective oxidation resistance than that produced with higher current. This behavior could be correlated with the dilution promoted by the PTA process, which changes the chemical composition of coatings. As a consequence, different kinds of oxide scales were detected in each coating after isothermal oxidation. In the specimen produced with a lower arc current and lower dilution a protective layer of Si–O is formed, while in the specimen produced with a higher current two layers could be identified: an external one of Fe<sub>2</sub>O<sub>3</sub>, with small features of Fe<sub>3</sub>O<sub>4</sub> and NiFe<sub>2</sub>O<sub>4</sub> spinel rich phases, and an internal one of Fe<sub>3</sub>O<sub>4</sub> with small amount of a dark phase evenly distributed rich in silicon, nickel and iron. The isothermal oxidation curve at 900 °C of the coating with higher dilution showed two stages: at an early stage, the weight increase over time is almost linear whereas, in a second stage, a parabolic law could be fitted to the experimental data. The other specimens followed only a parabolic law.

© 2012 Elsevier B.V. All rights reserved.

### 1. Introduction

Cast irons and copper-alloys are commonly used in the production of glass molds and accessories for the glass industry [1]. In service, molds are subjected to very severe abrasion, wear, oxidation, and fatigue at high temperatures, due to contact with melted glass, which limit their surface life. As a rule, automated manufacturing processes are operated with mold temperatures close to the critical temperature of the mold material. Although the temperature of melted glass is about 1050 °C the surface temperature of molds is currently in the range of 500–900 °C, due to an internal cooling system in the molds. Above a critical temperature the glass body starts to adhere to the mold surface. Higher temperatures lead to mold failure. Therefore, protective coatings are normally applied to give the molds high temperature resistance, with the aim of increasing their lifetime in harsh environments [2,3].

Nickel-based superalloys gain an extremely important role in protection of surfaces in components for the glass industry due to their excellent performance under conditions of abrasion and corrosion at elevated temperatures [4–6]. Several processes have been used to apply coatings to protect the surfaces of these components, as follows: (i) thermal spraying processes such as high velocity oxy fuel (HVOF), atmospheric plasma spraying (APS) and flame spraying (FS); and (ii) hardfacing processes such as plasma transferred arc (PTA) and gas tungsten arc

welding (GTAW) processes. However, since hardfacing processes give rise to a metallurgical bonding with the substrate they have been used preferentially in the protection of mold surfaces as opposed to thermal spraying processes which produce only mechanical bonding of the layer to the substrate. Among the hardfacing processes above, PTA has been widely used to protect the surface of molds, especially their edges, because they are submitted to heavy wear duty cycles. This process gives rise to thicker deposits of very high quality, providing a high deposition rate in a single layer [7–9]. However, the chemical composition and properties of the coatings, as well their quality, are strongly influenced by the dilution of the substrate promoted by the PTA process. Low dilution provides coatings with a chemical composition similar to the added metal powder, which is a prerequisite to getting improved wear and oxidation resistance [10]. However, as dilution is decreased by reducing process current the occurrence of defects such as lack of fusion increases, which is catastrophic in terms of the behavior of molds in service. So during coating deposition, the tendency is to increase the dilution of the base material even if oxidation resistance can be undermined. As oxidation is one of the major failure factors at high temperature in molds for the glass industry, it is imperative to understand how the different coatings provided by different process conditions behave under the harsh and oxidizing atmospheres.

Technical literature reports a lot of studies on the high temperature oxidation behavior of nickel alloys. Liu et al. [11], who studied the oxidation behavior in air of a single-crystal Ni-base superalloy at 900 and 1000 °C, reported two oxidation steps for both temperatures. The first

<sup>\*</sup> Corresponding author. Tel.: +351 239 790 700; fax: +351 239 790 701.  
E-mail address: [filipe.fernandes@dem.uc.pt](mailto:filipe.fernandes@dem.uc.pt) (F. Fernandes).

**Table 1**  
Nominal chemical composition (wt.%) of substrate and nickel alloy.

Base material	C	Mn	Si	P	S	Cr	Ni	Mo	V	Ti	Fe
Gray cast iron	3.60	0.60	2.00	<0.20	<0.04	<0.20	<0.50	0.50	0.10	0.20	Balance
Hardfacing	C	Cr	Si	B	Fe	Al	F	Co	Ni		
Ni-alloy		0.14	2.45	2.56	0.86	1.08	1.30	0.01	0.08		Balance

one is controlled by NiO growth and the second by Al<sub>2</sub>O<sub>3</sub> growth until a continuous Al<sub>2</sub>O<sub>3</sub> layer formed under the previously grown NiO layer. Li et al. [12] studied the oxidation of a NiCrAlYSi overlayer with or without a diffusion barrier deposited by one-step arc ion plating. They showed that the duplex coating system exhibits a more effective protection for the substrate, where thin and continuous scales are adhered to the overlayer surface, and very limited oxidation and interdiffusion attacks are detected. Zhou et al. [13] studied the oxidation behavior of pure and doped nickel alloys with different Co contents in air at 960 °C. They observed that increasing the Co content increases the mass oxidation gain of the coatings.

Since oxidation is one of the main drawbacks that limit the life of glass molds, the aim of this research is to study the effect of PTA current variation on the oxidation behavior of coatings deposited on gray cast iron using a nickel-based alloy. The oxidation behavior of the coatings was studied by thermal gravimetric analysis (TGA). The surface and cross-section morphologies of coatings after isothermal oxidation were observed and characterized by scanning electron microscopy provided with energy dispersion spectrometry (SEM-EDS) and x-ray diffraction. Further, the high temperature oxidation mechanisms are discussed.

## 2. Experimental procedures

Nickel based Colmonoy 215 (from Colmonoy Company) powder was deposited by plasma transferred arc (PTA) onto specimen blocks of gray cast iron, currently used in the production of molds for the glass industry. The deposits were executed using a Commercald Group ROBO 90 machine using two different arc currents (100 and 128 amperes). The goal of using two different arc currents was to achieve coatings with dissimilar levels of dilution with the substrate. The nominal compositions of the cast iron and Colmonoy 215 powder are displayed in Table 1. The principal surfacing parameters employed are shown in Table 2. Before coating, the blocks of cast iron were induction heated at 480 °C, in order to reduce susceptibility to cracking during coating deposition.

After coating, specimens containing cast iron and coating were removed from each block for microstructural analysis. Metallographic analysis was done using conventional procedures. Small samples for oxidation tests were also removed from each coating. The surfaces of these samples were ground using number 1000 SiC abrasive paper in order to produce even surface preparations. Further, the specimens were ultrasonically cleaned in alcohol.

Isothermal oxidation tests were conducted at 800 and 900 °C in air for 2 h in a thermal gravimetric analysis (TGA) machine. The air flux used was 50 ml/min and the heating rate up to the isothermal temperature was 20 °C/min. After thermal exposure the samples were cooled naturally in air to room temperature. The weight gain of samples was evaluated at regular 2 s intervals using a microbalance with an accuracy of 0.01 mg. After oxidation the surface morphology of specimens was

examined by scanning electron microscopy with x-ray spectroscopy (SEM-EDS). Further, the same equipment was used to identify the layers forming the oxide scale from the cross-section of samples. In this case the specimens were mounted in epoxy resin, polished and then surfaced with a thin layer of gold for perfect observation. X-ray diffraction (XRD) using Co K $\alpha$  radiation was conducted on the oxidized surface of specimens. In order to ensure the reproducibility of results, three specimens were analyzed for each coating and set of test conditions.

## 3. Results

### 3.1. Microstructure of the as-deposited coatings

Fig. 1 displays the microstructure of the coatings deposited on the surface of gray cast iron coupons. The coatings show dense microstructure without lack of fusion of the substrate, free of microcracks and few solidification voids. Their typical microstructure consists of dendrites of the Ni-Fe solid solution phase aligned along the direction of heat flow. Furthermore, it displays C-flakes (dark-floret like structures) randomly distributed in the matrix. The increase in arc current gives rise to a higher dilution of the gray cast iron, changing the original chemical composition of the filler metal. Following the procedure detailed in reference [9], dilutions of 28% and 54% were measured for the coatings deposited using 100 and 128 A arc current, respectively. These levels of dilution can explain the increase in C-flakes with increasing arc current, as shown in Fig. 1. Table 3 shows the chemical composition measured by energy dispersive spectrometry (SEM-EDS) from an area of 400  $\times$  400  $\mu$ m, from the cross-section at the middle thickness of each coating. With this procedure it is assured that chemical composition values are measured from a representative volume of material in that zone, avoiding erroneous measurements that could arise from point analyses of the heterogeneous microstructure. As can be seen, the main differences in chemical composition are related to the higher iron, carbon and silicon contents achieved with increasing dilution. The detailed characterization of the microstructure of each coating can be found in a previous publication by the authors [9].

### 3.2. Isothermal oxidation in air

The results of the thermo gravimetric analysis performed on the coatings at different isothermal temperatures (800 and 900 °C) are shown in Fig. 2a and b for the coatings deposited using 100 and 128 A arc currents, respectively. From now on and throughout the text, the coatings deposited using 100 and 128 amperes will be identified as “C100” and “C128”, respectively. The C100 coating exhibits parabolic oxidation weight gain as a function of time for both testing temperatures as does the C128 coating at 800 °C. On the other hand, oxidation of the C128 coating at 900 °C starts with a linear increase in mass gain but after 1400 s it starts to

**Table 2**  
Main deposition parameters for PTA weld surfacing.

	Main arc current (A)	Powder feed rate (rpm)	Travel speed (mm/s)	Powder feed gas flow rate (l/min)	Plasma gas flow rate (l/min)	Shielding gas flow rate (l/min)	Torch work distance (mm)	Oscillation (mm)	Preheat temperature, (°C)
Coating 1	100	20	2	2	2.2	20	13	4	480
Coating 2	128	20	2	2	2.2	20	13	4	480



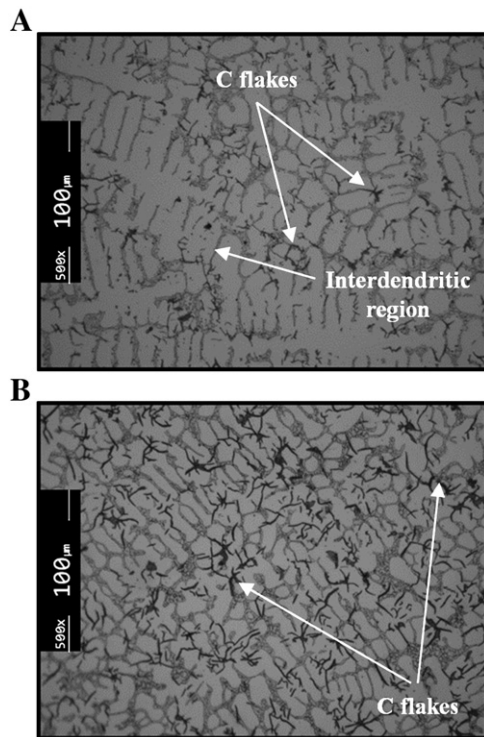


**Fig. 1.** Typical microstructure of: A) coating deposited using 100 A of arc current, B) coating deposited using 128 A of arc current.

follow a parabolic path. The figures also reveals that for both oxidation temperatures, coating C100 displays less oxidation weight gain than coating C128. The dissimilar levels of oxidation observed in the specimens can be correlated with the dilution promoted by the PTA process, that changed their chemical composition, as shown in Table 3, which will interfere with the oxidation process. As mentioned before, the main differences in chemical composition of coatings are related to silicon, carbon and, particularly, iron content. Wallwork [14] and Ezugwu [15] reported that if iron content is increased in nickel-based alloys, it tends to decrease their oxidation resistance, as is the case in our study. This behavior was attributed to a progressively higher cation diffusion rate in the scale. Therefore, increasing the dilution of gray cast iron by increasing the arc current proves to be detrimental, since the oxidation resistance of coatings is reduced due to a further increase of iron content in the coatings. Moreover, it is observed that the oxidation gain of specimens increases with increasing isothermal temperature. This is an expected effect since all diffusion phenomena ruling the oxidation process are enhanced as the temperature is increased. In conclusion, the thermo gravimetric results show that increasing dilution decreases the oxidation resistance of the coatings.

### 3.3. X-ray diffraction

Figs. 3 and 4 show the XRD spectra found at the oxidized surface of the coatings. The oxide products revealed differences between the two coatings; however, in each coating the phases produced after oxidation at 800 and 900 °C are similar, although different oxidation weight gains were measured. According to XRD patterns, the main oxide phase sets

**Table 3**  
Nominal chemical composition (wt.%) analyzed at middle thickness of coatings deposited using 100 and 128 A arc current.

Elements	Ni	Fe	C	Si	Al	Cr
Coating deposited using 100 A	85.40	8.47	0.30	2.17	0.81	2.86
Coating deposited using 128 A	51.09	43.29	1.01	2.54	0.50	1.87

detected at 800 °C and 900 °C were: (i)  $B_2O_3$ ,  $SiO_2$  and  $OAIB$  for coatings produced with lower dilution and (ii)  $Fe_2O_3$  (hematite),  $Fe_3O_4$  (magnetite) and spinels of  $NiFe_2O_4$  for higher dilution coatings. The indexation of oxide phases of coating C128 is in agreement with the results from the literature, where similar oxide phases were detected after thermal exposure [16,17]. Both coatings also display a high intensity peak close to 60°, which corresponds to the face centered cubic (Ni-Fe) solid solution (ICDD card 47-1405). Furthermore, coating C100 displays low intensity XRD peaks which correspond to a Ni-Si phase, such as  $Ni_3Si$  (ICDD card 32-0699), and a Cr-boride phase  $Cr_5B_3$  (ICDD card 32-0278). All these phases are currently identified in this type of microstructure [9]. The large amount of iron oxide detected at the oxidized surface of coating C128 can be attributed to the higher content of iron in this sample. As referred to before, the higher iron content in this coating is attributed to higher dilution of the base material induced by the use of a higher arc current. Comparing the peaks intensity of coating C128, oxidized at 800 °C and 900 °C, the amount of oxide products  $Fe_3O_4$ ,  $Fe_2O_3$  and  $NiFe_2O_4$  increased with temperature. The  $NiFe_2O_4$  spinel phase (ICDD card 10-0325), identified at the oxidized surface, results from the reaction of NiO (which was also identified as an oxide phase on the surface of coating C128) with the  $Fe_2O_3$  phase, as reported by Musić et al. [18]. Furthermore, B-O phases (ICDD card 06-0297 ( $B_2O_3$ ) and ICDD card 50-1505 ( $B_6O$ )) could be identified from the XRD pattern of coating C128.

### 3.4. Surface morphology

The different chemical compositions of coatings brought about by dilution led to the formation of different kinds of oxide scales during isothermal oxidation, as shown above. The SEM surface morphologies of the oxidized coatings at 900 °C are shown in Figs. 5 and 6 for coatings C100 and C128, respectively. EDS examinations were conducted of the oxidized surface of coatings to characterize their composition. Coating C100, oxidized at 900 °C, displays two phases: a gray dark phase, identified in Fig. 5a by letter A, and an evenly distributed white phase, identified by letter B. A magnification of each zone is shown in Fig. 5b

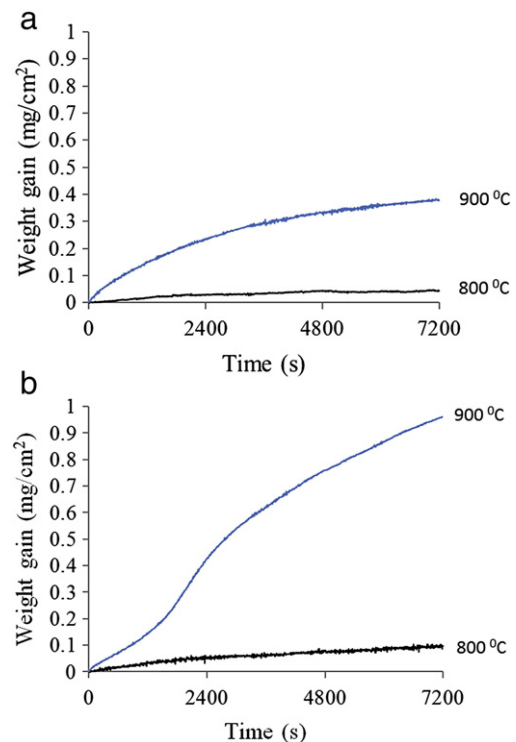


**Fig. 2.** Isothermal oxidation curves at 800 and 900 °C of: a) coating deposited using 100 A arc current, b) coating deposited using 128 A arc current.



the original source of elements which diffused outwards to form oxide scales.

The oxide scale of coating C128 is different from that of coating C100, being composed of two layers. Combining the XRD analysis, with the SEM-EDS results, the external layer can be identified as  $\text{Fe}_2\text{O}_3$ , the main phase containing small features of  $\text{Fe}_3\text{O}_4$  and spinel  $\text{NiFe}_2\text{O}_4$ . On the other hand, the internal layer is composed of a continuous Fe–O rich phase (phase identified with point 2) with small evenly distributed amounts of a dark oxide rich in silicon, nickel and iron, as point 3 of EDS analysis shows. The lower iron content in the internal layer in relation to the external one suggests that the internal Fe–O rich phase respects the  $\text{Fe}_3\text{O}_4$  oxide. This result is coherent with the oxidation of Fe-based materials and so hematite ( $\text{Fe}_2\text{O}_3$ ) and spinel of  $\text{NiFe}_2\text{O}_4$  can be expected to form in the region of higher oxygen potential while magnetite ( $\text{Fe}_3\text{O}_4$ ) will form in the lower oxygen potential region [24]. Similar iron oxide layers were observed by Guo et al., after oxidation of Fe–36% Ni bicrystals in air at high temperature [16]. Between these outer and inner layers, a continuous thin layer of a dark phase appears at the interface, as revealed by SEM. A boron rich phase could be detected at the top of the outer layer (see point 4), which is in good agreement with the boron oxide detected by XRD. Finally, clusters of carbon are distributed evenly in the oxide layers. The accumulation of C at the interface

between the coating and the oxide scale (point 5) is a consequence of the oxide layer serving as a diffusion barrier for C coming from the decarburization of the sample mentioned above. Analogous oxide products were observed in the cross-sections of the oxide scale of coating C128 oxidized at 800 °C.

A good correlation was found between the scale microstructure and the isothermal oxidation curve of coating C100 oxidized at 900 °C. The oxidation kinetics of metals and alloys is often controlled by a parabolic rate law at high temperature [25] due to the presence of protective scales. This may well be the case in this specimen, as the evolution of the oxidation weight gain is controlled by the silicon oxide, the main phase present in the oxide scale, as suggested by Fig. 9. At lower temperatures, a boron oxide starts forming on the surface of the specimen due to the high affinity of boron to oxygen. However, for higher temperatures, due to the intense segregation of silicon through the interface and its great affinity for oxygen, a silicon oxide layer starts to be formed beneath the boron oxide. At the same time small amounts of Ni–Si and O–Al–B phases are formed due to the diffusion of other elements through the interface. At a temperature of approximately 577 °C, boron oxide melts, covering the oxidized surface of the coating and inhibiting the transport of species through the melted oxide layer. Above this temperature it is expected that melted  $\text{B}_2\text{O}_3$  starts to evaporate: however, this vaporization does not

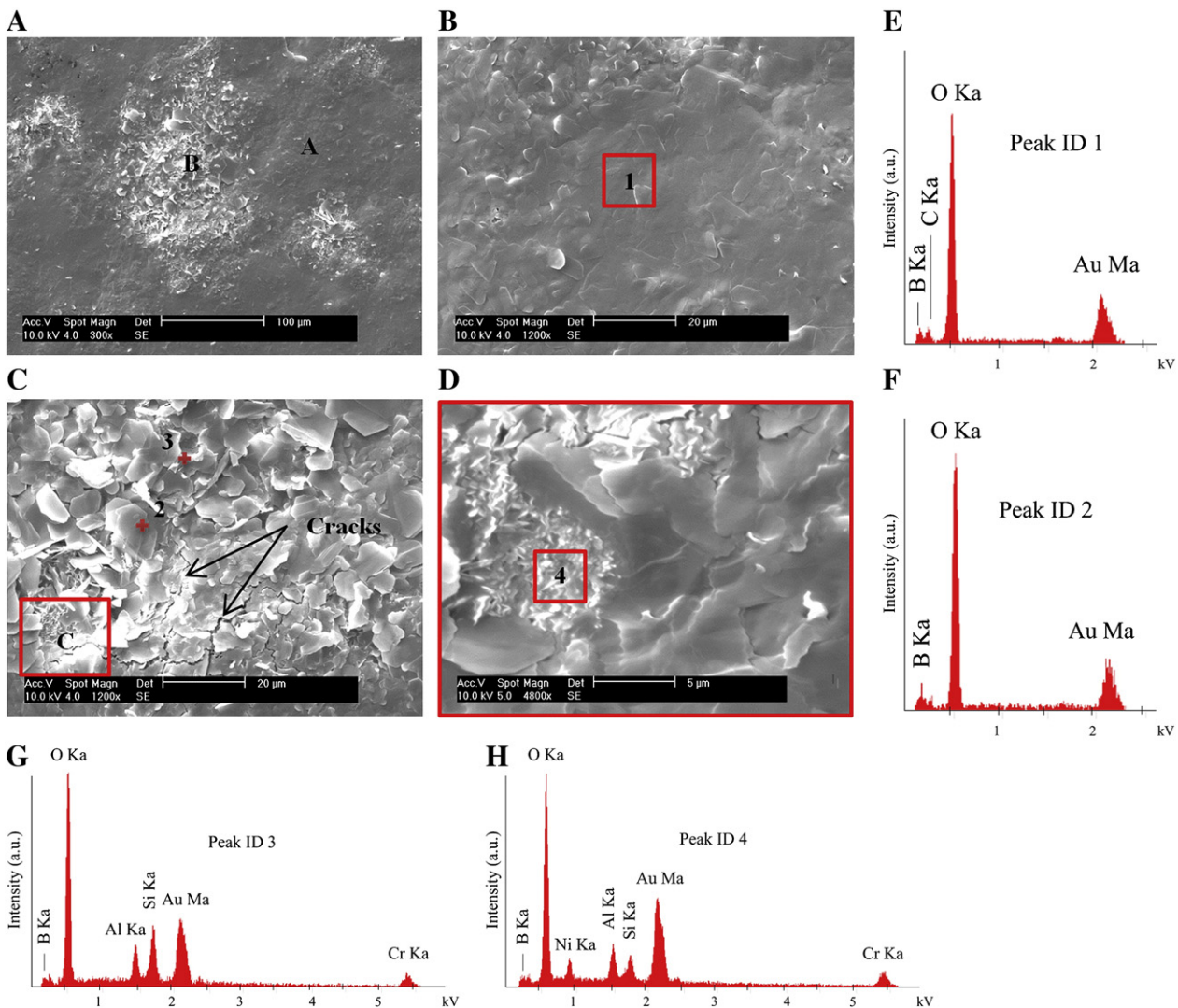
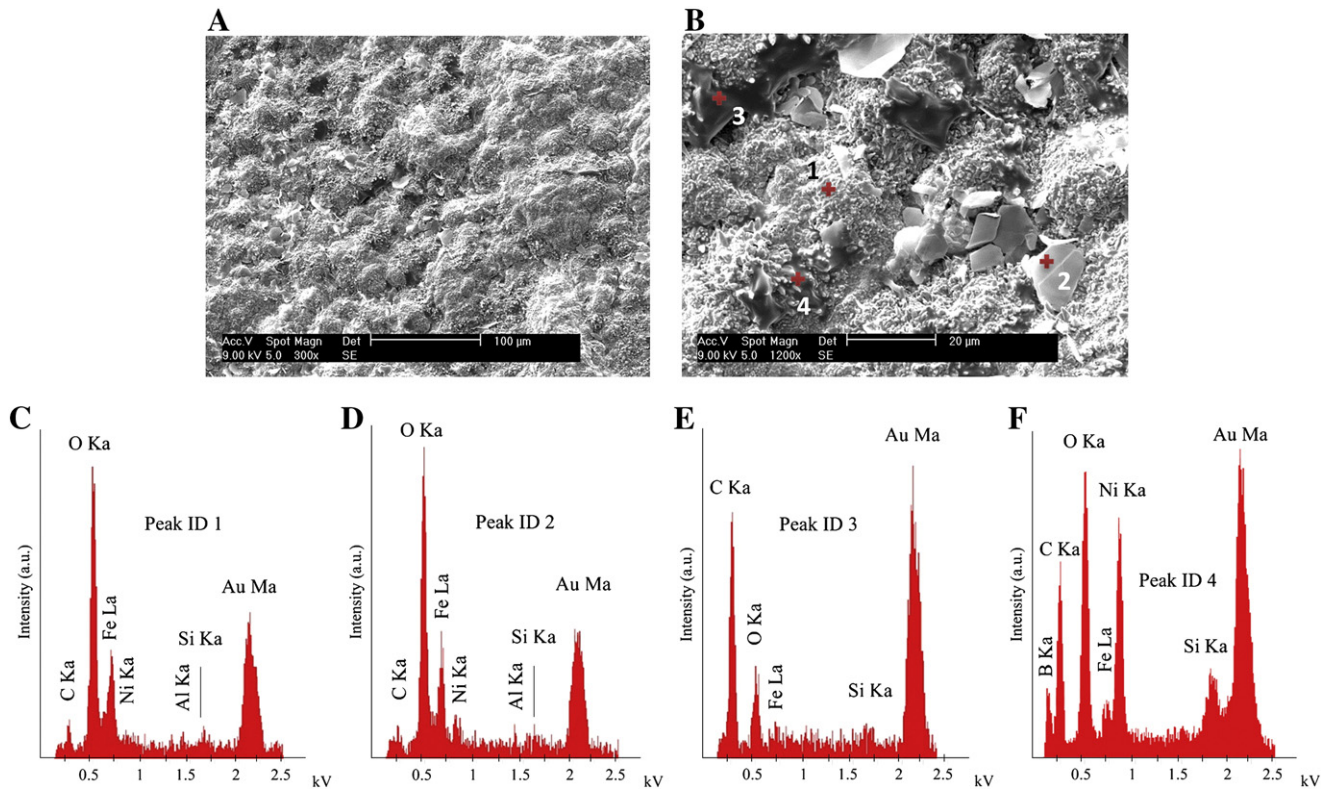
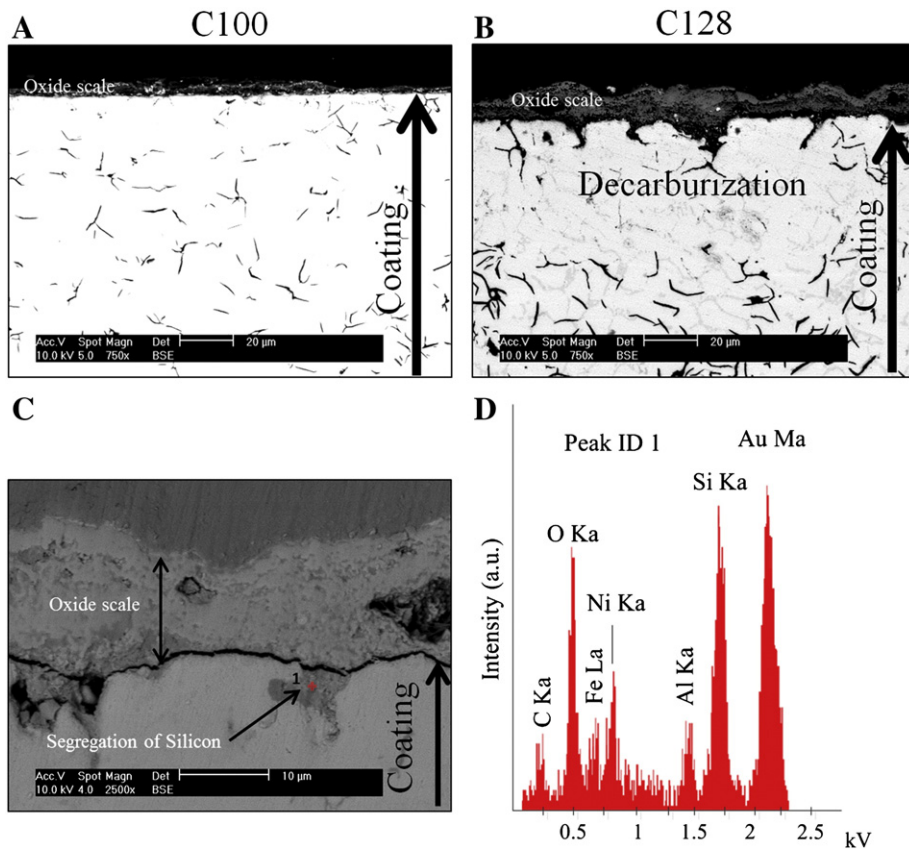


Fig. 5. A) SEM observation of surface morphology of the coating deposited using 100 A arc current, after 2 h oxidation at 900 °C, B) and C) magnification of the zones A and B identified in A), D) magnification of the zone C identified in C). SEM/EDS spectra of: E) zone 1, F) point 2, G) point 3, H) zone 4.



**Fig. 6.** A) SEM observation of surface morphology of the coating deposited using 128 A arc current, after 2 h oxidation at 900°C, B) magnification of the microstructure in A). SEM EDS spectra of: D) point 1, D) point 2, E) point 3, F) point 4.



**Fig. 7.** Back-scattered SEM image of the cross-section of the oxide scale obtained at 900°C of: A) coating deposited using 100 A arc current, B) coating deposited using 128 A arc current. C) Segregation of silicon in the coating deposited using higher arc current, oxidized at 900°C. D) SEM EDS spectra of point 1.

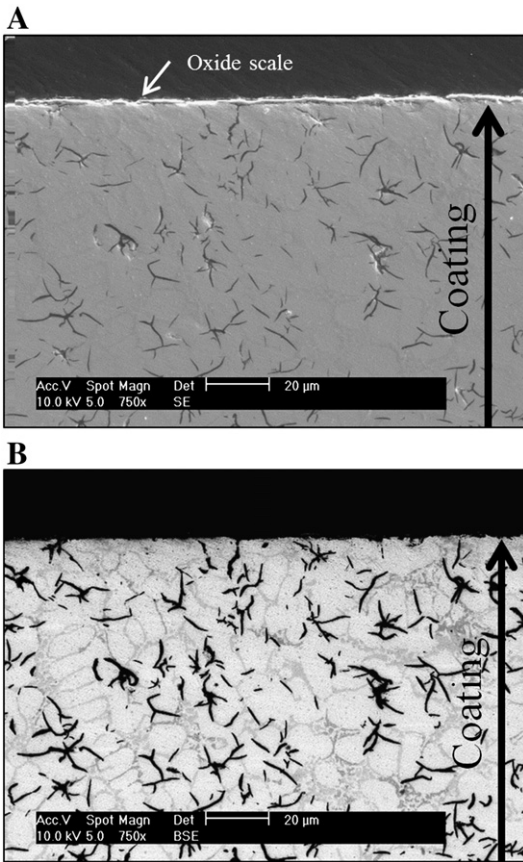


**Fig. 8.** SEM images of the cross-section of the oxide scale obtained at 800 °C of the coating deposited using 128 A arc current: A) SEM secondary electron (SE) image, B) back-scattered SEM image.

**Table 4**

Ratio between the peak intensity of each element with the peak intensity of oxygen (O Ka).

	Point	B Ka	C Ka	Fe La	Ni La	Al Ka	Si Ka
Coating C100	1	0.12	0.14	–	0.16	0.34	0.60
	2	0.10	0.15	0.23	0.58	0.34	0.63
	3	1.61	–	–	–	0.25	0.89
	4	0.44	0.83	2.57	6.06	–	0.94
Coating C128	1	–	0.06	0.33	–	–	–
	2	–	0.04	0.25	0.16	0.05	0.05
	3	–	0.11	0.23	0.13	0.10	0.31
	4	1.00	1.33	0.31	–	–	0.37
	5	–	1.84	0.16	0.23	0.08	0.20

significantly influence the slope of the kinetics curve at 800 and 900 °C, since it only has an important impact at temperatures above 1000 °C [19,20]. Finally, due to the continuous segregation of silicon, its oxide layer will progressively thicken. A protective layer was therefore established and the reaction rate becomes governed by the rate of species diffusion through this thicker silicon oxide layer, as observed in the cross-section of the oxide scale of the specimen. As with coating C100, a strong correlation can be found between the microstructure of the oxide scale and the isothermal oxidation curve of coating C128. At 800 °C, parabolic behavior is displayed; however, at 900 °C, two steps can be detected, see Fig. 2b. The isothermal oxidation curve at first exhibits a linear increase in mass gain and then starts to conform to a parabolic law. The microstructural analysis of the cross-section of the oxide scale revealed that at 800 °C there is no decarburization of the coating, which is not what was observed at 900 °C. Like the specimen coated using the lower arc current, at low temperatures boron oxide starts forming on the surface of specimen due to the high affinity of boron to oxygen. Moreover, for high temperatures, due to the high iron content, a consistent layer of  $\text{Fe}_2\text{O}_3$  with small features of  $\text{Fe}_3\text{O}_4$  and  $\text{NiFe}_2\text{O}_4$  is formed, which is thickened by outward Fe diffusion. At the same time the specimen loses carbon by decarburization, due to the formation of  $\text{CO}_2$ . However, carbon

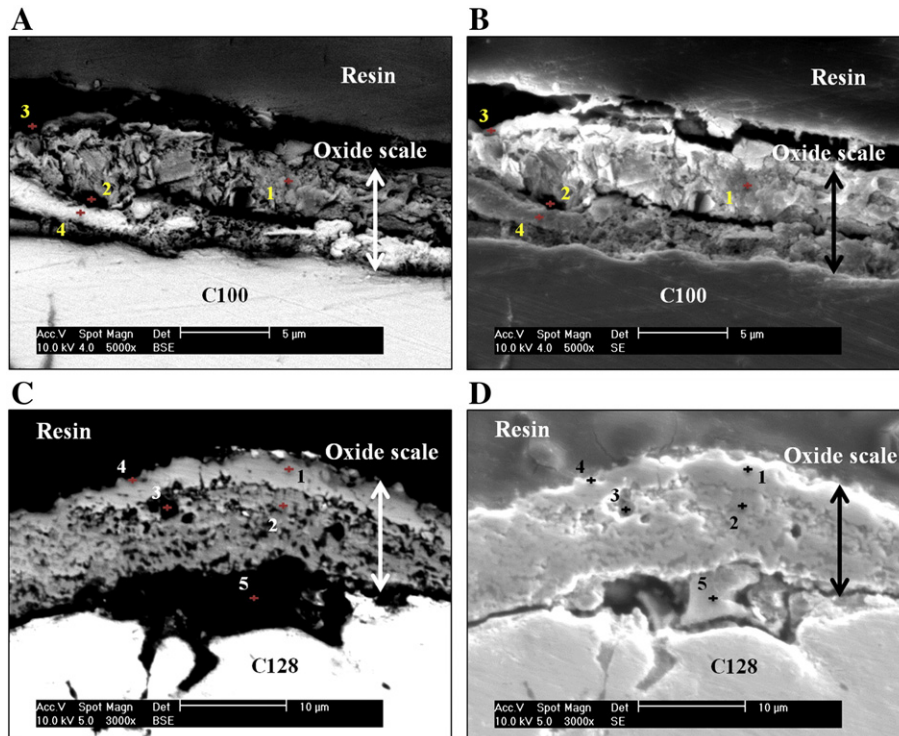


**Fig. 9.** SEM images of the cross-section of the oxide scale of the coatings deposited using 100 and 128 A arc current oxidized at 900 °C: A) and C) in back-scattered SEM images, B) and D) in SEM secondary electron (SE) images.

has increasing difficulties diffusing outwards through the oxide layer and stays either inside or beneath the oxide scale, as shown by morphological analysis of the cross-section. Therefore, after the first step where the weight gain is partially compensated by C liberation, the oxidation curve will deviate to a normal parabolic trend. According to the Richardson-Ellingham diagram, Si has higher affinity for O than Ni and Fe, and Fe forms  $\text{Fe}_3\text{O}_4$  more easily than Ni forms NiO. Therefore, during oxidation it would be expected that Si-O would be the first layer to be formed. However, its much lower content in the specimen relative to iron, indicates that considerable time is required to form a continuous and protective  $\text{SiO}_2$  layer, as suggested by Douglass and Armijo [26]. So, after a critical time a layer of  $\text{SiO}_2$  starts being formed below the  $\text{Fe}_2\text{O}_3$  scale, but it never becomes thick enough to determine the oxidation kinetics. Further, due to the continuous segregation of iron through the surface of the specimen and due to the decrease in oxygen content at the coating's surface as a result of the volume growth of the  $\text{Fe}_2\text{O}_3$  layer, a continuous and consistent  $\text{Fe}_3\text{O}_4$  layer starts forming in this zone, with small uniformly distributed amounts of the dark phase.

#### 4. Conclusion

This investigation concerned the effect of PTA current variation on the oxidation behavior in air at 800 and 900 °C of coatings of a nickel-based hardfacing alloy deposited on gray cast iron using two different arc currents (100 and 128 A). Samples were analyzed by thermal gravimetric analysis, x-ray diffraction (XRD) and scanning electron microscopy with energy dispersion spectrometry analysis (SEM-EDS). The thermo gravimetric results show that increasing the arc current from 100 to 128 A decreases the oxidation resistance of coatings, a result that can be correlated with the different chemical compositions of the coatings, promoted by different dilutions of the base material. The coating with lower dilution follows a parabolic oxidation weight gain as a function of time, as this behaviour is essentially controlled by the growth of a Si-O layer. The coating with higher dilution follows the same trend at 800 °C. However, at 900 °C two stages in the oxidation curve were detected, the first with a linear increase in mass gain, a compromise between outward Fe diffusion through a growing layer of  $\text{Fe}_2\text{O}_3$  and the loss of carbon by decarburization and formation of  $\text{CO}_2$ . The second step obeys a parabolic law from the moment that C liberation is impeded by a thickened scale consisting of an external  $\text{Fe}_2\text{O}_3$  phase, with small amounts of  $\text{Fe}_3\text{O}_4$  and  $\text{NiFe}_2\text{O}_4$  spinel rich film, and

an internal layer of  $\text{Fe}_3\text{O}_4$  film with small evenly distributed amounts of a dark phase rich in silicon, nickel and iron. In summary, an increase in arc current from 100 to 128 A in the deposition of nickel-rich layers on substrates of cast iron by the PTA process is very harmful, as it reduces the oxidation resistance of the coatings at high temperature.

#### Acknowledgements

The authors wish to express their sincere thanks to the Portuguese Foundation for the Science and Technology (FCT), through COMPETE program from QREN and to FEDER, for financial support in the aim of the project number "13545", as well as for the grant SFRH/BD/68740/2010.

#### References

- [1] M. Cingi, F. Arisoy, G. Basman, K. Sesen, *Mater. Lett.* 55 (2002) 360.
- [2] L. Luo, S. Liu, J. Li, W. Yucheng, *Surf. Coat. Technol.* 205 (2011) 3411.
- [3] R. Vaßen, M.O. Jarligo, T. Steinke, D.E. Mack, D. Stöver, *Surf. Coat. Technol.* 205 (2010) 938.
- [4] C. Guo, J. Zhou, J. Chen, J. Zhao, Y. Yu, H. Zhou, *Wear* 270 (2011) 492.
- [5] K. Gurumoorthy, M. Kamaraj, K.P. Rao, A.S. Rao, S. Venugopal, *Mater. Sci. Eng., A* 456 (2007) 11.
- [6] W. Li, Y. Li, C. Sun, Z. Hu, T. Liang, W. Lai, *J. Alloys Compd.* 506 (2010) 77.
- [7] A. Gatto, E. Bassoli, M. Fornari, *Surf. Coat. Technol.* 187 (2004) 265.
- [8] K. Siva, N. Murugan, R. Logesh, *Int. J. Adv. Manuf. Technol.* 41 (2009) 24.
- [9] F. Fernandes, B. Lopes, A. Cavaleiro, A. Ramalho, A. Loureiro, *Surf. Coat. Technol.* 205 (2011) 4094.
- [10] V. Balasubramanian, A.K. Lakshminarayanan, R. Varahamoorthy, S. Babu, *J. Iron Steel Res. Int.* 16 (2009) 44.
- [11] C.T. Liu, J. Ma, X.F. Sun, *J. Alloys Compd.* 491 (2010) 522.
- [12] W.Z. Li, Y.Q. Li, Q.M. Wang, C. Sun, X. Jiang, *Corros. Sci.* 52 (2010) 1753.
- [13] K.-c. Zhou, L. Ma, Z.-y. Li, *Trans. Nonferrous Met. Soc. China* 21 (2011) 1052.
- [14] G.R. Wallwork, *Rep. Prog. Phys.* 39 (1976) 401.
- [15] E.O. Ezugwu, Z.M. Wang, A.R. Machado, *J. Mater. Process. Technol.* 86 (1998) 1.
- [16] X. Guo, K. Kusabiraki, S. Saji, *Oxid. Met.* 58 (2002) 589.
- [17] A.R. Lashin, O. Schneeweiss, M. Svoboda, *Oxid. Met.* 69 (2008) 359.
- [18] S. Musić, S. Popović, S. Dalipi, *J. Mater. Sci.* 28 (1993) 1793.
- [19] Y.Q. Li, T. Qiu, *Mater. Sci. Eng., A* 444 (2007) 184.
- [20] V.A. Lavrenko, Y.G. Gogotsi, *Oxid. Met.* 29 (1988) 193.
- [21] Y. Wu, Y. Niu, *Scr. Mater.* 53 (2005) 1247.
- [22] H.K. Lee, S. Zerbetto, P. Colombo, C.G. Pantano, *Ceram. Int.* 36 (2010) 1589.
- [23] I.E. Gönenli, T.A. C., *Powder Diffract.* 15 (2000) 104.
- [24] V.B. Trindade, B. Rodrigo, B.Z. Hanjari, S. Yang, U. Krupp, C. Hans-Jürgen, *Mater. Res.* 8 (2005) 365.
- [25] Y. Nakamura, *Metall. Mater. Trans. A* 6 (1975) 2217.
- [26] D.L. Douglass, J.S. Armijo, *Oxid. Met.* 2 (1970) 207.

---

## Annex C

---

**F. Fernandes, A. Ramalho, A. Loureiro, A. Cavaleiro, *Wear resistance of a nickel-based coating deposited by PTA on grey cast iron, International Journal of Surface Science and Engineering, 6 (2012) 201-213.***





---

## **Wear resistance of a nickel-based coating deposited by PTA on grey cast iron**

---

**Filipe Fernandes\***

CEMUC – Department of Mechanical Engineering,  
University of Coimbra,  
Rua Luís Reis Santos, 3030-788 Coimbra, Portugal  
and  
Intermolde, Rua de Leiria, 95, Apartado 103,  
2431-902 Marinha Grande, Portugal  
Fax: +(351) 239-790-701  
E-mail: filipe.fernandes@dem.uc.pt  
\*Corresponding author

**Amilcar Ramalho, Altino Loureiro and  
Albano Cavaleiro**

CEMUC – Department of Mechanical Engineering,  
University of Coimbra,  
Rua Luís Reis Santos, 3030-788 Coimbra, Portugal  
Fax: +(351)-239-790-701  
E-mail: amilcar.ramalho@dem.uc.pt  
E-mail: altino.loureiro@dem.uc.pt  
E-mail: albano.cavaleiro@dem.uc.pt

**Abstract:** The moulds for the production of glass bottles, made of cast iron, are subjected to very severe conditions of wear during use. Thus, it is essential to understand the wear mechanisms involved, in order to increase the equipment life. The present study intends to study the abrasion resistance of moulds submitted for long time at working conditions. The investigation was conducted on nickel-based coatings deposited by plasma transferred arc (PTA) on grey cast iron, using different arc currents. Micro-scale ball cratering abrasive wear test was used to evaluate the tribological properties of the as-deposited and heat treated coatings. The results show that micro-scale abrasion tests induce grooving and pitting wear mechanisms. Increasing the arc current decreased the hardness of the coatings and, consequently, their wear resistance. The hardness and wear resistance of the coatings was improved by increasing heat treatment holding time.

**Keywords:** plasma transferred arc; PTA; Ni-based alloy; wear; ageing; glass moulding; surface engineering.

**Reference** to this paper should be made as follows: Fernandes, F., Ramalho, A., Loureiro, A. and Cavaleiro, A. (2012) 'Wear resistance of a nickel-based coating deposited by PTA on grey cast iron', *Int. J. Surface Science and Engineering*, Vol. 6, No. 3, pp.201–213.

**Biographical notes:** Filipe Fernandes is a PhD student in the Mechanical Engineering Department of the University of Coimbra. He obtained his MSc in 2009. He is currently dedicated to the surface engineering field applied to the moulds for the glass industry. He is focused on the study of new methods to protect the surface of those components. His research interests include thermal spraying of coatings (PTA, HVOF, APS and PVD), oxidation and wear resistance of materials suitable for high temperature applications.

Amílcar Ramalho received his PhD in Mechanical Engineering from Universidade de Coimbra, Portugal in 1994. He is currently a Professor of Maintenance and Mechanical Vibrations. His research interests include friction and wear of materials and components, fretting, tribotesting and biotribology. He is the co-author of more than 150 papers in international journals and conferences. He belongs to the editorial board and collaborates as a reviewer of several international journals.

Altino Loureiro is currently Associate Professor of Welding and Related Technologies in the University of Coimbra (UC) and Researcher from the Center of Mechanical Engineering at the same university (CEMUC). His research interests are focused on technological and metallurgical aspects of welding and thermal spaying processes. He is the author or co-authored over 150 articles in international journals and conferences and reviewer of several international scientific and technical journals. His is also coordinated and collaborated on more than a dozen of research projects and is a consultant to companies in the field of metal construction.

Albano Cavaleiro is full Professor in the Mechanical Engineering Department of the University of Coimbra. He is dedicated to the surface engineering field for more than 25 years. He is mainly concerned with the deposition and characterisation of sputtered coatings for mechanical applications, such as, low friction and self-lubricant, high temperature resistant, oxidation and corrosion protective and DLC. He published more than 150 papers in international peer reviewed journals and presented more than 30 invited talks in international scientific events.

---

## 1 Introduction

Cast iron is commonly used in the production of moulds and accessories for glass industry. Wear and oxidation are the main failure mechanisms that limit the surface life of moulds (Cingi et al., 2002). Therefore, it is necessary to protect mould surfaces with hard and wear resistant materials.

The plasma transferred arc (PTA) process has been usually applied to coat the surfaces of moulds and, especially, their edges where the wear is higher. It produces very high quality deposits, offering optimal protection with minimal thermal distortion of the parts, and provides high deposition rate (Gatto et al., 2004). It allows very precise deposit layers of complex alloys on mechanical parts that are subjected to harsh environments, significantly extending their service life (Siva et al., 2009). However, the hardness and the wear resistance of the coatings are strongly influenced by the dilution of the substrate promoted by the PTA process. Low dilution provides coatings with similar chemical composition to the metal powder added, condition to have an improved wear and

corrosion resistance (Balasubramanian et al., 2009). Therefore, it is essential to control the relevant process parameters to minimise the dilution.

A significant number of coating materials, such as cobalt, iron and nickel alloys, can be applied by PTA process to extend the working life of tribological components subjected to wear. In glass industry nickel alloys gain extremely important role in protection of surfaces, due to their excellent performance under conditions of abrasion and corrosion at elevated temperature. The microstructure and wear behaviour of nickel-based hard-facing alloy deposits have been studied using various alloy compositions and different substrates. Nickel-based alloys are usually strengthened by alloying elements which improve their wear properties (Ezugwu et al., 1998; Chang et al., 2010). Technical literature reports a lot of tribological studies done by pin-on-disc tests in deposits of Ni alloys on stainless and carbon steels, though the sliding contact conditions of pin-on-disc do not reproduce the interaction conditions between melted glass and the surface of the mould. Because of that, the ball cratering wear test was selected as the first step to investigate the micro-abrasion resistance of the coatings at room temperature.

Guo et al. (2011) studied the high temperature wear resistance and wear mechanism of NiCrBSi and NiCrBSi/WC-Ni coatings deposited on stainless steel by laser cladding. They found that the wear resistance of the coatings is much greater than that of stainless steel when sliding against Si<sub>3</sub>N<sub>4</sub> counterpart ball. Furthermore, NiCrBSi/WC-Ni composite coating showed better wear resistance at high temperature than NiCrBSi coating. Kesavan and Kamaj (2010), who worked with a Colmomoy 5 hard-facing alloy deposited by PTA on a stainless steel, studied the room and high temperature wear behaviour using pin-on-disc wear tests. They showed that the wear resistance of the coatings improved significantly with increasing test temperature. Further, they observed different operating wear mechanisms depending on the sliding and testing temperature. In turn, Gurumoorthy et al. (2007) studied the sliding wear of a nickel hard-facing alloy AWS NiCr-B deposited on the same stainless steel at three different temperatures (room temperature, 300°C and 500°C), and the influence of an ageing treatment on its microstructure, hardness and wear behaviour. The investigation revealed a significant weight loss at room temperature and an abrupt decrease in mass loss at high temperature. However, after ageing treatment they demonstrated that there is no significant change in the weight loss or the wear behaviour at room and high temperature.

Since wear and oxidation are the main drawbacks that limit the surface life of glass moulds, the aim of this research is to study the effect of PTA current on the microstructure, hardness and three-body abrasion behaviour of a nickel-based hard-facing alloy coating deposited on grey cast iron. Ageing studies were also conducted to evaluate the influence of temperature holding time on the microstructure, hardness and tribological properties of the coating processed with the highest current.

## **2 Experimental procedure**

A nickel-based hard-facing alloy named Colmonoy 215 (from Colmonoy Company) was deposited on flat surfaces of grey cast iron blocks by PTA process. Before coating, each cast iron block was preheated at 480°C, in order to reduce the thermal shock and cooling rate to avoid cracks in both the coating and heat-affected zone. The same process

parameters were used for all coatings except arc current, which was 100 A for specimen 1, 128 A for specimen 2 and 140 A for specimen 3. The composition of cast iron and metal powder is given in Table 1 and the process parameters used in Table 2. After coating, the blocks were left to cool to room temperature. Samples were removed from each block, transversely to welding direction, for further analysis. Ageing studies were carried out at 500°C for 5, 10 and 20 days on specimen 3.

**Table 1** Nominal chemical composition (wt.%) of substrate and hard-facing alloy

<i>Base material</i>	<i>C</i>	<i>Mn</i>	<i>Si</i>	<i>P</i>	<i>S</i>	<i>Cr</i>	<i>Ni</i>	<i>Mo</i>	<i>V</i>	<i>Ti</i>	<i>Fe</i>
Grey cast iron	3.60	0.60	2.00	< 0.20	< 0.04	< 0.20	< 0.50	0.50	0.10	0.20	Balance
Hard-facing	C	Cr	Si	B	Fe	Al	F	Co	Ni		
Ni-alloy			0.14	2.45	2.56	0.86	1.08	1.30	0.01	0.08	Balance

**Table 2** Deposition parameters for PTA weld surfacing.

	<i>Main arc current (A)</i>	<i>Powder feed rate (rpm)</i>	<i>Travel speed (mm/s)</i>	<i>Powder feed gas flow rate (l/min)</i>	
Specimen 1	100	20	2	2	
Specimen 2	128	20	2	2	
Specimen 3	140	20	2	2	
	<i>Plasma gas flow rate (l/min)</i>	<i>Shielding gas flow rate (l/min)</i>	<i>Torch work distance (mm)</i>	<i>Oscillation (mm)</i>	<i>Preheat temperature °C</i>
Specimen 1	2.2	20	13	4	480
Specimen 2	2.2	20	13	4	480
Specimen 3	2.2	20	13	4	480

Microstructural analysis was done in cross section of the samples. Optical and scanning electron microscopies (OM and SEM) were used to characterise the microstructure of the coatings. Vickers micro-hardness profiles were measured in the cross section of treated samples using a load of 5 N.

Micro abrasive wear tests were carried out in as-deposited and heat treated surfaces at room temperature in a ball cratering devices. Figure 1 shows a schematic diagram of the equipment used. In this test a specific normal load is applied to press a rotating ball into the flat surface of the coated sample in the presence of a slurry suspension of abrasive. The abrasive slurry, agitated by a magnetic stirrer, was continuous and gravitationally drip fed onto the rotating ball to produce a spherical cup depression. Preliminary tests using different contact conditions were done to reproduce the interaction conditions in the surface of the moulds which have been in service for a long time. The wear mechanism was studied by SEM. High purity silica SS40 with angular particles of averaging of 3.10 µm in size was used as an abrasive to replicate the effect of the melted glass. The slurry used was prepared with a concentration of 103 g per 1 × 10<sup>-4</sup> m<sup>3</sup> of distilled water. A steel ball bearing (AISI 52100) with 0.0254 m was used. Several scars were made in each sample with different durations, 100, 200, 300, 400 and 500 turns, respectively 7.98, 15.96, 23.94, 31.92, 39.90 meters of sliding distance for all the specimens, under the action of a normal load of 0.1 N. In order to minimise the scatter of results, previously to starting the tests, the ball surface was etched with chloridric acid (33%) during ten

minutes. The dimensions of spherical depressions were measured in order to calculate the wear volume, which is given by the equation (1). In this equation, R represents the ball radius and b the crater chordal diameter of the spherical cup depression. The b value was evaluated using the average of two perpendicular measurements performed at the wear scar chordal diameter. Those values were measured with a Mitutoyo Toolmaker Microscope with x-y micrometer table.

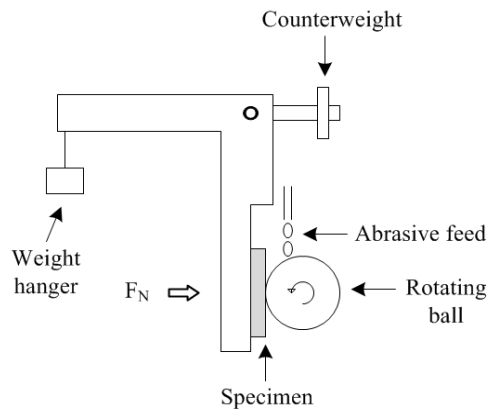
$$V = (\pi \times b^4) \times (64 \times R) \quad (1)$$

In order to obtain the specific wear rate, to quantify the wear behaviour, Archard's law was applied, see equation (2). This is the most applied law to determine a parameter to quantify the wear behaviour of materials. In this equation, P is the normal load, l is the sliding distance and k is the specific wear rate.

$$V = k \times P \times l \quad (2)$$

To quantify the specific wear rate a linear approach of Archard's model was applied and a statistical analysis was used to estimate the error of measurements, as described elsewhere (Ramalho, 2010).

**Figure 1** Schematic diagram of the micro-scale abrasion tests



### 3 Results

#### 3.1 Microstructure

Figure 2 shows the microstructure of the coatings performed using different arc currents [Figures 2(a), 2(b) and 2(c)], as well as the fusion boundary of specimen 3 [Figure 2(d)], and SEM pictures of specimen 3 before and after heat treatment [Figures 2 (e) and 2(f)]. The typical microstructure of deposits consists of dendrites of Ni-Fe solid solution phase with columnar morphology oriented along the direction of heat flow, with C-flakes (dark floret-like structures) randomly distributed. However, near the interface it was observed the presence of a cellular microstructure finer than the dendrite structure with diminution of the size of C-flakes, as illustrated in Figure 2(d) for specimen 3. This behaviour could be explained by the higher solidification rates involved in the boundary because of the

efficient thermal exchange ensured by the high volume ratio substrate/coating of the base material, as suggested by Gatto et al. (2004) and Navas et al. (2006). Moreover, the presence of the ‘dark’ phase on the coatings cannot be explained by the chemical composition of the metal powder added, so it can be only attributed to the high dilution of cast iron induced by the PTA process. The dilution was evaluated by the ratio between the area of the melted base material and the total area of the melted zone, both measured in the cross section of the coatings. Dilutions of 28%, 50% and 59% were measured respectively for specimen 1, 2 and 3. These results agree with the observed increasing proportion of C-flakes for higher arc currents, as can be seen in Figures 2(a), 2(b) and 2(c). Therefore, the chemical composition of the coatings is largely influenced by the dilution of cast iron. A detailed characterisation of this type of coatings can be found in a previous publication of the authors (Fernandes et al., 2011).

**Figure 2** Microstructure of (a) specimen 1, (b) specimen 2, (c) specimen 3, (d) interface of specimen 3 and SEM pictures of sample 3 (e) in non-heat-treated condition and (f) in heat treated condition during ten days

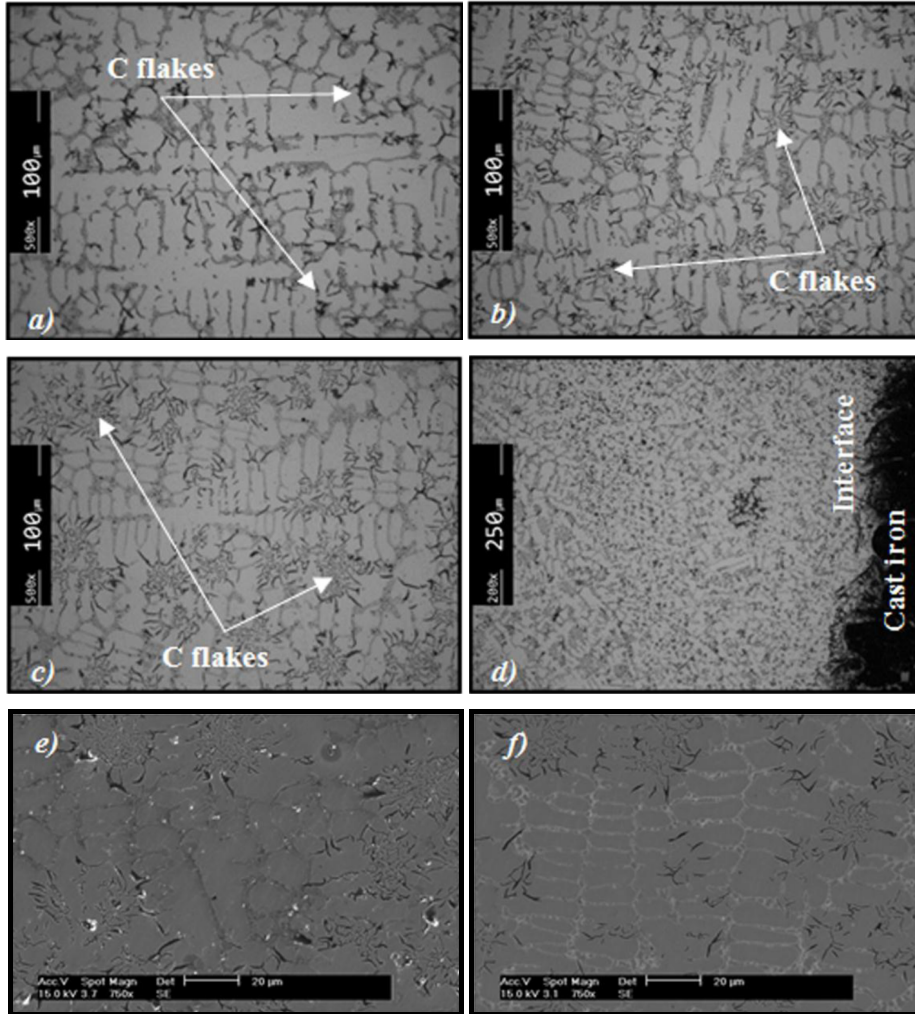


**Table 3** SEM chemical analysis of the deposit and base material of specimen 3

	Elements wt%						
	C	Al	Si	Cr	Fe	Ni	
1	0.8	0.7	2.6	1.4	54.7	39.8	Deposit
2	0.8	0.7	2.8	1.6	54.8	39.2	
3	0.9	1.4	2.5	1.9	50.4	42.8	
4	1.6	1.1	2.2	1.4	59.4	34.2	Interface
5	3.9	-	2.7	-	93.3	-	Base material

**Figure 3** SEM magnification of microstructure of the coating 3 (a) in non-heat treated condition and (b) in heat-treated condition after ten days exposed at 500°C and SEM EDAX spectra of (c) point 1, (d) point 2, and (e) point 3 (see online version for colours)

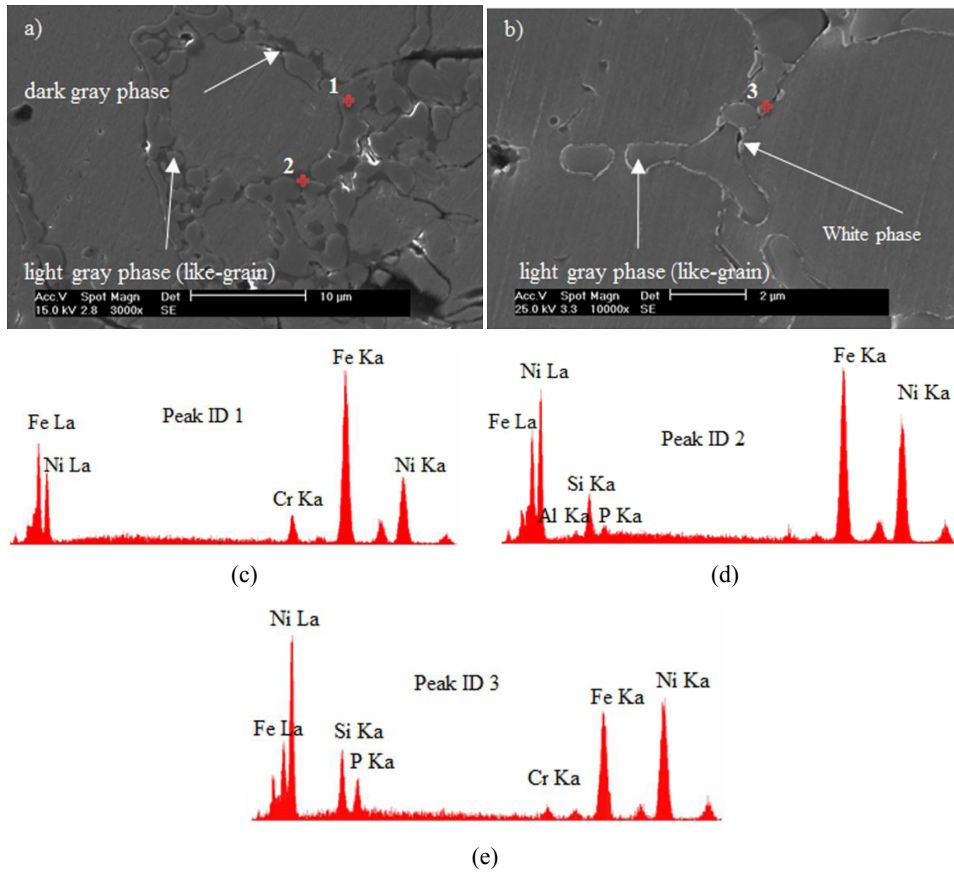
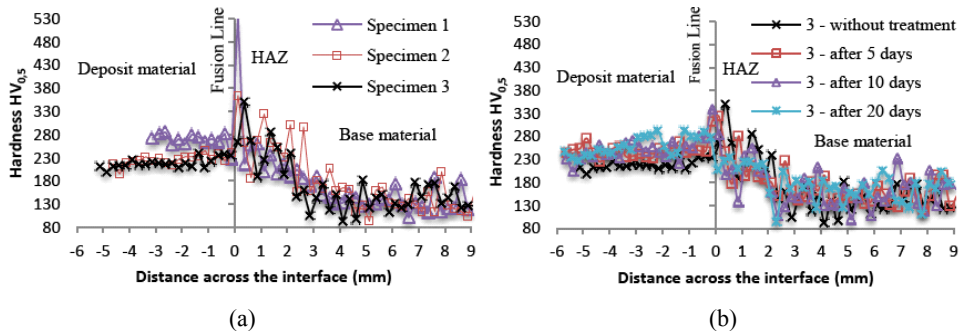


Table 3 shows the chemical composition in area measured by SEM-EDS at various zones on the coating and the substrate of specimen 3. Zone 1 and 2 are located close to the coating surface, zone 3 at the mid-thickness of the coating, zone 4 in the coating close to the fusion boundary and zone 5 in the bulk cast iron. This analysis showed that PTA process promotes an evenly distribution of the elements inside the coating. The same observation was done in specimens 1 and 2. Due to the dilution, the amount of iron in the

coating increases reducing its nickel content. Ezugwu et al. (1998) reported that the increase of iron content in the coatings tends to decrease their oxidation resistance, because of the formation of a less adherent oxide scale.

Figures 2(e) and 2(f) reveals that the heat treatment induces significant changes in the original microstructure of specimen 3. It promotes the formation of a white phase on the grain boundaries. Magnifications of the two microstructures are shown in Figure 3. SEM-EDS spectra analyses were conducted on the coatings to give a detailed characterisation of their microstructure. From the EDS analysis, it can be stated that the grain boundaries of the non-heat-treated sample is formed by two phases: a light grey and a dark grey rich in chromium and silicon, respectively. Inversely, the specimen in heat-treated condition is formed by the light grey phase as observed in the non-heat-treated sample and a new phase (white phase) which is replacing the dark phase. The amount of the white phase grows with increasing time of heat treatment. According to Fernandes et al. (2011), who studied a nickel alloy deposited on grey cast iron, the dark grey phase is a  $\text{Ni}_3\text{Si}$  phase. The EDS spectrum reveals that both phases (the dark and the white) are rich in Ni-Si. However, the white phase presents a higher content of phosphorous on the heat treated sample suggesting a dispersion of Ni-P precipitates on the grain boundaries, as observed by Sahoo and Das (2011) in electroless nickel coatings.

**Figure 4** Hardness profile across the interface of (a) as-deposited specimens and (b) specimen 3 before and after heat treatment (see online version for colours)



### 3.2 Hardness

The micro-hardness profiles of the different as-deposited and heat treated specimens are shown respectively in Figures 4(a) and 4(b). Figure 4(a) reveals that the hardness through the coatings is approximately constant and tends to decrease with increasing arc current. The dilution induced by the PTA process can explain this behaviour. The partial melted zone (PMZ) displays the highest hardness. According to Pouranvari (2010), who studied the weldability of grey cast iron using nickel-based filler metals, the highest hardness observed in PMZ is due to the formation of hard and brittle phases during surfacing, such as martensite and white cast iron. The heat treatment promotes the progressive hardening of the coatings with increasing thermal exposure time [see Figure 4(b)]. Some scatter of the hardness values can be observed too. Harsha et al. (2008), who studied the influence of CrC in a nickel flame sprayed coatings, observed similar behaviour. According to them, the scatter in the values is due to the presence of a harder eutectic network around the cells. As described before, heat treatment promotes the formation of Ni-P precipitates

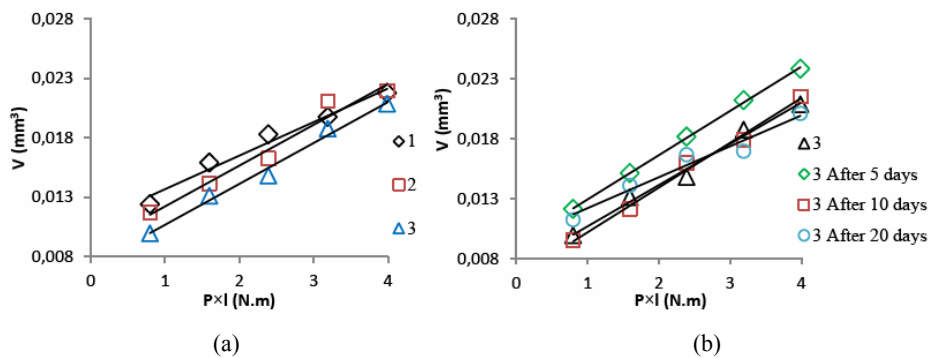


on the grain boundaries. The greater hardness observed on the ageing treated samples can be attributed to the presence of these precipitates similarly to what is currently observed in Ni-P electroless coating when annealed at increasing temperatures (Sahoo and Das, 2011). This type of coatings is a supersaturated alloy in the as-deposited state and can be strengthened by the precipitation of nickel phosphide crystallites. The phosphides act as barriers for dislocation movement and improve the mechanical strength of the coatings.

### 3.3 Wear behaviour of coatings

Micro-scale abrasion tests were performed on the coatings at room temperature to predict the effect of the different process parameters on their wear behaviour. The goal in a first step was to study the abrasion resistance present in the surface of in-service moulds, in order to quantify the wear loss of coatings. The response of materials under micro abrasion tests depends on the nature of the motion of particles in the contact zone, which determines the stress state arising near the contact. Three-body wear mechanism (rolling or pitting) and two-body wear mechanism (grooving), or a combination of both mechanisms could be detected. Rolling occurs when the abrasive particles are able to free rotate between the sphere and the material in test; on the other hand, grooving occurs if the particles follow the rotation of the sphere, scratching the specimen surface (Ramalho et al., 2011; Gant and Gee, 2011). In spite of this general tendency to the occurrence of three-body or two-body abrasion, the characteristics of the materials will influence the process; mild materials will stabilise the grooving mode.

**Figure 5** Evolution of the wear volume as function of the parameter 'normal load  $\times$  sliding distance' of (a) as-deposited coatings and (b) specimen 3 before and after thermo exposure at 500°C during several days (see online version for colours)



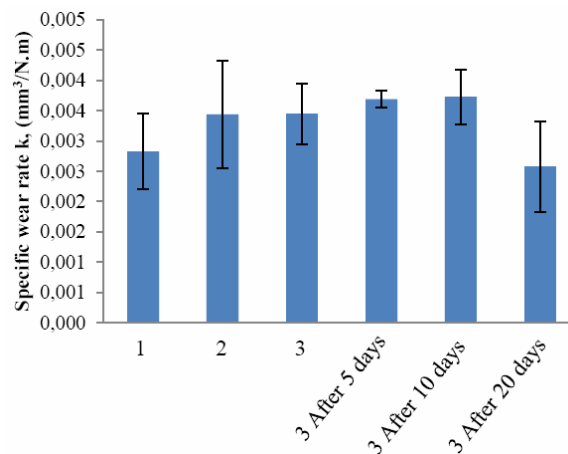
The results of the micro-scale abrasion tests from specimens in as-deposited and heat treated conditions are plotted respectively in Figures 5(a) and 5(b), as the material volume loss as a function of the product of the sliding distance ( $l$ ) by the normal load ( $P$ ). The reliability analysis of the data is presented in Table 4 and the confidence interval for the specific wear rate plotted in Figure 6. For each sample, a straight linear trend was fitted to the experimental points in order to obtain the specific wear rate, which corresponds to its slope [see equation (2)]. From Figure 5(a), it is possible to conclude that specimen 1 exhibits slightly lower specific wear rate, therefore it is the more resistant to wear. This result is in accordance with its greater hardness when compared to the others as-deposited coatings. Specimens 2 and 3 displays similar wear volumes, which is

again attributed to their similar hardness profiles. Figure 5(b) reveals that specimens exposed during five and ten days at 500°C displayed similar specific wear rate to the non-heat-treated specimen. However, the specimen exposed during 20 days exhibits lower specific wear rate, therefore, it is the most resistant to wear. This last result is again in accordance with the higher hardness of this sample after the heat treatment.

**Table 4** Results of the linearisation analysis of samples in as-deposited and heat treated conditions

	<i>Specific wear rate, <math>k(\text{mm}^3/\text{N m})</math></i>			
	<i>Average</i>	<i>STD</i>	<i>Confidence interval 90%</i>	<i>r2</i>
Specimen 1	$2.83 \times 10^{-3}$	$2.65 \times 10^{-4}$	$2.20 \times 10^{-3}$ to $3.45 \times 10^{-3}$	0.974
Specimen 2	$3.44 \times 10^{-3}$	$3.78 \times 10^{-4}$	$2.55 \times 10^{-3}$ to $4.33 \times 10^{-3}$	0.965
Specimen 3	$3.45 \times 10^{-3}$	$2.14 \times 10^{-4}$	$2.94 \times 10^{-3}$ to $3.95 \times 10^{-3}$	0.989
After 5 days at 500°C	$3.69 \times 10^{-3}$	$5.57 \times 10^{-5}$	$3.56 \times 10^{-3}$ to $3.83 \times 10^{-3}$	0.999
After 10 days at 500°C	$3.73 \times 10^{-3}$	$1.91 \times 10^{-4}$	$3.28 \times 10^{-3}$ to $4.18 \times 10^{-3}$	0.992
After 20 days at 500°C	$2.58 \times 10^{-3}$	$3.18 \times 10^{-4}$	$1.83 \times 10^{-3}$ to $3.33 \times 10^{-3}$	0.956

**Figure 6** Confidence interval for a confidence level of 90%, for the specific wear rate of specimens in as-deposited and heat treated conditions (see online version for colours)



In order to identify the wear mechanisms and to compare the worn surfaces with those observed in the surface of moulds, SEM examinations were carried out. Figure 7(a) displays a SEM micrograph of the surface of a coating of a mould after long time in service. From this picture is possible to see that the surface failure regions display pits and cracks. Considering the in-service conditions the surface damage probably was induced by synergetic effects of several mechanisms, namely thermal fatigue, corrosion and abrasion. However, pitting is the main active failure mechanism of the moulds. Figures 7(b) and 7(c) illustrates spherical cup depressions induced by the micro-scale abrasion tests on the specimen 3, before and after holding time for 20 days, produced after 500 ball rotations. Both scars display similar wear behaviour with two modes of wear: three-body abrasion (pitting) and two-body abrasion (grooving). The two-body abrasion mode is preferentially localised in the area of higher pressure (input slurry area)

and three-body abrasion mode is localised in the area of less pressure. Figure 8 shows these two modes of wear at higher magnification. The same wear mechanisms were observed in the other specimens in as-deposit and heat treated conditions. Although the scars displayed two modes of wear it can be stated that the region corresponding to three-body mode reproduces closely the wear mechanism present in the moulds surface. However, one should keep in mind that these results do not reproduce with accuracy the in-service condition of the moulds, since in service they are exposed to other damage mechanisms such as thermal and mechanical fatigue, oxidation and corrosion at high temperature.

**Figure 7** SEM micrograph (a) of the surface of a coating of a mould after long exposure to high temperature, (b) scar with 500 rotations induced by the micro-scale abrasion tests on specimen 3, and (c) scar with 500 rotations induced by the micro-scale abrasion tests on specimen 3 after thermal exposure for 20 days (see online version for colours)

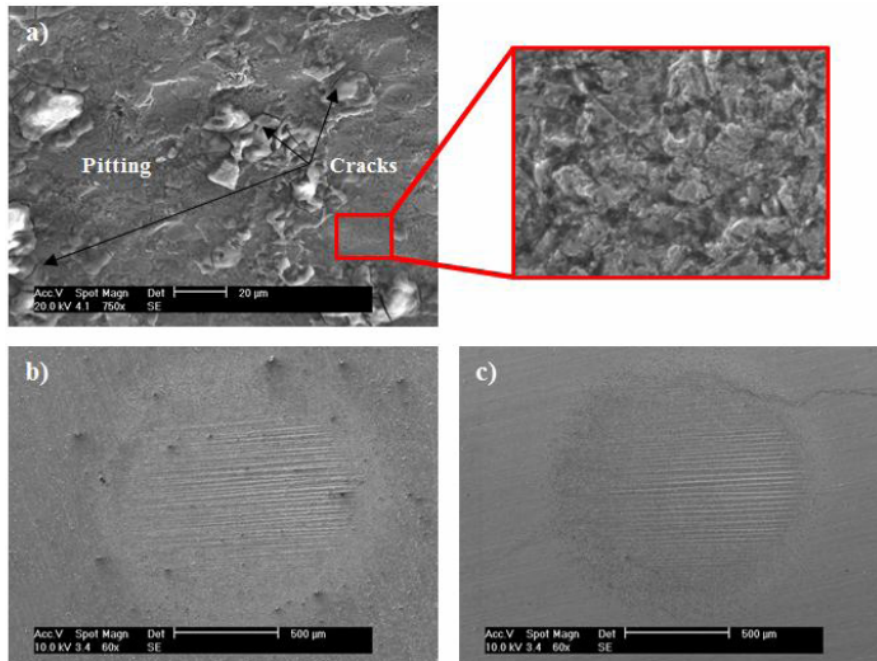
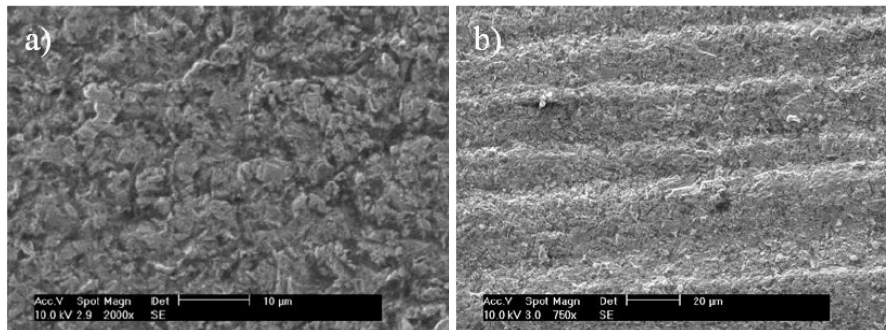


**Figure 8** SEM micrograph of (a) three-body abrasion and (b) two-body abrasion



#### 4 Conclusions

Micro-scale abrasion testing was used to study the interaction conditions between melted glass and the surface of the moulds. The influence of the arc current used in PTA process, as well as the effect of heat treatments, on the microstructure, hardness and wear resistance of the coatings was analysed. The increase in arc current increased the dilution of the base material changing the composition and microstructure of the deposits and reducing their hardness. Furthermore, the wear loss of material increased with increasing arc current. The micro-scale abrasion tests displayed two modes of wear: three-body abrasion (pitting) and two-body abrasion (grooving). Although the scars displayed two modes of wear it can be stated that the wear mechanism of the abrasion test reproduces with success the wear mechanism present in the moulds surface. The heat treatment performed on the sample 3 promotes increasing hardness of the coating with thermal exposure time. The enhanced hardness of the coatings is partially attributed to Ni-P precipitates on the grain boundaries. Specimen 3 heat treated for 20 days showed the best resistance to wear.

Future experiments will be devoted to study the high temperature abrasion resistance of the coatings, in order to reproduce the in service conditions of moulds.

#### Acknowledgements

The authors would like to thank the company 'Intermolde', for supplying the coated samples, and the Portuguese Foundation for the Science and Technology (FCT), through COMPETE programme from QREN and to FEDER, for financial support in the aim of the project number '013545', as well as for the grant SFRH/BD/68740/2010.

#### References

- Balasubramanian, V., Lakshminarayanan, A.K., Varahamoorthy, R. and Babu, S. (2009) 'Application of response surface methodology to prediction of dilution in plasma transferred arc hardfacing of stainless steel on carbon steel', *International Journal of Iron and Steel Research*, Vol. 16, No. 1, pp.44–53.
- Chang, J.H., Chang, C.P., Chou, J.M., Hsieh, R.I. and Lee, J.L. (2010) 'Microstructure and bonding behavior on the interface of an induction-melted Ni-based alloy coating and AISI 4140 steel substrate', *Surface and Coatings Technology*, Vol. 204, No. 2, pp.3173–3181.
- Cingi, M., Arisoy, F., Basman, G. and Sesen, K. (2002) 'The effects of metallurgical structures of different alloyed glass mold cast irons on the mold performance', *Materials Letters*, Vol. 55, No. 6, pp.360–363.
- Ezugwu, E.O., Wang, Z.M. and Machado, A.R. (1998) 'The machinability of nickel-based alloys: a review', *Journal of Materials Processing Technology*, Vol. 86, Nos. 1–3, pp.1–16.
- Fernandes, F., Lopes, B., Cavaleiro, A., Ramalho, A. and Loureiro, A. (2011) 'Effect of arc current on microstructure and wear characteristics of a Ni-based coating deposited by PTA on gray cast iron', *Surface and Coatings Technology*, Vol. 205, No. 16, pp.4094–4106.
- Gant, A.J. and Gee, M.G. (2011) 'A review of micro-scale abrasion testing', *Journal of Physics D: Applied Physics*, Vol. 44, No. 7, 073001.
- Gatto, A., Bassoli, E. and Fornari, M. (2004) 'Plasma transferred arc deposition of powdered high performances alloys: process parameters optimisation as a function of alloy and geometrical configuration', *Surface and Coatings Technology*, Vol. 187, Nos. 2–3, pp.265–271.

- Guo, C., Zhou, J., Chen, J., Zhao, J., Yu, Y. and Zhou, H. (2011) 'High temperature wear resistance of laser cladding NiCrBSi and NiCrBSi/WC-Ni composite coatings', *Wear*, Vol. 270, Nos. 7–8, pp.492–498.
- Gurumoorthy, K., Kamaraj, M., Rao, K.P., Rao, A.S. and Venugopal, S. (2007) 'Microstructural aspects of plasma transferred arc surfaced Ni-based hardfacing alloy', *Materials Science and Engineering: A*, Vol. 456, Nos. 1–2, pp.11–19.
- Harsha, S., Dwivedi, D. and Agarwal, A. (2008) 'Influence of CrC addition in Ni-Cr-Si-B flame sprayed coatings on microstructure, microhardness and wear behaviour', *The International Journal of Advanced Manufacturing Technology*, Vol. 38, No. 1, pp.93–101.
- Kesavan, D. and Kamaraj, M. (2010) 'The microstructure and high temperature wear performance of a nickel base hardfaced coating', *Surface and Coatings Technology*, Vol. 204, No. 24, pp.4034–4043.
- Navas, C., Colaço, R., Damborenea, J. and Vilar, R. (2006) 'Abrasive wear behaviour of laser clad and flame sprayed-melted NiCrBSi coatings', *Surface and Coatings Technology*, Vol. 200, No. 24, pp.6854–6862.
- Pouranvari, M. (2010) 'On the weldability of grey cast iron using nickel based filler metal', *Materials & Design*, Vol. 31, No. 7, pp.3253–3258.
- Ramalho, A. (2010) 'A reliability model for friction and wear experimental data', *Wear*, Vol. 269, Nos. 3–4, pp.213–223.
- Ramalho, A., Rodríguez, J. and Rico, A. (2011) 'Microabrasion resistance of nanostructured plasma-sprayed coatings', *Int. J. Surface Science and Engineering*, Vol. 5, No. 4, pp.250–260.
- Sahoo, P. and Das, S.K. (2011) 'Tribology of electroless nickel coatings – a review', *Materials & Design*, Vol. 32, No. 4, pp.1760–1775.
- Siva, K., Murugan, N. and Logesh, R. (2009) 'Optimization of weld bead geometry in plasma transferred arc hardfaced austenitic stainless steel plates using genetic algorithm', *The International Journal of Advanced Manufacturing Technology*, Vol. 41, No. 1, pp.24–30.



---

## Annex D

---

**F. Fernandes, A. Ramalho, A. Loureiro, A. Cavaleiro, *Mapping the micro-abrasion resistance of a Ni-based coating deposited by PTA on gray cast iron*, *Wear*, 292-293 (2012) 151-158.**







# Mapping the micro-abrasion resistance of a Ni-based coating deposited by PTA on gray cast iron

F. Fernandes\*, A. Ramalho, A. Loureiro, A. Cavaleiro

CEMUC, Department of Mechanical Engineering, University of Coimbra, Rua Luís Reis Santos, 3030-788 Coimbra, Portugal

## ARTICLE INFO

### Article history:

Received 2 February 2012

Received in revised form

28 May 2012

Accepted 30 May 2012

Available online 7 June 2012

### Keywords:

Mapping

Micro-scale abrasion

Three-body abrasion

Two-body abrasion

Hardfacing

Wear testing

## ABSTRACT

Micro-scale abrasion was used to characterize abrasion resistance of a nickel-based hardfacing alloy deposited by Plasma Transferred Arc on gray cast iron using silica as abrasive agent. In order to investigate the occurrence of different abrasion mechanisms, several test conditions were used, namely: different silica abrasive contents and a range of normal loads and test durations. A scanning electron microscope (SEM) was used to study the morphologies of the spherical cup-shaped depressions induced by different test conditions. The results are discussed in terms of the effect of the dominant wear mechanisms on the abrasion resistance and the influence of the test conditions on the mechanism transition. The wear results lead to the conclusion that the specific wear rate essentially depends on the wear mechanisms (rolling or grooving) involved and not on the tests conditions employed, since these do not produce changes in the wear mechanism.

© 2012 Elsevier B.V. All rights reserved.

## 1. Introduction

The micro-scale abrasion wear test is a suitable experimental method for evaluating and comparing the abrasive wear performance of a wide variety of materials. This technique has been successfully applied to characterize metallic and non-metallic, bulk and coating materials, under the influence of a wide diversity of abrasive slurries [1,2]. It is well known that in the industry, the main wear problems in components are related to abrasion, which could co-exist, whether associated or not, with other forms of wear, such as adhesion or tribo-corrosion [3–5]. The usefulness of the laboratory characterization depends on the ability of the test conditions to reproduce real working conditions as closely as possible.

In the micro-scale abrasion test, three distinct wear modes have been identified, three-body or rolling abrasion, two-body or grooving abrasion and the ridging wear mechanism [1,2,5–8]. Additionally transitions between these wear modes could be observed (rolling to grooving, grooving to ridging and ridging to rolling); these are referred to as “mixed-mode” wear mechanisms. Rolling abrasion is characterized by a hertzian type contact which occurs when the abrasive particles are able to freely rotate between the sphere and the material in test, producing multiple indentations, while grooving occurs if the particles remain fixed to the sphere and scratch the specimen surface. On the other

hand, ridging wear mechanism is produced when the abrasive particles disappear in the contact region, the contact being made directly between the sphere and the specimen tested. Therefore, the ridging wear mode should be considered as transition from abrasion to metal–metal sliding. Furthermore, according to some authors [8,9], associated with the complex regimes above mentioned, tribo-chemical interactions must be taken into account in the wear calculations specially at high applied loads. This phenomenon is known to enhance wear resistance with an increase in applied load due to oxide formation on the surface.

In order to use micro-abrasion tests to evaluate the abrasive wear resistance of a system, either three-body or two-body abrasions need to be considered in the study; each wear mode is characterized by significantly different values of specific wear rate, which can differ by more than one order of magnitude [1,10]. Some authors stated that, in micro-scale abrasion tests, the rolling abrasion wear mode leads to results that are more easily reproduced [11,12]. Williams and Hyncica [13,14] discussed the possibility of applying the continuum mechanics abrasion model to explain the wear transitions. They verified that the quantitative models can be only applied to processes or materials where the boundary conditions are well established, which is not the case for the micro-scale abrasion test. Nevertheless, Williams and Hyncica suggested that the transition from rolling to grooving must be a function of the critical thickness of the abrasive slurry in the contact. Following this suggestion, Adachi and Hutchings [6] used an indentation model to analyze the grooving wear conditions and they proposed a dimensionless parameter for the severity of contact ( $S'$ ), to be correlated with the transition

\* Corresponding author. Tel.: +351 239 790 700; fax: +351 239 790 701.  
E-mail address: [filipe.fernandes@dem.uc.pt](mailto:filipe.fernandes@dem.uc.pt) (F. Fernandes).

conditions. The ratio of hardnesses between the specimen and the ball,  $H_s/H_b$ , was identified as the key parameter in the transition from three-body to two-body abrasion. The results showed that with increasing severity of contact ( $S'$ ) a transition from uniform three-body to two-body abrasion occurs through a mixed three and two body abrasion regime.

The technical literature reports several studies undertaken using micro-scale abrasion equipment and describes how the dissimilar test conditions (volume fraction of abrasive in the slurry, abrasive material, applied load, ball and specimen materials, sliding distance and surface condition of the ball) influence the dominant wear modes of different materials [1,6,10,15–18]. The main objective of these studies is to track the dominant wear modes created with different conditions to produce an associate wear-mode map, to serve as data to predict the conditions to ensure either three-body or two-body abrasion. With regard to the type of abrasive material to be used in micro-scale abrasion tests, the BS-EN 1071-6: 2007 standard recommends the use of SiC F1200 abrasive; however, dissimilar abrasive materials with different grain sizes have been used and, normally, the studies also report the use of diamond and  $Al_2O_3$ . It has been shown that the relative wear rates of the materials depended strongly upon the abrasive type selected (abrasive shape and hardness) [19]. Nevertheless, there are few references regarding the use of silica as abrasive material. Because silica is the most common abrasive material, therefore responsible for the majority of practical abrasion problems, it is important to study the test conditions which produce different wear mechanisms using silica abrasive slurry.

Thus, the purpose of this investigation was to study the test conditions which produce rolling and grooving wear modes with silica slurry. An associate wear mode-map should be produced to use as data to ensure either one or the other abrasion wear mechanism's intended further aim was to show that the specific wear rate essentially depends on the wear mechanisms (rolling or grooving) involved and not on the test conditions employed, since these do not produce changes in the wear mechanism. The wear tests were conducted in fixed ball equipment on a nickel-based hardfacing alloy coating deposited by PTA – Plasma Transferred Arc on gray cast iron. Regimes of wear behavior were identified by scanning electron microscope (SEM) and the results were analyzed with a focus on the effects of wear mechanisms.

## 2. Experimental procedure

In this study, micro-scale abrasion equipment was used to study the influence of the test conditions on the dominant wear modes of a nickel-based hardfacing coating. The coating analyzed was produced by plasma transferred arc process (PTA) on a flat surface of gray cast iron using a 128 A arc current. Fig. 1 shows the typical microstructure of the as-deposited coating. As can be observed, the coating has a relatively dense microstructure, free of microcracks and few solidification voids with dendrites of Ni-Fe solid solution phase aligned along the direction of heat flow. Furthermore, it displays C-flakes (dark-floret like structures) randomly distributed in the matrix. The chemical composition of the materials, the conditions and the procedure adopted for the deposition and the characterization of the coatings as well as their main physical structural and mechanical properties can be found in a previous publication of the authors [20].

Fig. 2 represents a schematic diagram of the micro-abrasive wear equipment (fixed ball equipment). In this device, a specific normal load is applied to press a rotating ball (located between two-coaxial shafts) into the surface of the coated specimen (placed in a pivoted specimen holder) in the presence of a specific abrasive slurry. The abrasive slurry was continuously agitated by

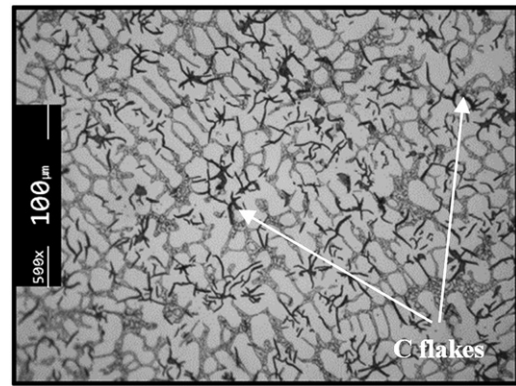


Fig. 1. Typical microstructure of the as-deposited coating.

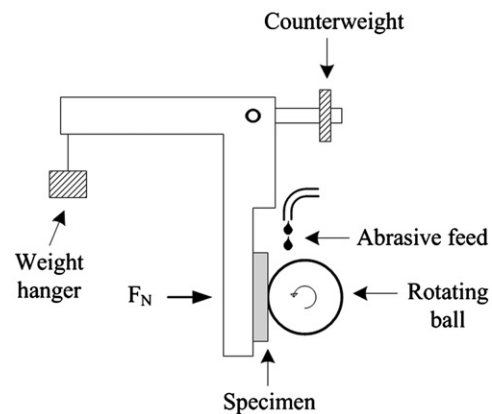


Fig. 2. Schematic diagram of the of the micro-abrasive wear equipment used.

a magnetic stirrer and dropped steadily onto the rotating ball to produce a spherical cup depression. In this investigation, high purity silica from Lusosilica, Lda (Portugal) company, with an average particle size of  $3.1 \mu\text{m}$  and hardness around 1000 HV was used as abrasive to produce spherical cup depressions in the flat surface of the coated sample. As shown in Fig. 3(a), the silica particles are highly irregular and angular. The particle size distribution is plotted in Fig. 3(b). The slurry was prepared with different silica contents (25, 50 and 65 vol%) in distilled water. An AISI 52100 steel ball bearing, 25.4 mm in diameter and with a hardness of approximately 740 HV, was used as the counterpart to produce wear scars in the sample surface. The specimen tested has a hardness of approximately 225 HV. The rotation speed of the ball was kept at 75 rpm (0.1 m/s of tangential speed) in all the tests. The coating was tested using three different normal load values (0.1, 0.2 and 0.5 N) and five test durations (50, 80, 150, 200 and 300 rpm), respectively 4, 6.4, 12, 16 and 24 m of sliding distance. The test conditions are summarized in Table 1.

In order to produce an evenly prepared surface, the specimen was polished with SiC abrasive paper up to 1000 grit before wear tests. A new ball was used in the abrasion tests. The ball's surface was prepared using the run-in procedure described by Gee et al. [21], and the orientation of the ball was changed randomly before each test. Following the tests, the wear scars were examined by a scanning electron microscope (SEM), in order to discriminate the dissimilar wear modes. Abrasion maps of the material volume loss as function of the sliding distance were plotted for each value of normal load used. The results were discussed in terms of either the tribological properties or the dominant wear mechanisms involved. The material wear volume was calculated by using Eq. (1). In this equation  $b$  represents the crater chordal diameter of the

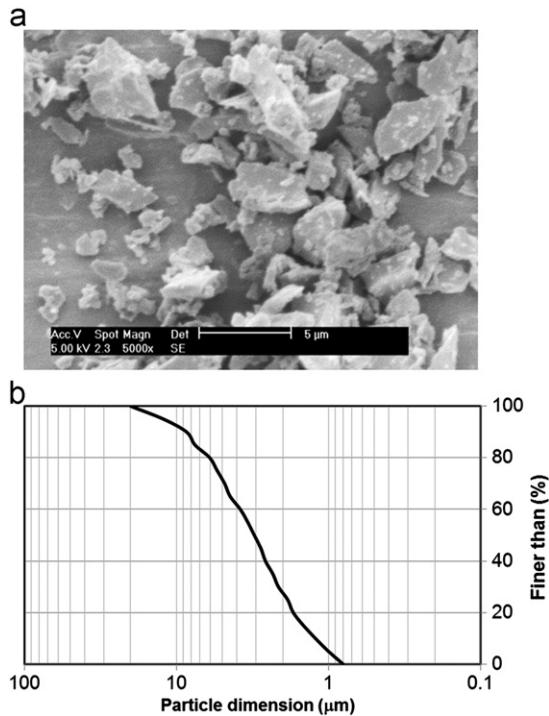


Fig. 3. Silica abrasive particles. (a) Morphology and (b) particle size distribution.

Table 1  
Test conditions.

Ball material	Steel AISI 52100
Ball diameter (mm)	25.4
Abrasive	Silica SS40 (mean size: 3.1 µm)
Abrasive concentration	25, 50 and 65 vol% in H <sub>2</sub> O
Test duration (rotations)	50, 80, 150, 200, 300
Normal load (N)	0.1, 0.2, 0.5
Speed (rpm)	75

spherical cup depression produced and  $R$  is the ball radius used. The  $b$  value was calculated using the average of two perpendicular measurements performed at the wear scar chordal diameter, with the help of a Mitutoyo Toolmaker Microscope with x–y micrometer table. All the data was then collected in a single graph, and represented as function of the volume loss, with the product between the sliding distance and the normal load, to identify the conditions that produce similar wear mechanisms. To quantify the specific wear rate of the material a linear approach to Archard’s law was used. This law is given by Eq. (2). In this equation  $V$  represents the wear volume,  $k$  is the specific wear rate,  $N$  is the normal applied load and  $x$  is the sliding distance. Moreover, a statistical analysis was applied to estimate the error of measurements, as described elsewhere [22].

$$V = (\pi \times b^4) / (64 \times R) \tag{1}$$

$$V = k \times N \times x \tag{2}$$

Eq. (1) allows the approximate calculation of the wear volume of a spherical cup depression, with an implied assumption that the wear scar has a spherical geometry conforming to that of the ball bearing used. In order to elucidate users, an analysis of the error of Eq. (1) is given in Appendix A. Moreover, a correction factor is proposed to enhance the accuracy of this equation. The analysis carried out in Appendix A, showed that for  $b/R$  values up to 0.35 the equation assures an error lower than 1%.

### 3. Results

The micro-scale abrasion results for the different test conditions are shown in Fig. 4. Each graph plots the volume loss ( $V$ ) as function of the sliding distance ( $x$ ), for each normal load. The results of the tests performed with the lowest load (see Fig. 4(a)) reveal that there are no effective changes in the wear volume with the change in the concentration of abrasive slurry, especially for the scar produced with low sliding distance. Inversely, for the highest load (see Fig. 4(c)), the results show that the material volume loss increases with increasing concentration of abrasive and the difference is sharper for higher sliding distances. The tests conducted with an intermediary load (see Fig. 4(b)), displayed mixed behavior. The scars produced with the lowest concentration of abrasive slurry showed lower wear volume than those produced with higher concentrations of abrasive slurry (50% and 65% in volume), which displayed similar values of material volume loss. Moreover, it is observed that the wear volume

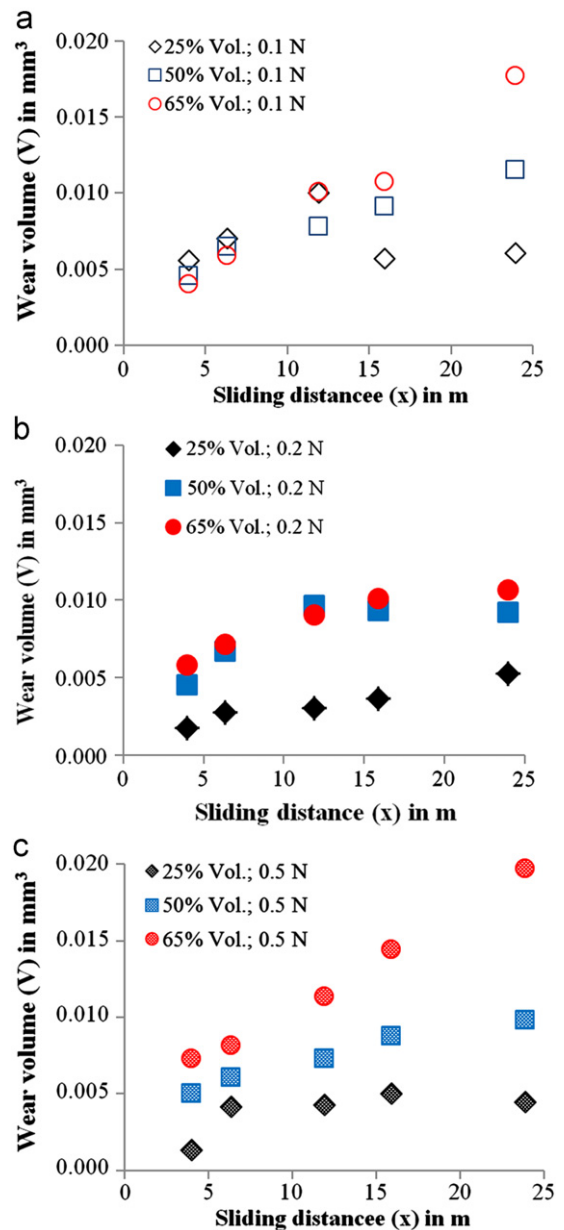
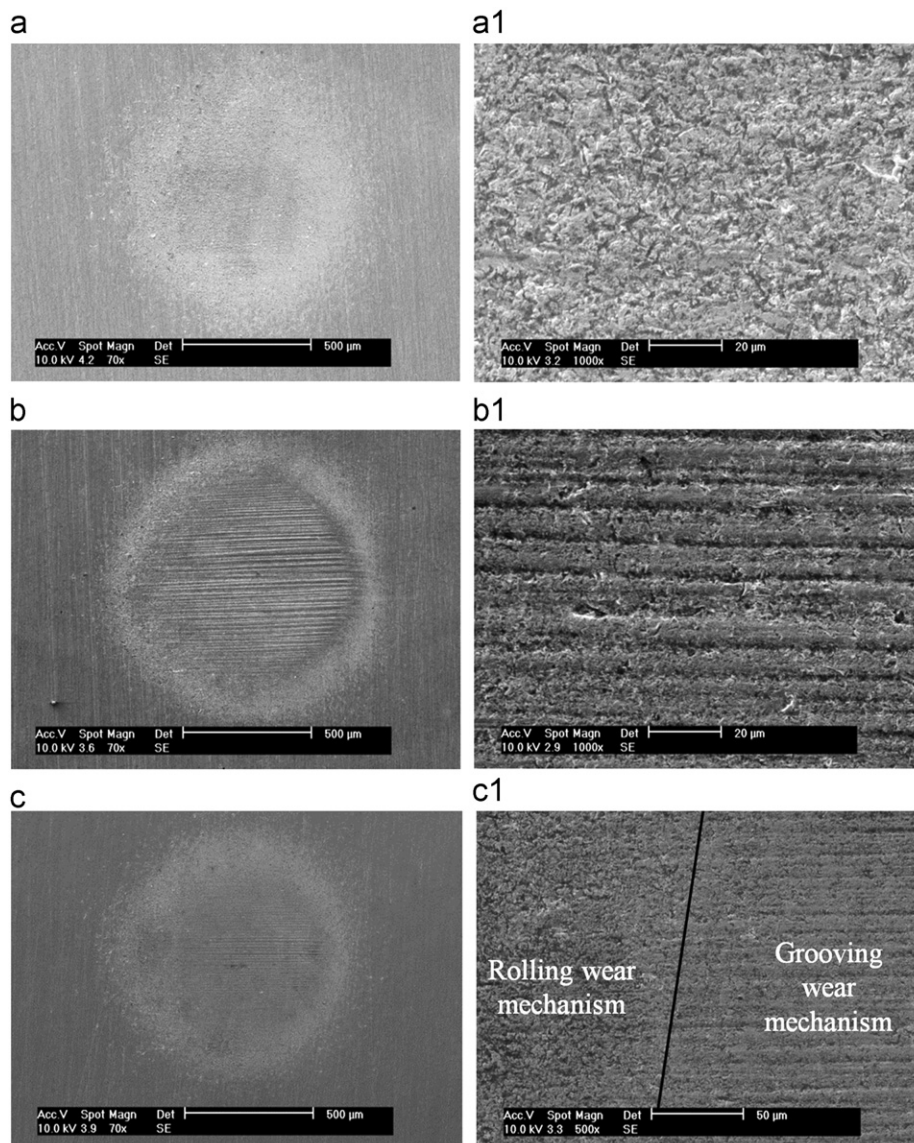


Fig. 4. Results of the micro-scale abrasion wear test for the different test conditions used.

stabilizes with increasing sliding distance, whatever the concentration of abrasive used. This behavior could be associated with two effects: the running-in effect [23] and the variation of the contact area/wear volume ratio throughout the duration of the test. According to Blau [23], the running-in behavior is the net result of simultaneous transitional processes occurring within the interface, which may lead to non-linear evolution of the wear for short sliding distances. Furthermore, at the start of the wear tests (with very small craters, consequently with small amounts of the radius of the spherical depression) it is well known that the area of the crater grows much faster than the volume; at that point, the rate of pressure reduction is greater than the rate of change in the volume, which may also justify the reduction in wear rate. In fact, the severity of contact index, proposed by Adachi and Hutchings [6], is inversely proportional to the crater area; therefore, a sudden increase in the area results in a reduction of the severity index, which will induce a change in the wear rate. The changes in the wear volume described above are only partially correlated with the test conditions, encouraging the investigation of the interactions between the abrasive slurry and the surface of the specimen in the contact zone. Scanning electron microscopy

analyses were conducted on different spherical cup depressions in order to identify the wear mechanism produced by the dissimilar test conditions.

Fig. 5 shows SEM micrographs of the dissimilar morphologies of the spherical cup depressions induced by different test conditions of the micro-scale abrasion tests. As these images show, two different wear mechanisms were identified, rolling abrasion (see Fig. 5(a)) and grooving abrasion (see Fig. 5(b)). Moreover, a combination of both wear mechanisms (see Fig. 5(c)) was also identified for several contact conditions. In order to facilitate identification of the wear mechanisms present in each worn surface, magnified images are shown in Fig. 5(a1)–(c1). Rolling abrasion is characterized by multiple indentations in the worn surface, (see Fig. 5(a1)), whereas grooving abrasion (see Fig. 5(b1)) is characterized by parallel grooves in the worn surface which results from the plastic deformation of the material. In turn, the surface morphology, which displays a mixed-mode (rolling and grooving abrasion), corresponds to a transition zone characterized by a mixture of grooves and indentations, as shown in Fig. 5(c1). The transition of rolling to grooving abrasion occurs due to the embedding of particles in the surface. In this case grooving starts



**Fig. 5.** SEM morphologies of the worn surfaces of the sample performed with the combination of load, volume fraction of abrasive and sliding distance of: (a) 0.5 N, 50% and 4 m, (b) 0.5 N, 50%, 16 m and (c) 0.1 N, 25%, 16 m. Magnification of the wear mechanism present in the wear scar of: (a1) Figure a), (b1) Figure b), (c1) Figure c).

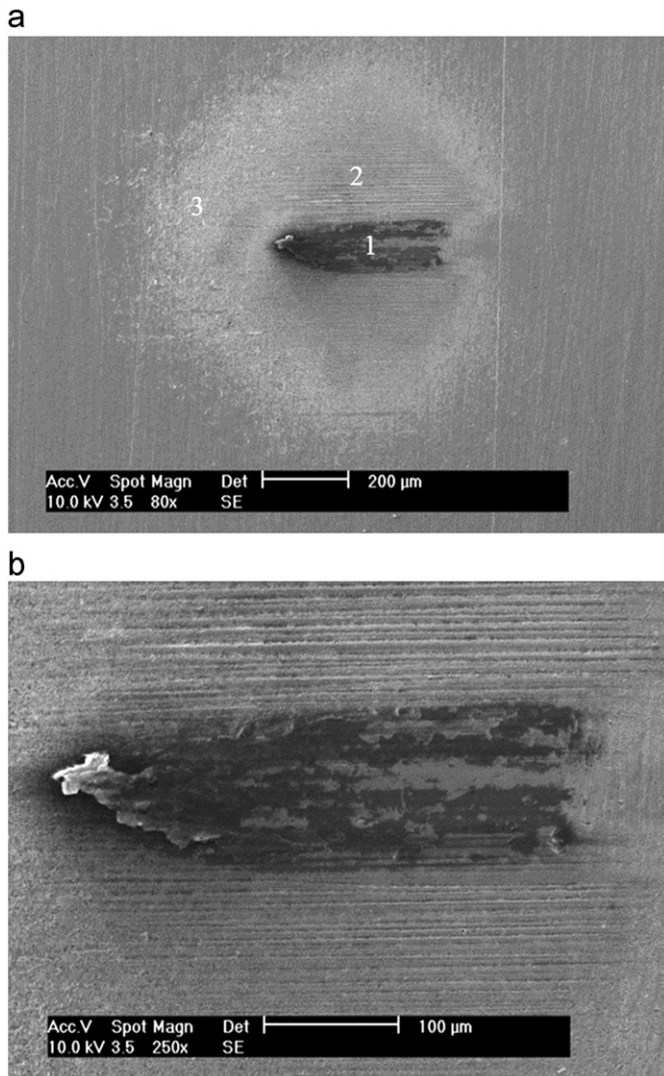


**Fig. 6.** (a) Scanning electron micrograph of the wear scar produced with 25% of volume fraction of abrasive, load of 0.5 N and a sliding distance of 6.4 m: 1–ridging wear mechanism zone, 2–grooving wear mechanism zone and 3–rolling wear mechanism zone. (b) Magnification of the ridging wear mechanism zone.

to occur in the zone of higher contact pressure, while rolling is more commonly located in the surrounding area of less pressure, as shown in Fig. 5(c). Furthermore, in the tests performed with 25 vol% abrasive and a load of 0.5 N, especially for the shorter tests, the wear scars displayed areas with ridge wear mechanism, as Fig. 6 shows. Normally, this wear mechanism occurs for high values of normal load when the abrasive particles are absent from the contact region and contact is made directly between the sphere and the specimen tested, leading to ridging marks in the surface [8], see zone 1 marked in Fig. 6(a). In this investigation the ridging points will be disregarded since, in this type of wear, the abrasive particles do not influence the formation of the wear scars and, therefore, the abrasion mechanism does not consider the effect of the abrasive slurry.

**4. Discussion**

Considering the cumulative effect of the normal load multiplied by the sliding distance ( $N \times x$ ) product, the wear map for the different test conditions was plotted on a wear volume against  $N \times x$  graph by identifying the regimes of interactions based on

SEM observations. As can be seen in Fig. 7, three well defined zones (rolling abrasion zone, grooving abrasion zone and a mixed-mode wear) can be perceived. The graph reveals that different combinations of test conditions can produce the same wear mechanism. Moreover, it is observed that for some combinations of concentration of abrasive slurry and load, the same wear mechanism is maintained even if the sliding distance is changed (conditions of (50 vol%; 0.1 N), (65 vol%; 0.1 N) and (25 vol%; 0.2 N)). In these cases the wear volume always increases with increasing sliding distance, even if the dominant wear mechanism is grooving or rolling abrasion. However, some conditions of abrasive slurry concentration and load are more prone to induce one type of wear mechanism even when changing the sliding distance. These changes are related to transitions in rolling to mixed-mode mechanism and mixed-mode to rolling wear mechanisms. For example, the wear scars produced with 25 vol% abrasive using a load of 0.1 N produces both rolling abrasion and the mixed-mode wear mechanism depending on the sliding distance. Table 2 summarizes the main wear mechanisms produced by the different test conditions. The rolling, grooving and rolling–grooving abrasion regimes are differentiated by using different symbols. The Table shows that low loads and high volume fraction of abrasive slurry enable three-body abrasion, while grooving abrasion becomes stable at high loads and low volume fraction of abrasive slurry. These last results are in good agreement with previous studies [6,18].

Archard’s model is a suitable way to estimate a parameter able to quantify the wear behavior of materials (the specific wear rate). However experimental results only fit the model well if a single wear mechanism occurs in all the tests. The results displayed in Fig. 7 show that different combination of test conditions can produce the same wear mechanism. So, in this study the experimental results were organized into two groups depending on the wear mechanism involved; rolling or grooving.

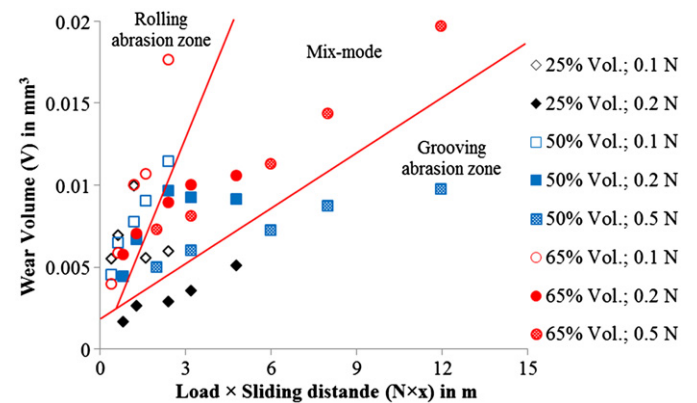


**Fig. 7.** Wear modes observed in the wear scars produced by the different test conditions.

**Table 2**  
Micro abrasion mechanism map as function of the % of volume fraction of abrasives and loads used.

% of volume fraction of abrasive	Load (N)		
	0.1	0.2	0.5
25	O	//	//
50	O	θ	//
65	O	θ	θ

O–Rolling wear mechanism, θ–Mixed-mode wear mechanism and //–Grooving wear mechanism

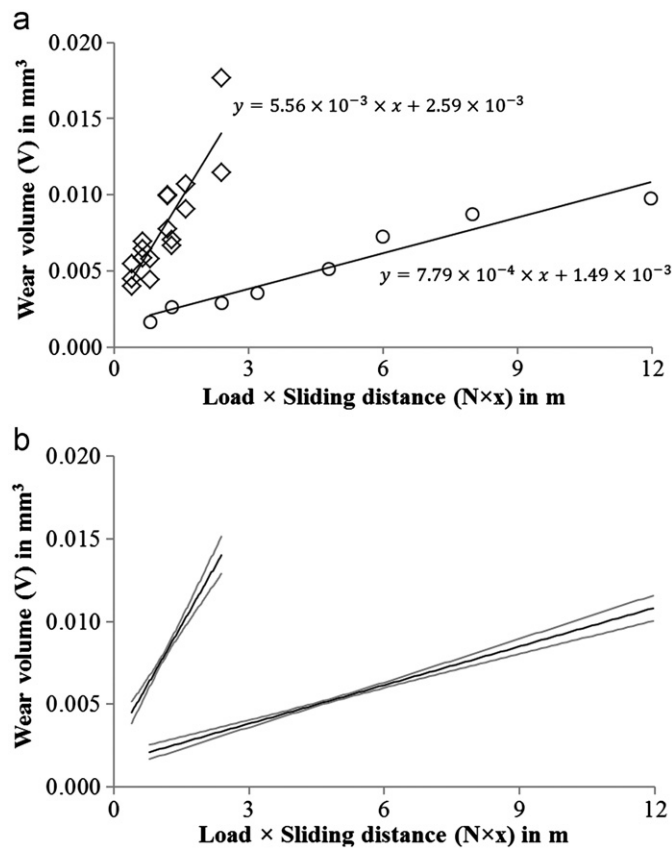


Fig. 8. (a) Results of the micro-scale abrasion wear test for the rolling and grooving wear points and (b) error bars of the specific wear rate for a confidence interval of 90%.

Table 3  
Results of the linearization analysis of the rolling and grooving zones.

	Specific wear rate, $k$ (mm <sup>3</sup> /N m)			$r^2$
	Average	STD	Confidence interval 90%	
Rolling zone	$5.56 \times 10^{-3}$	$7.15 \times 10^{-4}$	$4.03\text{--}7.09 \times 10^{-3}$	0.812
Grooving zone	$7.79 \times 10^{-4}$	$8.21 \times 10^{-5}$	$6.20\text{--}9.39 \times 10^{-4}$	0.937

Subsequently, Archard's model was applied to quantify the specific wear volume characteristic of each wear mechanism.

The micro-scale abrasion test results of the rolling and grooving abrasion points are shown in Fig. 8, as is the material volume loss function of the product of the sliding distance by the normal load. For each set of data, a straight linear trend was fitted to the points, obtaining the specific wear rate as the slope of the respective linear trend line, as shown by Eq. (2). A complete reliability analysis of the specific wear rate is summarized in Table 3 and, for each case, the confidence bands are plotted in Fig. 8(b) for a confidence level of 90%. The results show that the specific wear rate obtained from the rolling experimental data points is around one order of magnitude higher than in the corresponding grooving points. In fact, the rolling wear mode is a more effective wear mechanism than the grooving mode, leading to higher values of specific wear rate [5,18,24]. Furthermore, the reliability of results indicates that the correlation coefficient for the specific wear rate calculated from the rolling and grooving points is high, meaning that the quality of the linear fittings displayed in Fig. 8 is suitable. Therefore, according to

these results, the specific wear rate can be estimated using points produced with different test conditions, since a single wear mode is sustained. Furthermore, these results lead to the conclusion that the specific wear rate essentially depends on the wear mechanisms (rolling or grooving) involved and not on the tests conditions employed, since these do not produce changes in the wear mechanism.

## 5. Conclusion

- (i) In this investigation, silica slurry was used as an abrasive in micro-scale abrasion equipment to study the influence of different test conditions on the dominant wear modes of a Ni-based coating deposited by PTA on gray cast iron.
- (ii) The effect of different concentrations of abrasive slurry, sliding distances and normal loads on the micro-abrasion of a Ni-based coating were investigated and showed significant differences between micro-abrasion rates and wear mechanisms as a function of these parameters.
- (iii) The micro-abrasion mechanism maps were represented in terms of volume loss as a function of the sliding distance multiplied by the normal load. The results showed that different combinations of tests can produce the same wear mechanism. Low values of normal load and high contents of abrasive particles enable rolling abrasion, while grooving abrasion is stabilized at high loads and low volume fraction of abrasive slurry.
- (iv) The micro-scale abrasion results involving rolling and grooving abrasion data, based on calculations of the specific wear rate, revealed that this parameter can be successfully calculated using data points produced by dissimilar test conditions since they give rise to a single wear mode. This result led to the conclusion that the specific wear rate essentially depends on the wear mechanisms involved and not on the test conditions employed, since a single wear mode is sustained (grooving or rolling abrasion).
- (v) Abrasion by rolling wear induced a specific wear rate around one order of magnitude higher than the value obtained under grooving abrasion.

## Acknowledgments

The authors wish to express their sincere thanks to the company "Intermolde", for supplying the coated samples, and the Portuguese Foundation for the Science and Technology (FCT), through COMPETE program from QREN and to FEDER, for financial support in the aim of the project number "013545", as well as for the grant (SFRH/BD/68740/2010).

## Appendix A. Error analysis of the equation of the wear volume

This section aims to elucidate authors about the resultant error by using an approximate equation to calculate the volume of a spherical cup depression induced by the micro-scale abrasion tests.

The original equation used to calculate the volume of the spherical cup depression is given by the Eq. (A1), where  $b$  and  $h$  represent respectively the crater chordal diameter and the depth of the spherical cup depression (see Fig A.1). However, in micro-scale abrasion testing an approximate equation of Eq. (A1) is currently used (see Eq. (A2)). In this equation  $R$  represents the ball radius of the ball bearing used. The error of using an approximate

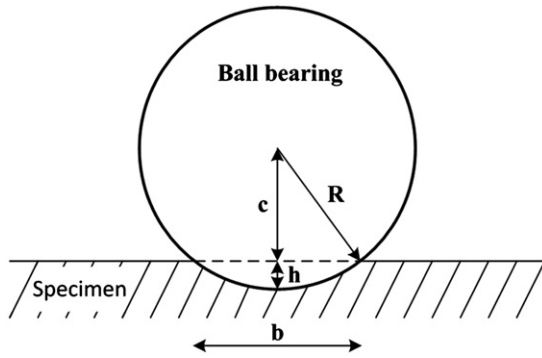


Fig. A.1. Schematic diagram of a crater induced by the micro-scale abrasion tests..

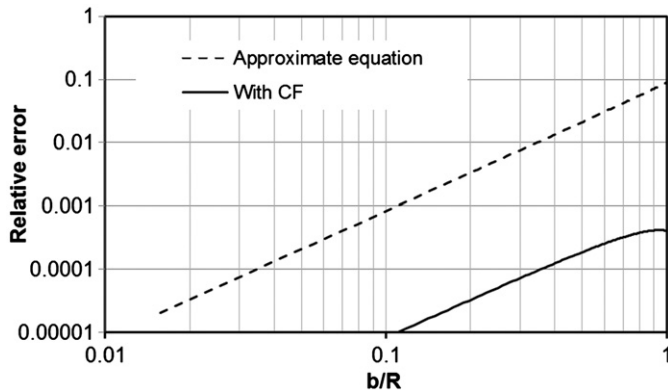


Fig. A.2. Error associated to the approximate equation to estimate the volume of a wear scar without and with corrective factor..

equation can be calculated by using Eq. (A3).

$$V = (1/6) \times \pi \times h \times (3 \times (b/2)^2 + h^2) \tag{A1}$$

$$V^* = (\pi \times b^4)/(64 \times R) \tag{A2}$$

$$\text{error} = (V^* - V)/V \tag{A3}$$

It is evident from Fig A.1 that increasing the depth  $h$  of the spherical cup depression increases the value of the chordal diameter  $b$  of the wear scar, until a maximum value of  $b$  equal to  $2R$  is reached. So, discretizing the value of  $b$  in small intervals it is possible to calculate the associated values of  $V$  and  $V^*$  for each relation between  $b$  and  $h$ . The value of  $h$  (given by Eq. (A4)), can be easily deduced by subtracting the value of  $c$  from the value of  $R$ , as represented in Fig A.1. The value of  $c$  is obtained by applying Pythagoras' Theorem at the triangle. Applying Eq. (A3) at the dissimilar combinations of  $b$  and  $h$  it is possible obtain the error associated by using an approximate equation to estimate the volume of a spherical cup depression induced by the micro-scale abrasion test. The results of the error are plotted in Fig A.2, dashed line, as function of the ratio between the crater's chordal diameter and the radius of the ball with the relative error associated. As can be seen in this figure, the resulting error is very small for low ratios of  $b/R$ , however with an increase in this ratio, the error increases. For example considering a spherical cup depression with a chordal diameter equal to the radius of the ball, the error committed in the calculations is about 10 percent.

$$h = R - (R^2 - (b/2)^2)^{1/2} \tag{A4}$$

The level of correlation between the ratios of the depth of the spherical cup depression and the ball radius with the error proved to be linear. So, according to this relationship it is possible to establish a

correction factor for a desired value of error. For example, for a desired error less than 1% a correction factor can be calculated as indicated by Eq. (A5). By manipulating the equation it is possible to determine the limits as a function of the ratio between  $b$  and  $R$  (see Eq. (A6)). Fig A.2 displays the error obtained when the approximate equation to estimate the volume of the wear scar is used, correction factor applied (continuous lines) and without the correction factor (dashed lines). As can be seen in the figure, the error of using the expression with the corrective factor is one hundred times smaller than that obtained with the expression without the corrective factor. Although, the correction factor gives more accurate results for low ratios between the chordal crater and the radius of the ball bearing, the approximate equation to evaluate the volume of a spherical cup depression is appropriate, due to the small error induced.

$$CF = \begin{cases} 1 & \Leftarrow (h/R) \leq 0.015 \\ 1/(1 - 0.66 \times (h/R)) & \Leftarrow 0.015 \leq (h/R) \leq 0.55 \end{cases} \tag{A5}$$

$$CF = \begin{cases} 1 & \Leftarrow (b/R) \leq 0.345 \\ 1/(1 - 0.66 \times (1 - (1 - (b/(2 \times R))^2)^{1/2})) & \Leftarrow 0.345 \leq (b/R) \leq 1.786 \end{cases} \tag{A6}$$

### References

- [1] K. Bose, R.J.K. Wood, Optimum tests conditions for attaining uniform rolling abrasion in ball cratering tests on hard coatings, *Wear* 258 (2005) 322–332.
- [2] A.J. Gant, M.G. Gee, A review of micro-scale abrasion testing, *Journal of Physics D: Applied Physics* 44 (2011) 073001.
- [3] M.F.C. Andrade, R.P. Martinho, F.J.G. Silva, R.J.D. Alexandre, A.P.M. Baptista, Influence of the abrasive particles size in the micro-abrasion wear tests of TiAlSiN thin coatings, *Wear* 267 (2009) 12–18.
- [4] T.S. Eyre, Wear characteristics of metals, *Tribology International* 9 (1976) 203–212.
- [5] D. Braga, A. Ramalho, P.N. Silva, A. Cavaleiro, Study of abrasion resistance of steels by micro-scale tests, in: P.M. Vilarinho (Ed.), *Advanced Materials Forum III*, Parts 1 and 2, Trans Tech Publications Ltd., Zurich-Uetikon, 2006, pp. 544–548.
- [6] K. Adachi, I.M. Hutchings, Wear-mode mapping for the micro-scale abrasion test, *Wear* 255 (2003) 23–29.
- [7] R.C. Cozza, D.K. Tanaka, R.M. Souza, Friction coefficient and wear mode transition in micro-scale abrasion tests, *Tribology International* 44 (2011) 1878–1889.
- [8] M.M. Stack, M. Mathew, Micro-abrasion transitions of metallic materials, *Wear* 255 (2003) 14–22.
- [9] R.J.K. Wood, Tribo-corrosion of coatings: a review, *Journal of Physics D: Applied Physics* 40 (2007) 5502–5521.
- [10] R.C. Cozza, J.D.B. de Mello, D.K. Tanaka, R.M. Souza, Relationship between test severity and wear mode transition in micro-abrasive wear tests, *Wear* 263 (2007) 111–116.
- [11] E. Rabinowicz, L.A. Dunn, P.G. Russell, A study of abrasive wear under three-body conditions, *Wear* 4 (1961) 345–355.
- [12] J.C.A. Batista, A. Matthews, C. Godoy, Micro-abrasive wear of PVD duplex and single-layered coatings, *Surface and Coatings Technology* 142–144 (2001) 1137–1143.
- [13] J.A. Williams, A.M. Hyncica, Mechanisms of abrasive wear in lubricated contacts, *Wear* 152 (1992) 57–74.
- [14] J.A. Williams, A.M. Hyncica, Abrasive wear in lubricated contacts, *Journal of Physics D: Applied Physics* 25 (1992) A81–A90.
- [15] F.J.G. Silva, R.B. Casais, R.P. Martinho, A.P.M. Baptista, Role of abrasive material on micro-abrasion wear tests, *Wear* 271 (2011) 2632–2639.
- [16] R.I. Trezona, D.N. Allsopp, I.M. Hutchings, Transitions between two-body and three-body abrasive wear: influence of test conditions in the microscale abrasive wear test, *Wear* 225–229 (1) (1999) 205–214.
- [17] M.M. Stack, M.T. Mathew, Mapping the micro-abrasion resistance of WC/Co based coatings in aqueous conditions, *Surface and Coatings Technology* 183 (2004) 337–346.
- [18] A. Ramalho, J.R. Pérez, Á.R. Garcia, Microabrasion resistance of nanostructured plasma-sprayed coatings, *International Journal of Surface Science and Engineering* 5 (2011) 250–260.
- [19] P.H. Shipway, J.J. Hogg, Wear of bulk ceramics in micro-scale abrasion—the role of abrasive shape and hardness and its relevance to testing of ceramic coatings, *Wear* 263 (2007) 887–895.
- [20] F. Fernandes, B. Lopes, A. Cavaleiro, A. Ramalho, A. Loureiro, Effect of arc current on microstructure and wear characteristics of a Ni-based coating deposited by PTA on gray cast iron, *Surface and Coatings Technology* 205 (2011) 4094–4106.

- [21] M.G. Gee, A.J. Gant, I.M. Hutchings, Y. Kusano, K. Schiffman, K.V. Acker, S. Poulat, Y. Gachon, J.v. Stebut, P. Hatto, G. Plint, Results from an inter-laboratory exercise to validate the micro-scale abrasion test, *Wear* 259 (2005) 27–35.
- [22] A. Ramalho, A reliability model for friction and wear experimental data, *Wear* 269 (2010) 213–223.
- [23] P.J. Blau, On the nature of running-in, *Tribology International* 38 (2005) 1007–1012.
- [24] K. Adachi, I.M. Hutchings, Sensitivity of wear rates in the micro-scale abrasion test to test conditions and material hardness, *Wear* 258 (2005) 318–321.



---

## Annex E

---

**F. Fernandes, T. Polcar, A. Loureiro, A. Cavaleiro, *Room and high temperature tribological behavior of Ni-based coatings deposited by PTA on gray cast iron*, (2014), under review, “Tribology International”.**



## Room and high temperature tribological behavior of Ni-based coatings deposited by PTA on gray cast iron

F. Fernandes<sup>1,\*</sup>, T. Polcar<sup>2,3</sup>, A. Loureiro<sup>1</sup>, A. Cavaleiro<sup>1</sup>

<sup>1</sup>CEMUC - Department of Mechanical Engineering, University of Coimbra, Rua Luís Reis Santos, 3030-788 Coimbra, Portugal.

<sup>2</sup>Department of Control Engineering Czech Technical University in Prague Technicka 2, Prague 6, 166 27 Czech Republic.

<sup>3</sup>n-CATS University of Southampton Highfield Campus SO17 1BJ Southampton, UK.

\*Email address: [filipe.fernandes@dem.uc.pt](mailto:filipe.fernandes@dem.uc.pt), tel. + (351) 239 790 745, fax. + (351) 239 790 701

### Abstract

In the present investigation the effect of the substrate dilution on room and high temperature (550 and 700 °C) tribological behavior of nickel based hardfaced coating deposited by plasma transferred arc onto a gray cast iron was investigated and compared to the uncoated gray cast iron. At room temperature, the wear loss of coatings was independent of the substrate dilution and similar to the gray cast iron. At high temperatures, coating produced with high dilution displayed the highest wear resistance between all the samples. This is attributed to the formation of a protective tribo-layer resulting from the agglomeration of a high amount of oxide debris due to its lower oxidation resistance when compared to the sample produced with low dilution.

Keywords: Plasma transferred arc, Ni-based alloy, Substrate dilution effect, Tribology, High temperature wear

### 1. Introduction

Cast irons and copper-alloys are commonly used in the production of glass molds and accessories for glass industry, owing to their excellent thermal conductivity and relatively low cost [1]. Molds are often exposed to severe conditions of abrasion, oxidation, wear, fatigue at high temperature, due to repeated contact with melted glass, causing deformation or failure of

parts and, thus, compromising the product quality and increasing the maintenance costs. To overcome this shortcoming protective coatings are normally applied at molds surfaces with the aim of increasing their lifetime in harsh environments [2, 3]. A wide diversity of coating materials have been successfully applied to protect the surface of these components, such as: cobalt, iron and nickel alloys [2, 4, 5]. The latter have been especially used due to their outstanding performance under extreme high temperature conditions [5-8]. Several hardfacing and thermal spraying processes have been used to coat the molds: (i) plasma transferred arc (PTA) and gas tungsten arc welding (GTAW), (ii) flame spraying (FS), high velocity oxy fuel (HVOF) and atmospheric plasma spraying (APS). Hardfacing processes have been preferentially used in the protection of mold surfaces because they promote a strong metallurgical bonding between the coating and the substrate, condition required to achieve high quality adherent coatings and to avoid the catastrophic failure in service, as opposed to thermal spraying processes where only a mechanical bonding is established. Among the hardfacing processes referred to above, PTA has been widely used to protect the surface of molds, since it produces high quality thick coatings, offering both optimal protection with minimal thermal distortion of parts and high deposition rates in single layer deposits [4, 5]. However, the properties and the quality of deposits are strongly dependent on the dilution of the substrate promoted by the PTA process. Low dilution provides coatings with similar chemical composition to the added metal powder, condition for achieving enhanced mechanical properties, wear and oxidation resistance [9]. To avoid adhesion problems and, therefore, not to compromise the performance of molds in service, it is common to increase the dilution through the change of the most relevant deposition parameters even if the mechanical properties, wear and oxidation resistance are diminished. In our previous studies [10, 12] the effect of increasing dilution, promoted by change of arc current on the structure, mechanical properties, oxidation resistance and wear behavior of a nickel-based alloy deposited onto a gray cast iron have been investigated. Regarding the wear behavior of coatings, ball cratering wear tester has been selected to reproduce the wear mechanism produced by the interaction between the melted glass and the surface of molds (three body abrasion). However, this equipment does not allow consider the high temperature effect. Hence, as a way to complement the previous studies, the aim of this investigation is to study the effect of increasing substrate dilution on the tribological performance at room and essentially at high temperature of as deposited Ni-based coating deposited onto gray cast iron, using a pin on disc tribometer apparatus. Comparison of these results with those achieved for the base material is also provided.

## 2. Experimental procedure

A nickel-based hardfacing alloy powder named Colmonoy 215 (from Colmonoy company) was deposited by plasma transferred arc using a Commercald Group ROBO 90 machine onto flat surfaces of gray cast iron blocks, currently used in the production of molds for the glass industry. Two different arc currents (100 and 140 amperes) were used on the depositions to produce coatings with two dissimilar levels of dilution. Hereinafter, the coatings deposited using 100 and 140 amperes will be designated as C100 and C140, respectively. Table 1 gives the optimized parameters used in the depositions, while Table 2 depicts the nominal chemical composition of the base material and Colmonoy 215 powder. Before coating, the substrate blocks were preheated at 480 °C to reduce the cooling rate and therefore to avoid the susceptibility to cracking during deposition. Using the same deposition conditions, several weld beads, each with approximately 3 to 5 mm thick, were deposited in parallel on the cast iron, ensuring some overlapping between them in order to obtain a 35×35 mm coated surface area and a quasi-flat surface. Specimens containing cast iron and coating were removed from each block for microstructural and micro-hardness analysis. Further, specimens with dimension of 20×20×5 mm were removed from each block for tribological testing. The coated surfaces were first machined to provide flatness and then grinded and polished following standard procedures to obtain a uniform roughness of about 0.51 – 0.62 μm.

The tribological behavior of the coatings and gray cast iron was evaluated at room and high temperatures using a pin-on-disk tribometer. As the operating surface temperature of molds is currently in the range of 500 - 900 °C, temperatures of 550 and 700 °C were selected to perform the experiments. Although in the real working conditions of molds glass acts as an abrasive material, due to its melted state at high temperature, for the tribological tests we have selected as counterpart a harder and more resistant material: Al<sub>2</sub>O<sub>3</sub> balls. Thus we ensure that the wear volume loss of coatings will be overestimated in relation to the expected loss in actual service conditions. All the wear tests were conducted at a constant linear speed of 0.10 m.s<sup>-1</sup>, a load of 5 N, a relative humidity of 48±5%, and 5000 cycles. The radius of the wear tracks was set to 5.3 mm. During the tests, the friction coefficient was continuously recorded. Two tests were performed under identical conditions for each coating. After tribological tests, the wear rate of the coatings was determined from the cross section wear track area using a 3D optical profilometer and the wear tracks and wear debris were characterized by scanning

electron microscopy with energy dispersive X-ray spectroscopy (SEM-EDS) and by Raman spectroscopy.

Table 1 – Main deposition parameters.

	Main arc current (A)	Powder feed rate (rpm)	Travel speed (mm/s)	Powder feed gas flow rate (l/min)	Plasma gas flow rate (l/min)	Shielding gas flow rate (l/min)	Torch work distance (mm)	Oscillation (mm)	Preheat temperature °C
C100	100	20	2	2	2.2	20	13	4	480
C140	140	20	2	2	2.2	20	13	4	480

Table 2 - Nominal chemical composition (wt.%) of the gray cast iron and nickel-based alloy powder.

Base material	C	Mn	Si	P	S	Cr	Ni	Mo	V	Ti	Fe
Gray cast iron	3.60	0.60	2.00	< 0.20	< 0.04	< 0.20	< 0.50	0.50	0.10	0.20	Balance
Hardfacing			C	Cr	Si	B	Fe	Al	F	Co	Ni
Ni-alloy			0.14	2.45	2.56	0.86	1.08	1.30	0.01	0.08	Balance

### 3. Results and discussion

#### 3.1. Microstructure, composition and hardness of the as deposited coatings

The typical microstructure of gray cast iron and coatings produced with 100 and 140 A is depicted in Fig. 1. Both coatings display relatively dense microstructure with excellent adhesion to the substrate, free of microcracks and only a few solidification voids. Their typical microstructure consists of dendrites of Ni-Fe solid solution phase aligned along the direction of heat flow. Flakes of carbon (dark-floret like phase) randomly distributed in the matrix can be perceived too, being more notorious on C140 coating. The high amount of dark-floret phase on C140 coating is in good agreement with the observed increase of dilution with increasing arc current. Following the procedure described in reference [11], dilutions of ~28 and ~59% were measured for C100 and C140 coatings, respectively. The dilution is beneficial in terms of improving the adhesion, but it can bring some disadvantages, such as change in the hardness and chemical composition, and lowering of wear and oxidation resistance of the coatings [9]. The chemical composition of coatings, assessed by SEM-EDS given in Table 3, were evaluated from the average of several measurements performed on an area 400×400 μm in the cross section at middle thickness of each coating. This procedure was used to ensure that the chemical composition was determined in a representative volume of material in that zone, thus avoiding problems that punctual analyses can give in heterogeneous materials. The

results show that the main differences were in the iron, silicon and carbon contents, in good agreement with the different dilutions in the samples. The gray cast iron shows flakes of graphite evenly distributed in a ferritic matrix.

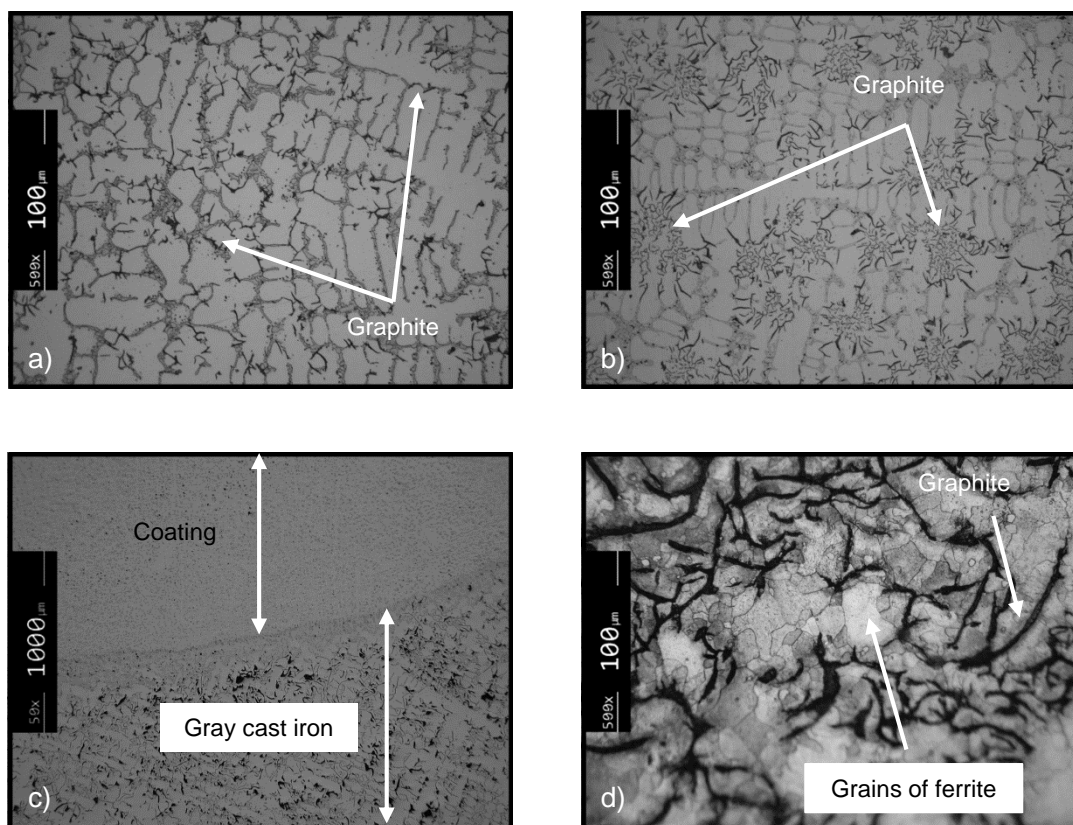


Figure 1 - Optical micrograph of: a) C100 coating, b) C140 coating, c) interface between coating and substrate of C140 coating, d) gray cast iron.

Table 3 - Nominal chemical composition (wt.%) of coatings evaluated by SEM-EDS.

Coating	wt. % of elements					
	Ni	Fe	C	Si	Al	Cr
C100	85.40	8.47	0.30	2.17	0.81	2.86
C140	55.71	37.73	1.26	2.52	0.62	2.16

Fig. 2 shows the Vickers hardness profiles across the interface of the deposited coatings, measured with 5 N applied load. As it would be expected, the increase in the weld current, and therefore increase in dilution, gives rise to a decrease of the hardness either in the coating, undesirable in terms of wear, or in the heat affected zone (HAZ), which is favourable in terms of toughness of this region. The average surface hardness of coatings C100, C140 and gray cast iron was 300, 195 and 150 Vickers ( $HV_{0.5}$ ), respectively. The high hardness of the HAZ zone in relation to the non-thermal affected based material is related to the formation of hard and brittle phases. The detailed characterization of the microstructure of each coating

and the hardness variations with increasing dilution can be found in a previous publication of the authors [11].

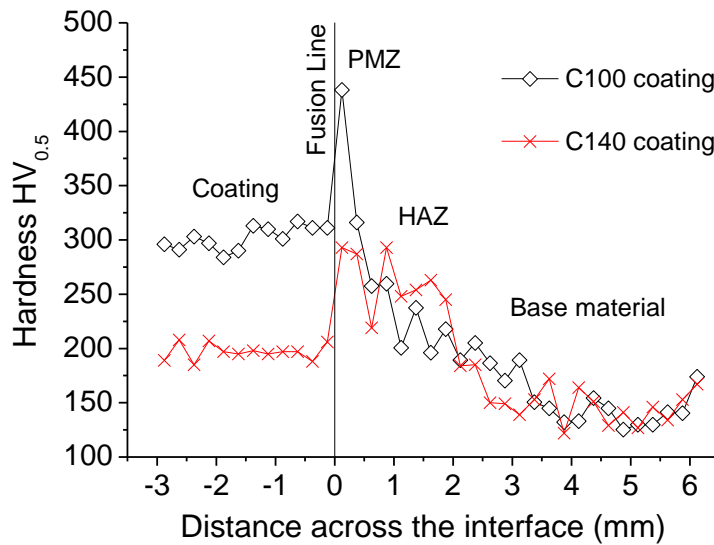


Figure 2 - Hardness profile across the interface of C100 and C140 coatings.

## 4. Tribological behavior of coatings

### 4.1. Wear rate

Figure 3 shows the wear loss rate of coatings and gray cast iron tested at different temperatures. It clearly shows that at room temperature the wear loss of coatings and gray cast iron is very low, and almost independent of the substrate dilution. C100 coating displays a little higher wear resistance than C140 coating, in agreement with its higher hardness. The observed similar level of wear rate of the gray cast iron as compared to the Ni coatings at RT is due to its higher amount of graphite that can act as solid lubricant, leading to a less volume loss of material. It should be pointed out that the low hardness displayed by the gray cast iron compared to the coated samples is compensated by the presence of graphite on the sliding contact [13, 14].

At temperature of 550 °C an abrupt increase of the wear rate of coatings was observed; however, it dropped with further increase to 700 °C. The first increase of the wear rate can be attributed to the spontaneous oxidation, while, as it will be seen later, following decrease of wear loss at 700 °C could be related to the formation of high amount of oxides on the wear track preventing further wear of the coatings. Besides, coating produced with high dilution displayed much higher wear resistance at elevated temperatures than C100 coating. This



behavior is a result of the low oxidation resistance of C140 coating that will contribute to the formation of a high amount of oxides in the contact zone. A continuous increase of the wear rate with increasing temperature was observed for the gray cast iron. This material showed much higher wear rate than the Ni-based coatings, indicating that the latter should perform better at high temperature. This is an expected result since rapid loss of the material mechanical strength and increasing oxidation rate with temperature are typical of gray cast iron.

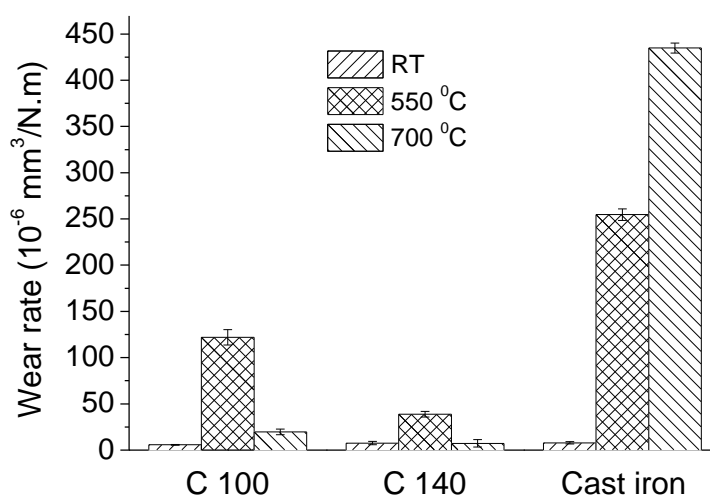


Figure 3 - Variation of the wear rate of coatings and gray cast iron with test temperature.

#### 4.2. Friction coefficient

The evolution of the friction coefficient of coatings and gray cast iron with increasing test temperature is shown in Figure 4. As expected, all the friction curves displayed two distinct regions: running-in stage and steady state stage. At RT, the running-in stage for both Ni-based coatings is similar and characterized by strong increase of the friction coefficient to the highest value of 0.74, followed by rapid decrease down to 0.41, after the first 1000 laps. On the other hand, in gray cast iron, friction coefficient slightly increased over time reaching the steady state after 4000 laps with a friction coefficient of about 0.39. Gray cast iron exhibited relatively low friction coefficient at RT as compared to the Ni-based alloys. According to the literature [13, 14], this behavior is related to the presence of graphite on the worn surface that acts as a solid lubricant compensating the lower hardness displayed by the material and thus leading to wear rate values similar to Ni-based coatings.

A long running-in period was also noticed with a progressive increase of the friction coefficient for the gray cast iron when the temperature was 550 °C; however, friction was much higher suggesting different contact conditions. Ni-based coatings displayed very short running-in periods with friction stabilized at similar values as in RT tests. Finally, the tests at 700 °C exhibited different trends between cast iron and coatings. In the first case, a small decrease in the final friction coefficient value was achieved whereas an inverse situation was observed for coated samples, with friction stabilized at values of approximately 0.6 and 0.65 for C100 and C140 coatings, respectively. Such trends suggest that different contact conditions should have been taking place in both situations.

In many cases, especially at high temperatures, the friction curves displayed quite unstable values. According to Kesavan and Kamaj [15], such behavior demonstrates the presence of tribolayer on the sliding surfaces; the tribolayer is continually worn out and formed again, which results in short-term friction coefficient oscillations.

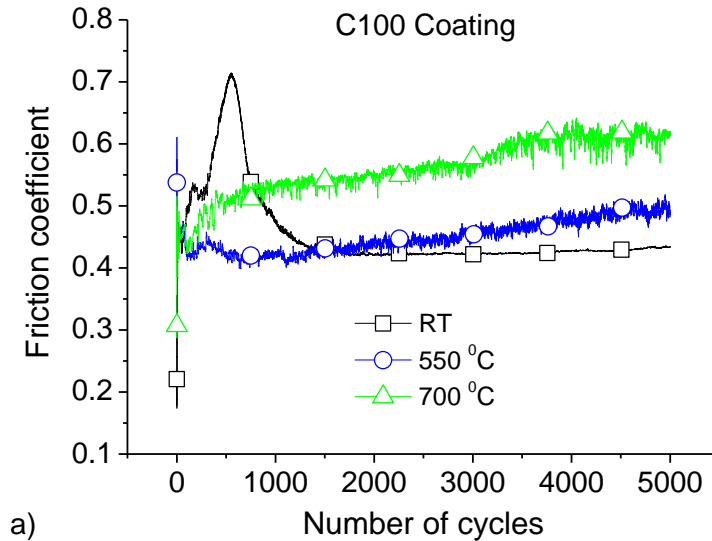


Figure 4 - Friction coefficient evolution with increasing test temperature of: a) C100 coating, b) C140 coating, c) gray cast iron.

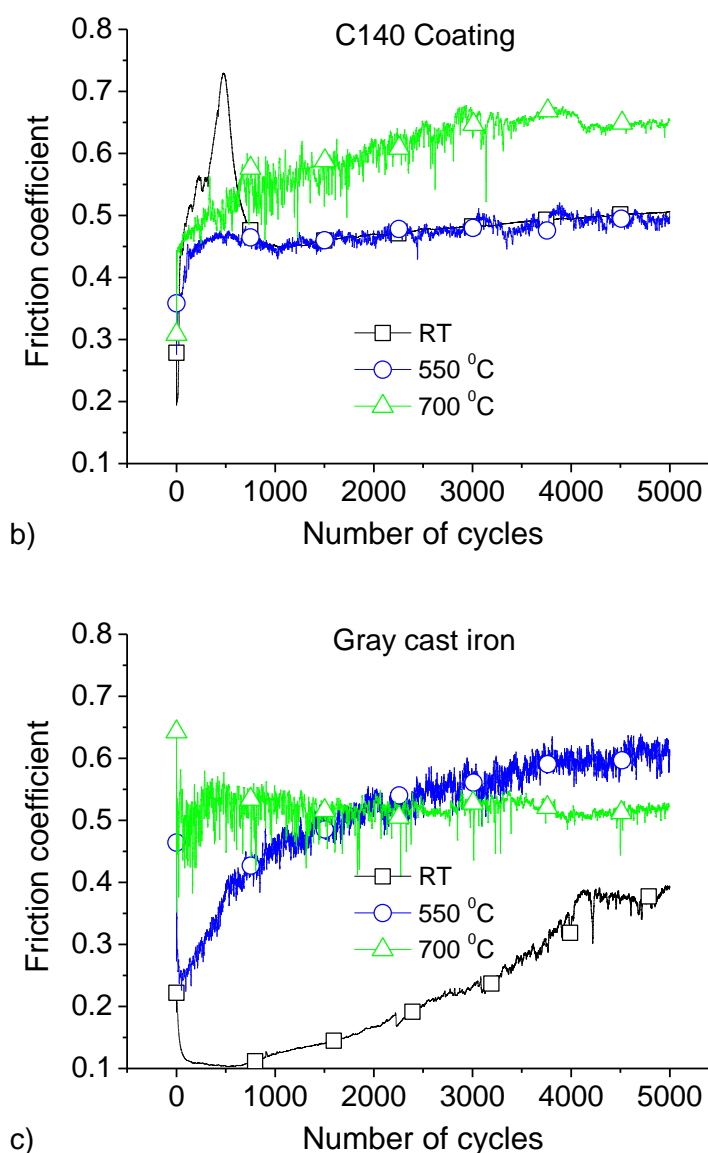


Figure 4 (continued).

#### 4.3. Wear mechanisms and surface analysis of coatings

The changes of the wear rates and friction coefficients described above can be attributed to a great number of factors, such as the chemical composition, physical properties of materials, or applied test conditions. Therefore, the investigation of the interaction between the specimen-counterpart pair was carried out. Scanning electron microscopy with energy dispersive X-ray spectroscopy (SEM-EDS) and Raman spectroscopy were used to characterize the dominant wear mechanisms and the wear debris originated by the tribological testing.

#### 4.3.1. Worn surfaces at room temperature

Typical SEM micrographs in secondary electrons of the worn surface of coatings and gray cast iron tested against  $\text{Al}_2\text{O}_3$  balls at RT are depicted in Figure 5. The wear tracks of Ni-based coatings are similar; they present a rough morphology with evidence of tribo-oxidation. The oxide adhered layer is cracked, which reveals its brittle nature. Raman spectra performed at the oxidized worn surface of the coatings (see spectra a) and b) in Fig. 6 for C100 and C140 coatings, respectively) confirmed the presence of the oxides, namely Raman active modes assigned to Ni-O [16] and C [17]; the latter almost inexistent in C100 sample spectrum as a consequence of its much lower dilution. These results are in good agreement to EDS analysis (see Fig. 5 d) for C100 coating as an example), which showed essentially strong signals of Ni and O; vestiges of Fe, Si, Al and C were also detected. Similar wear debris was found on the wear scars of the balls too. During the wear tests the friction, generated by the sliding of the ball against the coating surface, causes the increase of the local temperature, mainly in the protuberances contact, promoting the tribo-oxidation of the surface. During this phase, the metal-ceramic contact will progressively decrease with more and more surface being covered by an oxide phase. With the test running, the oxide tribo-layer will grow and the contact shall be governed between this growing tribo-layer and the counterpart, until a steady state will occur. Metal-ceramic contact gave rise to a higher friction coefficient that should decrease until a constant and lower value corresponding to the same oxide, NiO as shown by Raman spectroscopy, formed on the top surface. It explains the similar level of wear resistance and friction values of the coatings even despite of their discrepancy in hardness and chemical composition due to different dilution levels. The high hardness of the metallic coatings, in conjunction with the protective effect of the hard NiO oxide, led to very low wear volumes.

Distinct wear behavior was found for the gray cast iron. Its wear track displays a very clean surface with fine scratches parallel to the relative sliding movement (suggesting abrasion wear mechanism) and some adherent wear debris. Further, in some places, black regions can be noticed, which can be attributed to either the presence of graphite or its pull-out from the material [18]. EDS analysis performed at the wear debris revealed that they represent a mixture of original and oxidized material, including a weak signal from graphite lamellas. Similar phases were detected on clean worn surface, although C peak was much more intense there. Raman spectroscopy analysis showed the presence of hematite ( $\alpha\text{-Fe}_2\text{O}_3$ ) [19] and nanocrystalline graphite through the characteristic D and G bands [20] (see spectrum c) and d) of Fig. 6 for wear debris and clean surface, respectively). During sliding

experiments the movement of the ball promotes the wear of surface specimen with production of both oxide and graphite debris. Graphite will act as a solid lubricant in tribo-film, promoting a decrease of friction coefficient and having, indirectly, an important impact on the wear [13, 14]. As a consequence, similar level of wear resistance was observed between base material and coatings, in spite of the lower hardness of gray cast iron.

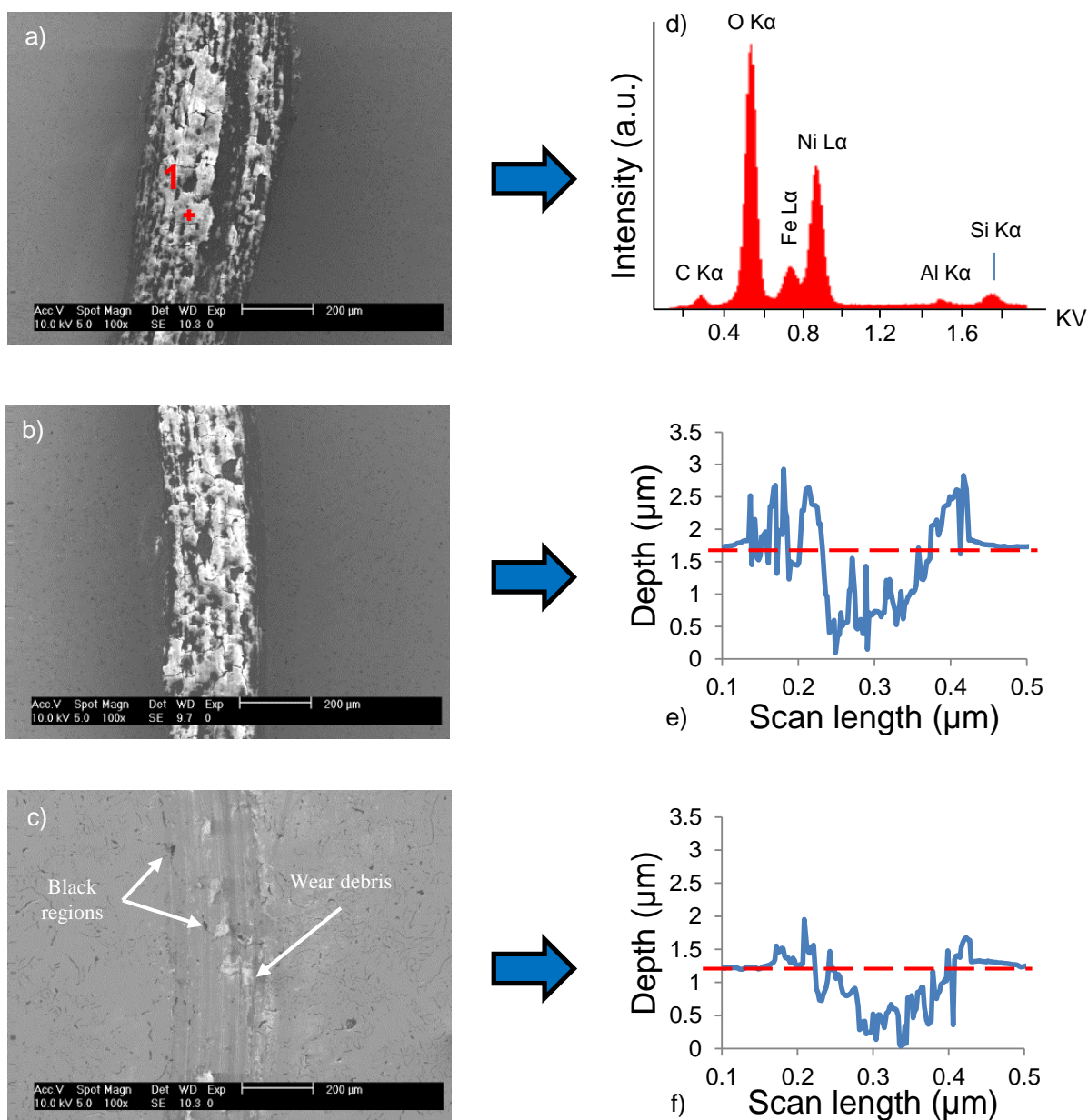


Figure 5 - SEM morphology in secondary electrons of worn surface of: a) C100 coating, b) 140 coating, c) cast iron; all tested at room temperature. d) SEM/EDS spectra of point 1 marked in Fig. 5 a). e) and f) wear track profiles of: C140 coating, and gray cast iron, respectively.

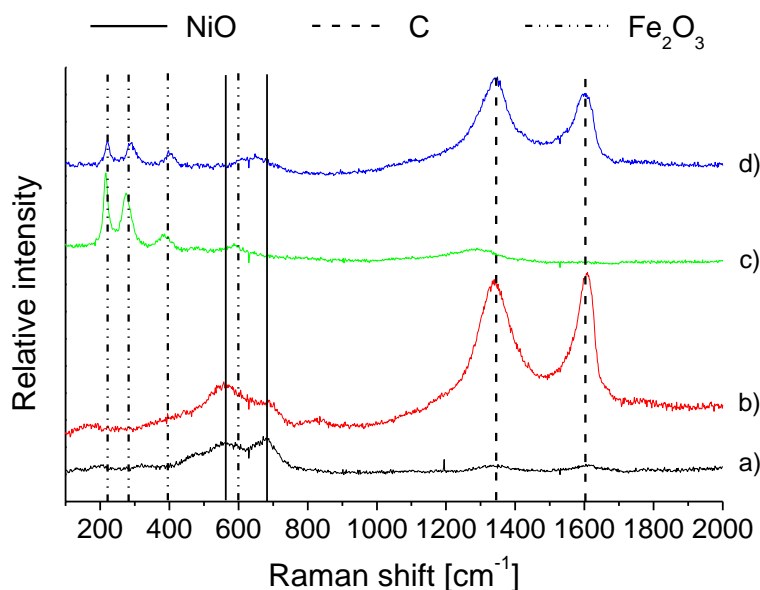


Figure 6 - Typical Raman spectra performed on the worn surface of: a) C100 coating tested at RT, b) C140 coating tested at RT, c-d) adherent wear debris and clean surface of gray cast iron, respectively, tested at room temperature.

#### 4.3.2. High Temperature

When sliding occurred at 550 °C, C100 and C140 coatings also showed oxides on the contact surface. However, C140 wear track was almost fully covered whereas C100 exhibited an irregular surface with a mixture of clean wear zones and oxidized ones with signs of adhesive and abrasive wear (see Fig. 7 a-b), suggesting an incomplete formation of an oxide transfer layer. The difference between the two samples can be interpreted considering their oxidation behavior. In fact, C100 sample oxidizes through the formation of a protective mixture of oxides based on B / Si over a Ni-based oxide layer [10]. Although these oxides are protective in static oxidation conditions, B-oxide melts below 600 °C [21, 22], which leads to its easy removal hindering the formation of a stable oxide layer over the surface. As the process requires some time, since temperatures are still low being oxidation rates reduced [10], the destruction of the growing oxide layers is relatively easy and the formation of a transfer layer is limited due to the dragging effect caused by the ball sliding and melted B-oxide. Therefore, high wear volumes are expected and indeed the steep increase in the wear rate can be noticed in Fig. 3. In the case of C140 sample, besides Ni-based oxides, iron oxide is also formed during oxidation at these temperatures [10]. The oxidation rates are much higher compared to C100 sample due to higher dilution. Therefore, a higher amount of oxide debris can be produced facilitating the formation of a continuous oxide transfer layer. The surface is thus protected quickly and, in spite of the much higher wear rate in comparison to

RT test, the wear resistance is higher than that for C100 sample. Raman analysis performed at the adhesive wear debris on C100 coating indicated that they were mainly Ni-O, although, according to the EDS analysis, Fe-O, Si-O and Al-O should also coexist in much less amount. It is in good agreement to our previous work on the oxidation behavior of this coating [10]. At the clean zone (bottom part) of the worn surface EDS showed non-oxidized coating material. For C140 coating, Raman analysis showed similar oxides but, in this case, a significant amount of iron oxides (hematite and magnetite ( $\text{Fe}_3\text{O}_4$ )) were also detected, in good agreement to higher level of dilution and to the oxidation studies where this oxide was found to be the main constituent of the oxide scale [10]. Additionally, strong signals of C-based phases were detected by EDS.

Gray cast iron was fully covered with an oxide layer at this temperature, with scratches parallel to the movement of the sliding. The main oxides identified in the wear track were hematite and magnetite (see Raman spectrum c) of Figure 8). The softening of the material, induced by the temperature increase, together with the total depletion of graphite from the track surface justify the sharp increase in the wear rate, as well as the increase in the friction coefficient in comparison to results at RT.

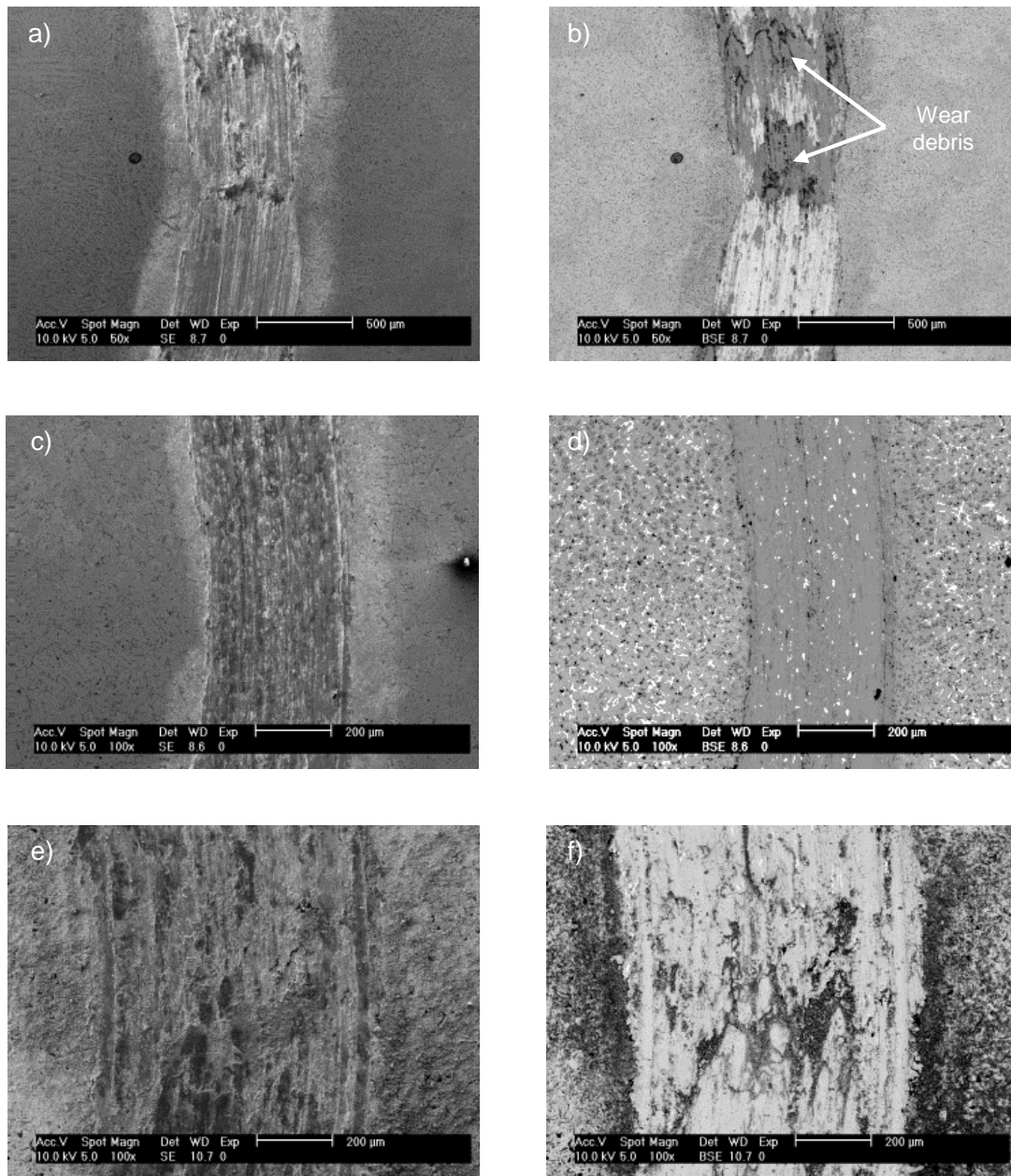


Figure 7 - SEM morphology in secondary and backscattered electrons of worn surface of: a-b) C100 coating, c-d) 140 coating, e-f) cast iron; all tested at 550 °C.



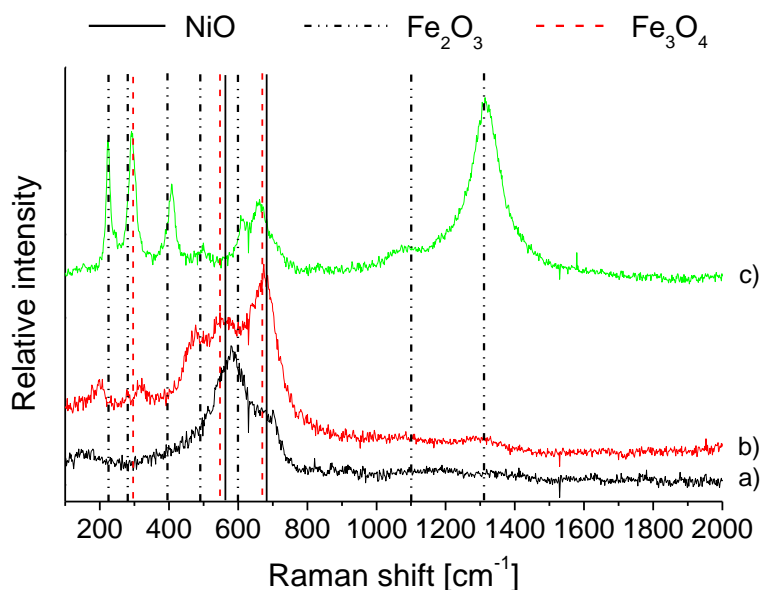


Figure 8 - Raman spectra performed on the worn surface of: a) C100 coating tested at 550 °C, b) C140 coating tested at 550 °C, c) gray cast iron tested at 550 °C.

At 700 °C the oxidation rate of Ni-based coatings increased significantly allowing rapid and easy formation of a continuous oxide layer on the worn surfaces (see Fig. 9). The oxide acts as a protective layer decreasing the wear loss of coatings. As the major wear volume loss is produced during the formation of the protective oxide layer, faster production of tribolayer decreased the wear rate in relation to 550 °C testing (see Fig. 3). Similar results were achieved and in detail explained by Kesavan et al. [15]. Furthermore, since the oxidation rate of C140 coating is higher than that of C100 coating, the latter will take more time to form the oxide layer generating a higher coating wear volume in the initial stage of the wear process. As a consequence, total wear rate after the test will be higher as well. Raman analysis of the wear tracks of both coatings showed the presence of Ni-O (see spectra a) and b) of Fig. 10); moreover, iron oxides were identified in C140 coating.

On the other hand, gray cast iron oxidizes easily but the oxide does not support the sliding process and does not protect efficiently the base material. The increase in the temperature promotes a severe softening of the material and a high oxidation rate leading to a strong abrasion and, therefore, a very high wear loss. Raman analysis confirms the extensive formation of hematite in the wear track (spectra c) of Fig. 10); signs of magnetite were also detected.

In summary, although dilution reduces the hardness of coatings, it has beneficial effect at high temperature tribological behavior due to the faster formation of an oxide layers (owing to its less oxidation resistance) which protect the coating surface against wear.

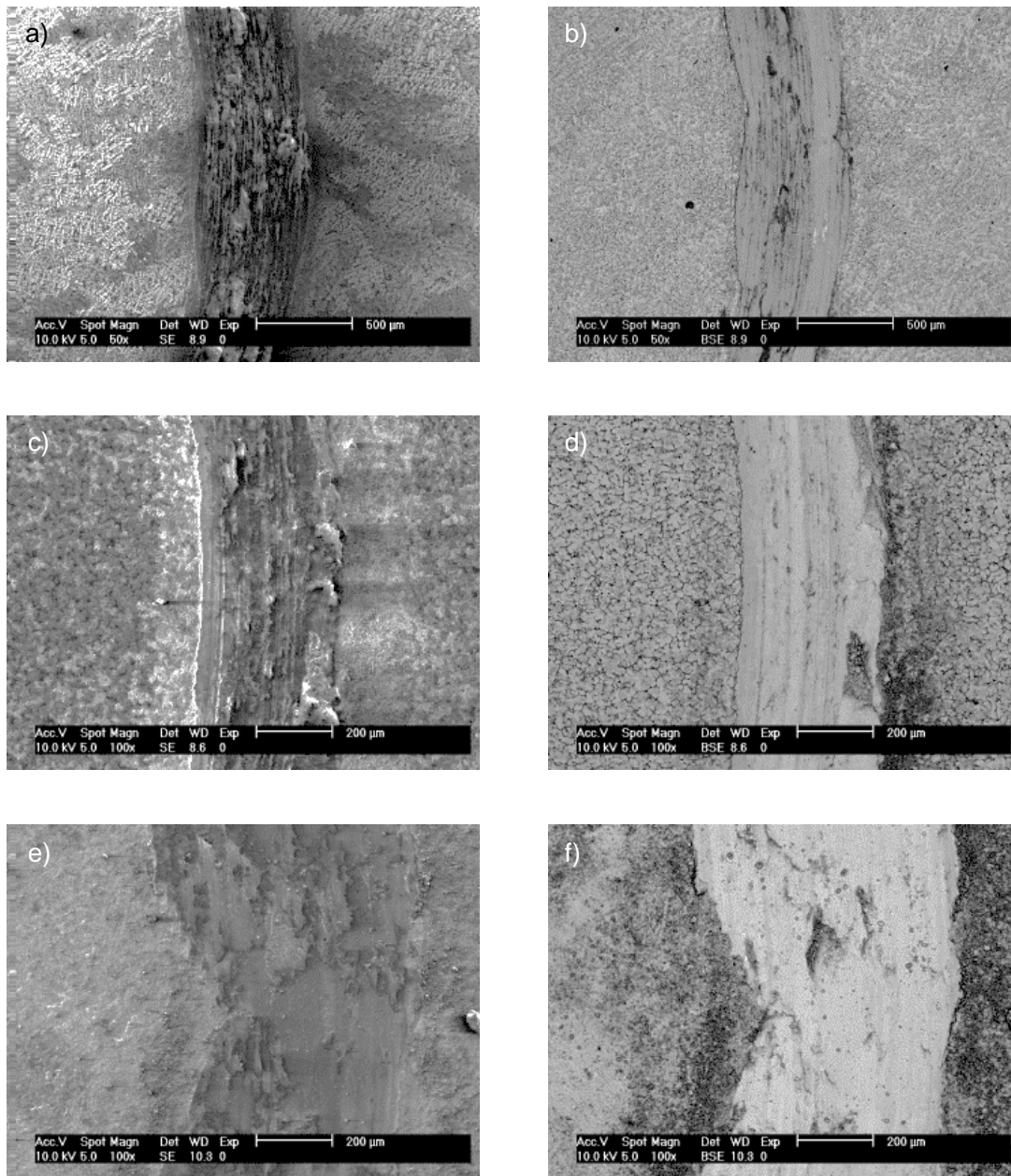


Figure 9 - SEM morphology in secondary and backscattered electrons of worn surface of: a-b) C100 coating, c-d) 140 coating, e-f) cast iron; all tested at 700 °C.

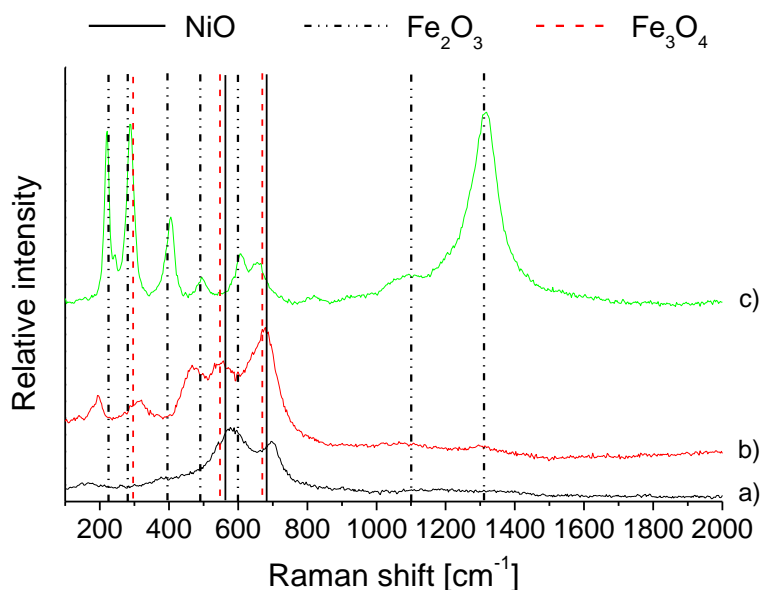


Figure 10 - Raman spectra performed on the worn surface of: a) C100 coating tested at 700 °C, b) C140 coating tested at 700 °C, c) gray cast iron tested at 700 °C.

## Conclusions

Nickel based hardfaced coating deposited by plasma transferred arc on gray cast iron with two dissimilar levels of dilution, were tribologically tested at room and high temperatures and compared to uncoated gray iron. The results showed that the wear loss of the coatings was independent of the substrate dilution at room temperature; tribo-oxidation was the main wear mechanism. Despite its lower hardness, gray cast iron showed similar wear rate as Ni-based coatings due to the lubricious effect of a C tribo-layer formed on the sliding surfaces. Increase sliding test temperature to 550 °C led to an abrupt increase of the wear rate of the coatings and the gray cast iron due to the material softening and oxidation. Gray cast iron showed extremely high wear values due to the continuous removal of the oxides, which exposed the soft non-oxidized material. Ni-O based layer protected more efficiently the Ni-based coatings. Further increase in test temperature to 700 °C led to the improvement of the wear resistance of coatings and an intensification of the wear on gray cast iron. The coating produced with the highest dilution displayed the highest wear resistance at elevated temperatures. This behavior was related to its lower oxidation resistance, which promoted the easier formation of high amounts of oxide wear debris and their agglomeration into compact oxide tribolayer acting as protection of wearing surfaces.

## Acknowledgments

This research is sponsored by FEDER funds through the program COMPETE – Programa Operacional Factores de Competitividade – and by national funds through FCT – Fundação para a Ciência e a Tecnologia –, under the projects PTDC/EME-TME/122116/2010, PEst-C/EME/UI0285/2013 and CENTRO -07-0224 -FEDER -002001 (MT4MOBI), as well as the grant (SFRH/BD/68740/2010).

## References

- [1] Cingi M, Arisoy F, Basman G, Sesen K. The effects of metallurgical structures of different alloyed glass mold cast irons on the mold performance. *Mater Lett*. 2002;55:360-3.
- [2] Luo L, Liu S, Li J, Yucheng W. Oxidation behavior of arc-sprayed FeMnCrAl/Cr3C2-Ni9Al coatings deposited on low-carbon steel substrates. *Surf Coat Technol*. 2011;205:3411-5.
- [3] Vaßen R, Jarligo MO, Steinke T, Mack DE, Stöver D. Overview on advanced thermal barrier coatings. *Surf Coat Technol*. 2010;205:938-42.
- [4] Gatto A, Bassoli E, Fornari M. Plasma Transferred Arc deposition of powdered high performances alloys: process parameters optimisation as a function of alloy and geometrical configuration. *Surf Coat Technol*. 2004;187:265-71.
- [5] Siva K, Murugan N, Logesh R. Optimization of weld bead geometry in plasma transferred arc hardfaced austenitic stainless steel plates using genetic algorithm. *Int J Adv Manuf Technol*. 2009;41:24-30.
- [6] Guo C, Zhou J, Chen J, Zhao J, Yu Y, Zhou H. High temperature wear resistance of laser cladding NiCrBSi and NiCrBSi/WC-Ni composite coatings. *Wear*. 2011;270:492-8.
- [7] Gurumoorthy K, Kamaraj M, Rao KP, Rao AS, Venugopal S. Microstructural aspects of plasma transferred arc surfaced Ni-based hardfacing alloy. *Materials Science and Engineering: A*. 2007;456:11-9.

- [8] Li W, Li Y, Sun C, Hu Z, Liang T, Lai W. Microstructural characteristics and degradation mechanism of the NiCrAlY/CrN/DSM11 system during thermal exposure at 1100 °C. *J Alloys Compd.* 2010;506:77-84.
- [9] Balasubramanian V, Lakshminarayanan AK, Varahamoorthy R, Babu S. Application of Response Surface Methodology to Prediction of Dilution in Plasma Transferred Arc Hardfacing of Stainless Steel on Carbon Steel. *J Iron Steel Res Int.* 2009;16:44-53.
- [10] Fernandes F, Cavaleiro A, Loureiro A. Oxidation behavior of Ni-based coatings deposited by PTA on gray cast iron. *Surf Coat Technol.* 2012;207:196-203.
- [11] Fernandes F, Lopes B, Cavaleiro A, Ramalho A, Loureiro A. Effect of arc current on microstructure and wear characteristics of a Ni-based coating deposited by PTA on gray cast iron. *Surf Coat Technol.* 2011;205:4094-106.
- [12] Fernandes F, Ramalho A, Loureiro A, Cavaleiro A. Wear resistance of a nickel-based coating deposited by PTA on gray cast iron. *Int J Surf Sci Eng.* 2012;6:201-13.
- [13] Vadiraj A, Balachandran G, Kamaraj M, Gopalakrishna B, Venkateshwara Rao D. Wear behavior of alloyed hypereutectic gray cast iron. *Tribology International.* 2010;43:647-53.
- [14] Prasad BK. Sliding wear response of a gray cast iron: Effects of some experimental parameters. *Tribology International.* 2011;44:660-7.
- [15] Kesavan D, Kamaraj M. The microstructure and high temperature wear performance of a nickel base hardfaced coating. *Surf Coat Technol.* 2010;204:4034-43.
- [16] Mironova-Ulmane N, Kuzmin A, Steins I, Grabis J, Sildos I, Pärs M. Raman scattering in nanosized nickel oxide NiO. *Journal of Physics: Conference Series.* 2007;93:012039.
- [17] Jian S-R, Chen Y-T, Wang C-F, Wen H-C, Chiu W-M, Yang C-S. The Influences of H<sub>2</sub> Plasma Pretreatment on the Growth of Vertically Aligned Carbon Nanotubes by Microwave Plasma Chemical Vapor Deposition. *Nanoscale Research Letters.* 2008;3:230-5.

- [18] Pandya SN, Nath SK, Chaudhary GP. Friction and Wear Characteristics of TIG Processed Surface Modified Gray Cast Iron 2009.
- [19] de Faria DLA, Venâncio Silva S, de Oliveira MT. Raman microspectroscopy of some iron oxides and oxyhydroxides. *Journal of Raman Spectroscopy*. 1997;28:873-8.
- [20] Ferrari AC, Robertson J. Raman spectroscopy of amorphous, nanostructured, diamond-like carbon, and nanodiamond. *Philosophical Transactions of the Royal Society of London Series A: Mathematical, Physical and Engineering Sciences*. 2004;362:2477-512.
- [21] Li YQ, Qiu T. Oxidation behavior of boron carbide powder. *Materials Science and Engineering: A*. 2007;444:184-91.
- [22] Lavrenko VA, Gogotsi YG. Influence of oxidation on the composition and structure of the surface layer of hot-pressed boron carbide. *Oxid Met*. 1988;29:193-202.

---

## Annex F

---

**F. Fernandes, A. Ramalho, A. Loureiro, J.M. Guilemany, M. Torrell, A. Cavaleiro, *Influence of nanostructured ZrO<sub>2</sub> additions on the wear resistance of Ni-based alloy coatings deposited by APS process, Wear, 303 (2013) 591-601.***







# Influence of nanostructured ZrO<sub>2</sub> additions on the wear resistance of Ni-based alloy coatings deposited by APS process

F. Fernandes<sup>a,\*</sup>, A. Ramalho<sup>a</sup>, A. Loureiro<sup>a</sup>, J.M. Guilemany<sup>b</sup>, M. Torrell<sup>b</sup>, A. Cavaleiro<sup>a</sup>

<sup>a</sup> CEMUC—Department of Mechanical Engineering, University of Coimbra, Rua Luís Reis Santos, 3030-788 Coimbra, Portugal

<sup>b</sup> Thermal Spray Centre (CPT-UB), University of Barcelona, C/Martí i Franques n 1, Barcelona, Spain

## ARTICLE INFO

### Article history:

Received 19 December 2012

Received in revised form

8 April 2013

Accepted 15 April 2013

Available online 22 April 2013

### Keywords:

Sliding wear

Thermal spray coatings

Metal–matrix composite

Surface analysis

Wear testing

## ABSTRACT

In the present investigation, the influence of the addition of nanostructure zirconia particles on the microstructure, micro-hardness and wear performance of a Ni-based alloy (Colmonoy 88) deposited by atmospheric plasma spraying (APS) on low carbon steel has been reported. Two different procedures were tested: (i) spraying powders of Colmonoy 88 and zirconia mixed by mechanical alloying and (ii) spraying powders separately using a dual powder injection system available at the APS equipment. The microstructure and the mechanical properties of coatings were characterized by scanning electron microscopy/energy dispersive X-ray analysis (SEM-EDS), X-ray diffraction (XRD) and micro-hardness measurements. The tribological properties were evaluated at room temperature in reciprocating sliding wear equipment. The results indicate that the as-sprayed modified coatings were mainly composed by Ni, Ni–Cr–Fe, Cr<sub>23</sub>C<sub>6</sub>, Cr<sub>5</sub>B<sub>3</sub>, and tetragonal zirconia. Evenly distribution of zirconia can be seen in the coatings produced by powders prepared by mechanical alloying, while dispersive ones can be seen in the other case. Hardness and wear resistance of coatings is increased with nanostructured zirconia additions, while their friction coefficient is decreased. Coatings produced with mechanical alloying show the highest wear resistance of all tested coatings. Nanostructured ZrO<sub>2</sub> coating displays the worst wear resistance.

© 2013 Elsevier B.V. All rights reserved.

## 1. Introduction

Improvement of the surface properties by thermal spraying hard and wear resistant materials is a commonly used industrial practice [1–3]. The base material provides the overall mechanical strength of the components while coatings provide a way of extending the limits of their use at the upper end of their performance capabilities.

A wide variety of coating materials such as cobalt, iron and nickel alloys can be successfully applied by thermal spraying technologies to protect the surface of components subjected to harsh environments [4–6]. Superalloys and cermet APS (atmospheric plasma spraying) coatings have been widely employed to improve the oxidation, corrosion, abrasion and wear resistance of engineering components, such as plungers, molds, wearing plats, turbines, tools, etc, whose surface is submitted to extreme tribological conditions in service [7–10]. Nickel-based alloys have been especially used in the protection of parts due to their unique combination of properties (mechanical, tribological, and high temperature properties) [11–14]. The microstructure and the wear

behavior of cobalt, iron and nickel alloys coatings have been studied using several alloy compositions, several processes of deposition and different substrates. Regarding the wear resistance of these coatings, some special composite systems were studied and developed. The incorporation of hard and stable carbides and oxide phases, such as CrC, SiC, WC, Al<sub>2</sub>O<sub>3</sub>, TiO<sub>2</sub>, ZrO<sub>2</sub>, CeO<sub>2</sub>, etc, in these coatings, has been reported as a way to improve their wear resistance. For example, Hou et al. [15] showed the beneficial effect of nano-Al<sub>2</sub>O<sub>3</sub> particles on the microstructure and wear resistance of a nickel-based alloy coating deposited by plasma transferred arc (PTA). Harsha et al. [1] studied the influence of CrC on the microstructure, microhardness and wear resistance of a nickel-based alloy deposited by flame spraying process. They observed that the wear resistance of the Ni modified coating is increased relatively to the CrC-free Ni-based alloy. Wang et al. [16] investigated the effect of three nano-particles additions (Al<sub>2</sub>O<sub>3</sub>, SiC, CeO<sub>2</sub>) on the high temperature wear behavior of a Ni-based alloy coatings produced by laser cladding technique and reported that the addition of these nanoparticles increased the wear resistance of the coatings. Regarding the effect of incorporation of ZrO<sub>2</sub> particles in a Ni matrix, it has also been extensively studied [17–20]; however, only electrodeposited coatings have been concerned. Despite of these studies to improve the wear resistance of Ni electrodeposited coatings, at our knowledge no reports

\* Corresponding author. Tel.: +351 239 790 745; fax: +351 239 790 701.  
E-mail address: [filipe.fernandes@dem.uc.pt](mailto:filipe.fernandes@dem.uc.pt) (F. Fernandes).

have been published as regards to the effect of nanostructured zirconia additions on the properties of Ni-based thermal sprayed coatings. Since zirconia is a ceramic material of high level of

hardness, wear and oxidation resistance, its use as reinforcement material in nickel-based alloy coatings deposited by thermal spraying processes should be investigated.

Therefore, the main goal of the present work was to study the effect of nanostructured zirconia additions on the microstructure, micro-hardness and wear performance of a nickel-based hardfacing alloy deposited on low carbon steel by atmospheric plasma spraying (APS). The coatings with nanostructured zirconia additions were produced by spraying either powders prepared by mechanical alloying or separate powders using a dual system of powder injection. The microstructure, the mechanical and tribological properties were characterized by scanning electron microscopy/energy dispersive X-ray analysis (SEM-EDAX), X-ray diffraction (XRD), Vickers indentation tests and reciprocating sliding wear tests. All the

**Table 1**

Nominal chemical composition (wt.%) of the as-received powders.

Powders	W	B	C	Cr	Fe	Si	Ni
Colmonoy 88	13.5	2.6	0.6	14.1	3.5	3.7	Balance
	HfO <sub>2</sub>	Y <sub>2</sub> O <sub>3</sub>	ZrO <sub>2</sub>				
Nanostructured ZrO <sub>2</sub>	2.5	7.5	Balance				

**Table 2**

Plasma spraying parameters of the dissimilar coatings.

Parameter	Ni	ZrO <sub>2</sub>	Ni+20% Dual	Ni+40% Dual	Ni+20% MA	Ni+40% MA
Arc current (A)	550	600	550	550	550	600
Voltage (V)	66	74	75	73	73	73
Gun speed (mm/s)	1250	1250	1250	1250	750	750
Leap (mm)	5	5	5	5	–	–
Spray distance (mm)	130	60	60	60	120	120
Primary gas (Ar) flow rate (l/min)	54	34	34	34	34	34
Secondary gas (H <sub>2</sub> ) flow rate (l/min)	9	12	15	15	15	15
Carrier gas (O) flow rate (l/min)	2.3	3	ZrO <sub>2</sub> /Ni 3/2.3	ZrO <sub>2</sub> /Ni 3/2.3	3	3
Powder feed rate (rpm)	25	30	ZrO <sub>2</sub> /Ni 5/20	ZrO <sub>2</sub> /Ni 10/15	15	15
Agitation (rpm)	40	40	ZrO <sub>2</sub> /Ni 40/40	ZrO <sub>2</sub> /Ni 40/40	40	40
Injector diameter (mm)	2	2	2	2	2	2
Number of passes	12	12	12	12	28	28
Angle	90	90	90	90	90	90
Substrate rotation (rpm)	–	–	–	–	16	16
Injector(s) position (°)	90	90	90	90	90	90

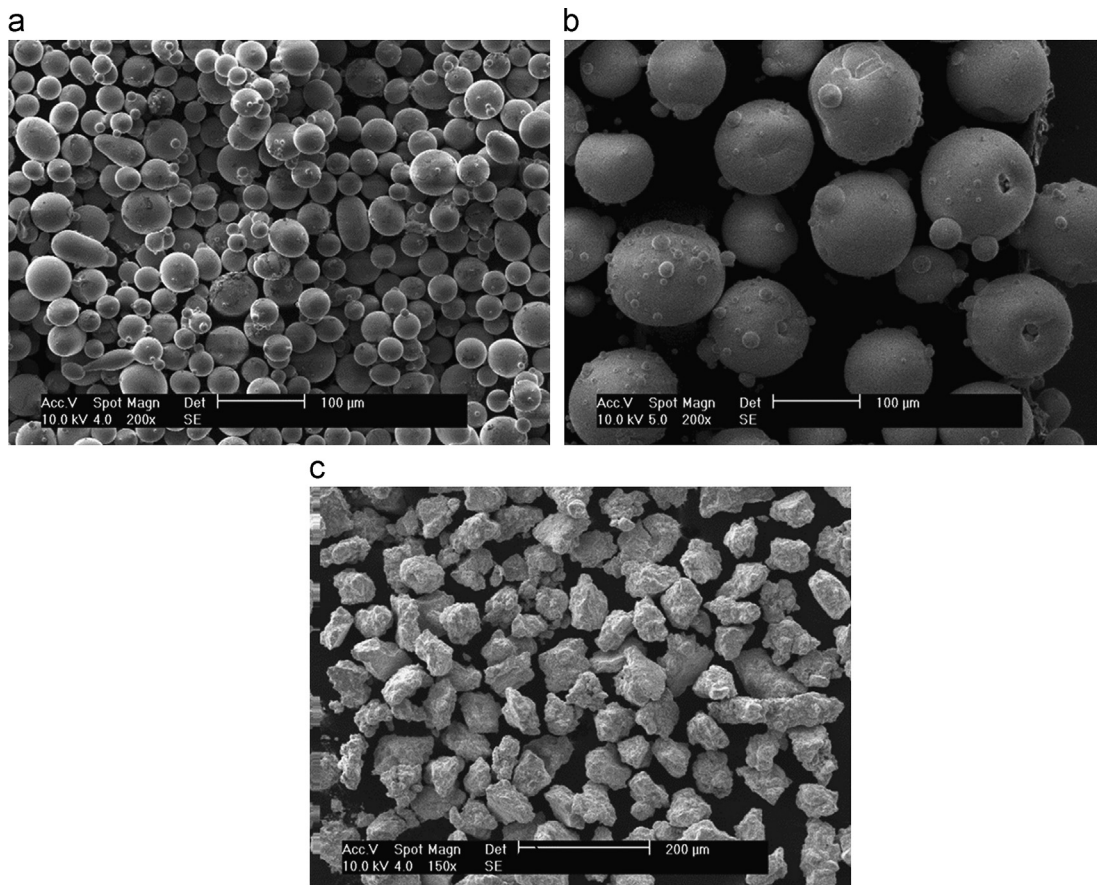


**Fig. 1.** SEM morphologies of: (a) nickel-based alloy powders, (b) nanostructured zirconia powders, (c) powders prepared by mechanical alloying, (condition with 40% ZrO<sub>2</sub>).

properties of the doped coatings were compared with the unmodified nickel and nanostructured zirconia coatings.

## 2. Experimental procedure

### 2.1. Materials

In this investigation commercial powders of a Ni-based alloy (Colmonoy 88) and nanostructured zirconia from the “Wall Colmonoy” and “Innovnano” companies, respectively, were used as feedstock to produce coatings with Atmospheric Plasma Spraying process (APS) onto a low carbon steel substrate (AISI 8620). The Ni-based alloy powders have been characterized as a spherical morphology with an average size D50 of 45  $\mu\text{m}$  and density of 7900 ( $\text{kg}/\text{m}^3$ ), whilst nanostructured  $\text{ZrO}_2$  powders have an average primary particle size of 60 nm with granule size D50 of 60  $\mu\text{m}$  and density 1700 ( $\text{kg}/\text{m}^3$ ). The chemical compositions of the as-received powders are displayed in Table 1. The plasma sprayed coatings were deposited with an APS A3000 system from “Sulzer Metco”, using either pure as-received powders and a dual system for powder injection available at the APS equipment (designated as “Dual”) or mixtures of powders prepared by mechanical alloying (MA) process (designated as “MA”). The substrate material was grit-blasted with alumina grade 24 from “Alodur Germany” before coating (which induced a corresponding superficial roughness ( $R_a$ ) of 5  $\mu\text{m}$ ), to increase the surface roughness and achieve the proper mechanical interlocking between the coating and the substrate. For pure colmonoy and zirconia coatings and Dual procedure, the substrates were fixed positioned, being the spraying of the surface ensured by the movement of the torch. On the other hand,

in the MA method the substrates were placed in a rotatory table and the spraying was performed by combining this rotation with the vertical movement of the torch. Before final depositions, preliminary coatings were produced changing the main deposition parameters and, then, characterized in order to properly select the depositions conditions that allowed achieving the best results. Moreover, during depositions the substrates were cooled down by two pressurized air guns keeping the temperature below 150  $^\circ\text{C}$ , in order to avoid cracking and residual stresses formation.

Powders mixtures were prepared by mechanical alloying in a Fritsch planetary ball mill using a 250 ml hardened steel vial and fifteen balls with 20 mm diameter of the same material. Two proportions of nanostructured zirconia were added to the nickel-based alloy powder, 20% and 40% in volume, i.e. 5.1 and 12.5 gr of nanostructured  $\text{ZrO}_2$  powder for 94.9 and 87.4 gr of nickel-based alloy powder, respectively. The MA process was carried out at 400 rpm for 2 h in a protective atmosphere of argon. After 1 h of milling, the process was interrupted for 10 min to cool the vial and to reserve rotation. Finally, after milling, the powder was mechanical sieved to obtain particles with a size distribution in the range [28–71  $\mu\text{m}$ ]. Two different coatings also containing nanostructured zirconia additions of 20% and 40% were also performed by using the dual system of powder injection available at the APS equipment. In this case the proportion was easily achieved by controlling the flow of powders through the rotation control of the powder feeders. Henceforth, coatings produced using as received pure powder of nickel-based alloy and nanostructured zirconia will be designated as “Ni”, and “ $\text{ZrO}_2$ ”, respectively, coatings produced with powders prepared by mechanical alloying using 20% and 40% of nanostructured  $\text{ZrO}_2$  will be termed as “Ni+20% MA” and “Ni+40% MA”, respectively, and coatings deposited using the dual system of powder injection with 20% and 40% of nanostructured  $\text{ZrO}_2$  will be designated as “Ni+20% Dual” and “Ni+40% Dual”, respectively. The process parameters employed in the dissimilar coating depositions are shown in Table 2.

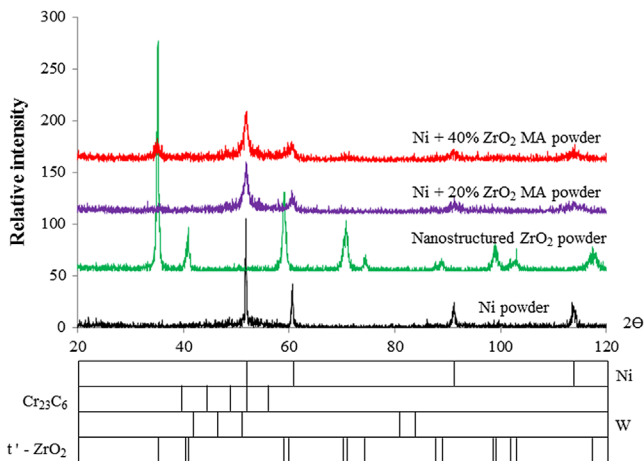


Fig. 2. X-ray diffraction pattern of the dissimilar powders used in the depositions.

### 2.2. Powders and coatings characterization

Powders morphology were observed and characterized by scanning electron microscopy with X-ray spectroscopy (SEM/EDS) and X-ray diffraction (XRD) using  $\text{Co K}\alpha$  radiation. Transverse section of APS coatings was polished using conventional metallographic procedure which consisted grinding followed by polishing. The microstructure of coatings was studied and characterized by optical microscope (OM) and SEM/EDS. Further, the structure of the coatings was studied by X-ray diffraction. The micro-hardness of coatings was determined by Vickers testing using a 3 N load at 15 s holding time. A total of 30 measurements of hardness were done in each coating.

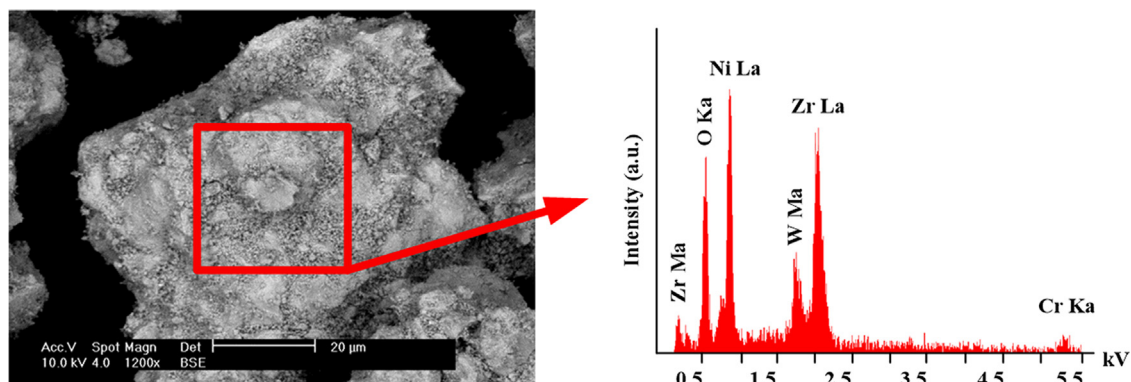
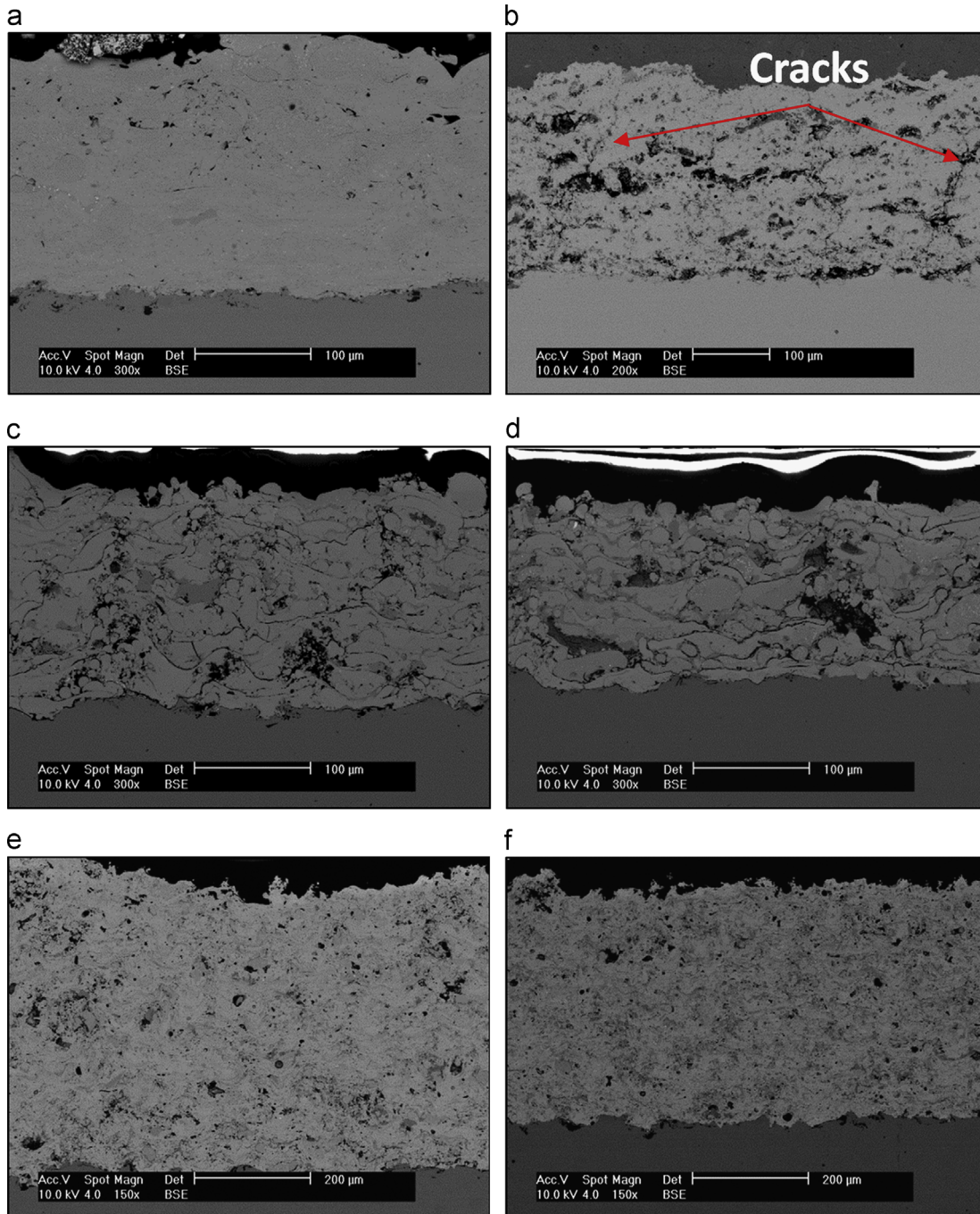


Fig. 3. Energy dispersive spectroscopy analysis (EDS) of a powder produced by mechanical alloying (condition Ni+40%  $\text{ZrO}_2$ ).

### 2.3. Wear tests

Wear behavior of APS coatings was studied using reciprocating wear equipment. An harmonic wave generated by an eccentric and rod mechanism imposed a stroke length of 2.05 mm at a frequency of 1 Hz. A detailed description of the equipment can be found in reference [21]. Before wear tests, the surface of coatings were grounded and then polished using a 3  $\mu\text{m}$  diamond past. A superficial roughness  $R_a$  of: 0.51, 0.65, 0.49 and 0.98  $\mu\text{m}$  was measured respectively for Ni, Ni Dual, Ni MA and  $\text{ZrO}_2$  coatings. In the scope of the present study, the values of normal load applied to the coated samples were 5, 7, 8.5 and 10 N. All the tests were conducted at a constant rotational speed of 190 rpm during 2 h. The acquisition time

of signal used was 60 s. A soda-lime glass sphere with 500  $\text{HV}_{0.5}$  of hardness and 10 mm in diameter was used as counterpart, in order to study the interaction of glass with the different coatings. After wear tests, the volume loss was estimated through the transverse profile of each wear scar at the middle and near the end of both sides of the scar. To ensure the reproducibility of results, a set of three scars for each test condition was performed at the coating, and the volume loss calculated by using the volume average of these marks. An approach of the Archard's law was applied; see Eq. (1), in order to obtain the specific wear rate. In this equation,  $V$  represents the wear volume,  $P$  is the normal load,  $k$  is the specific wear rate and  $l$  the sliding distance. To estimate the error of the measurements, a statistical analysis described elsewhere by A. Ramalho [22] was used.



**Fig. 4.** SEM morphology of the: (a) Ni-based alloy coating, (b) nanostructured  $\text{ZrO}_2$  coating, (c) and (d) Ni+20% Dual and Ni+40% Dual, respectively, (e) and (f) Ni+20% MA and Ni+40% MA.

After wear tests, the morphology of depressions was observed and characterized by scanning electron microscopy.

$$V = k \times P \times l \tag{1}$$

### 3. Results and discussion

#### 3.1. Powders characterization

Fig. 1(a–c) shows SEM morphologies of nickel-based alloy, nanostructured zirconia and one of the MA prepared powders.

Ni and ZrO<sub>2</sub> powders clearly display spherical-shaped particles, while MA powders have irregular shapes. XRD patterns in Fig. 2 shows that Ni powders consist essentially in a Ni solid solution (ICDD card 01-1258) with some traces of chromium carbide (ICDD card 85-1281) and tungsten (ICDD card 47-1319). This indexation is in agreement with the results from the literature where similar phases were detected [23]. Nanostructured ZrO<sub>2</sub> powders are essentially formed by tetragonal zirconia. In respect to MA powders XRD pattern reveal the same phases indexed from the pure Ni and nanostructured ZrO<sub>2</sub> powders, suggesting only physical mixing, not having occurred chemical reactions. Fig. 3 shows a SEM-EDS analysis performed at a

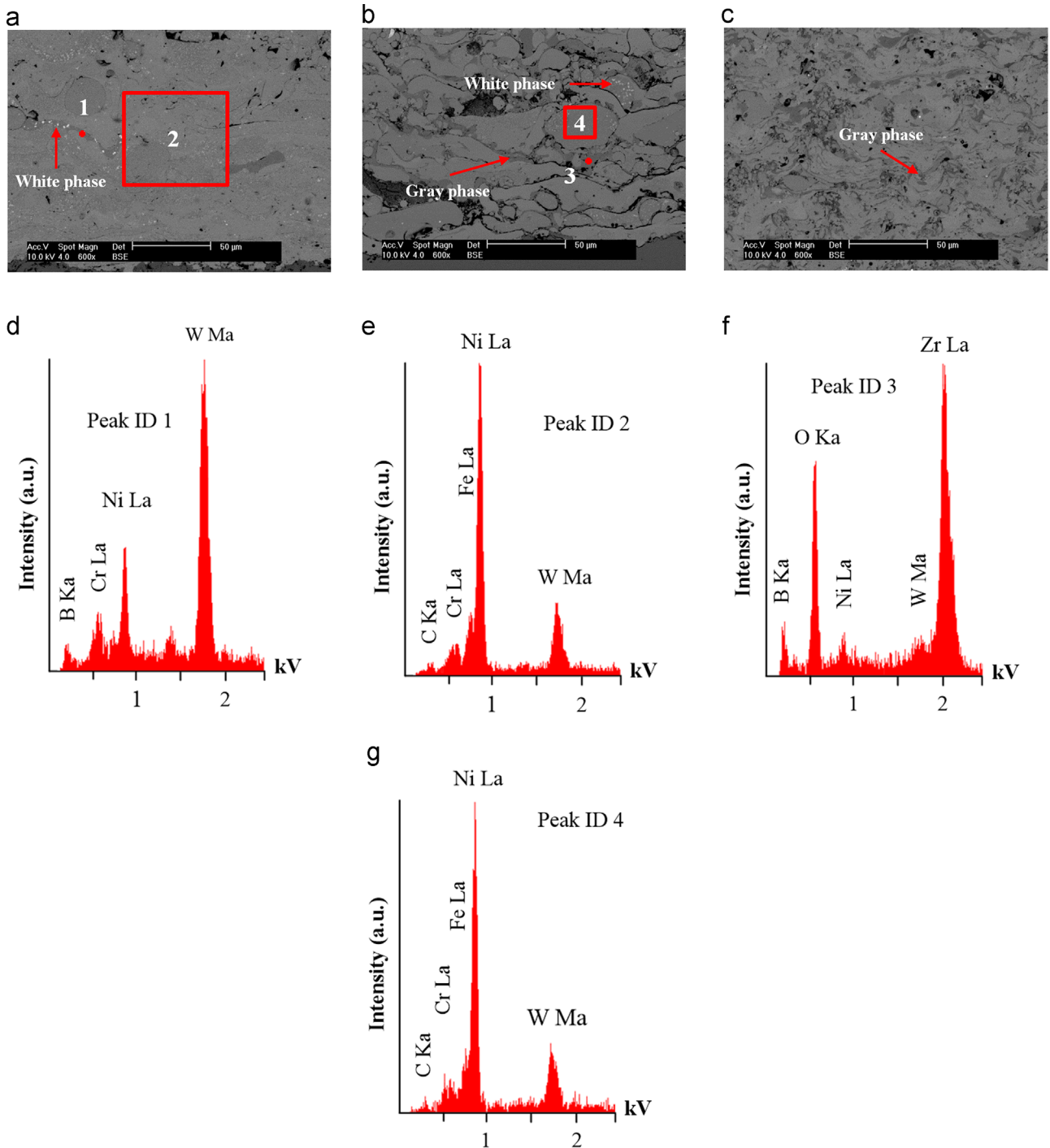


Fig. 5. SEM-EDS analysis performed at the: (a) Ni coating, (b) Ni+40% Dual coating, (c) Ni+40% MA coating. SEM-EDS spectra of: (d) point 1, (e) zone 2, (f) point 3, (g) zone 4.

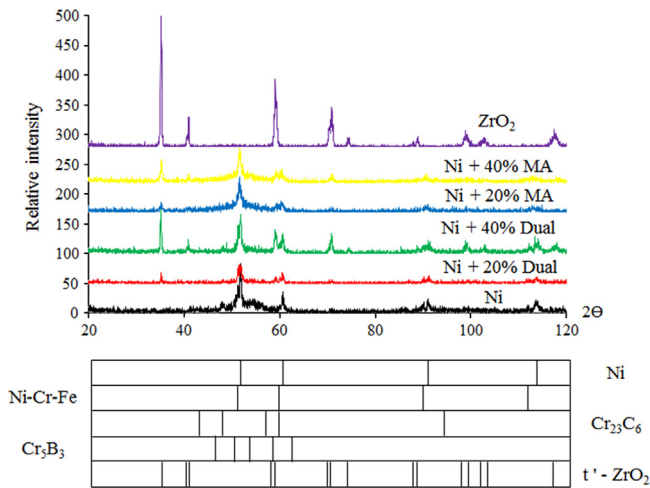


Fig. 6. X-ray diffraction pattern of the dissimilar coatings.

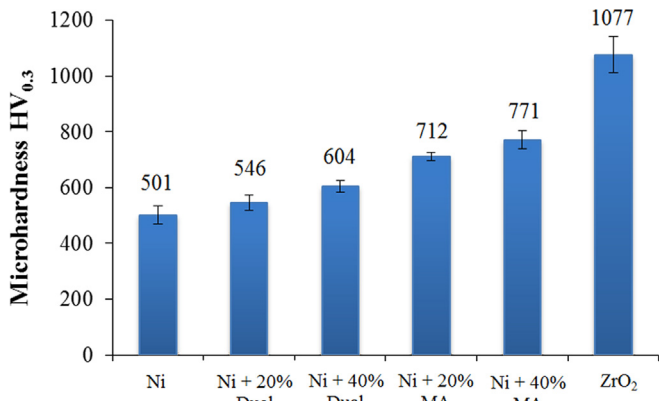


Fig. 7. Microhardness of coatings.

MA powder (Ni+40% ZrO<sub>2</sub>). As the EDS spectra displays, the powder is essentially formed by nickel, zirconia, oxygen and tungsten, supporting the results from the XRD analysis.

3.2. Microstructure

Fig. 4 shows SEM micrographs of the cross section of the coatings. All coatings present the typical morphology of plasma spraying, with pores, lamellae, partially melted and un-melted particles and good adhesion to the substrate. ZrO<sub>2</sub> (see Fig. 4b) and Ni+ZrO<sub>2</sub> Dual coatings (Fig. 4(c and d)) show a higher level of porosity than the other coatings. Very often, small pores were found within the flattened particles and result from shrinkage porosity and big pores were normally located between lamellae and were caused by gas porosity phenomenon [24]. In all cases the melting states of particles influence the level of porosity and, usually, low melting state of particles gives rise to a porous microstructure. Furthermore, pure ZrO<sub>2</sub> coating, (see Fig. 4b) reveals the presence of some cracks in the coating, resulting from tensile residual stresses generated during cooling down to room temperature. Ni and MA coatings (see Fig. 4(a), (e) and (f)) display a compact and homogenous structure, while Dual coatings revealed a microstructure full of semi-melted particles, suggesting a brittle character based on low level of agglomeration between particles. It is well known that in the thermal spraying processes the melting level depends on the thermal energy added to the particles, on the plasma temperature and on the particles flying time. During plasma spraying, molten particles impact the surface

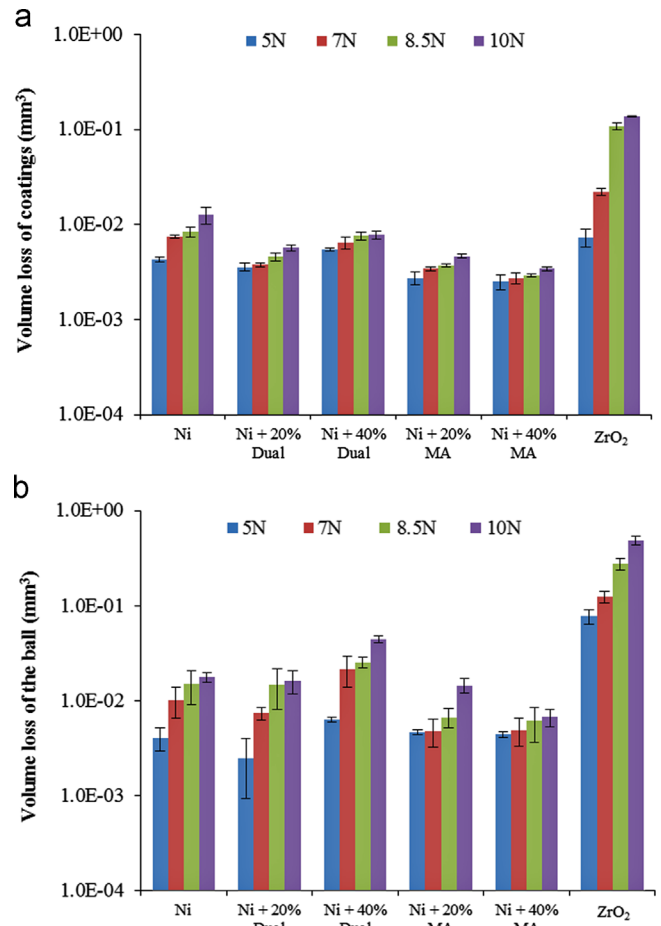


Fig. 8. Volume loss of: (a) coatings, (b) ball; after wear tests as function of the applied load.

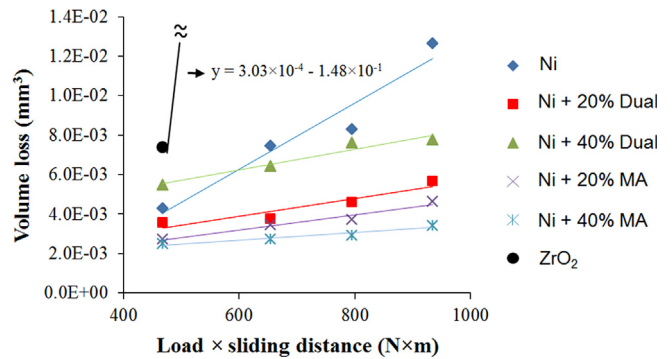


Fig. 9. Evolution of the wear behavior as a function of the parameter “normal load × sliding distance”.

Table 3 Results of the linearization analysis of the dissimilar coatings.

Coating	Specific wear rate, $k(\text{mm}^3/\text{N} \times \text{m})$			
	Average	STD	confidence interval 90%	$r^2$
Ni	$1.68 \times 10^{-5}$	$3.06 \times 10^{-6}$	$7.83 \times 10^{-6}$ – $2.57 \times 10^{-5}$	0.938
Ni+20% Dual	$4.45 \times 10^{-6}$	$1.14 \times 10^{-6}$	$1.12 \times 10^{-6}$ – $7.79 \times 10^{-6}$	0.884
Ni+40% Dual	$5.26 \times 10^{-6}$	$8.65 \times 10^{-7}$	$2.74 \times 10^{-6}$ – $7.78 \times 10^{-6}$	0.949
Ni+20% MA	$3.83 \times 10^{-6}$	$5.56 \times 10^{-7}$	$2.21 \times 10^{-6}$ – $5.46 \times 10^{-6}$	0.960
Ni+40% MA	$1.90 \times 10^{-6}$	$3.97 \times 10^{-7}$	$7.38 \times 10^{-7}$ – $3.06 \times 10^{-6}$	0.919
ZrO <sub>2</sub>	$3.03 \times 10^{-4}$	$7.15 \times 10^{-5}$	$9.48 \times 10^{-5}$ – $5.12 \times 10^{-4}$	0.900

of substrate, then deform, solidify and transform into lamellae. During spraying, the particles can be in all of the following states on impact: fully molten, superheated, semi-molten and molten then re-solidified [24,25], depending on the deposition parameters. It is well known that in plasma spraying the electric arc current, the primary plasma gas flow rate, the second plasma gas flow rate and powder size are the main parameters that influence the in-flight particle behaviors. From Table 2, comparing the process parameters for the Ni and Ni+20% and 40% ZrO<sub>2</sub> Dual coatings, differences can be observed in relation to the spray distance, primary and secondary gas flow rates, and powder feed rate. According to the literature, an increase of argon flow rate leads to a gentle decrease of particle temperature but a rapid increase of velocity [26]. On the other hand, increasing the hydrogen flow rate increases both, temperature and velocity, though temperature is more sensitive to the hydrogen flow rate than velocity. So, due to the lower primary gas flow rate (Ar) and higher secondary gas flow rate (H<sub>2</sub>) used in the Ni +ZrO<sub>2</sub> Dual coatings, would be expected a great level of melting particles and consequently an homogenous structure, if the particles do not oxidize during the in-flight time. However, such fact was not observed. The lower primary gas flow rate (Ar) used in the production of these coatings might suggest that independently of the high melting state of particles, the velocity given by the flow could be not enough to accelerate the particles onto the specimen surface. Nevertheless, the same process parameters were used in the deposition of the Ni+20% MA coating, with exception of the spraying distance, and the microstructure revealed to be homogenous and compact. In fact, the spraying distance also plays an important role in the thermal treatment of particles during their in-flight time [27]. Thereby, for short spraying distances, due to the short exposure of particles in the flame, the energy added by the flame could be not enough to semi-molten or molten the particles, giving rise to a microstructure similar to those observed for these coatings. Furthermore, it can also be speculated that the two different ways to add zirconia at the nickel alloy can change the entropy of the system, and therefore change the running-on of

the deposition. In fact, according to the literature the nature of powders has a detrimental effect in their interaction with the plasma spraying flame and, therefore, on the properties of the coatings [28]. The low level of melting particles can also explain the high level of porosity observed in these coatings.

For better characterization and perception of the different coatings microstructure, magnifications of the Ni, Ni+40% Dual and Ni+40% MA coatings, as well as EDS analyses are shown in Fig. 5. The EDS analysis revealed that Ni coating is essentially formed by Ni, W, Cr and Fe, which matches well with the chemical composition of the as received Ni powders. Moreover, small particles rich in W (white phase) can be observed evenly distributed in the microstructure. The semi-molten particles in the microstructure of the Ni+40% Dual coating are from the same nature of the Ni coating matrix, therefore, they can be identified as semi-molten Colmonoy powders. Similar to Ni coating a white phase rich in W is also detected in the microstructure, co-existing with a coarse gray phase, entrapped between the boundaries of the semi-molten particles, revealed by EDS to be zirconia. Such a distribution is in the basis of a brittle behavior. Contrary to this coating, Ni+40% MA displays a compact and homogeneous microstructure, with small zirconia particles evenly distributed along the microstructure improving the coating toughness. Therefore, from these results, it can be inferred that the addition of nanostructured zirconia can be successfully achieved by using both procedures, powders prepared by mechanical alloying or dual projection. However, in coatings deposited with MA powders zirconia is finer and more homogeneously distributed in the Ni-matrix giving rise to better mechanical performance.

XRD patterns of the coatings are displayed in Fig. 6. As the spectrum reveals, the nickel-based coating consists mainly of Ni, Ni-Cr-Fe, Cr<sub>23</sub>C<sub>6</sub> and Cr<sub>5</sub>B<sub>3</sub> phases. These results are in accordance with the literature where similar phases were identified [23]. Moreover, all the coatings with nanostructured zirconia additions showed diffraction lines corresponding to the same phases identified at both the Ni and ZrO<sub>2</sub> coatings. In the latter, is mainly formed by tetragonal zirconia.

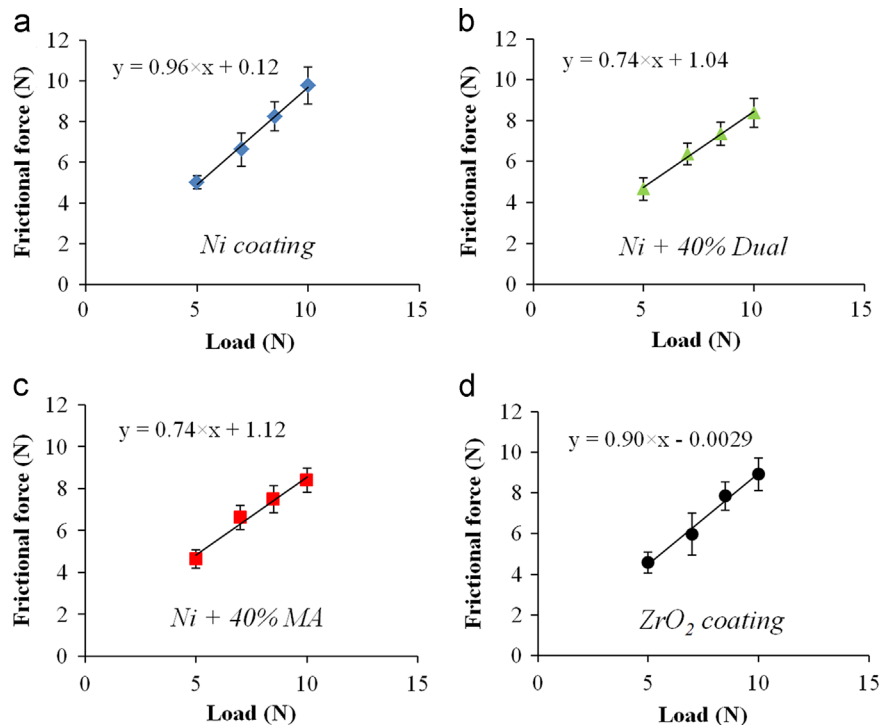


Fig. 10. Variation of the friction force of coatings with applied load for: (a) Ni coating, (b) Ni+40% Dual coating, (c) Ni+40% MA coating (d) nanostructured ZrO<sub>2</sub> coating.

### 3.3. Micro-hardness

Fig. 7 shows that nanostructured  $ZrO_2$  additions increases the hardness of the nickel-based alloy. The same behavior was reported by other authors after addition of hard particles such as ( $Al_2O_3$ ,  $CeO_2$ , SiC, WC) at a nickel alloy [1,3,16]. However, MA coatings have higher hardness than Dual ones. This result is coherent with either the lower porosity or the finer and more homogeneous distribution of nanostructured zirconia in Ni+ $ZrO_2$  MA coatings.

### 3.4. Wear behavior

The volume loss due to wear of the coatings and counterpart increases with increasing applied load, as it is shown in Fig. 8(a) and (b), respectively, being this trend more notorious for  $ZrO_2$  coating. As it will be shown later, the higher volume loss for this coating can be correlated with the brittle behavior as displayed on its worn surface. Nanostructured zirconia additions have a positive effect, decreasing the volume loss of material, independently of the deposition procedure used. However, efficiency seems to be higher in Ni+ $ZrO_2$  MA coatings which display higher decreases of the volume loss than Ni+ $ZrO_2$  Dual coatings. Furthermore, increasing zirconia content in MA coatings continues to have a beneficial effect whereas the inverse is observed in Dual coatings. The better wear performance of Ni+ $ZrO_2$  MA coatings can be attributed to the combination of a higher hardness, an evenly distribution of smaller zirconia domains in the Ni-based matrix and a more compact microstructure. In fact, the presence of hard phases increases the overall hardness of the coating and, on the other hand, smaller and uniformly distributed hard

domains in a soft matrix gives rise to tougher materials, which combined lead to a decrease of the volume loss due to wear. Similar behavior was observed by other author after adding hard particles to a nickel based alloy [1,15]. In the case of Ni+ $ZrO_2$  Dual coatings nanostructured hard  $ZrO_2$  phases have initially a similar influence, by increasing the hardness. However, the agglomeration of  $ZrO_2$  particles, localized in-between Ni-based lamellae makes microstructure less tough with its consequent detrimental effect on the wear performance when high contents of the hard phase exist.

In order to normalize the wear results, they were plotted in Fig. 9 in terms of material volume loss as function of the product of sliding distance by the applied load. For each set of data, a straight linear trend was fitted in order to obtain the specific wear rate from the slope (see Eq. 1). Further, a complete reliability analysis of the specific wear rate is presented in Table 3 for a confidence interval of 90%. Because of the high volume loss displayed by the  $ZrO_2$  coating, only the point produced with lower load and the beginning of the straight adjustment were plotted in Fig. 9. Crossing the information of Fig. 9 and Table 3 it is possible conclude the specific wear rate of Ni-modified coatings is lower than that of the un-modified Ni coating. Ni+40%  $ZrO_2$  dual coating display the lowest specific wear rate, being this result attributed to the higher hardness displayed by this coating. Further, coatings produced by the dual system of powder injection display higher specific wear rate than coatings produced by powders prepared by mechanical alloying.  $ZrO_2$  coating displays the highest specific wear rate, being one and two orders of magnitude greater than the un-modified and modified coatings, respectively.

The average values of the frictional force of the Ni, Ni+40% Dual, Ni+40% MA and  $ZrO_2$  coatings linearly increases with the applied

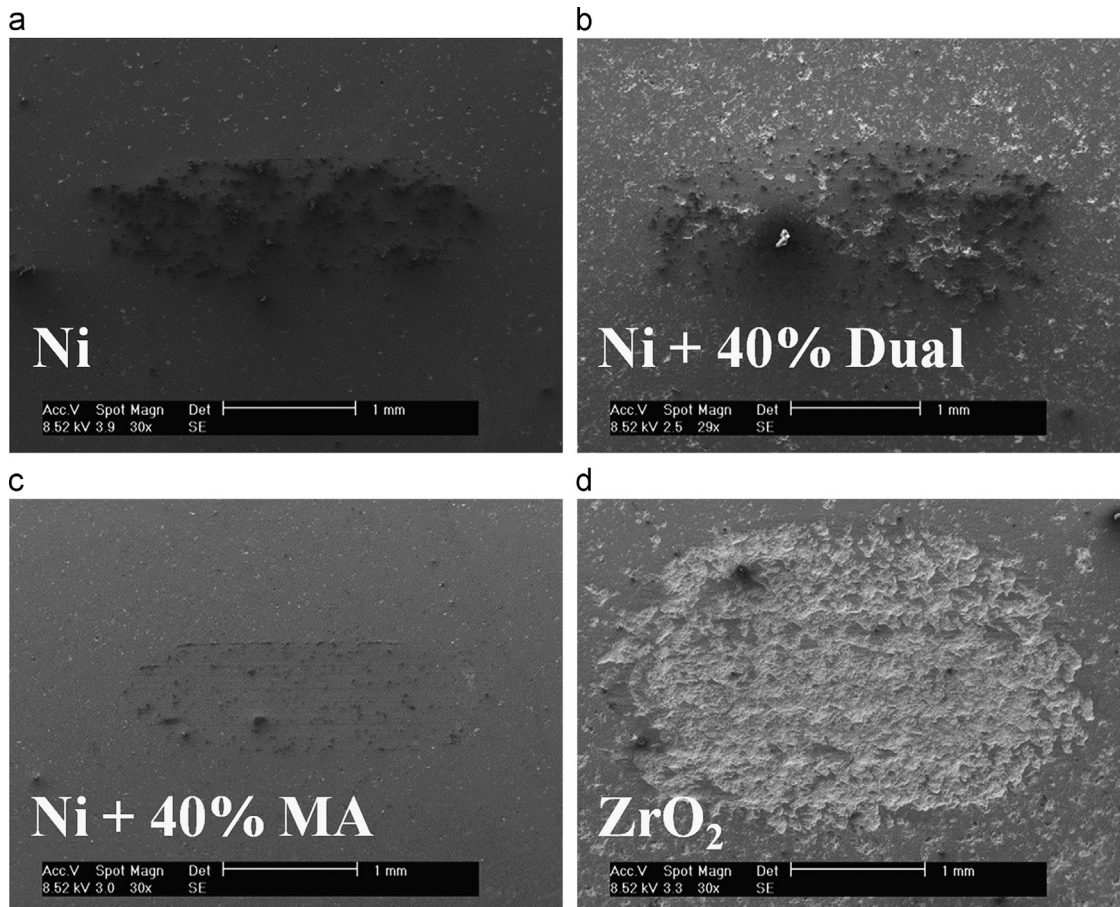
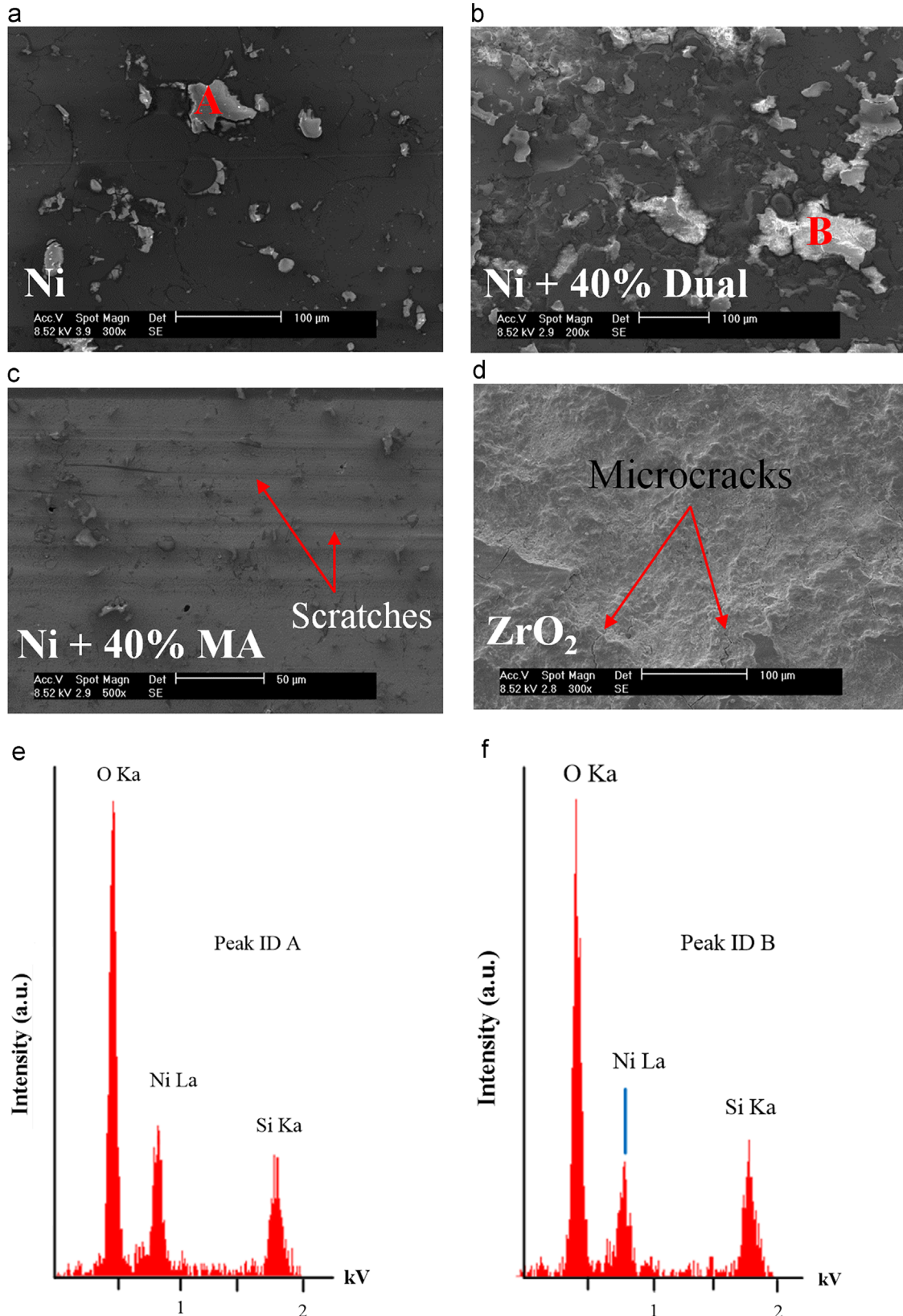


Fig. 11. SEM morphologies of the worn surfaces tested at 8.5 N load of the: (a) Ni coating, (b) Ni+40% dual, (c) Ni+40% MA, (d)  $ZrO_2$  coating.



load, as shown in Fig. 10. This is in good agreement with Amontons–Coulomb model. By fitting a linear trend to the experimental results, the friction coefficient calculated from the slope decreases

with the nanostructured zirconia additions, independently of the deposition method. Pure nanostructured zirconia shows higher friction coefficient than composite coatings, but lower than the



**Fig. 12.** Magnification of the worn surfaces tested with a load of 8.5 N of the: (a) Ni coating, (b) Ni+40% dual, (c) Ni+40% MA, (d) ZrO<sub>2</sub> coating. SEM-EDS spectra of: (e) point A, (f) point B.

pure nickel one. The changes in the specific wear rate and friction coefficient described above are only partially correlated with the applied test conditions and properties of the materials, which can produce dissimilar wear mechanisms during wear tests, and therefore dissimilar volume loss of coatings. These reasons have encouraged the investigation of the interaction between the pair specimens-counterpart. Scanning electron microscopy (SEM) analysis was conducted on the dissimilar worn surfaces of coatings in order to identify the main wear mechanisms produced.

Typical SEM morphologies of worn surfaces of the coatings tested with 8.5 N against a glass sphere are shown in Fig. 11. Distinct wear mechanisms were identified in the worn surfaces. In Ni and Ni+ZrO<sub>2</sub> Dual coatings significant amount of adherent material is shown in the wear scar, while Ni+ZrO<sub>2</sub> MA and ZrO<sub>2</sub> coatings show clean worn surfaces. EDS analysis performed in adhered debris, marked in Fig. 12(a) and (b) by letters A and B, allows concluding that they are made of silicon oxides and Ni, suggesting a mechanical mixing by the friction process, joining the softer Ni phase with the silica type wear debris from the ball wear. Being softer, the compact wear debris can stick at the worn track as well as at the ball wear scar, as can be observed in Fig. 13. During contact the friction generated by the movement of the counterpart against the surface specimen, causes an increase of temperature promoting local plastic deformation. At this time, both materials will adhere to each other. In the wear track of the Ni coating, see Fig. 12(a), the wear debris tend to be incorporated in the specimens, more precisely in the boundaries of the semi-melted powders, remaining adherent and leading to removal of material. This mechanism explains simultaneously the high friction values reported for Ni coating. On the other hand, ZrO<sub>2</sub> coating shows clean wear scars without traces of adhered material. The surface has a brittle appearance, where micro cracks can be seen, as shown in Fig. 12(d), revealing a rough surface from which particles of several tens of micrometers were detached. This morphology suggests mechanical interlocking during the contact which can explain the higher values of the friction coefficient. Furthermore, it should promote a strong abrasion in the counterpart, giving rise to much higher wear rate as shown in Fig. 8(b). Moreover, the evolution of the wear amount with the increase of normal load, (see Fig. 8), allow identifying a made severe wear volume for loads higher than 7 N, which should be correlated to a transition for a made brittle behavior. Similar behavior was observed by Chen et al. [29] during the evaluation of un-lubricated wear properties of plasma-sprayed nanostructures and conventional zirconia coatings. The wear scars of Ni+ZrO<sub>2</sub>

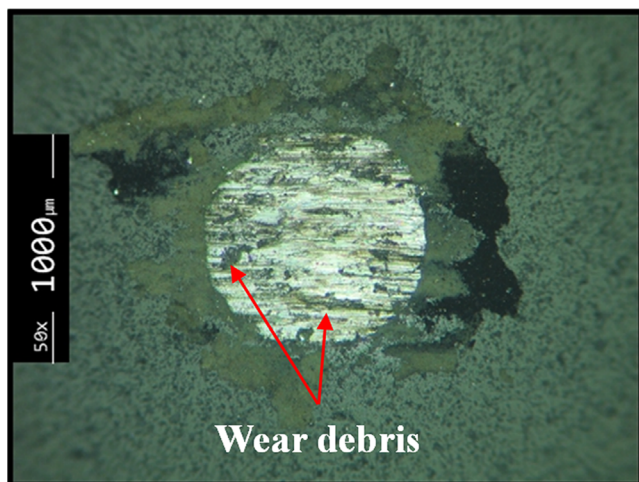


Fig. 13. Optical micrograph of the ball wear scars tested against the Ni coating with 7 N of load.

Dual coatings show a mix morphology of pure Ni and ZrO<sub>2</sub> coatings, i.e. adhered debris can be observed over a rough brittle-appearance surface, whose number decreases with nanostructured zirconia additions. In these coatings, zirconia particles are localized in the boundaries of the semi-melted Ni-based powders (see Fig. 4c and d). Despite of the particles operating as reinforcement of the coatings, leading to a lower volume loss, the area of the nickel exposed to the glass sphere remains higher. Therefore, it is expected similar debris adhesion as for Ni coating. At the same time, due to the continuous removal of material, ZrO<sub>2</sub> particles in the boundaries of the semi-melted powders loses their support capacity being removed from the boundaries. These particles will slide through the wear track acting as a removal of the wear debris. Increasing the volume of nanostructured zirconia from 20 to 40%, higher levels of brittleness in the boundaries are achieved, increasing the volume loss of material, as reported before, and giving rise to the rough and brittle appearance shown below the adhered debris. The higher level of porosity of these coatings also accounts for higher levels of volume loss of material.

The coatings produced from MA powders show also clean wear surfaces but with a different failure type from pure zirconia coating. Ni+ZrO<sub>2</sub> MA coatings reveal surfaces with scratches identifying some sort of grooving abrasion, see Fig. 12(c). The uniform distribution of small nanostructured zirconia particles and the higher hardness and toughness of these coatings avoids the plastic deformation, the adhesion and the liberation of large wear debris either from the coating or the counterpart. The smooth worn surfaces can be in the basis of the low friction coefficient [30]. In these coatings, the matrix cutting occurs through a process of two body abrasion, as shown Fig. 12(c). Despite of the dissimilar wear mechanisms observed in the wear track of the coatings, during the wear tests it was observed that most of the material resulting from the wear was blown out, due to the movement of the ball.

#### 4. Conclusions

- The influence of nanostructured zirconia additions on the microstructure, micro-hardness and wear performance of a nickel-based hardfacing alloy deposited by atmospheric plasma spraying (APS) on low carbon steel is reported in the present paper.
- The coatings containing nanostructured zirconia additions were produced either using powders prepared by mechanical alloying or using separate powders that are sprayed simultaneously via a dual system of powder injection.
- Nanostructured zirconia can be successfully incorporated into nickel-based alloy powders by mechanical alloying. Coatings produced with these powders present evenly distributed zirconia as opposed to coatings produced by separate powder injection, where the nanostructured zirconia particles were entrapped in the boundaries of the semi-melted Ni lamellae.
- The microstructure of the nickel coating consists mainly of Ni, Ni–Cr–Fe, Cr<sub>23</sub>C<sub>6</sub> and Cr<sub>5</sub>B<sub>3</sub> phases. The same diffraction lines were identified in the modified nickel coatings with tetragonal zirconia, independently of the procedure used in depositions.
- The hardness and wear behavior of coatings was improved with nanostructured zirconia additions while the friction coefficient is decreased.
- The nanostructured ZrO<sub>2</sub> coating shows the highest hardness values but also the highest specific wear rate, one to two orders of magnitude higher than the other prepared coatings, in particular those deposited with MA powders.
- Adhesive wear mechanism was observed in the worn surface of the nickel coating and coatings prepared by Dual deposition,

while abrasive wear was observed in ZrO<sub>2</sub> coating and coatings deposited using MA powders.

## Acknowledgments

The authors wish to express their sincere thanks to the Portuguese Foundation for the Science and Technology (FCT), through COMPETE program from QREN and to FEDER, for financial support in the aim of the Project number “13545”, as well as for the Grant (SFRH/BD/68740/2010).

## References

- [1] S. Harsha, D. Dwivedi, A. Agarwal, Influence of CrC addition in Ni–Cr–Si–B flame sprayed coatings on microstructure, microhardness and wear behaviour, *International Journal of Advanced Manufacturing Technology* 38 (2008) 93–101.
- [2] J.M. Miguel, J.M. Guilemany, S. Vizcaino, Tribological study of NiCrBSi coating obtained by different processes, *Tribology International* 36 (2003) 181–187.
- [3] J.C. Miranda, A. Ramalho, Abrasion resistance of thermal sprayed composite coatings with a nickel alloy matrix and a WC hard phase. Effect of deposition technique and re-melting, *Tribology Letters* 11 (2001) 37–48.
- [4] A.K. Basak, S. Achanta, J.P. Celis, M. Vardavoulias, P. Matteazzi, Structure and mechanical properties of plasma sprayed nanostructured alumina and FeCuAl–alumina cermet coatings, *Surface and Coatings Technology* 202 (2008) 2368–2373.
- [5] Y. Wu, S. Hong, J. Zhang, Z. He, W. Guo, Q. Wang, G. Li, Microstructure and cavitation erosion behavior of WC–Co–Cr coating on 1Cr18Ni9Ti stainless steel by HVOF thermal spraying, *International Journal of Refractory Metals and Hard Materials* 32 (2012) 21–26.
- [6] R.A. Mahesh, R. Jayaganthan, S. Prakash, Oxidation behavior of HVOF sprayed Ni–5Al coatings deposited on Ni- and Fe-based superalloys under cyclic condition, *Materials Science and Engineering: A* 475 (2008) 327–335.
- [7] H. Liao, B. Normand, C. Coddet, Influence of coating microstructure on the abrasive wear resistance of WC/Co cermet coatings, *Surface and Coatings Technology* 124 (2000) 235–242.
- [8] C.-J. Li, C.-X. Li, Y.-Z. Xing, M. Gao, G.-J. Yang, Influence of YSZ electrolyte thickness on the characteristics of plasma-sprayed cermet supported tubular SOFC, *Solid State Ionics* 177 (2006) 2065–2069.
- [9] M.H. Staia, T. Valente, C. Bartuli, D.B. Lewis, C.P. Constable, A. Roman, J. Lesage, D. Chicot, G. Mesmacque, Part II: tribological performance of Cr<sub>3</sub>C<sub>2</sub>–25% NiCr reactive plasma sprayed coatings deposited at different pressures, *Surface and Coatings Technology* 146–147 (2001) 563–570.
- [10] G.J. Gibbons, R.G. Hansell, Thermal-sprayed coatings on aluminium for mould tool protection and upgrade, *Journal of Materials Processing Technology* 204 (2008) 184–191.
- [11] J.H. Chang, C.P. Chang, J.M. Chou, R.I. Hsieh, J.L. Lee, Microstructure and bonding behavior on the interface of an induction-melted Ni-based alloy coating and AISI 4140 steel substrate, *Surface and Coatings Technology* 204 (2010) 3173–3181.
- [12] W. Li, Y. Li, C. Sun, Z. Hu, T. Liang, W. Lai, Microstructural characteristics and degradation mechanism of the NiCrAlY/CrN/DSM11 system during thermal exposure at 1100 °C, *Journal of Alloys and Compounds* 506 (2010) 77–84.
- [13] C. Guo, J. Zhou, J. Chen, J. Zhao, Y. Yu, H. Zhou, High temperature wear resistance of laser cladding NiCrBSi and NiCrBSi/WC–Ni composite coatings, *Wear* 270 (2011) 492–498.
- [14] F. Fernandes, A. Cavaleiro, A. Loureiro, Oxidation behavior of Ni-based coatings deposited by PTA on gray cast iron, *Surface and Coatings Technology* 207 (2012) 196–203.
- [15] Q.Y. Hou, Z. Huang, J.T. Wang, Influence of nano-Al<sub>2</sub>O<sub>3</sub> particles on the microstructure and wear resistance of the nickel-based alloy coating deposited by plasma transferred arc overlay welding, *Surface and Coatings Technology* 205 (2011) 2806–2812.
- [16] H.-y. Wang, D.-w. Zuo, M.-d. Wang, G.-f. Sun, H. Miao, Y.-l. Sun, High temperature frictional wear behaviors of nano-particle reinforced NiCoCrAlY clad coatings, *Transactions of Nonferrous Metals Society of China* 21 (2011) 1322–1328.
- [17] W. Wang, H.T. Guo, J.P. Gao, X.H. Dong, Q.X. Qin, XPS, UPS and ESR studies on the interfacial interaction in Ni–ZrO<sub>2</sub> composite plating, *Journal of Materials Science* 35 (2000) 1495–1499.
- [18] K.F. Zhang, S. Ding, G.F. Wang, Different superplastic deformation behavior of nanocrystalline Ni and ZrO<sub>2</sub>/Ni nanocomposite, *Materials Letters* 62 (2008) 719–722.
- [19] F.Y. Hou, W. Wang, H.T. Guo, Effect of the dispersibility of ZrO<sub>2</sub> nanoparticles in Ni–ZrO<sub>2</sub> electroplated nanocomposite coatings on the mechanical properties of nanocomposite coatings, *Applied Surface Science* 252 (2006) 3812–3817.
- [20] W. Wang, F.Y. Hou, H. Wang, H.T. Guo, Fabrication and characterization of Ni–ZrO<sub>2</sub> composite nano-coatings by pulse electrodeposition, *Scripta Materialia* 53 (2005) 613–618.
- [21] A. Ramalho, P.V. Antunes, Reciprocating wear test of dental composites against human teeth and glass, *Wear* 263 (2007) 1095–1104.
- [22] A. Ramalho, A reliability model for friction and wear experimental data, *Wear* 269 (2010) 213–223.
- [23] J.G. La Barbera-Sosa, Y.Y. Santana, E. Moreno, N. Cuadrado, J. Caro, P.O. Renault, E. Le Bourhis, M.H. Staia, E.S. Puchi-Cabrera, Effect of spraying distance on the microstructure and mechanical properties of a Colmonoy 88 alloy deposited by HVOF thermal spraying, *Surface and Coatings Technology* 205 (2010) 1799–1806.
- [24] X.B. Zhao and Z.H. Ye, Microstructure and wear resistance of molybdenum based amorphous nanocrystalline alloy coating fabricated by atmospheric plasma spraying, *Surface and Coatings Technology* <http://dx.doi.org/10.1016/j.surfcoat.2012.05.127>, in press.
- [25] T. Sidhu, S. Prakash, R.D. Agrawal, Studies on the properties of high-velocity oxy-fuel thermal spray coatings for gigher temperature applications, *Materials Science* 41 (2005) 805–823.
- [26] J.C. Fang, H.P. Zeng, W.J. Xu, Z.Y. Zhao, L. Wang, Prediction of in-flight particle behaviors in plasma spraying, *World Academy of Materials and Manufacturing Engineering* 18 (2006) 283–286.
- [27] O. Sarikaya, Effect of some parameters on microstructure and hardness of alumina coatings prepared by the air plasma spraying process, *Surface and Coatings Technology* 190 (2005) 388–393.
- [28] P. Fauchais, Understanding plasma spraying, *Journal of Physics D: Applied Physics* 37 (2004) R86–R108.
- [29] H. Chen, S. Lee, X. Zheng, C. Ding, Evaluation of unlubricated wear properties of plasma-sprayed nanostructured and conventional zirconia coatings by SRV tester, *Wear* 260 (2006) 1053–1060.
- [30] L.M. Chang, M.Z. An, H.F. Guo, S.Y. Shi, Microstructure and properties of Ni–Co/nano-Al<sub>2</sub>O<sub>3</sub> composite coatings by pulse reversal current electrodeposition, *Applied Surface Science* 253 (2006) 2132–2137.



---

## Annex G

---

**F. Fernandes, A. Loureiro, T. Polcar, A. Cavaleiro, "*The effect of increasing V content on the structure, mechanical properties and oxidation resistance of Ti-Si-V-N films deposited by DC reactive magnetron sputtering*", *Applied Surface Science*, 289, (2014) 114-123.**





# The effect of increasing V content on the structure, mechanical properties and oxidation resistance of Ti–Si–V–N films deposited by DC reactive magnetron sputtering



F. Fernandes<sup>a,\*</sup>, A. Loureiro<sup>a</sup>, T. Polcar<sup>b,c</sup>, A. Cavaleiro<sup>a</sup>

<sup>a</sup> CEMUC—Department of Mechanical Engineering, University of Coimbra, Rua Luís Reis Santos, 3030-788 Coimbra, Portugal

<sup>b</sup> Department of Control Engineering, Czech Technical University in Prague, Technická 2, Prague 6 166 27, Czech Republic

<sup>c</sup> nCATS, University of Southampton, Highfield Campus, SO17 1BJ Southampton, UK

## ARTICLE INFO

### Article history:

Received 26 June 2013

Received in revised form 18 October 2013

Accepted 19 October 2013

Available online 28 October 2013

### Keywords:

TiSi(V)N films

Structure

Mechanical properties

Oxidation resistance

Vanadium oxide

## ABSTRACT

In the last years, vanadium rich films have been introduced as possible candidates for self-lubrication at high temperatures, based on the formation of  $V_2O_5$  oxide. The aim of this investigation was to study the effect of V additions on the structure, mechanical properties and oxidation resistance of Ti–Si–V–N coatings deposited by DC reactive magnetron sputtering. The results achieved for TiSiVN films were compared and discussed in relation to TiN and TiSiN films prepared as reference. All coatings presented a fcc NaCl-type structure. A shift of the diffraction peaks to higher angles with increasing Si and V contents suggested the formation of a substitutional solid solution in TiN phase. Hardness and Young's modulus of the coatings were similar regardless on V content. The onset of oxidation of the films decreased significantly to 500 °C when V was added into the films; this behaviour was independent of the Si and V contents. The thermogravimetric isothermal curves of TiSiVN coatings oxidized at temperatures below the melting point of  $\alpha$ - $V_2O_5$  (~685 °C) showed two stages: at an early stage, the weight increase over time is linear, whilst, in the second stage, a parabolic evolution can be fitted to the experimental data. At higher temperatures only a parabolic evolution was fitted.  $\alpha$ - $V_2O_5$  was the main phase detected at the oxidized surface of the coatings. Reduction of  $\alpha$ - $V_2O_5$  to  $\beta$ - $V_2O_5$  phase occurred for temperatures above its melting point.

© 2013 Elsevier B.V. All rights reserved.

## 1. Introduction

High-speed cutting and dry machining processes without the use of environmental harmful lubrication requires milling tools capable to withstand severe conditions of wear, friction, oxidation and corrosion [1,2]. Solid lubricants coatings, such as WC/C,  $MoS_2$ , diamond-like carbon (DLC), hex-BN as well as their combinations in nanocrystalline or multilayer structures, have been successfully applied in such parts in order to increase their lifetime and performance for various tribological applications. However, considerable degradation of the tribological effectiveness of these coatings at elevated temperature has been reported due to their low resistance to oxidation [3–5]. To overcome this shortcoming, a new concept of lubrication based on the formation of lubricious oxides has been proposed. This is the case of the so-called Magnéli oxide phases based on Ti, Si, Mo, W and V, which have easy shear able planes [3,6]. Among these elements, particular attention has been given

to the vanadium-containing coatings (Magnéli phases  $V_nO_{3n-1}$ ), which showed interesting tribological properties in the temperature range 500–700 °C [3,7–12]. Dissimilar series of V-based hard coatings have been developed, such as ternary CrVN [13], (V,Ti)N [14], multilayer AlN/VN [15] and quaternary single layer or multilayered CrAlVN [16,17] and TiAlVN [2,8,18,19]. However, since other ternary coatings systems, based on (TiX)N with X = B, Cr, Al, Si, Cr, etc, have been attractive for advanced hard coating materials, the effect of vanadium doping to these systems should also be considered.

Among those ternary systems, most of the research works have been focused on TiSiN coatings deposited by CVD and/or PVD techniques [20,21]. Depending on the deposition conditions, these coatings could be deposited with a nanocomposite structure, consisting of nano-sized TiN crystallites surrounded by an amorphous matrix of  $Si_3N_4$  displaying very high hardness values [22], compared to any other ternary (TiX)N compound, with extremely good oxidation resistance [23,24]. In other deposition conditions, substitutional solid solution of Si in TiN structure (not predicted by the Ti–Si–N phase diagram) could be achieved [22,25,26]. Relatively to the friction coefficient of Ti–Si–N coatings, the studies have reported values in the range [0.6–1.3] at room and high temperatures

\* Corresponding author. Tel.: +351 239 790 745/+351 963 239 877; fax: +351 239 790 701.

E-mail address: [filipe.fernandes@dem.uc.pt](mailto:filipe.fernandes@dem.uc.pt) (F. Fernandes).

**Table 1**  
Sample designation and deposition parameters of the coatings.

	Sample	Target power density (W/cm <sup>2</sup> )		Deposition time (min)	Pellets of V at the Ti target
		Ti	TiSi <sub>2</sub>		
	Interlayer Ti	10	–	5	–
	Interlayer TiN	–	–	15	–
TiSiN	S1-0	6.5	1	210	0
	S1-4				4
TiSiVN	S1-8				8
	S1-12				12
TiSiN	S2-0	6	1.5	193	0
	S2-4				4
TiSiVN	S2-8				8
	S2-12				12
TiSiN	S3-0	5	2.5	153	0
	S3-4				4
TiSiVN	S3-8				8
	S3-12				12
	TiN	10	–	73	–

[27–29]. Since the addition of V successfully decreased the friction coefficient of binary and ternary systems (down to reported values of 0.2–0.3 at temperatures between 550 and 700 °C), similar studies on the effect of V-addition should be performed on TiSiN coatings exhibiting unique mechanical properties and oxidation resistance.

This paper reports the first results on the effect of increasing vanadium content to Ti–Si–V–N films deposited by DC reactive magnetron sputtering. It is focused on coating structure, mechanical properties and oxidation resistance. Comparison of the results with those achieved for reference TiN and TiSiN coatings is presented. The results of this study will support further research aimed at the tribological behaviour of the coatings at high temperatures.

## 2. Experimental procedure

Three series of TiSiN films with different Si contents, each series with increasing V contents (TiSiVN coatings), were deposited in a d.c. reactive magnetron sputtering machine equipped with two rectangular (100 × 200 mm) magnetron cathodes working in unbalanced mode. A high purity Ti (99.9%) target, with 18 holes of 10 mm in diameter (uniformly distributed throughout the preferential erosion zone of the target), and a high purity TiSi<sub>2</sub> (99.9%) composite target were used in the depositions. The different silicon contents were achieved by changing the power density applied to each target. The V content was varied by changing the number of high purity rods of Ti and V (with 10 mm in diameter) placed in the holes of the Ti target. 4, 8 and 12 cylindrical pieces of vanadium were used. In all the cases the total power applied to the targets was set to 1500 W. To serve as reference, a stoichiometric TiN coating was deposited from the Ti target. Hereinafter the coatings will be designated as Sx-y, where x is related to the specific power applied to the TiSi<sub>2</sub> target (see Table 1), and therefore associated to the Si content on the coatings, and y the number of V rods used in the depositions, giving an indication of V content in each series of TiSiVN films. Thus, denomination S2-0, S2-4, S2-8 and S2-12 represents coatings from the same series, i.e. with identical Si content (TiSi<sub>2</sub> target power 1.5 W/cm<sup>2</sup>), with increasing V content from 0 up to a maximum content achieved for the coating produced using 12 vanadium pellets embedded into the Ti target.

Polished high-speed steel (AISI M2) (Ø 20 × 3 mm, for mechanical properties measurements), FeCrAl alloy and alumina substrates (10 × 10 × 1 mm, for oxidation tests and structural analysis), stainless steel discs (Ø 20 × 1 mm, for residual stress measurements) and (1 1 1) silicon samples (10 × 10 × 0.8 mm, for thickness measurements and chemical composition evaluation) were used as

substrates. Prior to the depositions, all the substrates were ultrasonically cleaned in acetone for 15 min and alcohol for 10 min. The substrates were mounted in a substrate holder (which revolved with 18 rev/min around the centre axis) giving a target to substrate distance of 175 mm. Prior to deposition, the chamber was evacuated down to  $8.7 \times 10^{-4}$  Pa and the substrates were etched with Ar ion sputtering during 1 h with a bias voltage of –650 V to remove any surface contaminants. In order to enhance the adhesion of the coatings, Ti and TiN adhesion layers of approximately 0.24 and 0.45 µm, respectively, were deposited on the substrates before TiSi(V)N coatings. In all the depositions, the total working gas pressure was kept constant at 0.3 Pa, using approximately 30 sccm of Ar and 17 sccm of N<sub>2</sub>. The depositions were performed with a negative substrate bias of 50 V. The deposition time was set in order to obtain films with approximately 2.5 µm of total thickness (including interlayers). The deposition parameters are shown in Table 1.

The chemical composition of the coatings was evaluated by electron probe microanalysis (EPMA—Cameca SX 50). Crystallographic structure was investigated by X-ray diffraction (X' Pert Pro MPD diffractometer) using a grazing incidence angle of 1° and Cu K<sub>α1</sub> radiation ( $\lambda = 1.54060$  Å). The XRD spectra were fitted by using a pseudo-Voigt function to calculate either the full width at half maximum (FWHM) and the peak position ( $2\theta$ ). The fracture cross-section morphology and the thickness of the films were investigated by scanning electron microscopy (SEM). Further, profilometer was used to confirm coating thickness and to evaluate surface roughness.

The hardness and Young's modulus of films were measured in a nano-indentation equipment (Micro Materials NanoTest) using a Berkovich diamond pyramid indenter. In order to avoid the effect of the substrate, the applied load (10 mN) was selected to keep the indentation depth less than 10% of the coating' thickness. 32 measurements were performed in each sample. The level of residual stresses was calculated through the Stoney equation [30] by measuring the bulk deflection of the film-substrate body.

The oxidation resistance of the coatings was evaluated by thermogravimetric analysis (TGA) using industrial air (99.99% purity). The films deposited on alumina substrates were firstly heated with a constant temperature ramp of 20 °C/min from room temperature up to 1200 °C, in order to determine the onset point of oxidation. Then, coated specimens of FeCrAl alloy were subjected to isothermal tests at different selected temperatures and time. The weight gain of the samples was evaluated at regular 2 s intervals using a microbalance with an accuracy of 0.01 mg. The air flux used was 50 ml/min and the heating rate up to the isothermal temperature



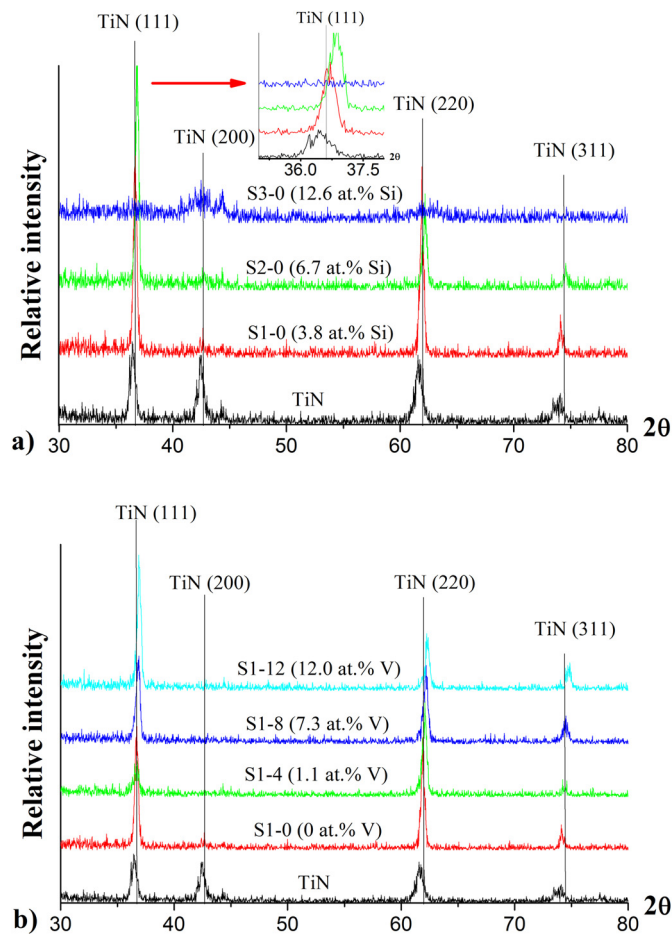


**Fig. 1.** XRD patterns of: (a) TiSiN coatings with Si content ranging from 0 to 12.6 at.%, (b) coating S1-0 with V additions.

was 20 °C/min. After oxidation tests, the surface morphology of the specimens was examined by scanning electron microscopy with energy dispersive X-ray spectroscopy (SEM–EDS) and their structure was evaluated by XRD diffraction. The oxide products on the surface were characterized by Raman spectroscopy.

### 3. Results and discussion

#### 3.1. Coatings characterization

##### 3.1.1. Chemical composition and microstructure

The elemental chemical composition of the coatings determined by EPMA is shown in Table 2. As could be expected, the simultaneous decrease in the power density of Ti target and increase in the power density of TiSi<sub>2</sub> target gave rise to higher Si content in the coatings. Only insignificant variations were detected on the Si/Ti ratios with incorporation of V in the Ti target. The nitrogen content of the coatings was close to 50 at.% regardless of Si and V.

The corresponding X-ray diffraction patterns of the as-deposited coatings are displayed in Fig. 1. The influence of increasing V content on TiSiN coatings is shown in Fig. 1b) for the film with lower Si content, as representative of all series containing vanadium. In all graphs TiN film pattern is shown as a reference. In all cases, the diffraction peaks could be generally assigned to the fcc NaCl-type crystalline TiN phase. The XRD pattern of the TiN reference coating reveals that all peaks are shifted to lower diffraction angles in relation to the standard ICDD card of TiN, probably indicating residual compressive stresses [31]. For TiSiN coatings with 3.8 and 6.7 at.% of Si, (200) peak vanishes and the sharpening of the peaks suggests

larger grain size. Based on Scherrer' equation, grain sizes of 16 and 24 nm were calculated for TiN and coatings with low Si content, respectively. With further increase of the Si content (12.6 at.% of Si) a strong decrease of the peaks intensity, as well as their significant broadening (a grain size of 6 nm was calculated), are observed suggesting a decrease of crystallinity. With increasing Si content, the fcc peaks are shifted to higher angles, behaviour associated to a smaller unit cell. This can be explained by the presence of Si in solid solution, since its smaller atomic radius promotes the contraction of the TiN lattice. Therefore, in this case the stoichiometric phases (TiN + Si<sub>3</sub>N<sub>4</sub>) do not segregate and nanocomposite structure is not formed. Such behaviour could be explained by the low deposition temperature together with low substrate ion bombardment, which do not provide the necessary mobility of the species for the nanocomposite formation [22]. This observation is in agreement with the results from the literature, where similar solid solutions and changes in the film orientation have been observed with silicon incorporation [21,25,32].

The coatings with V displayed similar XRD patterns and peaks to TiSiN. No significant changes in the peaks intensities or widths were observed, except for the highest Si content films where a small improvement in the crystallinity was detected. All the vanadium containing films had the XRD peaks shifted to higher angles, behaviour, once again, related to a smaller unit cell due to the substitution of Ti by the smaller V atoms. Similar trend was observed by Pfeiler et al. [2] for the TiAlVN system.

Fig. 2 displays typical surface and fracture cross section-micrographs of TiSiVN coatings. All coatings showed a typical columnar structure. As Si content was increased (see Fig. 2b)) for coating S1-0), the columns size and the surface roughness were firstly reduced, for silicon contents of 3.8 and 6.7 at.%, and then increased for the highest silicon content, which is an opposite trend than that observed for the grain size. The addition of V did not change the global type of columnar morphology and the coating cross-section was similar. The only exception was the strong increase of the size of the columns as well as the surface roughness (see Fig. 2c) for coating S1-12) for low silicon content coatings.

##### 3.1.2. Hardness, Young's modulus and residual stresses

The dependence of the hardness and Young' modulus on the Si and V content is shown in Fig. 3. As the silicon content in the TiSiN films increases, the hardness of coatings reached a maximum value of 27 GPa at a Si content of 6.7 at.%; then it dropped with further increasing Si content to a lower value than the reference TiN. Although the grain grow is observed with increasing Si additions up to 6.7 at.% of Si, the hardening of coatings is mostly result of the nitride lattice distortion, which improves the resistance to plastic deformation (solid solution hardening). Residual stresses should not be a factor of hardness differentiation between the coatings, since all films have approximately the same level of compressive residual stresses, with any Si addition (~3 GPa). This result also supports what was stated above that the shift of the peaks to the right with Si additions is exclusively due to substitutional solid solution. The decrease in hardness with further Si addition is due to the loss of crystallinity associated with the lower degree of phase nitriding regardless on the lower grain size [26]. Young's modulus progressively decreases with increasing Si content, which is related to changes in the binding energy between ions due to Si incorporations. Similar hardness and Young's modulus evolution as a function of Si content has been reported in Refs [25,33].

Concerning the effect of V addition on the hardness and Young' modulus, similar evolution was observed for all films (see e.g. Fig. 3b) for S1-y films). Although the variations are very small and often within the error bars of the hardness values, general trend is a slight increase in hardness followed by drop for the highest vanadium content. Coatings with the higher silicon content and with

**Table 2**  
Chemical composition of the dissimilar coatings in at.%.

Coating		at.%				
		N	O	Si	Ti	V
	TiN	49.8 ± 0.1	0.4 ± 0.1	–	49.6 ± 0.4	–
TiSiN	S1-0	51.1 ± 0.6	0.4 ± 0.1	3.8 ± 0.0	44.7 ± 0.7	–
	S1-4	51.4 ± 0.4	1.5 ± 0.3	3.1 ± 0.0	43.0 ± 0.7	1.1 ± 0.1
TiSiVN	S1-8	51.5 ± 0.2	1.2 ± 0.1	2.9 ± 0.0	37.1 ± 0.3	7.3 ± 0.1
	S1-12	49.7 ± 0.3	1.8 ± 0.1	2.8 ± 0.0	33.8 ± 0.3	12.0 ± 0.1
TiSiN	S2-0	51.5 ± 0.2	0.6 ± 0.1	6.7 ± 0.0	41.3 ± 0.3	–
	S2-4	52.1 ± 0.2	1.2 ± 0.1	5.7 ± 0.0	39.3 ± 0.4	1.6 ± 0.2
TiSiVN	S2-8	51.7 ± 0.1	1.4 ± 0.1	5.6 ± 0.1	33.6 ± 0.3	7.6 ± 0.2
	S2-12	51.1 ± 0.6	1.9 ± 0.2	5.3 ± 0.0	30.5 ± 0.6	11.3 ± 0.1
TiSiN	S3-0	51.4 ± 0.4	1.8 ± 0.1	12.6 ± 0.1	34.2 ± 0.5	–
	S3-4	52.9 ± 0.1	1.5 ± 0.1	10.7 ± 0.0	32.1 ± 0.2	2.7 ± 0.1
TiSiVN	S3-8	52.8 ± 0.2	2.0 ± 0.1	10.7 ± 0.1	27.2 ± 0.2	7.3 ± 0.1
	S3-12	52.4 ± 0.3	2.1 ± 0.2	10.3 ± 0.1	24.9 ± 0.9	10.4 ± 0.1

vanadium additions displayed lower hardness and Young's modulus values as compared to the other V rich coatings. The hardness enhance with V additions is probably due to the presence of V in solid solution. In fact, the similar level of residual stresses as function of V content measured, which revealed to be from the range of 3–4 GPa, and the observed shift of peaks to higher angles with V incorporation, supports the previous affirmation.

### 3.2. Continuous and isothermal oxidation in air

The effect of increasing Si and V content on the onset point of oxidation of the TiN and TiSiN systems, respectively, are shown in Fig. 4. Silicon incorporation strongly improved the onset of oxidation of the coatings, with the highest silicon content (S3-0) showing the highest oxidation resistance. Kacsich et al. [34,35] reported that the high oxidation resistance of these coatings was due to the presence of a protective silicon-rich oxide layer. This layer acted as an efficient diffusion barrier against oxygen and metal ions diffusion; thus, it protected the coating from further oxidation. Our results showed that the onset point of oxidation of films decreased significantly down to a temperature of approximately 500 °C (lower than TiN) for all coatings containing vanadium. Interestingly, this behaviour was independent of Si content of the films and, therefore, the vanadium incorporation interfered with the diffusion of silicon and the consequent formation of a continuous protective silicon oxide layer. Furthermore, all V-containing coatings were completely oxidized at a lower temperature than TiN film. Lewis et al. [7], Zhou et al. [36], and Franz et al. [37], who studied the effect of V doping on the oxidation behaviour of multilayered TiAlN/VN and CrAlVN coatings, respectively, also observed a similar decrease in the onset point of oxidation. In order to better characterize the oxidation behaviour of the V rich coatings, isothermal oxidation tests were conducted at selected temperatures using S2-8 coating deposited onto FeCrAl alloy substrates. The isothermal curves were compared with those of TiSiN coating with similar Si content and with TiN (see Fig. 5).

Comparing the mass gain of the coatings and taking into account the testing temperature in each case, it is possible to conclude that V-free TiSiN coating (S2-0 tested at 900 °C) is much more resistant to oxidation. This coating exhibits a typical parabolic oxidation weight gain as a function of time indicating the formation of protective silicon-rich oxide layer, as referred to above. Similar type of evolution is exhibited by TiN coating; however, in this case the titanium oxide scale does not protect the coatings and, thus, it is effective only at low isothermal temperature [38]. It should be remarked that during continuous oxidation test up to 1200 °C, at 900 °C TiN coatings was already half consumed. Regarding the

isothermal curves of TiSiN coating with V additions (S2-8), it can be concluded that, independently of the isothermal temperature and time of exposure, their mass gain is always much higher than TiN and V-free TiSiN coatings (S2-0). The isothermal curves tested at 550 and 600 °C showed two steps: at an early stage, the weight gain is rapidly increasing almost linearly up to approximately 0.1 mg/cm<sup>2</sup> (particularly at 600 °C), whereas in the second stage, a parabolic evolution can be fitted. Isothermal annealing of S2-8 at 700 °C shows significant increase of mass gain following the parabolic evolution.

#### 3.2.1. Surface structure

As it would be expected, both TiN annealed at 600 °C and S2-0 coating annealed at 900 °C exhibited several intense peaks belonging to the (1 1 0), (1 0 1), (2 0 0), (1 1 1) and (2 1 0) of a tetragonal phase related to rutile/TiO<sub>2</sub> (ICDD card 76-0649) (not shown here). Weak peaks assigned to TiN (ICDD card 87-0628) were observed in the XRD spectra of the S2-0 coating, which was in a good agreement with its annealing curve, since only partial oxidation of the film was expected. Moreover, diffraction peaks associated with Si oxide were not detected on the oxidized surface of S2-0 film suggesting an amorphous character of the protective oxide layer. This result is in agreement with literature, where similar observation was reported [34,35].

XRD patterns of S2-8 oxidized coatings in isothermal tests are shown in Fig. 6. The main phases detected by XRD were Ti–V–O and V–O oxides; however, depending on the isothermal temperature and time, different orientations and peaks assigned to V–O were perceived. After annealing at 550 °C during 1 h, the following phases could be identified: Ti(V)O<sub>2</sub> (ICDD card 77-0332) and α-V<sub>2</sub>O<sub>5</sub> (ICDD card 41-1426) with a preferred orientation following the (0 0 1) plane (peak at 20.3°), together with the f.c.c. nitride from the coating. The same phases were detected at 600 °C during 10 min, however, α-V<sub>2</sub>O<sub>5</sub> phase showed random orientation. Further increase in isothermal time (annealing at 600 °C during 30 min) resulted in loss of TiN peaks and the orientation of the α-V<sub>2</sub>O<sub>5</sub> phase is again following (0 0 1) plane. The absence of TiN peaks is in good agreement with the isothermal curve shown in Fig. 5. Progressive oxidation is demonstrated in the intensity of (0 0 1) reflection after 30 min of annealing, where the amount of α-V<sub>2</sub>O<sub>5</sub> is clearly higher. These changes in phase proportion and orientation have already been observed by several authors during the oxidation of TiAlN/VN multilayer and TiAlVN single layered coatings [1,7,8,36]. Increasing the heat treatment to 700 °C, which is temperature higher than the melting point of α-V<sub>2</sub>O<sub>5</sub> (~685 °C [10,36]), resulted in the random orientation of this phase; moreover, a sharp peak at 2θ = 12.8° identified as β-V<sub>2</sub>O<sub>5</sub> (ICDD card 45-1074) with (0 0 2) preferential

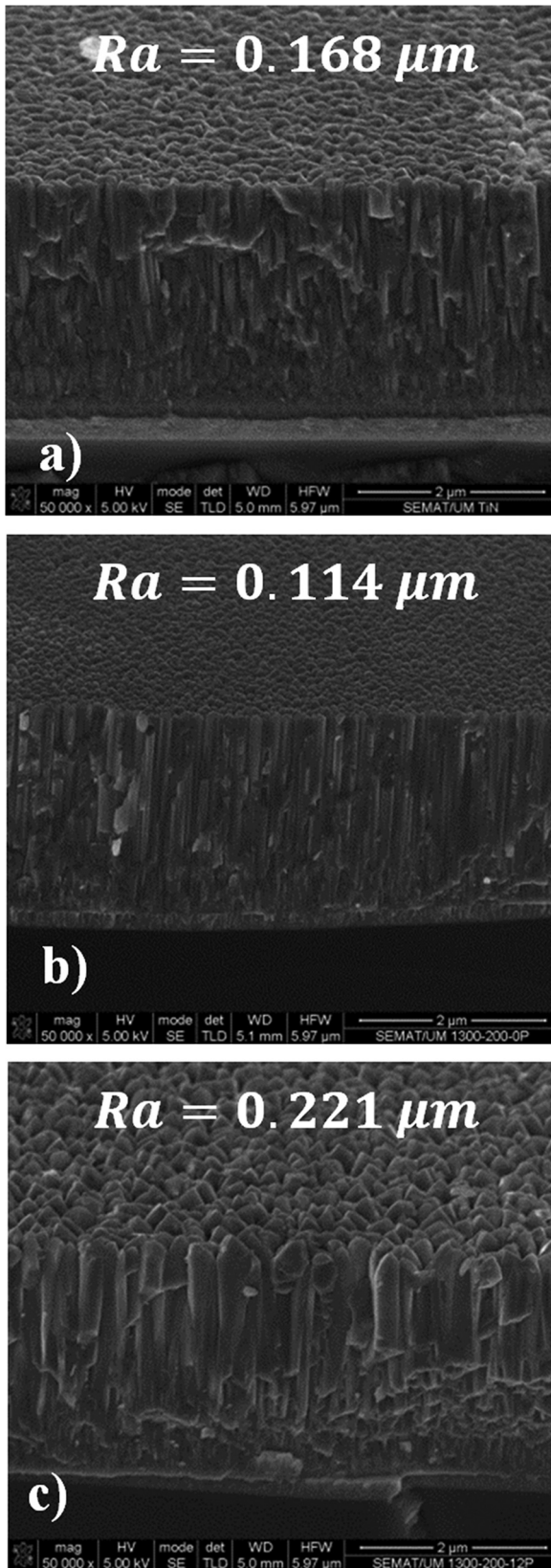


Fig. 2. SEM fracture cross section micrographs of: (a) coating TiN, (b) coating S1-0, (c) coating S1-12.

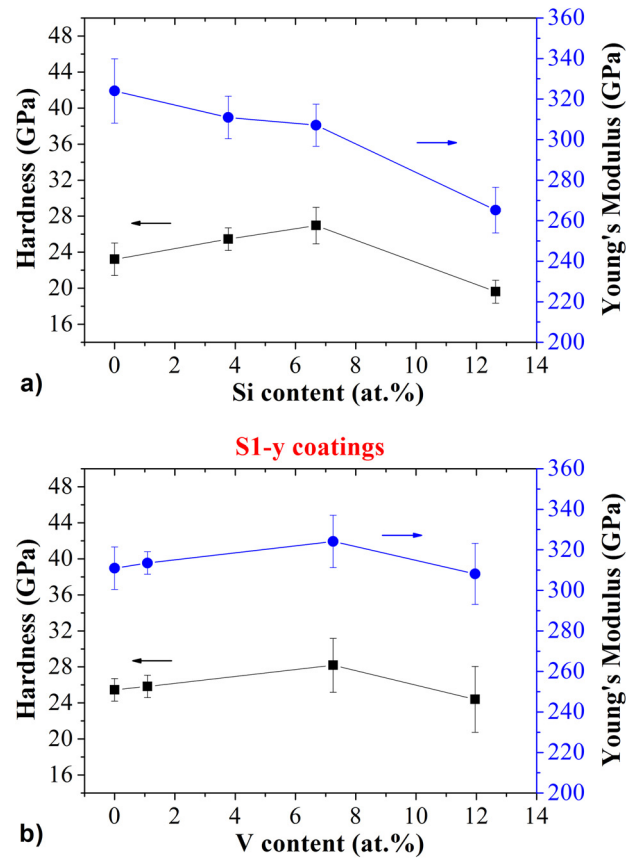


Fig. 3. (a) Effect of Si content on hardness and Young's modulus for the TiN system. (b) Effect of V content on hardness and Young's modulus for coating S1-0.

orientation appearing [39].  $\beta$ - $V_2O_5$  phase is a result of loss of O from  $\alpha$ - $V_2O_5$ , due to a reduction process [40]. We should emphasize here that vanadium oxides observed on the oxidized surface are optimal from the tribological point of view. Vanadium oxide could act as low-friction solid lubricant or, for higher temperatures, as liquid lubricant. Therefore the drop in onset oxidation temperature should not be considered as a significant drawback of TiSiVN coatings.

### 3.2.2. Surface morphology and characterization

Typical SEM surface micrographs of the S2-0 and V-rich coating (S2-8) isothermally oxidized at different temperatures and times

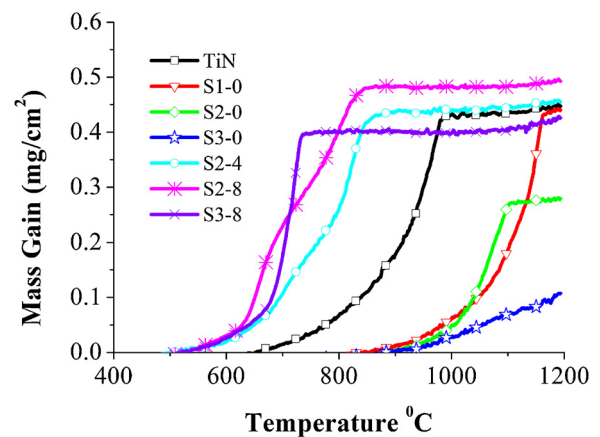
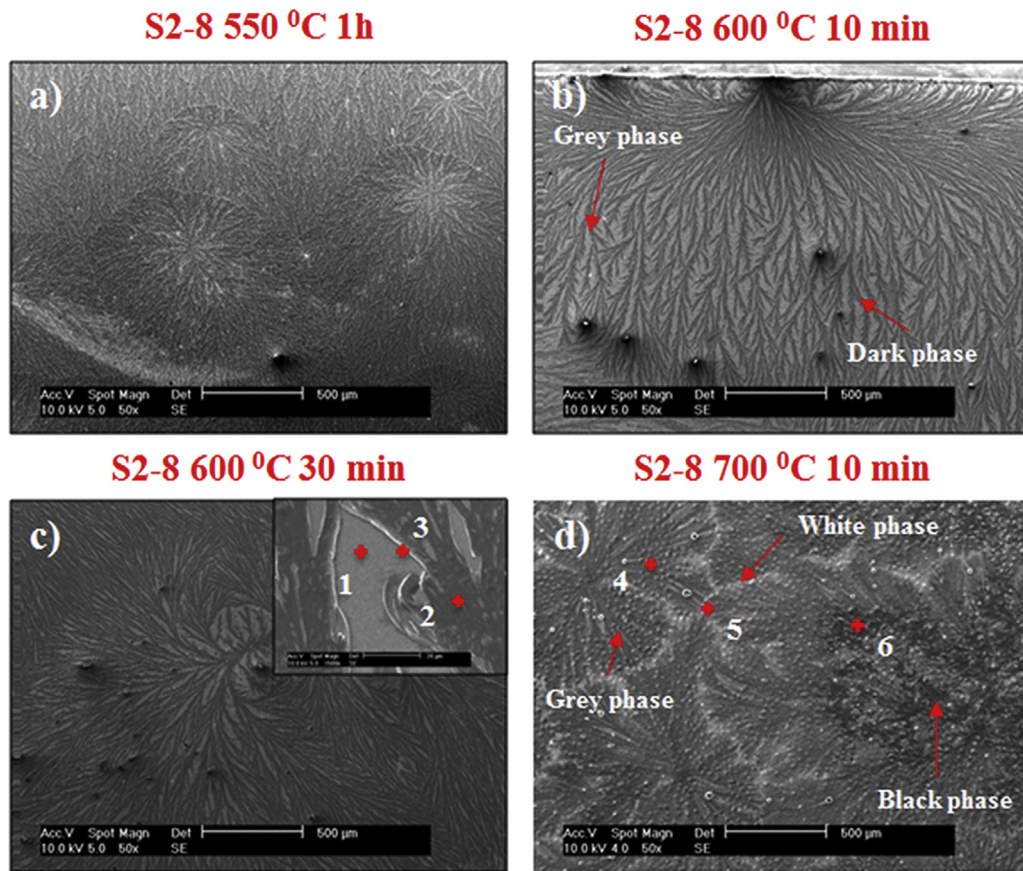
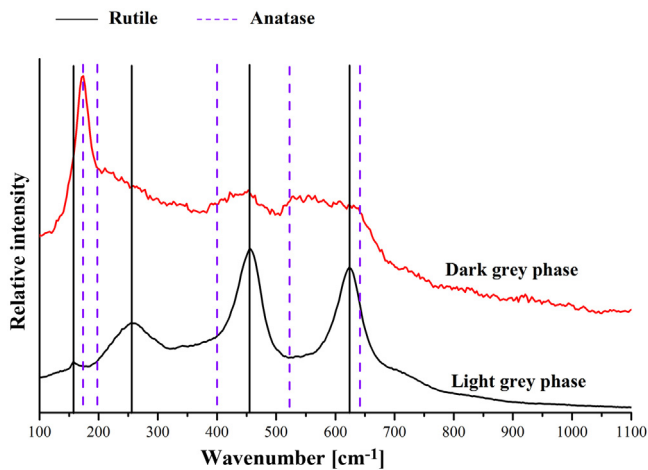


Fig. 4. Thermal gravimetric oxidation rate of coatings deposited on  $Al_2O_3$  substrates using the linear-temperature ramp (RT to 1200 °C at 20 °C/min).





**Fig. 8.** Typical surface morphology of oxidized coatings: (a) coating S2-8 exposed to 550 °C during 1 h, (b) coating S2-8 exposed to 600 °C during 10 min, (c) coating S2-8 exposed to 600 °C during 30 min, (d) coating S2-8 exposed to 700 °C during 10 min.



**Fig. 9.** Raman spectra of dark and light grey phases identified in Fig. 7.

coming from a sub-surface layer, an oxide layer rich in Ti and Si should coexist with a global chemical composition similar to that of light grey phase.

From the three different morphological zones of sample annealed at 700 °C for 10 min (Fig. 8d), EDS analysis showed that the two grey phases were mainly rich in vanadium and oxygen. Signals of elements from the substrate were detected in the dark phase, particularly Al, which in conjunction with XRD results, allowed identifying it as  $\beta$ - $V_2O_5$ . In fact, it is well known, that the loss of O from  $\alpha$ - $V_2O_5$ , due to a reduction process, leads to its transformation in  $\beta$ - $V_2O_5$  [40,43]. The presence of highly oxygen reactive elements, such as aluminum, in the substrate can reduce the molten  $\alpha$ - $V_2O_5$ , subtracting O and promoting the formation of  $\beta$ - $V_2O_5$ . The Raman spectra of the dark and light grey phases plotted in Fig. 12 show similar Raman patterns with peaks related to  $V_2O_5$ . Both  $\alpha$ - and  $\beta$ - $V_2O_5$  display similar Raman spectra [44]. The segregated white areas located at the boundaries of the grey phase (see ratio Si/Ti of point 5) were rich in Si and Ti, suggesting to be silicon and titanium oxides.

A good correlation was found between the isothermal oxidation curve, XRD measurements and surface morphology of S2-8 coating. At temperatures below the melting point of  $\alpha$ - $V_2O_5$ , the

**Table 3**

Ratio between the peaks intensities of V K $\beta$  (Si K $\alpha$ ) and Ti K $\alpha$  from EDS analyses of points marked in Fig. 8.

		Points					
		1	2	3	4	5	6
Ratios	V K $\beta$ /Ti K $\alpha$	0.04	0.1	0.15	0.63	0.01	0.68
	Si K $\alpha$ /Ti K $\alpha$	0.77	0.99	0.19	0.58	0.49	1.00

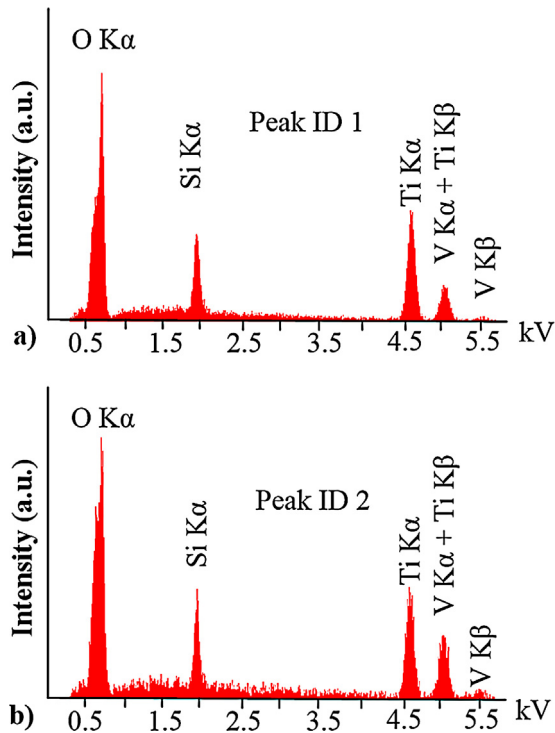


Fig. 10. Energy dispersive X-ray analysis (EDAX) of points 1 and 2 identified in Fig. 8.

isothermal oxidation curve starts with a linear increase in the mass gain and then changes to a parabolic law. The XRD spectra of specimen S2-8 oxidized during 10 min at 600 °C, in the first stage of the oxidation process, revealed the presence of intense peaks of  $\alpha$ -V<sub>2</sub>O<sub>5</sub>. Further increase in isothermal time to 30 min showed an increased amount of  $\alpha$ -V<sub>2</sub>O<sub>5</sub>, as confirmed by the increase of the grey dark phase, above attributed to V-rich zones. XRD pattern for this sample also showed an increase in Ti(V)O<sub>2</sub> peaks intensity suggesting a thickening of the oxide scale. Therefore, the first linear part of the isothermal curve is due to the oxidation of both titanium and vanadium to form Ti(V)O<sub>2</sub> and  $\alpha$ -V<sub>2</sub>O<sub>5</sub>, respectively.  $\alpha$ -V<sub>2</sub>O<sub>5</sub> is a non-protective oxide and Ti(V)O<sub>2</sub> is still not in enough amounts to form a continuous protective scale, reason why a linear oxidation rate is observed. For longer oxidation times, the progressive thickening of the Ti-rich oxide scale will make difficult the oxygen diffusion inward retarding the reaction and promoting the parabolic behaviour. However, the protection is not so efficient

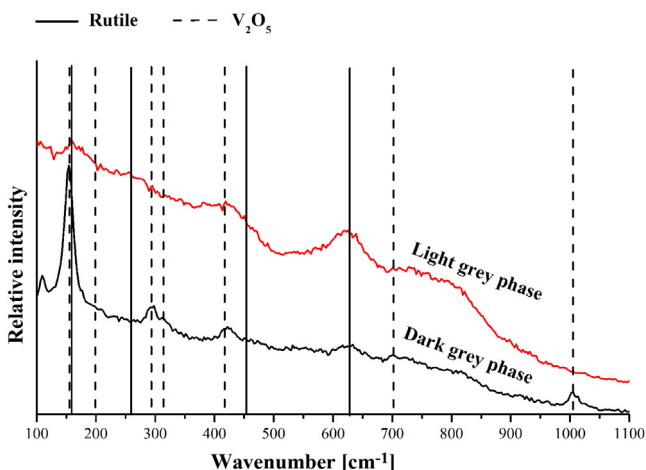


Fig. 11. Raman spectra of phase 1 and 2 identified in Fig. 8.

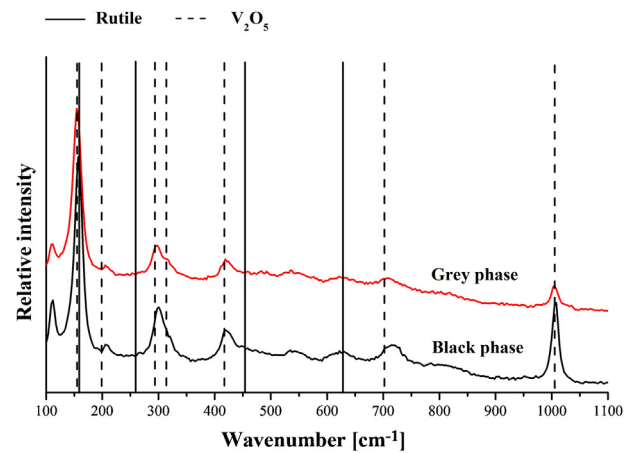


Fig. 12. Raman spectra of phase 4 and 5 identified in Fig. 8.

as in TiN and/or Ti–Si–N samples (see Fig. 5) due to the disruption induced by the outward/lateral diffusion of V ions through the oxide scale. In any condition the protective Si–O layer could be also formed. Similar isothermal evolution was reported by Zhou et al. [36], which during isothermal oxidation of multilayered TiAlN/VN coatings have detected  $\alpha$ -V<sub>2</sub>O<sub>5</sub> at the initial stage of oxidation. In their system, the mass gain curves also showed initially a linear evolution, followed by a parabolic growth, similar to what was observed here for TiSiVN films. Keller and Douglass [45] also showed that pure vanadium oxidizes linearly, whereas the addition of different elements (Al, Cr, Ti) could transform the initial linear mass gain for a parabolic one due to the modification of the formed oxide layer.

At 700 °C, temperature higher than the melting point of  $\alpha$ -V<sub>2</sub>O<sub>5</sub>, very high oxidation rates were measured and high amounts of V-oxides were detected by XRD. The extremely high parabolic evolution suggests a very high diffusion rate of the reactive ions through the oxide scales.

A comparison between TiSiVN with CrAlVN and TiAlVN (in single layered or multilayered configuration) coatings, reveals a lower onset point of oxidation of approximately 100 °C. In CrAlVN and TiAlVN coatings the onset point of oxidation was close to  $\sim$ 600 °C [8,36,37]. In the case of the TiAlVN films, signals of lubricious  $\alpha$ -V<sub>2</sub>O<sub>5</sub> were detected as soon as the oxidation started, while at high temperatures only AlVO<sub>4</sub> and TiO<sub>2</sub> were identified [8]. For CrAlVN coatings, AlVO<sub>4</sub>, (Al, Cr, V)<sub>2</sub>O<sub>3</sub> as well as  $\alpha$ -V<sub>2</sub>O<sub>5</sub> oxides were observed for an annealing temperature of 700 °C [37]. In these studies, the lower onset point of oxidation displayed by the V-containing coatings was explained by the reactions occurring between protective oxides and vanadium (such as formation of Al–V–O phases). In the present TiSiVN system combination of V with titanium or silicon oxide was not detected. Therefore, we suggest that the loss of oxidation resistance of TiSiVN coatings is due to the rapid oxidation of V and the outwards diffusion of its ions through the Ti-rich oxide scale. Further work is needed to understand the mechanisms involved during the oxidation deterioration of TiSiN coatings with V additions and their corresponding oxide scale formation. The performance of solid solution coatings for high temperature sliding application should be investigated in further work. Rapid formation of vanadium oxide could indeed reduce friction at temperatures higher than 500 °C; nonetheless, the wear resistance of the coating can be significantly compromised by low oxidation resistance. In future research, we propose to deposit nanocomposite structure of TiSiVN combining nanograins of c-TiVN embedded into amorphous Si–N matrix, to control the outwards diffusion of vanadium.

#### 4. Conclusion

This investigation concerned the influence of V additions on the structure, mechanical properties and oxidation resistance of Ti–Si–V–N coatings deposited by DC reactive magnetron sputtering. These coatings were compared to TiN and TiSiN films. According to XRD analyses, all coatings showed an fcc NaCl-type structure assigned to crystalline TiN. A shift of the peaks to the right was observed with Si and V additions, indicative of a substitutional solid solution. Hardness and Young modulus of TiSiN coatings was insignificantly changed with increasing V content. The onset of oxidation of the coatings decreased with V additions down to temperatures as low as 500 °C, independently of the Si and V content in the coatings. TiN and TiSiN coating exhibits a typical parabolic oxidation weight gain as a function of time, while a different evolution is displayed by TiSiVN films. At temperatures below the melting point of  $\alpha$ -V<sub>2</sub>O<sub>5</sub> (~685 °C) two stages were exhibited: at an early stage, the weight increase over time is linear, whilst, in a second stage a parabolic evolution could be fitted to the experimental data; on the other hand, at high temperatures only a parabolic evolution was fitted.  $\alpha$ -V<sub>2</sub>O<sub>5</sub> showed to be the main phase present at the oxidized surface of coatings. Reduction of this phase occurred for temperatures above their melting point. The relative amounts of V<sub>2</sub>O<sub>5</sub> detected at the oxidized surface of V rich films are promising to achieve the envisaged good tribological properties; however it can be significantly compromised by their low oxidation resistance.

#### Acknowledgments

This research is sponsored by FEDER funds through the program COMPETE–Programa Operacional Factores de Competitividade–and by national funds through FCT – Fundação para a Ciência e a Tecnologia, under the projects: PEST-C/EME/UI0285/2013, CENTRO-07-0224-FEDER-002001 (Mais Centro SCT.2011.02.001.4637), PTDC/EME-TME/122116/2010 and Plungetec, as well as the grant (SFRH/BD/68740/2010).

#### References

- [1] Z. Zhou, W.M. Rainforth, D.B. Lewis, S. Creasy, J.J. Forsyth, F. Clegg, A.P. Ehiassarian, P.E. Hovsepian, W.D. Münz, Oxidation behaviour of nanoscale TiAlN/VN multilayer coatings, *Surf. Coat. Technol.* 177–178 (2004) 198–203.
- [2] M. Pfeiler, K. Kutschej, M. Penoy, C. Michotte, C. Mitterer, M. Kathrein, The effect of increasing V content on structure, mechanical and tribological properties of arc evaporated Ti–Al–V–N coatings, *Int. J. Refract. Met. Hard Mater* 27 (2009) 502–506.
- [3] N. Fateh, G.A. Fontalvo, G. Gassner, C. Mitterer, Influence of high-temperature oxide formation on the tribological behaviour of TiN and VN coatings, *Wear* 262 (2007) 1152–1158.
- [4] E. Badisch, G.A. Fontalvo, M. Stoiber, C. Mitterer, Tribological behavior of PACVD TiN coatings in the temperature range up to 500 °C, *Surf. Coat. Technol.* 163–164 (2003) 585–590.
- [5] M. Stoiber, E. Badisch, C. Lugmair, C. Mitterer, Low-friction TiN coatings deposited by PACVD, *Surf. Coat. Technol.* 163–164 (2003) 451–456.
- [6] E. Lugscheider, O. Knotek, K. Bobzin, S. Bärwulf, Tribological properties, phase generation and high temperature phase stability of tungsten- and vanadium-oxides deposited by reactive MSIP–PVD process for innovative lubrication applications, *Surf. Coat. Technol.* 133–134 (2000) 362–368.
- [7] D.B. Lewis, S. Creasey, Z. Zhou, J.J. Forsyth, A.P. Ehiassarian, P.E. Hovsepian, Q. Luo, W.M. Rainforth, W.D. Münz, The effect of (Ti + Al):V ratio on the structure and oxidation behaviour of TiAlN/VN nano-scale multilayer coatings, *Surf. Coat. Technol.* 177–178 (2004) 252–259.
- [8] K. Kutschej, P.H. Mayrhofer, M. Kathrein, P. Polcik, C. Mitterer, Influence of oxide phase formation on the tribological behaviour of Ti–Al–V–N coatings, *Surf. Coat. Technol.* 200 (2005) 1731–1737.
- [9] K. Kutschej, P.H. Mayrhofer, M. Kathrein, P. Polcik, C. Mitterer, A new low-friction concept for Ti<sub>1-x</sub>Al<sub>x</sub>N based coatings in high-temperature applications, *Surf. Coat. Technol.* 188–189 (2004) 358–363.
- [10] G. Gassner, P.H. Mayrhofer, K. Kutschej, C. Mitterer, M. Kathrein, A new low friction concept for high temperatures: Lubricious oxide formation on sputtered VN coatings, *Tribol. Lett.* 17 (2004) 751–756.
- [11] P.H. Mayrhofer, P.E. Hovsepian, C. Mitterer, W.D. Münz, Calorimetric evidence for frictional self-adaptation of TiAlN/VN superlattice coatings, *Surf. Coat. Technol.* 177–178 (2004) 341–347.
- [12] A. Glaser, S. Surnev, F.P. Netzer, N. Fateh, G.A. Fontalvo, C. Mitterer, Oxidation of vanadium nitride and titanium nitride coatings, *Surf. Sci.* 601 (2007) 1153–1159.
- [13] M. Uchida, N. Nihira, A. Mitsuo, K. Toyoda, K. Kubota, T. Aizawa, Friction and wear properties of CrAlN and CrVN films deposited by cathodic arc ion plating method, *Surf. Coat. Technol.* 177–178 (2004) 627–630.
- [14] J.H. Ouyang, S. Sasaki, Tribo-oxidation of cathodic arc ion-plated (V,Ti)N coatings sliding against a steel ball under both unlubricated and boundary-lubricated conditions, *Surf. Coat. Technol.* 187 (2004) 343–357.
- [15] J.-K. Park, Y.-J. Baik, Increase of hardness and oxidation resistance of VN coating by nanoscale multilayered structurization with AlN, *Mater. Lett.* 62 (2008) 2528–2530.
- [16] R. Franz, J. Neidhardt, R. Kaendl, B. Sartory, R. Tessadri, M. Lechthaler, P. Polcik, C. Mitterer, Influence of phase transition on the tribological performance of arc-evaporated AlCrVN hard coatings, *Surf. Coat. Technol.* 203 (2009) 1101–1105.
- [17] Y. Qiu, S. Zhang, J.-W. Lee, B. Li, Y. Wang, D. Zhao, Self-lubricating CrAlN/VN multilayer coatings at room temperature, *Appl. Surf. Sci.* 279 (2013) 189–196.
- [18] W. Tillmann, S. Momeni, F. Hoffmann, A study of mechanical and tribological properties of self-lubricating TiAlVN coatings at elevated temperatures, *Tribol. Int.* 66 (2013) 324–329.
- [19] Q. Luo, Temperature dependent friction and wear of magnetron sputtered coating TiAlN/VN, *Wear* 271 (2011) 2058–2066.
- [20] S.H. Kim, J.K. Kim, K.H. Kim, Influence of deposition conditions on the microstructure and mechanical properties of Ti–Si–N films by DC reactive magnetron sputtering, *Thin Solid Films* 420–421 (2002) 360–365.
- [21] M. Nose, Y. Deguchi, T. Mae, E. Honbo, T. Nagae, K. Nogi, Influence of sputtering conditions on the structure and properties of Ti–Si–N thin films prepared by r.f.-reactive sputtering, *Surf. Coat. Technol.* 174–175 (2003) 261–265.
- [22] S. Veprek, H.D. Männling, P. Karvankova, J. Prochazka, The issue of the reproducibility of deposition of superhard nanocomposites with hardness of  $\geq 50$  GPa, *Surf. Coat. Technol.* 200 (2006) 3876–3885.
- [23] D. Pilloud, J.F. Pierson, M.C. Marco de Lucas, A. Cavaleiro, Study of the structural changes induced by air oxidation in Ti–Si–N hard coatings, *Surf. Coat. Technol.* 202 (2008) 2413–2417.
- [24] M. Diserens, J. Patscheider, F. Levy, Mechanical properties and oxidation resistance of nanocomposite TiN–SiN<sub>x</sub> physical-vapor-deposited thin films, *Surf. Coat. Technol.* 120 (1999) 158–165.
- [25] F. Vaz, L. Rebouta, P. Goudeau, J. Pacaud, H. Garem, J.P. Rivière, A. Cavaleiro, E. Alves, Characterisation of Ti<sub>1-x</sub>Si<sub>x</sub>N<sub>y</sub> nanocomposite films, *Surf. Coat. Technol.* 133–134 (2000) 307–313.
- [26] M. Diserens, J. Patscheider, F. Lévy, Improving the properties of titanium nitride by incorporation of silicon, *Surf. Coat. Technol.* 108–109 (1998) 241–246.
- [27] Y.H. Cheng, T. Browne, B. Heckerman, E.L. Meletis, Mechanical and tribological properties of nanocomposite TiSiN coatings, *Surf. Coat. Technol.* 204 (2010) 2123–2129.
- [28] J. Patscheider, T. Zehnder, M. Diserens, Structure–performance relations in nanocomposite coatings, *Surf. Coat. Technol.* 146–147 (2001) 201–208.
- [29] D. Ma, S. Ma, K. Xu, The tribological and structural characterization of nano-structured Ti–Si–N films coated by pulsed-d.c. plasma enhanced CVD, *Vacuum* 79 (2005) 7–13.
- [30] G. Stoney, The tension of metallic films deposited by electrolysis, *Proc. R. Soc. London, Ser. A* 82 (1909) 172–175.
- [31] C.P. Constable, D.B. Lewis, J. Yarwood, W.D. Münz, Raman microscopic studies of residual and applied stress in PVD hard ceramic coatings and correlation with X-ray diffraction (XRD) measurements, *Surf. Coat. Technol.* 184 (2004) 291–297.
- [32] F. Vaz, L. Rebouta, B. Almeida, P. Goudeau, J. Pacaud, J.P. Rivière, J. Bessa e Sousa, Structural analysis of Ti<sub>1-x</sub>Si<sub>x</sub>N<sub>y</sub> nanocomposite films prepared by reactive magnetron sputtering, *Surf. Coat. Technol.* 120–121 (1999) 166–172.
- [33] M. Diserens, J. Patscheider, F. Lévy, Mechanical properties and oxidation resistance of nanocomposite TiN–SiN<sub>x</sub> physical-vapor-deposited thin films, *Surf. Coat. Technol.* 120–121 (1999) 158–165.
- [34] T. Kacsich, S. Gasser, Y. Tsuji, A. Dommann, M.A. Nicolet, A. Nicolet, Wet oxidation of Ti<sub>34</sub>Si<sub>23</sub>B<sub>43</sub>, *Br. J. Appl. Phys.* 85 (1999) 1871–1875.
- [35] T. Kacsich, M.A. Nicolet, Moving species in Ti<sub>34</sub>Si<sub>23</sub>N<sub>43</sub> oxidation, *Thin Solid Films* 349 (1999) 1–3.
- [36] Z. Zhou, W.M. Rainforth, C. Rodenburg, N.C. Hyatt, D.B. Lewis, P.E. Hovsepian, Oxidation behavior and mechanisms of TiAlN/VN coatings, *Metall. Mater. Trans. A* 38 (2007) 2464–2478.
- [37] R. Franz, J. Neidhardt, C. Mitterer, B. Schaffer, H. Hutter, R. Kaendl, B. Sartory, R. Tessadri, M. Lechthaler, P. Polcik, Oxidation and diffusion processes during annealing of AlCrVN hard coatings, *J. Vac. Sci. Technol.*, A 26 (2008) 302–308.
- [38] M. Wittmer, J. Noser, H. Melchior, Oxidation kinetics of TiN thin films, *J. Appl. Phys.* 52 (1981) 6659–6664.
- [39] C.W. Zou, X.D. Yan, J. Han, R.Q. Chen, W. Gao, Microstructures and optical properties of  $\beta$ -V<sub>2</sub>O<sub>5</sub> nanorods prepared by magnetron sputtering, *J. Phys. D: Appl. Phys.* 42 (2009) 145402.
- [40] A. Bouzidi, N. Benramdane, S. Bresson, C. Mathieu, R. Desfeux, M.E. Marssi, X-ray and Raman study of spray pyrolysed vanadium oxide thin films, *Vib. Spectrosc.* 57 (2011) 182–186.
- [41] M. Fernández-García, X. Wang, C. Belver, J.C. Hanson, J.A. Rodriguez, Anatase-TiO<sub>2</sub> nanomaterials: morphological/size dependence of the crystallization and phase behavior phenomena, *J. Phys. Chem. C* 111 (2006) 674–682.

- [42] R.J. Gonzales, Raman, Infrared, X-ray, and EELS Studies of Nanophase Titania, in: Ph.D. Dissertation, Virginia Polytechnic Institute, Blacksburg, Virginia, 1996, pp. 426.
- [43] V.P. Filonenko, M. Sundberg, P.E. Werner, I.P. Zibrov, Structure of a high-pressure phase of vanadium pentoxide beta-V<sub>2</sub>O<sub>5</sub>, *Acta Crystallogr., Sect. B: Struct. Sci.* 60 (2004) 375–381.
- [44] P. Balog, D. Orosel, Z. Cancarevic, C. Schon, M. Jansen, V<sub>2</sub>O<sub>5</sub> phase diagram revisited at high pressures and high temperatures, *J. Alloys Compd.* 429 (2007) 87–98.
- [45] J.G. Keller, D.L. Douglass, The high-temperature oxidation behavior of vanadium–aluminum alloys, *Oxid. Met.* 36 (1991) 439–464.



---

## Annex H

---

**F. Fernandes, J. Morgiel, T. Polcar, A. Cavaleiro, *Oxidation and diffusion processes during annealing of TiSi(V)N films*, (2014), under review, “Thin Solid Films”.**



## Oxidation and diffusion processes during annealing of TiSi(V)N films

F. Fernandes<sup>1,\*</sup>, J. Morgiel<sup>2</sup>, T. Polcar<sup>3,4</sup>, A. Cavaleiro<sup>1</sup>

<sup>1</sup>SEG-CEMUC - Department of Mechanical Engineering, University of Coimbra, Rua Luís Reis Santos, 3030-788 Coimbra, Portugal.

<sup>2</sup>Institute of Metallurgy and Materials Science of Polish Academy of Sciences, Krakow, Poland

<sup>3</sup>National Centre for Advanced Tribology (nCATS), School of Engineering Sciences, University of Southampton, Highfield, Southampton, SO17 1BJ, UK.

<sup>4</sup>Department of Control Engineering Czech Technical University in Prague Technicka 2, Prague 6, 166 27 Czech Republic.

\*Email address: filipe.fernandes@dem.uc.pt, tel. + (351) 239 790 745, fax. + (351) 239 790 701

### Abstract

The effect of V additions on oxidation resistance, oxide scale formation and diffusion processes for TiSiVN system and their comparison to TiSiN is investigated. A dual layer oxide was formed in the case of TiSiN coating with a protective Si-O layer at an oxide/coating interface; however, in zones of film defects a complex oxide structure was developed. V additions increased the oxidation rate of the coatings as a result of the inversion of the oxidation mechanism due to ions diffusion throughout the oxide scale, which inhibited the formation of a continuous protective silicon oxide layer.

Keywords: TiSiVN system, structural evolution, oxidation, oxide scale, diffusion processes

### 1. Introduction

TiSiN solid solution or nanocomposite coatings are well established in applications like high speed cutting and dry machining processes due to their excellent oxidation resistance and high hardness. However, the main drawback of the aforementioned coating system is their high friction coefficient, typically in the range of 0.6 - 1.3 at room and high temperatures [1]. Recently, the formation of thin reaction films in sliding contacts has provided the basis for development of adaptive, self-lubricating coatings guaranteeing low friction at high temperature. Magnéli phase oxides based on Ti, Si, Mo, W and V, with low shear strength

have attracted the scientific community and particular attention has been given to vanadium oxide. The beneficial influence of Magnéli oxides formed by oxidation of vanadium on the friction has already been reported for ternary CrVN [2], (V,Ti)N [3], multilayer AlN/VN [4], quaternary single layer or multilayered CrAlVN [5-6], and TiAlVN [7-8] systems. Recently we have reported the effect of V incorporation on the structure, mechanical properties and oxidation resistance of TiSiVN films deposited by DC reactive magnetron sputtering [9]. Lubricious vanadium oxides have been successfully detected on the oxidized surface of these films. Here we show the thermal stability, oxide formation and, particularly, diffusion processes during annealing of TiSiVN films deposited by magnetron sputtering.

## 2. Experimental procedure

TiSiN and TiSiVN coatings with approximately the same silicon content and about 2.5  $\mu\text{m}$  of total thickness, were deposited on FeCrAl alloy substrates by a d.c. reactive magnetron sputtering machine equipped with two rectangular, Ti (99.9%) and TiSi<sub>2</sub> (99.9%), magnetron cathodes working in unbalanced mode. V incorporation was achieved by inserting 8 pellets of vanadium into the erosion zone of Ti target. In both cases Ti and TiN adhesion layers were deposited as bonding layers improving coating to substrate adhesion. The interlayer also contained V when V pellets are placed in the Ti target. A detail description of the deposition conditions is reported elsewhere [9]. Temperature effect on the structure of the V rich coating was characterized by in-situ hot-XRD analysis in the range from 500 °C up to 750 °C, in open air, using a grazing incidence angle of 2° and Co K $\alpha$  radiation (1.789010 Å). Between each selected temperature a step of 10 min holding time was allowed for thermal stabilization and 30 min time acquisition was used. Oxidation of films was assessed by thermogravimetric analysis (TGA) using industrial air (99.99% purity). The coatings were isothermal tested at different selected temperatures and times, based on the thermogravimetric oxidation curves of films performed at constant linear-temperature ramp (RT to 1200°C at 20°C/min) shown in reference [9]. These isothermal tests were performed having in consideration the temperatures where the oxidation showed takes mainly place. After annealing, the cross section thin foils of oxidized films was prepared by focused ion beam (FIB) and analyzed by transmission electron microscope (TEM) equipped with an energy-dispersive x-ray (EDS) spectroscopy system.

### 3. Results and discussion

#### 3.1. Phase evolution during annealing (in situ)

The investigated coatings with chemical composition of  $\text{Ti}_{0.80}\text{Si}_{0.13}\text{N}$  and  $\text{Ti}_{0.65}\text{Si}_{0.11}\text{V}_{0.14}\text{N}$  showed a typical columnar morphology and fcc NaCl-type structure assigned to crystalline TiN with Si and V in solid solution [9]. Fig. 1 plots the high temperature in-situ XRD spectra evolution for TiSiVN coating together with as deposited and cooled state patterns acquired at room temperature (RT). The first signs of oxides were detected at 500 °C and identified as rutile type phase with V in solid solution, the  $\text{Ti(V)O}_2$  (ICDD card 77-0332). Further increase in temperature to 550 °C led to an increase of the  $\text{Ti(V)O}_2$  peaks intensity and the appearance of a new phase: the  $\alpha\text{-V}_2\text{O}_5$  (ICDD card 41-1426) oxide with orthorhombic symmetry (peak at 23.6°). At 600 °C a strong increase in intensity of the  $\alpha\text{-V}_2\text{O}_5$  oxide peaks with a strong preferred orientation following the (001) plane was observed (peak at 23.5°). Moreover, a metastable phase was formed,  $\beta\text{-V}_2\text{O}_5$ , as a result of oxygen loss from  $\alpha\text{-V}_2\text{O}_5$  due to a reduction process [10]. It should be also pointed out that the higher intensity of  $\text{V}_2\text{O}_5$  peaks in relation to other peaks suggests higher quantity on the oxidized volume. The temperature increase to 650 °C led to TiN peaks vanishing suggesting the formation of a thick oxide scale. At 675 °C, the peaks associated with the  $\text{V}_2\text{O}_5$  phases disappeared, which was in a good agreement with the melting point of  $\text{V}_2\text{O}_5$  oxide (reported in the range of 670 – 685 °C [11]). On the other hand, peaks related to a  $\text{V}_3\text{O}_5$  phase, which resulted from the  $\alpha\text{-V}_2\text{O}_5$  reduction, were found. In fact, in case of oxygen deficiency, a shift to lower valence state leads to the formation of reduced oxides, such as  $\text{V}_3\text{O}_5$  identified in the current XRD pattern. Further increase in temperature resulted mostly in the increase of  $\text{V}_3\text{O}_5$  peaks intensities due to continuous reduction of liquid  $\text{V}_2\text{O}_5$  phase.  $\text{Ti(V)O}_2$ ,  $\text{V}_3\text{O}_5$ ,  $\text{V}_2\text{O}_3$  and VO reduced phases were found after annealing, as well as a new polymorph  $\text{V}_2\text{O}_5$  oxide:  $\gamma'\text{-V}_2\text{O}_5$  (ICDD card 85-2422). This oxide has an orthorhombic structure as  $\alpha\text{-V}_2\text{O}_5$  phase, but with different diffraction planes. These changes could be attributed to distortions on the structure motivated by the cooling of liquid-phase. Double chains exist in both phases, but  $\text{VO}_5$  pyramids alternate up and down individually for  $\gamma'\text{-V}_2\text{O}_5$ , whereas they alternate by pairs for normal  $\alpha\text{-V}_2\text{O}_5$  phase [12].

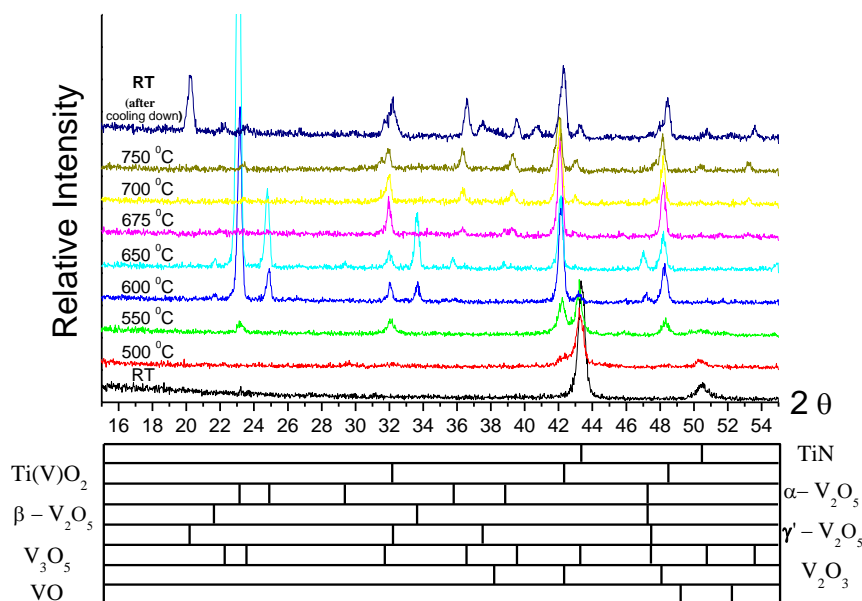


Figure 1 - XRD spectra of TiSiVN film at different temperatures (upper) and position of main peaks of corresponding phases (lower).

### 3.2. Isothermal oxidation in air, surface morphology and characterization

TiSiN film was annealed at 900 °C for 1 hour, TiSiVN coating was annealed at two different isothermal temperatures. The results of the thermo gravimetric analysis are presented in Fig. 2 a). As expected, TiSiN film is much more resistant to oxidation, showing a typical parabolic oxidation weight gain as a function of time, which indicates the presence of protective oxide scales. Vanadium addition to TiSiN film strongly reduced the oxidation resistance. The isothermal curves at 550 °C and 600 °C showed two steps: they started with a linear increase in mass gain and then followed with a parabolic evolution. The surface morphologies of the oxidized coatings are shown in Fig. 2 b-c) for coatings TiSiN tested at 900 °C and TiSiVN oxidized at 600 °C, respectively. The detailed description of the surface oxide constitution, based on XRD diffraction, Raman spectroscopy and SEM-EDS analyses, can be found in our previous study [9]. Therefore we will only summarize here the main results to support investigation aimed at diffusion processes and described later. Annealed TiSiN film (see Fig. 2b) displayed two different surface features: white and dark gray islands evenly distributed on the surface. Raman analyses revealed that white phase was rutile (TiO<sub>2</sub>), while dark gray phase was a mixture of rutile and anatase. However, only rutile peaks were detected by XRD diffraction suggesting very limited amount of anatase in the dark gray islands. Furthermore, strong signals of Si were detected on dark zone by EDS. However, the signals of silicon oxide were neither detected by XRD nor by Raman spectroscopy indicating

amorphous character, which corroborates previous reports [13-14]. Silicon oxide was positioned below Ti-O rich layer. Different morphology and oxide phases were detected on the oxidized surface of TiSiVN coating. At 600 °C, the film displayed a floret-like structure formed by light and dark gray phases. XRD diffraction showed the presence of  $\alpha$ -V<sub>2</sub>O<sub>5</sub> and Ti(V)O<sub>2</sub> oxides. Although EDS analysis revealed similar spectra for both phases, the much less intensity of the V peak on the light gray phase, and its conjugation with Raman analysis allowed identifying dark and light gray phases as  $\alpha$ -V<sub>2</sub>O<sub>5</sub> and Ti(V)O<sub>2</sub> oxides, respectively. Similar phases were detected at 550 °C by XRD; however, only small dark gray areas were observed at the surface. These results match well with high temperature in-situ XRD diffractograms (Fig. 1), where these phases were indexed. Similar to TiSiN coating, the signal from Si-O phase was neither detected by XRD nor by Raman.

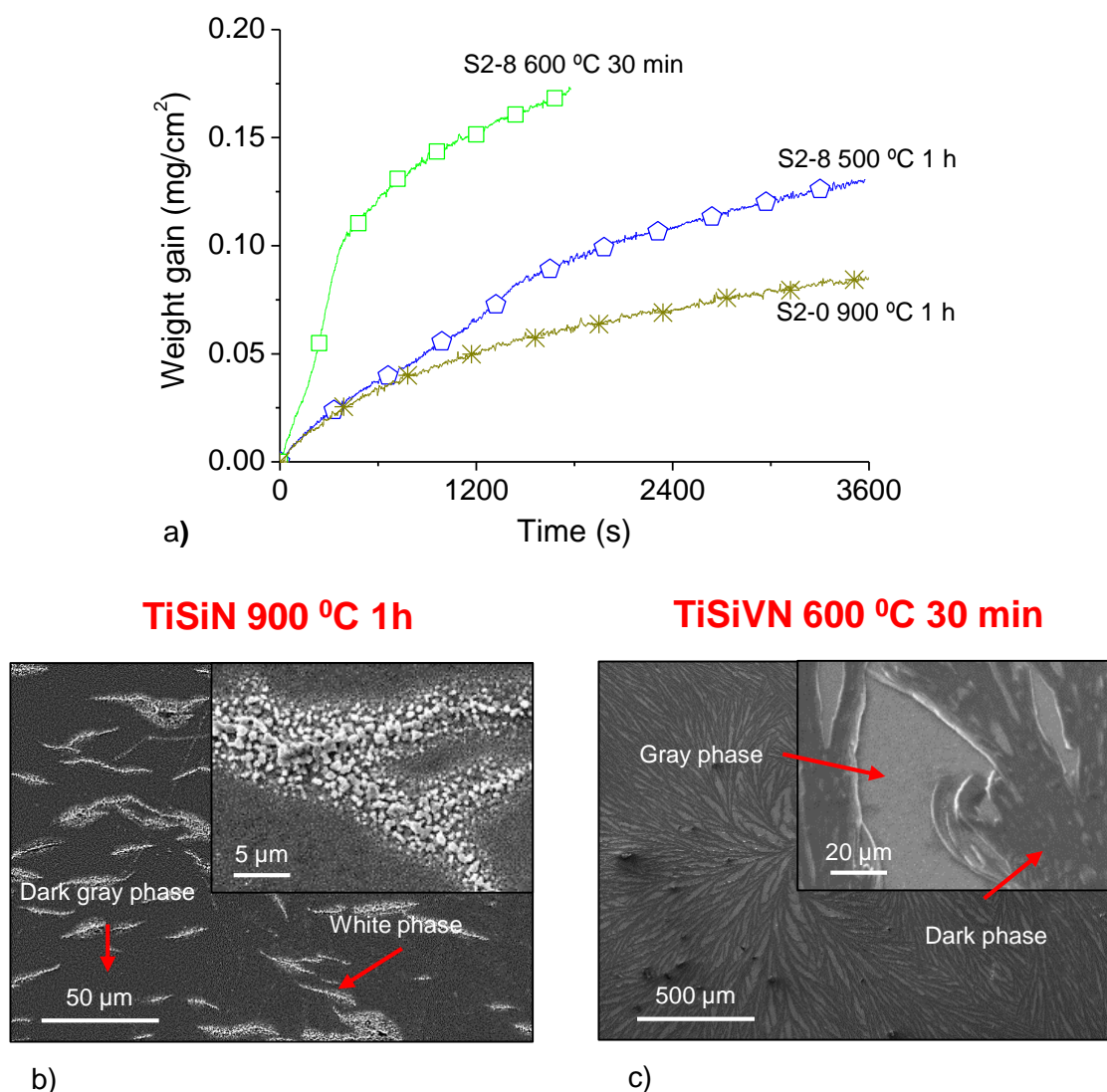


Figure 2 - a) Isothermal oxidation curves of coatings, b-c) typical surface morphologies.

Figure 3 shows the growing mechanism of the  $V_2O_5$  phase over the  $Ti(V)O_2$  oxide. Nucleation points of  $V_2O_5$  started being formed over the oxidized surface, growing up by vanadium lateral diffusion as suggested by the V depleted white and V rich black regions marked in the SEM micrograph. In order to investigate the oxide scale films growth, TEM cross-sections were prepared by FIB from TiSiN and TiSiVN films annealed at 900 and 600 °C, respectively.

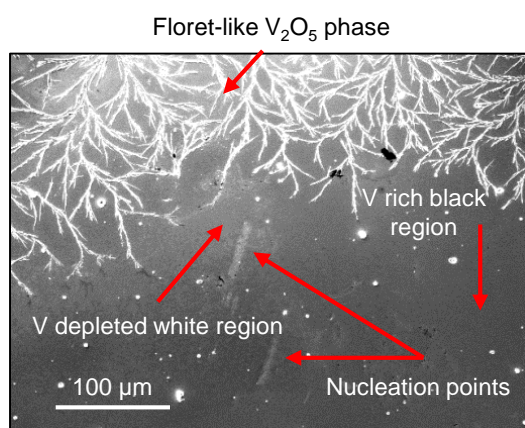


Figure 3 - Oxidized surface of TiSiVN coating showing the growing mechanism of  $V_2O_5$  phase.

### 3.3. Cross section of oxidized surfaces by TEM and oxidation kinetics

Fig. 4 and 5 displays the bright-field STEM images, associated elemental maps and scanning elemental profiles from cross section of oxidized TiSiN and TiSiVN coatings. In the case of TiSiN film a multilayer of oxides can be identified, being more complex close to the film defect (white zones) shown in Fig. 4a): (i) an outer Ti-rich layer comprised by shaped crystals with bigger size in the top of the film defect, zone corresponding to the white phase and, (ii) a Si-rich layer, which is itself divided in 3 layers on the zone around the defect, an intermediate layer containing Ti, sandwiched between two Ti-free layers, being the external porous and the internal one very compact. Far from the film defect (left zone of the micrograph), below to the  $TiO_2$  crystals only a homogeneous Si-rich layer was observed. The measured elemental cross-section depth profiles for two lines were plotted in Fig. 4b) and 4c), respectively. The profiles corroborated STEM/EDX elemental mapping showing in detail the composition of surface oxides. The surface layer formed exclusively of Ti-O was followed by a Si-rich layer with scattering in the signals intensity, in agreement with brightness intensity in figures 4 a). It is clear in Ti-signal a small increase in intensity in the zone of high-Si content. This variation is more intense in line 2 than in line 1, suggesting an influence of the film defect, which is closer to line 2. Continuous and compact Si-O layer at the oxide/coating



interface acts as an efficient barrier against oxygen and metal ions diffusion and thus protecting the coating from further oxidation [13-14].

It is evident that Ti oxide forms first on the surface of the film due to the higher affinity of Ti for O than Si [13-14] and then, with further increase in temperature, silicon oxide is formed due to the progressive segregation of Si. The oxidation process will then occur through the inwards diffusion of  $O^{2-}$  through the  $TiO_2$  layer and the outwards diffusion of  $Ti^{4+}$  through the Si-O layer [15]. Nevertheless, due to the presence of film defects, in the first stage of the oxidation process, a high amount of Ti ions will be supplied in that zone corresponding to the oxidation occurring in the defect walls. This process will promote the formation of a porous Si-O layer, with low diffusion barrier performance to the out diffusion of  $Ti^{4+}$  ions, leading to large  $TiO_2$  crystals on the oxide scale surface. From the moment that a Si-O barrier layer is formed in the defect walls (see Si signal in figure 4 a)) the oxidation process will be controlled by the  $O^{2-}$  inward and  $Ti^{4+}$  outward ions diffusion trough the Si-O layer [15]. It should be remarked that this phenomenon should not influence significantly the global oxidation behavior of the Ti-Si-N coating (which shows the parabolic behavior presented in Fig. 2 a), in agreement with literature [13-15]) since, on the one hand, it only occurs in a few defects in the films surface (see Fig. 2 b)) and, on the other, it should be more intense in the first stage of the oxidation, during heating up to the 900 °C isothermal oxidation temperature.

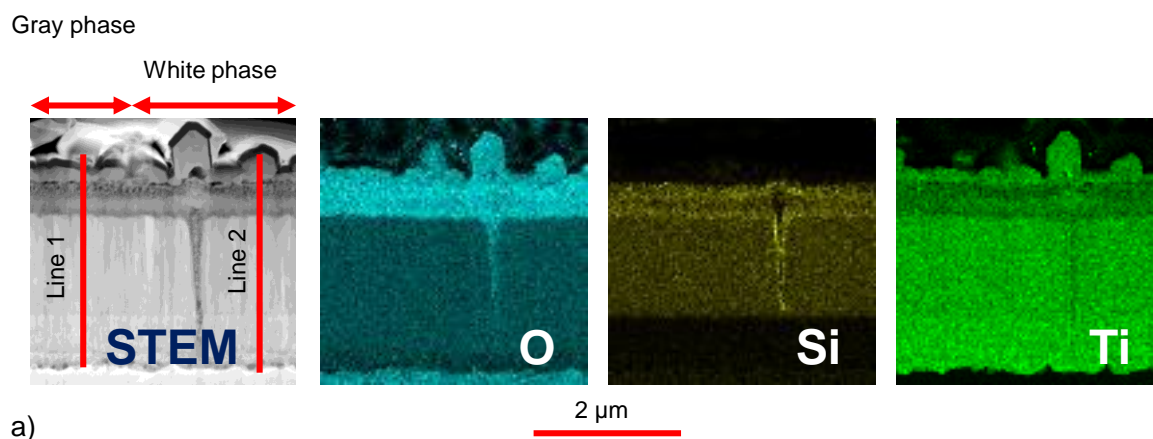


Figure 4 - a) Bright field STEM/EDX maps of TiSiN coating oxidized at 900 °C during 1h. b) and c). Elemental profiles along the cross section of the oxidized coating from: b) line 1, c) line 2.

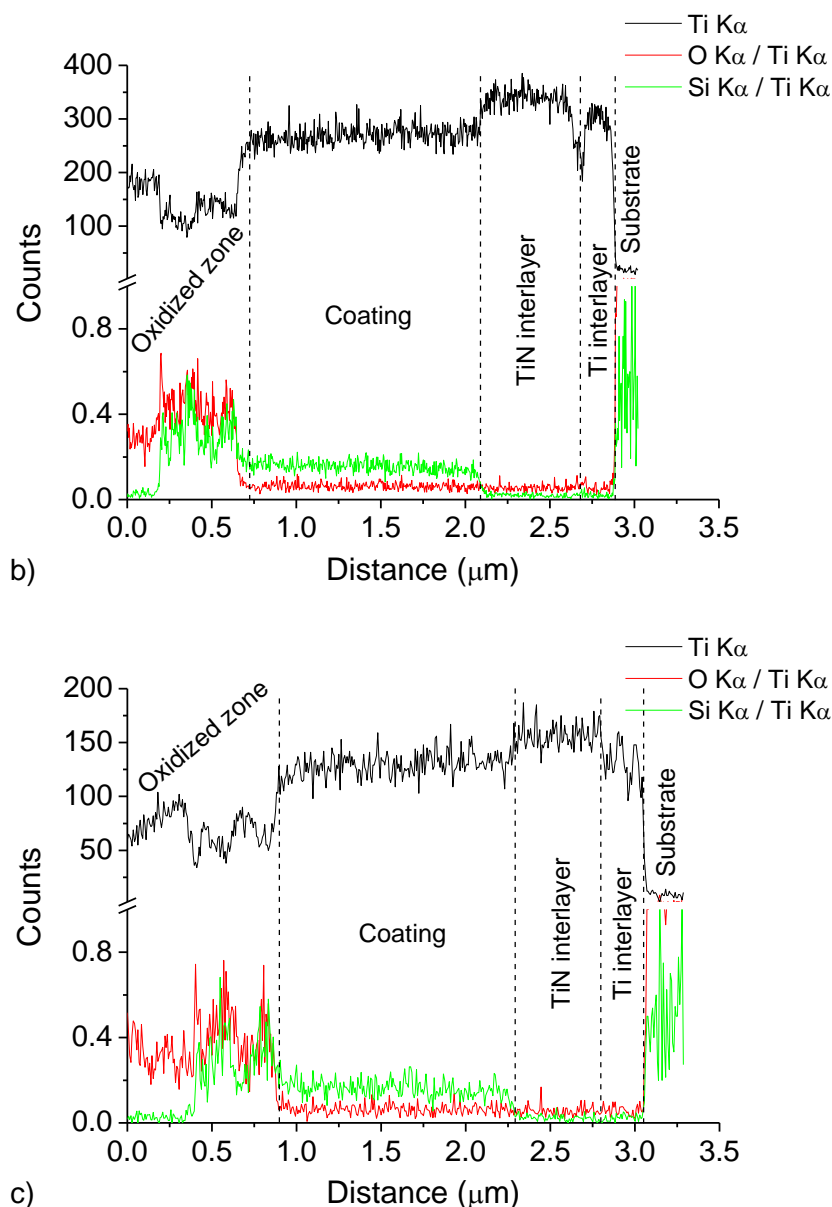


Figure 4 (continued).

TiSiVN coating exhibited, after annealing, two-layers oxide structure with a thick porous inner layer and an outer discontinuous layer of well-defined crystals; the latter corresponded to the gray areas described above. The elemental maps shown in Fig. 5a) suggested that the majority of vanadium was located in the outer crystal layer, whereas inner layer was Ti and Si rich. This result corroborates the detection of the rutile type compound  $\text{Ti(V)O}_2$  indexed by XRD and Raman spectroscopy in the light gray phase in Fig. 2 [9]. Elemental lines shown in Fig. 5b) and 5c) showed that diffusion of V occurred exclusively within the oxidized volume, since a constant signal was measured for the remaining non-oxidized coating. In general, we observed a thicker non oxidized layer in the regions covered by V-O crystal phase. Furthermore, comparing either the V content integrated intensities of

Fig. 5a) and b) or the brightness of V signal between the right and left part of Fig. 5 a), it can be concluded that V has to be diffused from the left to the right zone of this figure. Finally, it should be remarked that there is no indication of formation of any Si-rich layer, being Si signal uniformly distributed in both oxide scale and non-oxidized coating. Therefore, a dense compact protective silicon oxide layer localized in subsurface was not formed being Si-O randomly distributed in the  $\text{Ti(V)O}_2$  porous scale.

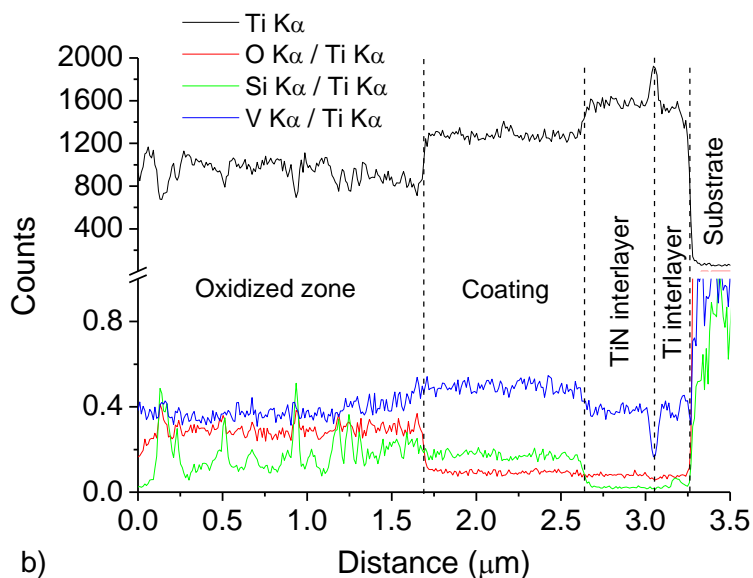
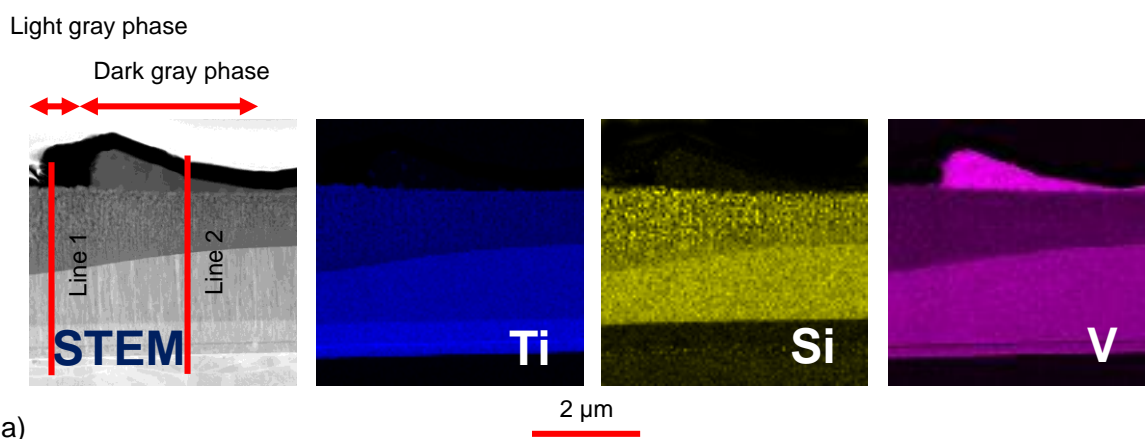


Figure 5 - a) Bright field STEM/EDX maps of TiSiVN coating oxidized at 600 °C during 30 min. Elemental profiles along the cross section of the oxidized coating from: b) line 1, c) line 2.

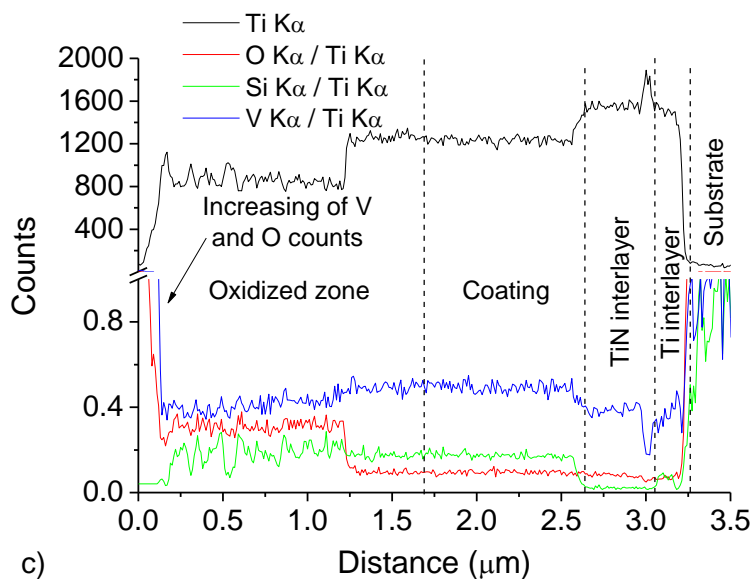


Figure 5 (continued).

Isothermal curve of TiSiVN coating oxidized at temperatures below the melting point of  $V_2O_5$  started with a linear increase in mass gain. This step, where a continuous  $Ti(V)O_2$  oxide layer was grown (see Fig. 1), should be attributed to the conjugation of a fast rate of mass transport in the oxide with a slow surface step accompanying the gas dissociation, adsorption and subsequent entry of oxygen into the  $Ti(V)O_2$  lattice. In fact, at the very beginning of the oxidation process, due to the high Ti content, a  $TiO_2$  layer starts growing. The presence of V ions and its high solubility with Ti promote the formation of  $Ti(V)O_2$  solid solution, which comprises vanadium cations with lower oxidation states as  $V^{3+}$  ions [16-17]. The substitution of  $Ti^{4+}$  by  $V^{3+}$  ions in the  $TiO_2$  lattice would increase the concentration of interstitial metallic  $Ti^{4+}$  ions and decrease the number of excess electrons. The oxidation mechanism is inverted in relation to Ti-N, being the outwards diffusion of metallic ions ( $Ti^{3+}$   $Ti^{n+}$ ) more favorable than the inwards diffusion of  $O^{2-}$  ions. There are several consequences of this inversion: (i) the oxidation rate increases substantially, (ii) the kinetics of the oxidation is not controlled any more by a diffusion process but by the rate of dissociation, adsorption and combination at the surface of  $O^{2-}$  with metallic ions, and (iii) continuous and compact Si-rich layer cannot be formed. In fact, the growing of  $Ti(V)-O$  on the external part of the scale leaves a less compact zone in the interface between the non-oxidized material and the oxide scale, facilitating the local segregation of Si inside the  $Ti(V)-O$  instead its segregation for the interface. The elemental maps suggest that Si-O and  $Ti(V)O_2$  coexist in the inner porous layer, being unable to protect the material from oxidation. As a consequence, the oxidation process is accelerated, which is demonstrated by the initial rapid oxidation observed in the

isothermal curve. Thongtem et al. [16] studied the effect of V doping to Ti-based alloys and observed similar behavior with increasing V content.

The experimental evidence shows that  $V_2O_5$  crystals were formed exclusively on the surface. When  $V^{3+}$  or  $V^{4+}$  arrive to the surface, they are further oxidized to  $V^{5+}$  combining with O ions and creating nucleation points for the  $V_2O_5$  growth (see Fig. 3), which will expand and grow up by vanadium lateral diffusion. The process develops leading to the formation of the observed floret-like dispersive  $V_2O_5$  phases that can comprise both  $\alpha$ - $V_2O_5$  and  $\beta$ - $V_2O_5$  phases as evidenced in the XRD patterns at high temperature. As soon as  $V_2O_5$  oxide expands laterally, the surface will be progressively covered by this oxide making more and more difficult the access of both types of ions, up to the moment that the rate of dissociation, adsorption and combination of  $O^{2-}$  with metallic ions is not anymore the kinetics controlling step but the ion diffusion through the oxide scale. Therefore, after this moment the isothermal curve will follow a parabolic law (see Fig. 2a)). It should be remarked that  $V_2O_5$  is more protective than  $(Ti,V)O_2$  since the non-oxidized coating underneath it is thicker.

#### 4. Conclusion

In this investigation, the effect of V additions on oxidation resistance, oxide scale formation and diffusion processes for TiSiVN system and their comparison to TiSiN was investigated. In summary, we demonstrated that oxidation of TiSiN is controlled by the formation of a dense and compact silicon oxide acting as a diffusion barrier, which can be affected by defects in the as-deposited film. The presence of  $V^{3+}$  ions in the  $TiO_2$  scale, during the oxidation of TiSiVN film, was responsible for an inversion in the ions diffusion process through the oxide scale leading to, simultaneously, a significant increase of the oxidation rate and the inability of formation of a Si-O protective oxide.

#### Acknowledgments

This research is sponsored by FEDER funds through the program COMPETE – Programa Operacional Factores de Competitividade – and by national funds through FCT – Fundação para a Ciência e a Tecnologia –, under the project: PTDC/EME-TME/122116/2010, as well as the grant (SFRH/BD/68740/2010). T. Polcar acknowledges support from the project MSM 6840770038.

## References

- [1] Y.H. Cheng, T. Browne, B. Heckerman, Mechanical and tribological properties of nanocomposite TiSiN coatings, E.I. Meletis, *Surf. Coat. Technol.*, 204 (2010) 2123-2129.
- [2] M. Uchida, N. Nihira, A. Mitsuo, K. Toyoda, K. Kubota, T. Aizawa, Friction and wear properties of CrAlN and CrVN films deposited by cathodic arc ion plating method, *Surf. Coat. Technol.*, 177–178 (2004) 627-630.
- [3] J.H. Ouyang, S. Sasaki, Tribo-oxidation of cathodic arc ion-plated (V,Ti)N coatings sliding against a steel ball under both unlubricated and boundary-lubricated conditions, *Surf. Coat. Technol.*, 187 (2004) 343-357.
- [4] J.-K. Park, Y.-J. Baik, Increase of hardness and oxidation resistance of VN coating by nanoscale multilayered structurization with AlN, *Mater. Lett.*, 62 (2008) 2528-2530.
- [5] R. Franz, J. Neidhardt, R. Kaindl, B. Sartory, R. Tessadri, M. Lechthaler, P. Polcik, C. Mitterer, Influence of phase transition on the tribological performance of arc-evaporated AlCrVN hard coatings, *Surf. Coat. Technol.*, 203 (2009) 1101-1105.
- [6] Y. Qiu, S. Zhang, J.-W. Lee, B. Li, Y. Wang, D. Zhao, Self-lubricating CrAlN/VN multilayer coatings at room temperature, *Applied Surface Science*, 279 (2013) 189-196.
- [7] Q. Luo, Temperature dependent friction and wear of magnetron sputtered coating TiAlN/VN, *Wear*, 271 (2011) 2058-2066.
- [8] K. Kutschej, P.H. Mayrhofer, M. Kathrein, P. Polcik, C. Mitterer, Influence of oxide phase formation on the tribological behavior of Ti–Al–V–N coatings, *Surf. Coat. Technol.*, 200 (2005) 1731-1737.
- [9] F. Fernandes, A. Loureiro, T. Polcar, A. Cavaleiro, The effect of increasing V content on the structure, mechanical properties and oxidation resistance of Ti-Si-V-N films deposited by DC reactive magnetron sputtering, *Applied Surface Science*, 289 (2014) 114-123

- [10] A. Bouzidi, N. Benramdane, S. Bresson, C. Mathieu, R. Desfeux, M.E. Marssi, X-ray and Raman study of spray pyrolysed vanadium oxide thin films, *Vibrational Spectroscopy*, 57 (2011) 182-186.
- [11] R. Franz, C. Mitterer, Vanadium containing self-adaptive low-friction hard coatings for high-temperature applications: A review, *Surf. Coat. Technol.*, 228 (2013) 1-13.
- [12] J.M. Cocciantelli, P. Gravereau, J.P. Doumerc, M. Pouchard, P. Hagemuller, On the preparation and characterization of a new polymorph of  $V_2O_5$ , *Journal of Solid State Chemistry*, 93 (1991) 497-502.
- [13] T. Kacsich, S. Gasser, Y. Tsuji, A. Dommann, M.A. Nicolet, A. Nicolet, Wet oxidation of  $Ti_{34}Si_{23}B_{43}$ , *Journal of Applied Physics*, 85 (1999) 1871-1875.
- [14] T. Kacsich, M.A. Nicolet, Moving species in  $Ti_{34}Si_{23}N_{43}$  oxidation, *Thin Solid Films*, 349 (1999) 1-3.
- [15] F. Deschaux-Beaume, N. Frety, T. Cutard, C. Colin, Oxidation modeling of a  $Si_3N_4$ -TiN composite: Comparison between experiment and kinetic models, *Ceram. Int.*, 35 (2009) 1709-1718.
- [16] S. Thongtem, T. Thongtem, M. McNallan, High-temperature nitridation and oxidation of Ti-based alloys, *Surface and Interface Analysis*, 32 (2001) 306-309.
- [17] A. Glaser, S. Surnev, F.P. Netzer, N. Fateh, G.A. Fontalvo, C. Mitterer, Oxidation of vanadium nitride and titanium nitride coatings, *Surface Science*, 601 (2007) 1153-1159





---

# Annex I

---

**F. Fernandes, T. Polcar, A. Cavaleiro, *Tribological properties of self-lubricating TiSiVN coatings at room temperature*, (2014), accept for publication, “Surface and Coatings Technology”, DOI: 10.1016/j.surfcoat.2014.10.016**



## Tribological properties of self-lubricating TiSiVN coatings at room temperature

F. Fernandes<sup>1\*</sup>, T. Polcar<sup>2,3</sup>, A. Cavaleiro<sup>1</sup>

<sup>1</sup>SEG-CEMUC - Department of Mechanical Engineering, University of Coimbra, Rua Luís Reis Santos, 3030-788 Coimbra, Portugal.

<sup>2</sup>Department of Control Engineering Czech Technical University in Prague Technicka 2, Prague 6, 166 27 Czech Republic.

<sup>3</sup>n-CATS University of Southampton Highfield Campus SO17 1BJ Southampton, UK.

\*Email address: [filipe.fernandes@dem.uc.pt](mailto:filipe.fernandes@dem.uc.pt), tel. + (351) 239 790 745, fax. + (351) 239 790 701

### Abstract

In the last years, vanadium rich coatings have been introduced as possible candidates for self-lubrication due to their optimum tribological properties. In the present investigation, the influence of V incorporation on the wear performance of TiSiN films deposited onto WC substrates by d.c. reactive magnetron sputtering is reported. The results achieved for TiSiVN films were compared and discussed in relation to  $\text{Ti}_{0.80}\text{Si}_{0.15}\text{N}$ , TiN and  $\text{Ti}_{0.82}\text{V}_{0.15}\text{N}$  coatings prepared as references. The tribological properties of the coatings were evaluated at room temperature on a pin on disc tribometer equipment using two different counterparts:  $\text{Al}_2\text{O}_3$  and HSS balls. The wear tracks, ball-wear scars and wear debris were characterized by scanning electron microscopy with energy dispersive X-ray spectroscopy (SEM-EDS). Tribological tests indicated that the wear rate and the friction coefficient of  $\text{Ti}_{0.80}\text{Si}_{0.15}\text{N}$  coating decreased with continuous increase of V content being the overall behaviour strongly dependent on the counterpart ball material. For  $\text{Al}_2\text{O}_3$  balls the wear rate and friction coefficient of coatings were much lower compared to sliding against HSS steel balls.  $\text{Ti}_{0.80}\text{Si}_{0.15}\text{N}$  showed the lowest wear resistance among all tested coatings, independently of the counter-body. For V rich coatings tested with  $\text{Al}_2\text{O}_3$  balls the polishing wear mechanism was observed, whereas adhesion wear took place when tested against HSS balls.

Keywords: TiSiVN coatings, Tribology, Wear resistance, Lubricious oxides

## 1. Introduction

Over the past years, ternary titanium-based nitride coatings, such as TiXN (X = B, Cr, Al, Si, Cr, C, etc.), have been largely employed in industrial applications involving cutting tools, wear protection, machinery components and high temperature parts, due to their high hardness and suitable wear and oxidation resistance [1, 2]. However, in dry machining operations, the tools experience extremely harsh conditions combining abrasion, adhesion, oxidation, mechanical and thermal loads, which limit their lifetime. Since low friction coefficients can effectively reduce the contact temperatures during sliding and, consequently, improve the tribological behavior of tools, a lot of efforts has been carried out in the last years to develop self-lubricant coatings. These films should retain beneficial properties of (TiX)N films and offer lubricity through the formation of low-friction surface oxides. Recently, the attention of the scientific community has been focused on the formation of thin reaction films of the so-called Magnéli oxide phases based on Ti, Si, Mo, W and V, which possess easy shear planes [3, 4]. Among these elements, particular attention has been given to vanadium-containing coatings which form  $V_nO_{3n-1}$  Magnéli phases. Over the whole ternary systems the effect of V doping was only extensively studied for ternary CrAlN [5, 6] and TiAlN [2, 7-9] coatings in single layer or multilayered configurations. In all the cases a beneficial influence of V additions on the tribological behaviour of the coatings at room and high temperatures has been demonstrated. Since other ternary coating systems with superior mechanical properties have been successfully used as protective coatings in tribological applications, the effect of vanadium doping on their structure should also be considered. This is the case of TiSiN system, which shows similar levels of oxidation resistance as CrAlN and TiAlN films. Preliminary studies on the effect of V additions on the structure, mechanical properties and oxidation resistance of TiSiN systems have been carried out in our previous investigation [10]. Hence, as a way to complement that study, the aim of this work was to characterize the tribological behaviour at room temperature of TiSiVN sputtered coatings, sliding against  $Al_2O_3$  and HSS balls. The influence of V addition on the TiSiN system was compared with the tribological results of TiN,  $Ti_{0.82}V_{0.15}N$  and  $Ti_{0.80}Si_{0.15}N$  coatings prepared and tested as a reference.

## 2. Experimental Procedure

TiSiVN coatings with dissimilar Si and V contents, evaluated in our previous work [10], were deposited by d.c. reactive magnetron sputtering from two rectangular (100×200 mm) magnetron cathodes working in unbalanced mode. High speed steel (AISI M2), FeCrAl alloy, cemented carbides, silicon and stainless steel substrates were coated for mechanical, structural, chemical composition and residual stress measurements. A high purity Ti (99.9%) target, with 10 mm diameter holes, and a high purity TiSi<sub>2</sub> (99.9%) target were used in the depositions. The coatings comprise three TiSiVN coatings with different V and Si contents and three other coatings deposited as a reference: TiN, Ti<sub>0.82</sub>V<sub>0.15</sub>N and Ti<sub>0.80</sub>Si<sub>0.15</sub>N. V incorporation was achieved by filling Ti holes with 4 and 8 V pellets being the remaining empty holes filled with pellets of Ti. Silicon content was varied by changing the power density applied to each target. Ti and TiN adhesion layers of approximately 0.24 and 0.45 μm, respectively, were deposited below final TiSi(V)N coatings. The interlayers also contained V when V pellets were placed in the Ti target. A negative bias of 50 V was applied to the substrate holder. All the depositions were performed at a total working gas pressure of 0.3 Pa. The deposition time was set in order to produce coatings with approximately 2.5 μm of total thickness, including interlayer referred to above. A full description of the deposition procedure is given elsewhere [10]. Summary of the deposition parameters used for the coatings production and their chemical composition determined by electron probe microanalysis (EPMA) are shown in Table 1 and Table 2, respectively. The denomination of the samples, as presented in tables 1 and 2, will be adopted throughout the paper in order to help the coatings identification and the paper reading. The subscript in Ti, Si and V letters represents the ratio between the at.% of each element in the coating in relation to the at.% of Nitrogen.

The structure of the films was analyzed by X-ray diffraction (X' Pert Pro MPD diffractometer) using a grazing incidence angle of 1° with Cu K<sub>α1</sub> radiation ( $\lambda = 1.54060 \text{ \AA}$ ). The adhesion of the films on the M2 steel substrate was evaluated by a scratch-test apparatus. Specimens were scratched as the normal force was increased linearly from 5 to 70 N, using a Rockwell C indenter with a spherical tip with a radius of 0.2 mm, a scratch speed of 10 mm/min and a loading speed of 100 N/min. Critical loads were determined by optical microscope analysis according to the standard for scratch-test evaluation [11]. For each specimen, the indicated critical loads results from the average of 3 different scratches. The hardness and Young's modulus of films were evaluated by depth-sensing indentation

technique (Micro Materials NanoTest) using a Berkovich diamond pyramid indenter. In order to avoid the effect of the substrate, the applied load (10 mN) was selected to keep the indentation depth less than 10% of the coating's thickness. The residual stress values were calculated through the Stoney equation [12] by measuring the differential deflection between an uncoated and coated stainless steel 25 mm diameter disk.

The tribological behaviour of the coatings was evaluated by dry-sliding tests at room temperature on a pin on disc tribometer. Al<sub>2</sub>O<sub>3</sub> and HSS steel balls (both with a diameter of 6 mm) were used as counterparts. The radius of the wear tracks was set to 5.3 and 4 mm for Al<sub>2</sub>O<sub>3</sub> and HSS steel balls, respectively. All the measurements were performed with a linear speed of 0.10 m.s<sup>-1</sup>, load of 5 N, relative humidity 48±5% and 5000 cycles. The wear rate of the coatings was determined from the area of the wear track cross section using a 3D optical profilometer; an average from four different locations was used. The ball wear rates were evaluated from the wear cap images taken in an optical microscope. To ensure the reproducibility of results a set of three tests was performed under identical conditions for each coating. After the wear tests, the wear tracks and wear debris were characterized by scanning electron microscopy with energy dispersive X-ray spectrometry (SEM-EDS).

Table 1 - Deposition parameters of the coatings.

Sample	Target power density (W/cm <sup>2</sup> )		Gas flow (sccm)		Deposition time (min)	Pellets of V at the Ti target
	Ti	TiSi <sub>2</sub>	Ar	N <sub>2</sub>		
Ti interlayer	10	-	35	-	5	-
TiN interlayer	10	-	35	17	15	-
TiN	10	-	35	17	73	-
Ti <sub>0.82</sub> V <sub>0.15</sub> N	10	-	35	17	73	8
Ti <sub>0.80</sub> Si <sub>0.15</sub> N	6	1.5	30	17	193	0
Ti <sub>0.75</sub> Si <sub>0.11</sub> V <sub>0.03</sub> N	6	1.5	30	17	193	4
Ti <sub>0.65</sub> Si <sub>0.11</sub> V <sub>0.15</sub> N	6	1.5	30	17	193	8
Ti <sub>0.52</sub> Si <sub>0.20</sub> V <sub>0.14</sub> N	5	2.5	30	17	153	8

Table 2 - Chemical composition of films in at. %.

Sample	Chemical composition (at.%)				
	Ti	Si	V	O	N
TiN	49.6 ± 0.4	-	-	0.38 ± 0.12	49.79 ± 0.13
Ti <sub>0.82</sub> V <sub>0.15</sub> N	41.3 ± 0.2	-	7.81 ± 0.11	0.53 ± 0.12	50.42 ± 0.10
Ti <sub>0.80</sub> Si <sub>0.15</sub> N	41.3 ± 0.3	6.68 ± 0.03	-	0.55 ± 0.06	51.5 ± 0.2
Ti <sub>0.75</sub> Si <sub>0.11</sub> V <sub>0.03</sub> N	39.3 ± 0.4	5.71 ± 0.06	1.6 ± 0.2	1.22 ± 0.10	52.1 ± 0.2
Ti <sub>0.65</sub> Si <sub>0.11</sub> V <sub>0.15</sub> N	33.6 ± 0.3	5.64 ± 0.05	7.6 ± 0.2	1.42 ± 0.13	51.71 ± 0.14
Ti <sub>0.52</sub> Si <sub>0.20</sub> V <sub>0.14</sub> N	27.2 ± 0.2	10.73 ± 0.06	7.32 ± 0.05	1.96 ± 0.11	52.8 ± 0.2

### 3. Results and discussion

#### 3.1. Structure and mechanical properties of films

The X-ray diffraction patterns of the as-deposited films are shown in Figure 1. All the coatings presents an fcc NaCl-type structure assigned to crystalline TiN phase, but different peaks position and intensities can be perceived. All films presented well defined peaks except for the coating with higher silicon content (Ti<sub>0.52</sub>Si<sub>0.20</sub>V<sub>0.14</sub>N) for which a strong decrease of the peaks intensity as well a significant broadening was observed. This result suggests a decrease of the crystallinity and grain size, in good accordance with literature where for TiSiN films with high Si contents amorphization of the structure is usually observed [13]. A closer analysis of the peaks positions indicated that in all cases a fcc solid solution should be expected. In fact, starting with the individual addition of V and Si to TiN, the peaks are shifted to higher angles, behaviour associated to a smaller unit cell (insert in Figure 1). Taking into account that the residual stresses are very similar among these coatings (see table 3), such a result can only be explained by the presence of V or Si in substitutional solid solution, due to their smaller radius (0.143 and 0.117 nm, respectively) in comparison with Ti (0.147 nm). When both Si and V are added to TiN, a synergetic effect of both elements are observed being the diffraction peaks shifted to further higher diffraction angles. A detailed description of the effect of Si and V additions on the structure of TiN is shown in our previous work [10].

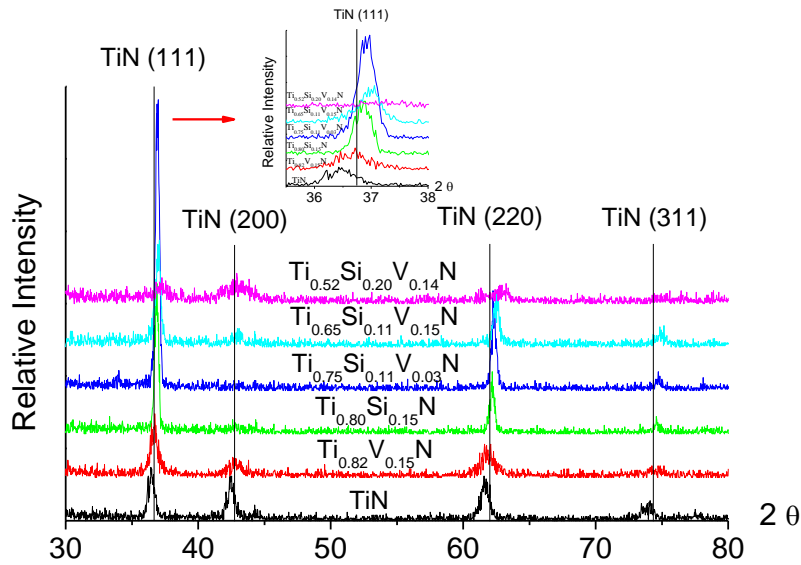


Figure 1 - Typical X-ray diffraction patterns of the dissimilar coatings.

Table 3 shows the hardness, Young's Modulus, residual stress and scratch test critical load values of the coatings. V incorporation at the TiN and TiSiN systems slightly increased the hardness and Young's modulus value of coatings.  $\text{Ti}_{0.52}\text{Si}_{0.20}\text{V}_{0.14}\text{N}$  coating exhibited the lowest hardness and Young's modulus as compared to the other films, a consequence of the above referred loss of crystallinity. Residual stresses were similar for all coatings (compressive; 3 – 4 GPa) suggesting that the shift of TiN peaks to higher angles should be exclusively attributed to the presence of V and/or Si in solid solution. Moreover, by similar reasons, the small enhancement in the hardness achieved with V additions is probably due to solid solution hardening. Similar correlations could be drawn for TiSiN system in comparison to TiN coating. In relation to the adhesion of films only two failure modes were observed on the scratch tracks of the coatings: the first cracking ( $L_{c1}$ ) and the first chipping ( $L_{c2}$ ). Globally, all the coatings are well adherent to the substrate exhibiting high  $L_c$  values with  $\text{Ti}_{0.82}\text{V}_{0.15}\text{N}$  and  $\text{Ti}_{0.52}\text{Si}_{0.20}\text{V}_{0.14}\text{N}$  being better and worse performing, respectively. In general, Si incorporation in TiN system globally decreased the critical load values of the coatings.



Table 3 –Mechanical properties and residual stresses of the dissimilar coatings.

Specimen	Nano-hardness (GPa)	Young's Modulus (Gpa)	Residual stresses (GPa)	Adhesion critical loads (N)	
				First coating cracking $L_{c1}$	First chipping $L_{c2}$
TiN	23.2 ± 1.8	324 ± 16	3.3	58.2± 1.4	> 70
Ti <sub>0.82</sub> V <sub>0.15</sub> N	24 ± 2	398 ± 21	3.7	62.1± 1.2	> 70
Ti <sub>0.80</sub> Si <sub>0.15</sub> N	27± 2	307 ± 10	3.4	46.0 ± 1.4	62.6± 1.1
Ti <sub>0.75</sub> Si <sub>0.11</sub> V <sub>0.03</sub> N	27 ± 3	327 ± 15	3.7	55.2 ± 1.1	64.6 ± 1.1
Ti <sub>0.65</sub> Si <sub>0.11</sub> V <sub>0.15</sub> N	28 ± 2	328 ± 7	4.1	53.6 ± 1.3	64.8 ± 1.3
Ti <sub>0.52</sub> Si <sub>0.20</sub> V <sub>0.14</sub> N	26± 2	288 ± 12	3.2	42.6 ± 1.1	60.6 ± 1.2

## 3.2 Tribological behaviour

### 3.2.1 The wear rate of coatings and balls

The wear rate of coatings tested at room temperature were dependent on the counterpart material, as shown in Figure 2. Generally, when Al<sub>2</sub>O<sub>3</sub> balls were used as counterparts, the wear rate of coatings was much lower compared to sliding against HSS steel balls. For reference coatings tested with Al<sub>2</sub>O<sub>3</sub> balls, the tribological behaviour of TiN coating was improved when vanadium was added; on the other hand, the addition of Si had a negative effect. As it will be shown later, there is a correlation between the wear rates and the cracking critical load values of these coatings, which suggests a possible relationship with the fracture toughness of the coatings and its influence on the wear debris production.

When Si and V were added simultaneously, V had predominant influence. In fact, any of the TiSiVN coatings showed lower wear rate than the TiN reference, with similar values to Ti<sub>0.82</sub>V<sub>0.15</sub>N sample. It should be remarked that these coatings have, generally, similar L<sub>c</sub> values as Ti<sub>0.82</sub>V<sub>0.15</sub>N, i.e. higher L<sub>c</sub> than the ones measured for Ti<sub>0.80</sub>Si<sub>0.15</sub>N. A similar trend has been observed for other nitride coating systems containing V [7, 14]. Besides the influence of V on the L<sub>c</sub> values, the high wear resistance of V-rich coatings can also be attributed to the formation of V lubricious oxides on the wear track of coatings (see further discussion below). This can explain why Ti<sub>0.52</sub>Si<sub>0.20</sub>V<sub>0.14</sub>N shows lower wear rate than TiN (and Ti<sub>0.80</sub>Si<sub>0.15</sub>N) in spite of its lower L<sub>c</sub> value.

The wear rate of the coatings increased significantly when tested against HSS balls, particularly for the coatings where the V-rich lubricious oxide was identified during the contact with Al<sub>2</sub>O<sub>3</sub> balls. The lower hardness of HSS ball associated with an easier incrustation of hard wear debris in the sliding contact promoted abrasion of the wear track

with increasing wear rates. Limited formation of vanadium oxides led to higher friction coefficient, more energy dissipated and more oxide particles in the wear track, as it will be discussed below.

As expected, the wear rate of the  $\text{Al}_2\text{O}_3$  balls is much lower than that of softer HSS balls. Different trends were found between the wear rates of the coatings and the balls: (i) HSS ball wear rate increased when the coating wear decreased, and (ii) the wear rate of the  $\text{Al}_2\text{O}_3$  balls was very low and almost constant for all the tests. In both cases, the ball surfaces were covered with the wear debris; however, HSS balls show large areas with shallow scratches parallel to the movement of the ball and higher amount of adhered material.

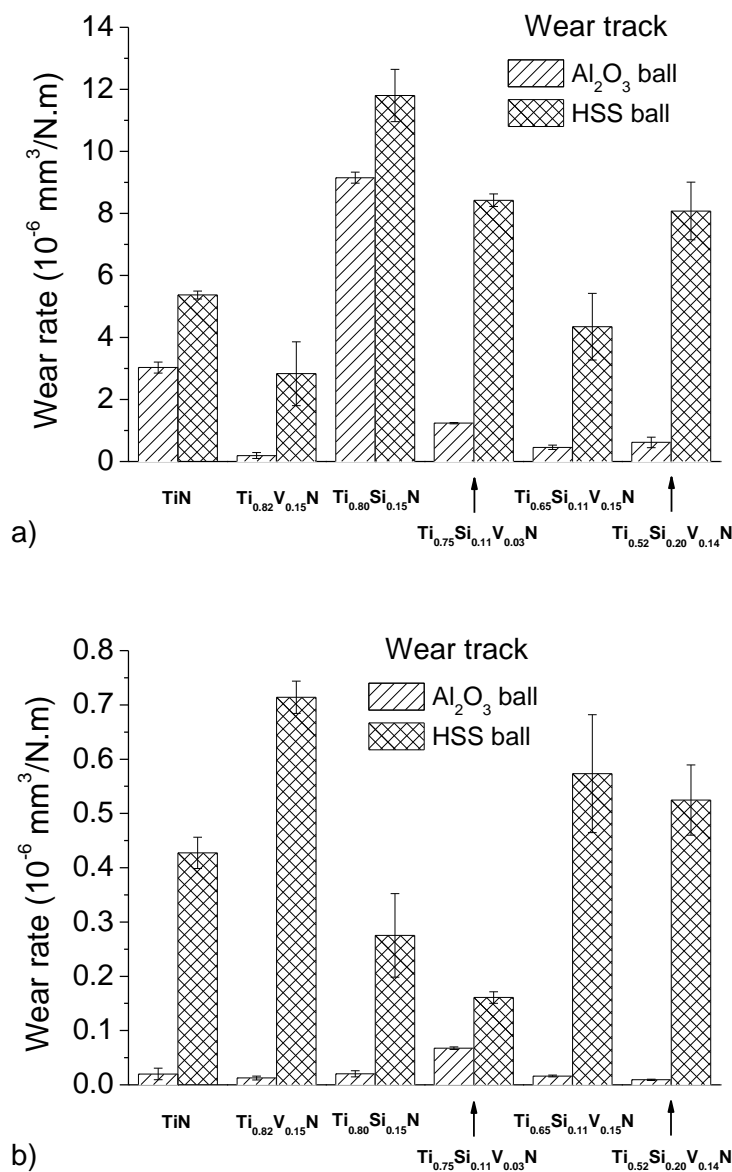


Figure 2 - a) Wear rates of coatings tested against  $\text{Al}_2\text{O}_3$  and HSS balls. b) Wear rates of  $\text{Al}_2\text{O}_3$  and HSS counterparts.

### 3.2.2 Friction coefficient

Figure 3 a) and b) shows the friction coefficient of the coatings tested against  $\text{Al}_2\text{O}_3$  and HSS balls, respectively. As the radius of the wear tracks used for  $\text{Al}_2\text{O}_3$  and HSS balls tests were not the same and consequently, the sliding distances were different, the evolution of the friction coefficient is plotted as a function of the total number of cycles (5000 cycles). All friction curves exhibited two stages: running-in and steady state. Generally, the coatings showed lower friction coefficient values against  $\text{Al}_2\text{O}_3$  showing thus similar trend to the wear rate. The highest friction coefficient was obtained for  $\text{Ti}_{0.80}\text{Si}_{0.15}\text{N}$  coating with values of 1.09 and 1.15 when tested against  $\text{Al}_2\text{O}_3$  and HSS balls, respectively; it should be pointed out that the wear rate was the highest as well. TiN coating presented also a high friction coefficient when tested against  $\text{Al}_2\text{O}_3$  ball, with a large variation in the values with the number of cycles.

Addition of Si and V had a significant impact on the frictional properties when  $\text{Al}_2\text{O}_3$  ball was used as a counterpart. Compared to  $\text{Ti}_{0.80}\text{Si}_{0.15}\text{N}$ , the friction dropped to one half when sufficient amount of vanadium was added and silicon content was kept low; the friction of  $\text{Ti}_{0.65}\text{Si}_{0.11}\text{V}_{0.15}\text{N}$  is below 0.5 being the lowest together with  $\text{Ti}_{0.82}\text{V}_{0.15}\text{N}$  coating. Testing with HSS balls showed only limited influence of coating composition on the friction coefficient. Again TiSiVN coatings exhibited the lowest friction, although it was only about 10% lower than that of  $\text{Ti}_{0.80}\text{Si}_{0.15}\text{N}$  and similar to that of TiN.

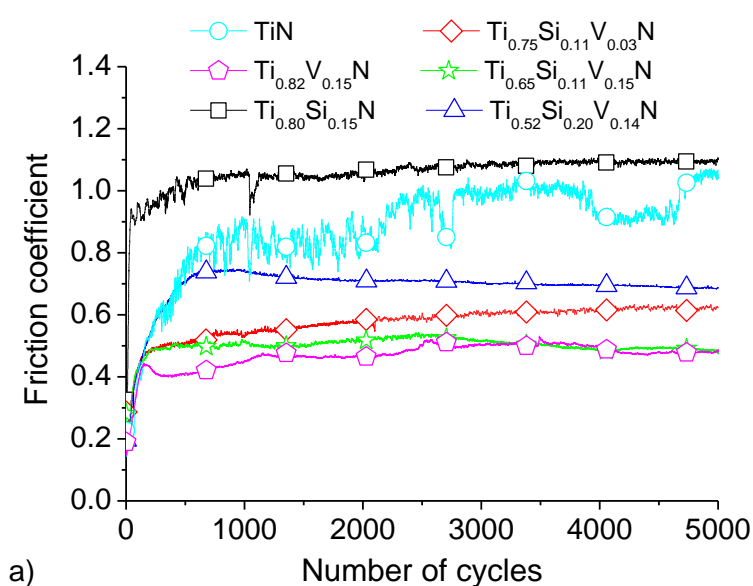


Figure 3 - Friction coefficient vs number of cycles of coatings tested against: a)  $\text{Al}_2\text{O}_3$  balls, b) HSS steel balls.

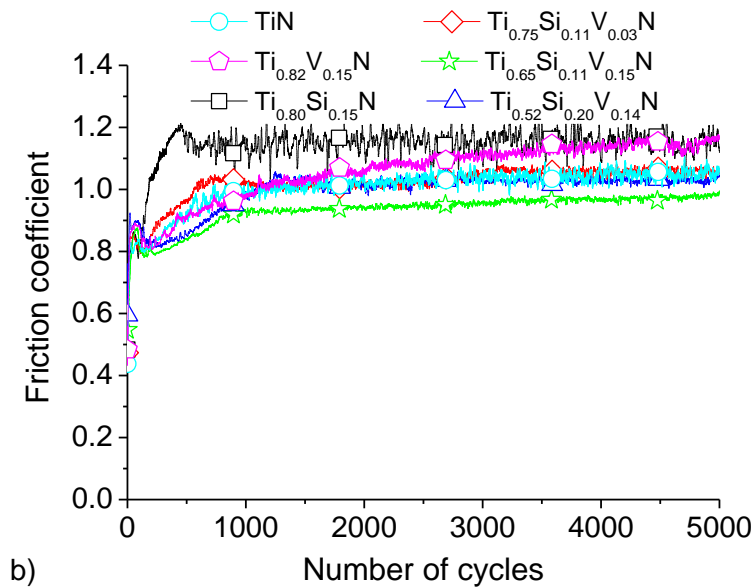


Figure 3 (continued).

### 3.2.3 Wear mechanisms: Sliding against $\text{Al}_2\text{O}_3$ balls

The changes in the friction coefficient and wear rates can be only partially correlated with the structural and mechanical properties of the films. To identify the dominant wear mechanisms scanning electron microscopy with energy dispersive X-ray spectroscopy (SEM-EDS) was used to analyze the worn surfaces and the wear debris produced in the contact. Typical 2D profiles of the wear tracks of the coatings tested against  $\text{Al}_2\text{O}_3$  are depicted in Figure 4 a). Profilometer measurements showed that with the addition of V to TiN and  $\text{Ti}_{0.80}\text{Si}_{0.15}\text{N}$  coatings the wear track became shallower.  $\text{Ti}_{0.80}\text{Si}_{0.15}\text{N}$  and TiN showed the deepest and widest wear tracks among all the coatings, which gave rise to their highest wear rates shown in Figure 2. The wear track of TiN coating was covered by fine scratches parallel to the relative sliding movement suggesting abrasion as the dominant wear mechanism. The scratches ended by the accumulation of the dragged material, which can well explain the fluctuations observed in the friction curve (Figure 5)). EDS analysis performed in the wear track revealed a mixture of as-deposited and oxidized coating material.  $\text{Ti}_{0.80}\text{Si}_{0.15}\text{N}$  coating showed a similar wear mechanism as TiN; however, due to lower fracture toughness the worn particles were larger and scratches deeper. The presence of large non-oxidized particles originated from the coating led to an intensive abrasion of TiN and, particularly,  $\text{Ti}_{0.80}\text{Si}_{0.15}\text{N}$  coating.

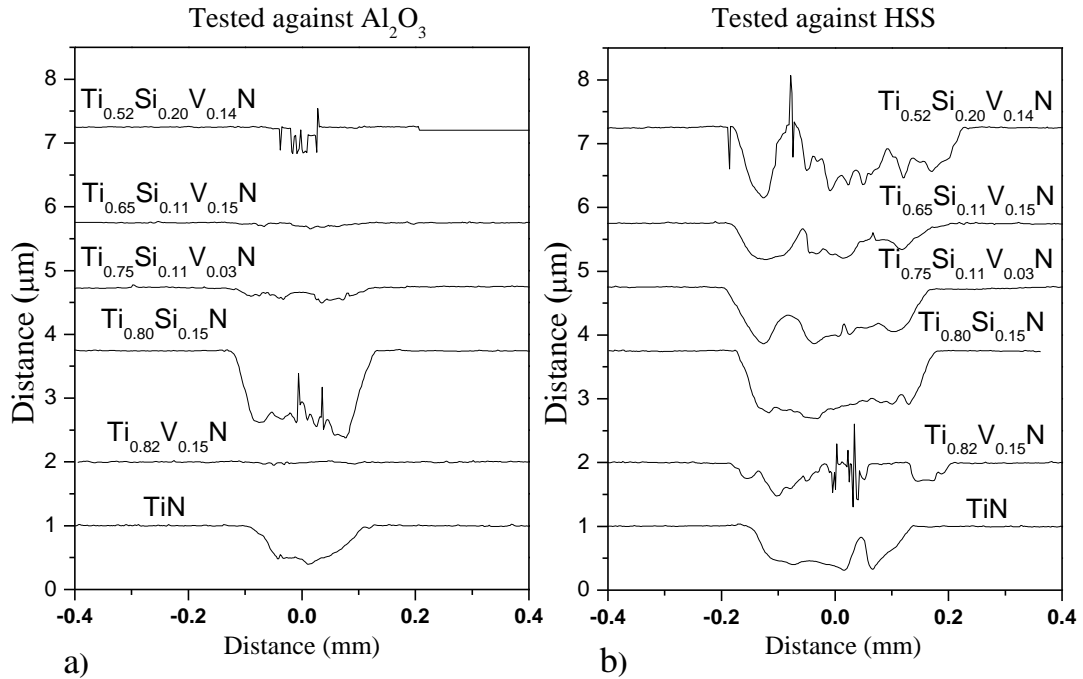


Figure 4 - 2D profiles of the wear track of coatings tested against: a)  $\text{Al}_2\text{O}_3$ , b) HSS.

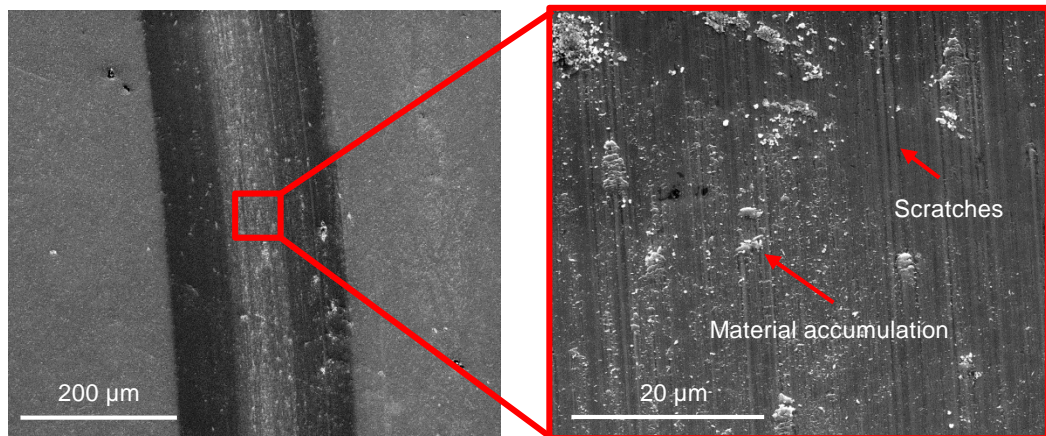


Figure 5 - Wear track of TiN film tested against  $\text{Al}_2\text{O}_3$  ball.

Vanadium-containing coatings exhibited a different wear mechanism. Polishing wear occurred in  $\text{Ti}_{0.82}\text{V}_{0.15}\text{N}$ ,  $\text{Ti}_{0.75}\text{Si}_{0.11}\text{V}_{0.03}\text{N}$  and  $\text{Ti}_{0.65}\text{Si}_{0.11}\text{V}_{0.15}\text{N}$  coatings as demonstrated by smooth worn surfaces (Figure 6 a)) whereas stick-slip adhesion wear occurred in  $\text{Ti}_{0.52}\text{Si}_{0.20}\text{V}_{0.14}\text{N}$  coating resulting in rough surface (Figure 6 b)). The wear track of  $\text{Ti}_{0.65}\text{Si}_{0.11}\text{V}_{0.15}\text{N}$  coating (representative of polishing wear), see Fig. 6 c), showed small black wear debris with vermicular morphology distributed throughout the wear surface. EDS analysis performed at these well adhered wear debris particles showed that they are mainly composed of V and O with traces of Ti and Si, suggesting the presence of V-O, Ti-O and Si-O

oxide phases. It should be remarked that all the other zones of the wear track showed EDS spectra identical to the as deposited films. After the test with  $\text{Ti}_{0.52}\text{Si}_{0.20}\text{V}_{0.14}\text{N}$  coating, the wear scar of the  $\text{Al}_2\text{O}_3$  ball was covered with wear debris forming a transfer layer identified by EDS analysis as a mixture of V-O, Ti-O and Si-O oxides. Friction induced oxidation of wearing surfaces containing vanadium leading to formation of V-O, which acts as a solid lubricant in sliding contact [2, 7, 8]. In this study, thick tribolayer consisting mostly of vanadium oxide was indeed formed on the surface of  $\text{Ti}_{0.82}\text{V}_{0.15}\text{N}$  coating. However, addition of silicon had detrimental effect on tribolayer formation and function during the sliding process. It seems that Si somehow limits the formation of thick well-distributed tribolayer. The higher wear rate and friction coefficient of  $\text{Ti}_{0.75}\text{Si}_{0.11}\text{V}_{0.03}\text{N}$  in relation to  $\text{Ti}_{0.65}\text{Si}_{0.11}\text{V}_{0.15}\text{N}$  coating was in good accordance to the lower amount of “vermicular” debris detected in the wear tracks. Although  $\text{Ti}_{0.82}\text{V}_{0.15}\text{N}$  and  $\text{Ti}_{0.65}\text{Si}_{0.11}\text{V}_{0.15}\text{N}$  showed similar V contents, the higher amount of transfer layer was formed in the case of  $\text{Ti}_{0.82}\text{V}_{0.15}\text{N}$ . The role of Si is not clear, although it is possible that Si-O top layer hinders ion diffusion [15] and thus protects the coating from oxidation required to form sufficient amount of lubricious vanadium oxide.

The worn surface of  $\text{Ti}_{0.52}\text{Si}_{0.20}\text{V}_{0.14}\text{N}$  film was found to be covered by fish-scale-like agglomerates along the worn surface indicating severe shear deformation of the tribofilm during the sliding test [8]. EDS analysis suggested the presence of V-O, Si-O and Ti-O oxides in this zone. Additionally, EDS analysis showed significantly stronger peak of Si in relation to the one found for the other TiSiVN films. Therefore, the oxide layer is dominated by Si-O. Due to low fracture toughness large wear debris particles are detached during the running-in stage; these particles are then either removed from the sliding contact (they were found on the side of the wear track) or oxidized forming adhered oxide layer both on coating and ball surface. However, due to the strong shear force that the ball imposes to the coating, and the more brittle nature of Si-O-rich oxide layer, a stick-slip adhesion process will take place, deforming and breakage the wear debris and giving rise to the above referred fish-like aspect. Therefore, the tribological efficiency will be lower in this coating in relation to the other V-containing films due to the combined effect of: i) lower fracture toughness, ii) less lubricious V-O phase formed due the high Si content and iii) stick-slip adhesion wear mechanism.

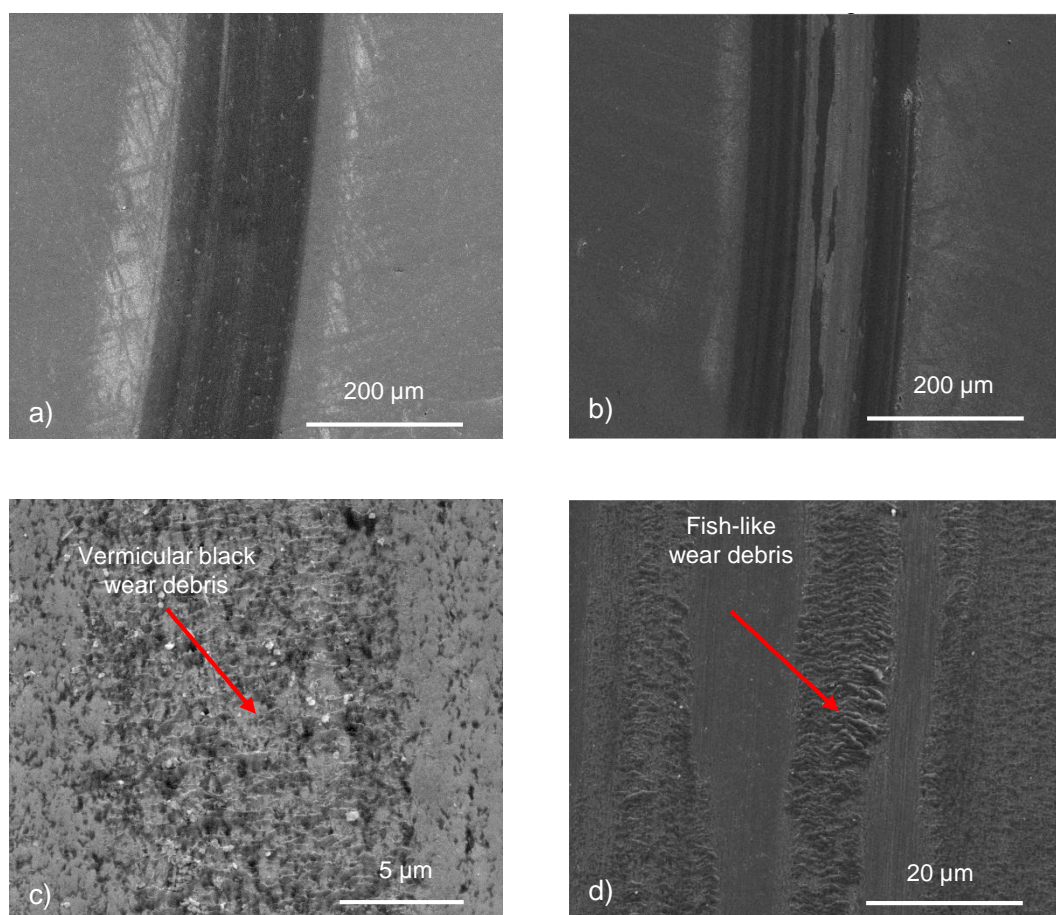


Figure 6 – SEM pictures of the wear track of: a)  $\text{Ti}_{0.65}\text{Si}_{0.11}\text{V}_{0.15}\text{N}$  coating tested against  $\text{Al}_2\text{O}_3$  ball, b)  $\text{Ti}_{0.52}\text{Si}_{0.20}\text{V}_{0.14}\text{N}$  coating tested against  $\text{Al}_2\text{O}_3$  ball, c) and d) magnification of the wear tracks of  $\text{Ti}_{0.65}\text{Si}_{0.11}\text{V}_{0.15}\text{N}$  and  $\text{Ti}_{0.52}\text{Si}_{0.20}\text{V}_{0.14}\text{N}$  coatings, respectively.

### 3.2.4 Wear mechanisms: Sliding against HSS balls

Low hardness of HSS balls compared to  $\text{Al}_2\text{O}_3$  resulted in high ball wear and wide wear tracks (see Figure 4 b)). In fact, one might expect that hard coatings will resist much more to sliding against relatively soft steel ball, whereas  $\text{Al}_2\text{O}_3$  counterpart should induce severe wear damage. However, Figure 2 and Figure 4 clearly indicate opposite behavior, i.e. higher wear with HSS balls.

Reference TiN and  $\text{Ti}_{0.80}\text{Si}_{0.15}\text{N}$  coatings exhibited slightly different wear track appearance. Figure 7 shows the typical morphology of the worn surfaces of these coatings and the corresponding wear scars of the balls. EDS analysis performed on the transfer layer of TiN coating, which was preferential formed in the central part of the wear track, evidenced material transfer from the ball to the coating surface. The transfer layer thus consisted of titanium and iron oxides. However, no oxygen was detected by EDS outside of the center part of unworn coating. Although the wear scars of the counterparts were covered with as-

deposited and oxidized material from the coating for both TiN and  $\text{Ti}_{0.80}\text{Si}_{0.15}\text{N}$  coatings, the latter exhibited higher material transfer to the HSS ball and, particularly, larger wear debris particles. Hard non-oxidized particles embedded into compact adhered tribolayer act as sharp cutting edges causing abrasive damage and accelerating wear. On the other hand, relatively thick and well-adhered layer on the ball wear scar protected ball material from further damage; thicker layer built during sliding against on  $\text{Ti}_{0.80}\text{Si}_{0.15}\text{N}$  resulted in lower ball wear (Figure 2 b)). It is clear here that higher amount of non-oxidized debris adhered on the ball protects the ball itself but produces higher wear of the coating; the absence of well-developed oxide layer on the coating surface is detrimental decreasing coating wear resistance.

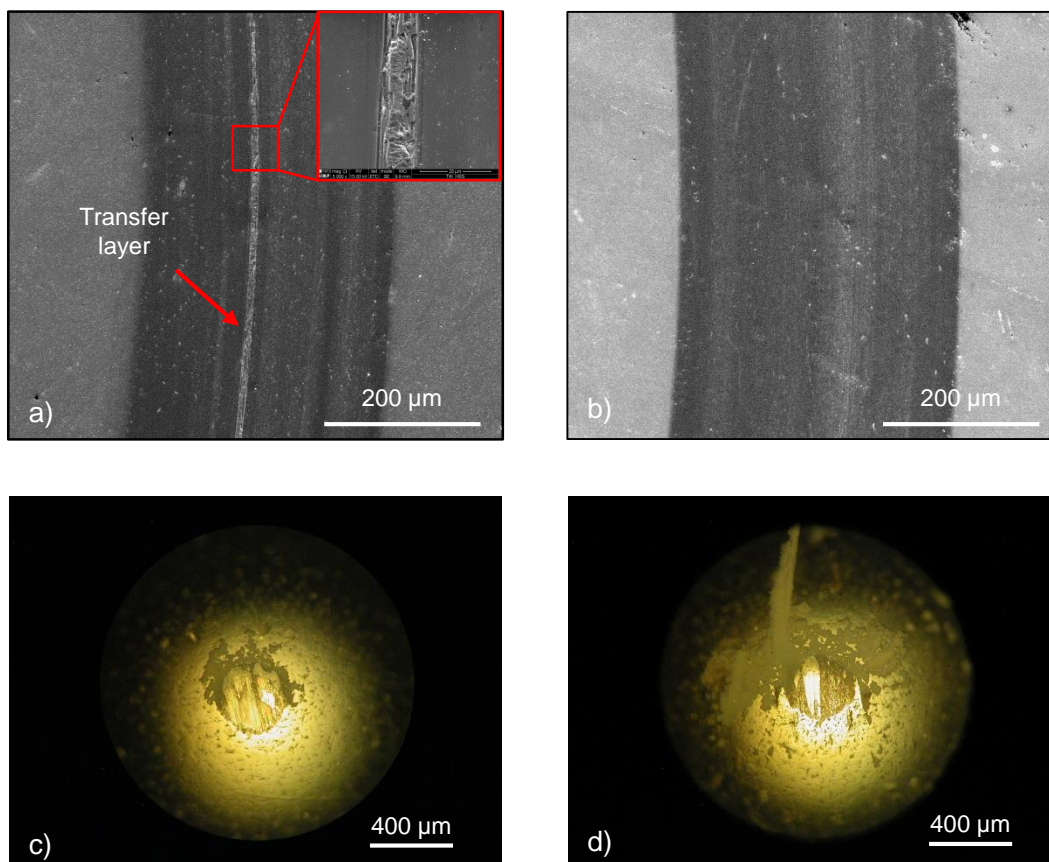


Figure 7 – Wear tracks induced by HSS ball sliding in: a) TiN coating, b)  $\text{Ti}_{0.80}\text{Si}_{0.15}\text{N}$  coating. Wear scar on HSS balls tested against: c) TiN coating, d)  $\text{Ti}_{0.80}\text{Si}_{0.15}\text{N}$  coating.

Absence of continuous tribolayer in the wear track was observed as well for the coatings containing vanadium. Typical worn surfaces of the coatings ( $\text{Ti}_{0.82}\text{V}_{0.15}\text{N}$  and  $\text{Ti}_{0.65}\text{Si}_{0.11}\text{V}_{0.15}\text{N}$ ) shown in Figure 8 were covered by stripes of adhered material, which covered only small part of the wear tracks, see Figures 8 a) and b), indicating that the wear is driven by a combination of adhesion and polishing wear. EDS analysis revealed that the stripes were composed of fully oxidized (i.e. no nitrogen observed) coating elements mixed



with iron originating from the ball. Outside of the stripes no oxygen was identified by EDS. The phenomenon of adhesive wear behaviour was believed to be a result of hard film and relatively soft bearing ball [16]. Nevertheless, some of the V-O oxide present on the stripe zones should still provide a lubricious effect since a decrease of the wear rate with V incorporation is observed. This behaviour is enhanced in case of  $\text{Ti}_{0.52}\text{Si}_{0.20}\text{V}_{0.14}\text{N}$  coating where an even higher wear rate is observed; its lower fracture toughness, due to the higher silicon content, constrains the V-O phase formation decreasing even more its content on the wear track.  $\text{Ti}_{0.82}\text{V}_{0.15}\text{N}$  film displayed the lowest wear rate of all the coatings due to the higher amount of V-O oxide formed at the surface.

In summary, we demonstrated that V additions successfully reduced the wear rate and friction coefficient of TiSiN system; moreover we also showed that the tribological behaviour of films is strongly dependent on the counterpart material due to the presence of dissimilar wear mechanisms.

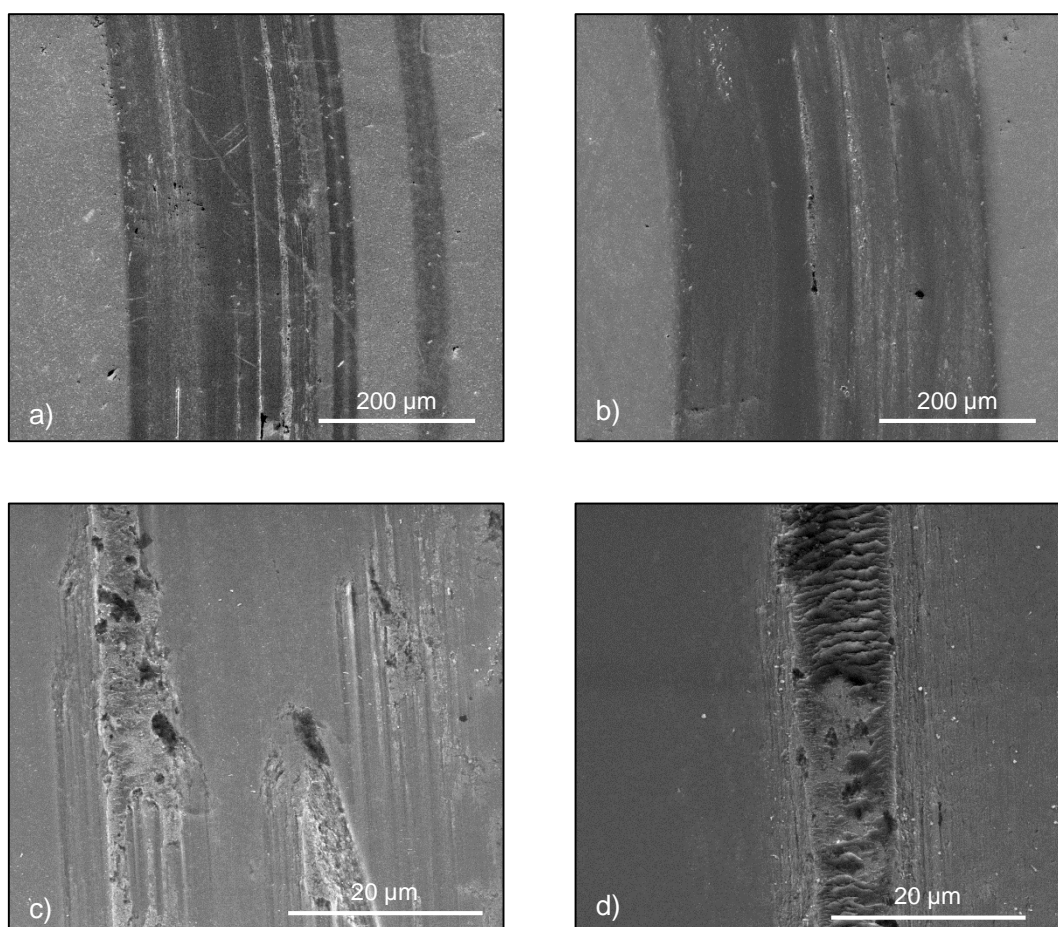


Figure 8 - SEM pictures of the wear track tested against HSS balls of: a)  $\text{Ti}_{0.82}\text{V}_{0.15}\text{N}$  coating, b)  $\text{Ti}_{0.65}\text{Si}_{0.11}\text{V}_{0.15}\text{N}$  coating. c) and d) magnification of the wear tracks of  $\text{Ti}_{0.82}\text{V}_{0.15}\text{N}$  and  $\text{Ti}_{0.65}\text{Si}_{0.11}\text{V}_{0.15}\text{N}$  coatings, respectively.

## 4. Conclusion

The results showed that alloying TiSiN system with increasing V content improves the resistance to wear and decreases the friction coefficient; however, the tribological behaviour is strongly dependent of the counterbody ball material. SEM and Raman analysis revealed that the influence of V was due to the formation of V-O lubricious oxide on the contact zone. When Al<sub>2</sub>O<sub>3</sub> balls were used in the tests, the wear was driven by polishing wear and oxides containing V-O are spread all over the wear track. On the other hand, when tested against HSS balls, adhesion wear took place with material transfer from the ball to specific zones of the wear track, being the lubricious effect of V-O significantly reduced. Ti<sub>0.80</sub>Si<sub>0.15</sub>N film displayed the lowest wear resistance among all the tested coatings due to its lower fracture toughness which promotes the formation of bigger wear debris acting as strong abrasion players.

## Acknowledgments

This research is sponsored by FEDER funds through the program COMPETE – Programa Operacional Factores de Competitividade – and by national funds through FCT – Fundação para a Ciência e a Tecnologia –, under the project: PTDC/EME-TME/122116/2010, as well as the grant (SFRH/BD/68740/2010).

## References

- [1] J.H. Ouyang, T. Murakami, S. Sasaki, *Wear*, 263 (2007) 1347-1353.
- [2] W. Tillmann, S. Momeni, F. Hoffmann, *Tribology International*, 66 (2013) 324-329.
- [3] E. Lugscheider, O. Knotek, K. Bobzin, S. Bärwulf, *Surf. Coat. Technol.*, 133–134 (2000) 362-368.
- [4] N. Fateh, G.A. Fontalvo, G. Gassner, C. Mitterer, *Wear*, 262 (2007) 1152-1158.
- [5] R. Franz, J. Neidhardt, R. Kaindl, B. Sartory, R. Tessadri, M. Lechthaler, P. Polcik, C. Mitterer, *Surf. Coat. Technol.*, 203 (2009) 1101-1105.

- 
- [6] Y. Qiu, S. Zhang, J.-W. Lee, B. Li, Y. Wang, D. Zhao, *Applied Surface Science*, 279 (2013) 189-196.
- [7] M. Pfeiler, K. Kutschej, M. Penoy, C. Michotte, C. Mitterer, M. Kathrein, *International Journal of Refractory Metals and Hard Materials*, 27 (2009) 502-506.
- [8] Q. Luo, *Wear*, 271 (2011) 2058-2066.
- [9] K. Kutschej, P.H. Mayrhofer, M. Kathrein, P. Polcik, C. Mitterer, *Surf. Coat. Technol.*, 200 (2005) 1731-1737.
- [10] F. Fernandes, A. Loureiro, T. Polcar, A. Cavaleiro, *Applied Surface Science*, 289 (2014) 114-123.
- [11] European Committee for standardization, *European Standard DIN ENV 1071-3* (1994), draft *European Standard prEN 1071-3*, (2002).
- [12] G.G. Stoney, *Proceedings of the Royal Society of London. Series A*, 82 (1909) 172-175.
- [13] S.H. Kim, J.K. Kim, K.H. Kim, *Thin Solid Films*, 420–421 (2002) 360-365.
- [14] K. Kutschej, P.H. Mayrhofer, M. Kathrein, P. Polcik, C. Mitterer, *Surf. Coat. Technol.*, 188–189 (2004) 358-363.
- [15] F. Deschaux-Beaume, N. Frety, T. Cutard, C. Colin, *Ceram. Int.*, 35 (2009) 1709-1718.
- [16] C.-L. Chang, C.-T. Lin, P.-C. Tsai, W.-Y. Ho, D.-Y. Wang, *Thin Solid Films*, 516 (2008) 5324-5329.